Supergene Mineralisation of the Boyongan Porphyry Copper-Gold Deposit, Surigao del Norte, Philippines

by

Allan Maglaya Ignacio
B.Sc. Geology, National Institute of Geological Sciences
University of the Philippines

Thesis submitted in partial fulfilment of the requirements of the Masters of Economic Geology Degree

Centre for Ore Deposit Research,
University of Tasmania

December, 2005

DECLARATION OF ORIGINALITY

This thesis contains no material which has been accepted for a degree of diploma by the University of Tasmania or any other institution, except by way of background information and duly acknowledged in the thesis, and contains no previous material previously published or written by another person except where due acknowledgement is given.

Allan Maglaya Ignacio

01 December 2005

_____

STATEMENT OF AUTHORITY OF ACCESS

This thesis may not to be made available for loan or copying for 1.5 years following the date this statement was signed. Following that time, the thesis may be available for loan and limited copying in accordance with *Copyright Act 1968*.

Allan Maglaya Ignacio

01 December 2005

_____

TABLE OF CONTENTS

LIST OF FIGURES

Page

LIST OF APPENDICES

ACKNOWLEDGEMENTS

- Thanks to all geologists and staff who were involved in the Boyongan project: Oliver Briola, Joel Briones, Edith Cabanisas, Andy Cabrera, Gerry Comia, Manny Corpuz, Rey Estacio, Max Estaris, Toto Grafil, Chona de Guzman, Letty Faguingas, Ray Flores, Ian Furigay, Rene Gonzales, Nory Juacalla, Eric Laurio, Noli Nuñez, Gabby Ogad, Melodie Pascual, Sanny Reyes, Hermie Santos and Norman Tamayo. The discovery of Boyongan would not be possible without their valuable contribution and skills.

- Thanks to Mr. Patrick J. Waters, Exploration Manager of Anglo American Exploration (Philippines), Inc. for believing in me and giving me the opportunity to undertake this Masters of Economic Geology project.

- Dr. Richard Sillitoe has greatly helped the Philippine team develop a geological model for the deposit. Thanks to Dick for his advises on how I should go about this Masters project.

- Thanks to Dr. David Cooke, Dr. Andrew Rae, and Dr. Anthony Harris, and Dave Braxton (PhD Student) of CODES for their constructive comments. Dr. Dave Cooke for patiently and meticulously editing this thesis. More thanks to Dave Braxton for teaching me how to use MS Access database, linking data to Map Info and helping me organise my data.

- Special thanks to Hermie Santos for his patience in teaching me how to use Map Info. It greatly helped me analysing data and plot all the figures that have been used in this thesis. And to Manny Corpuz who provided me all the desurveyed data from the main geological database.

- Special thanks to Simon Stephens for patiently preparing my thin sections, to Dr. David Steele of the Central Science Laboratory for analysing selected thin sections using the electron probe microanalyser, and to Christine Cook for analysing my samples for carbon and oxygen isotopes.

- To my family who has been a source of my inspiration. They have been very patient with me even though I work long hours at home.

- To our Lord God who was always been there to guide me.

ABSTRACT

Boyongan is a blind copper-gold porphyry deposit that was discovered by Anglo American Exploration (Philippines), Inc. in August 2000. It is located in Surigao del Norte, Philippines. Current inferred mineral resources for Boyongan are estimated at 219 million tonnes of combined oxide and sulfide material with an average grade of 0.51% copper and 0.74 grams of gold per tonne. Most of the high-grade mineral resource is within the oxide (supergene zone).

Deep oxidation at Boyongan has developed a thick supergene enrichment profile (up to 600 meters) which has a complex supergene mineralogy, consisting of chalcocite, digenite, pseudo-covellite, native copper, cuprite, malachite, pseudo-malachite, azurite, chrysocolla, pseudo-chrysocolla, and pseudo-neotocite. Fine gold (<100μm) has been observed in goethite, chalcocite, chrysocolla, and malachite. Supergene mineralisation is associated with iron oxides (goethite with minor hematite) and clays (kaolinite, halloysite, illite and montmorillonite). Oxidation and the development of supergene minerals has been controlled mainly by fracturing and the availability of hypogene sulfides. The low pyrite content of hypogene mineralisation at Boyongan allowed supergene mineralisation to develop in-situ from near-neutral pH groundwaters.

The initial stages of supergene mineralisation involved the replacement of hypogene sulfides such as chalcopyrite and bornite by chalcocite, digenite and pseudo-covellite. In some places, chalcocite replaced pyrite. Goethite formed during the weathering of pyrite, chalcopyrite, bornite and chalcocite. Copper that was released into solution precipitated as native copper, which has replaced chalcocite locally. Native copper was then oxidised to form cuprite, and also acicular and euhedral crystals of chalcotricite. Some cuprite may have precipitated directly from solution, and also where chalcocite reacted with oxygenated groundwaters. The final stages of supergene copper mineralisation at Boyongan produced

copper carbonate (malachite, pseudo-malachite, azurite and pseudo-neotocite) and a copper silicate overprint (chrysocolla and pseudo-chrysocolla) onto earlier-formed copper oxides and sulfides.

Copper generally has a more dispersed or erratic distribution than gold. Gold is restricted spatially to the early mineral intrusions. Copper grades in the cuprite-dominated zone in the west generally decrease with depth toward zones of patchy native copper. The copper carbonate (malachite-azurite)-dominated blanket above the cuprite zone contains both high grade copper and gold (>1% and >2 g/t, respectively). Chalcocite zones that have partially replaced hypogene copper sulfides have higher grades (>0.5% Cu and >1g/t Au) compared to zones of chalcocite replacing pyrite (<0.5% Cu and <0.5g/t Au). Chrysocolla and/or pseudo-chrysocolla is confined to zones that contain high copper and gold grades (>0.5% and >1 g/t, respectively).

Isotopic compositions of malachite and azurite from Boyongan are consistent with deposition from ambient temperature (15°C to 20°C) meteoric water. These low temperatures are consistent with Boyongan being a low-sulfide porphyry system. Higher pyrite contents would probably have led to greater degrees of sulfide oxidation as well as higher groundwater temperatures. $\delta^{13}C$ values of malachite are consistent with an organic carbon (soil?) source suggesting that malachite may have formed when Boyongan was uplifted and exposed. $\delta^{13}C$ values of azurite are much higher, and could be derived from seawater, or by remobilisation of an inorganic carbon from carbonate wallrocks, or by sulfide oxidation by supergene-related bacteria above the water table.

CHAPTER 1

INTRODUCTION

1.1 INTRODUCTION

Supergene copper mineralisation is formed when hypogene copper minerals are dissolved, carried and transported into solution, and re-deposited during weathering (Chavez, 2000). Residual iron and copper minerals can be used to interpret and understand the origin of supergene mineralisation and can lead to the discoveries of economic primary hypogene copper sulfide mineralisation (Anderson, 1982; Wilson, 2003).

Boyongan is a porphyry copper-gold deposit discovered in August 2000 by Anglo American Exploration (Philippines), Inc. (AAEPI). It is located in northern Surigao (Fig. 1.1). It possesses a substantial supergene mineralisation profile. The supergene zone profile extends up to 650 meters below the paleosurface, making it the most substantial in the Philippines (Sillitoe and Gappe, 1984), and one of the thickest supergene profiles associated with porphyry style mineralisation globally.

1.2 AIMS & OBJECTIVES

The aim of this project is to investigate the development and preservation of supergene mineralisation at Boyongan. In order to understand the deposit, the following questions will

be investigated:

- Supergene mineralogy and zonation - What is the composition and distribution of the supergene mineralisation?

- Copper and gold grade distribution and metal zonation - What is the relationship between the supergene profile and grade distribution? Where does gold occur in the supergene profile?

- Carbon and oxygen Isotopes - What is the source of the carbon in the secondary copper carbonates? Was the supergene profile developed during uplift, or was it developed after burial underneath lacustrine sediments and/or marine sediments?

The project aims to increase our understanding of the supergene mineralising processes at Boyongan, and to help guide exploration for similar types of supergene mineralised zones elsewhere in the Philippines and in southeast Asia.

This thesis provides a brief review of the deposit setting, including regional and local geology, and the hypogene mineralisation and alteration assemblages. Igneous petrology and geochemistry, detailed paragenetic relationships, geochronology, hypogene fluid chemistry, and uplift, exhumation and burial history of the Boyongan porphyry are currently being studied as a separate PhD project (Braxton, in prep.) and are therefore outside the scope of the current study.

1.3 METHODS EMPLOYED

Most of the work reported in this thesis has focussed on documenting the supergene mineralogy and zonation of Boyongan through core logging on two cross-sections (1062200N & 779700E), with drillholes projected into section from a maximum distance of

100 meters. Selected samples were analysed petrographically by the author to identify the mineral paragenesis. This has been supplemented by electron probe analyses to confirm mineral compositions, and by carbon-oxygen isotope analyses to determine the sources of carbon and oxygen in the supergene carbonates. PIMA (Portable Infrared Mineral Analyser) analyses were undertaken during the core logging exercise in Surigao. PIMA samples were analysed with an average spatial interval of 20 meters.

With the exception of the PIMA samples, all sample preparation and analytical work was undertaken at the Centre for Ore Deposit Research (CODES) and the Central Science Laboratory (CSL) at the University of Tasmania, Hobart, Australia.

1.4 LOCATION & ACCESSIBILITY

The Boyongan porphyry copper-gold deposit is located at the northeast tip of the island of Mindanao, Philippines (Fig. 1.1A). It is centered at 09°36'00"N latitude and 125°33'00"E longitude, and is situated within the municipalities of Placer and Tubod in the province of Surigao del Norte. It is approximately 22 kilometers SSE of Surigao City. There are regular direct flights from Manila to Surigao City (Fig. 1.1B). Boyongan can be accessed from a sealed highway that connects the cities of Surigao and Butuan. It is approximately 34km by road from Surigao City and another 2.7km on a gravel-paved road west from the main highway. Within the area, there are abundant foot trails that are used by local villagers to transport farm products. These were used by the drilling contractor to move drilling supplies and consumables.

The project area occurs in rolling countryside in the foothills of the central highlands of Surigao del Norte. The two most prominent andesite peaks within the project are Hill 664

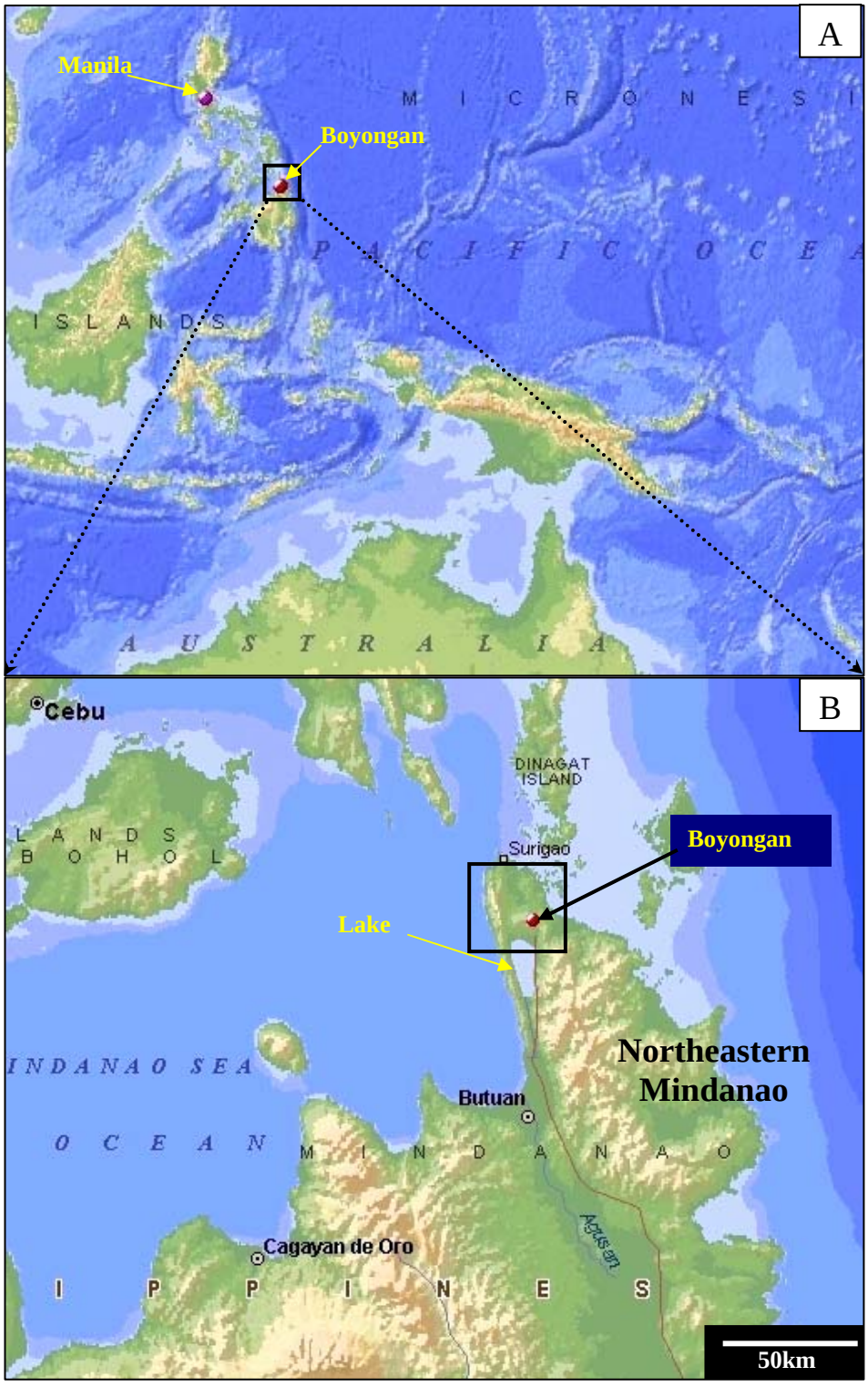

Fig. 1.1. A. Location of Boyongan in the Philippines **B.** An enlarged map from Fig. 1.1A. showing location of Boyongan in Northeastern Mindanao, Philippines. Lake Mainit is located south of Boyongan (modified from Microsoft Encarta World Atlas, 1998 Edition). The square represents the location of Figures 1.2 & 2.2

(664m elevation; UNDP, 1987), and Mt. Maniayao (644m elevation). The study area is drained by major river systems such as the Surigao River and Bayugo River to the north, which dumps their sediment load at river mouths in Surigao City and Placer, respectively (Fig. 1.2). To the south is the Timamana Creek, which is a major tributary of Magpayang River. This river descends into Lake Mainit (Figure 1.2). The Timamana limestone in the eastern highlands forms a high relief karstic topography with internal drainage and steep subvertical slopes (UNDP, 1987). In general, upland slopes are covered with coconut, other various crops, cogon grass, and secondary bush. The lowland areas mostly contain rice paddies.

1.5 CLIMATE

Surigao del Norte is hot and humid. It falls within the type II climate of the Philippines. This means that it has no definite wet or dry season. Heaviest rainfalls occur from November to January, when occasional typhoons occur. The average annual rainfall is 3.67m based on 50-year period. It is one of the wettest parts of the Philippines, with an average of 216 rainy days per year. Temperature ranges from 25°C to 31°C, averaging 27° C. The average humidity is approximately 85% (source: http://www.xs4all.nl/~jwjgendt/ surigao.html & http://202.90.139.50/placer).

1.6 PREVIOUS WORK

The earliest work on the Surigao district was regional mapping done by Crump (1941) and Santos-Yñigo (1944). Following this, a slightly modified stratigraphy on the Northern Diwata Range, covering the province of Surigao del Norte, was reported by the Mines and Geosciences Bureau (1981). These reports, however did not mention the Boyongan area.

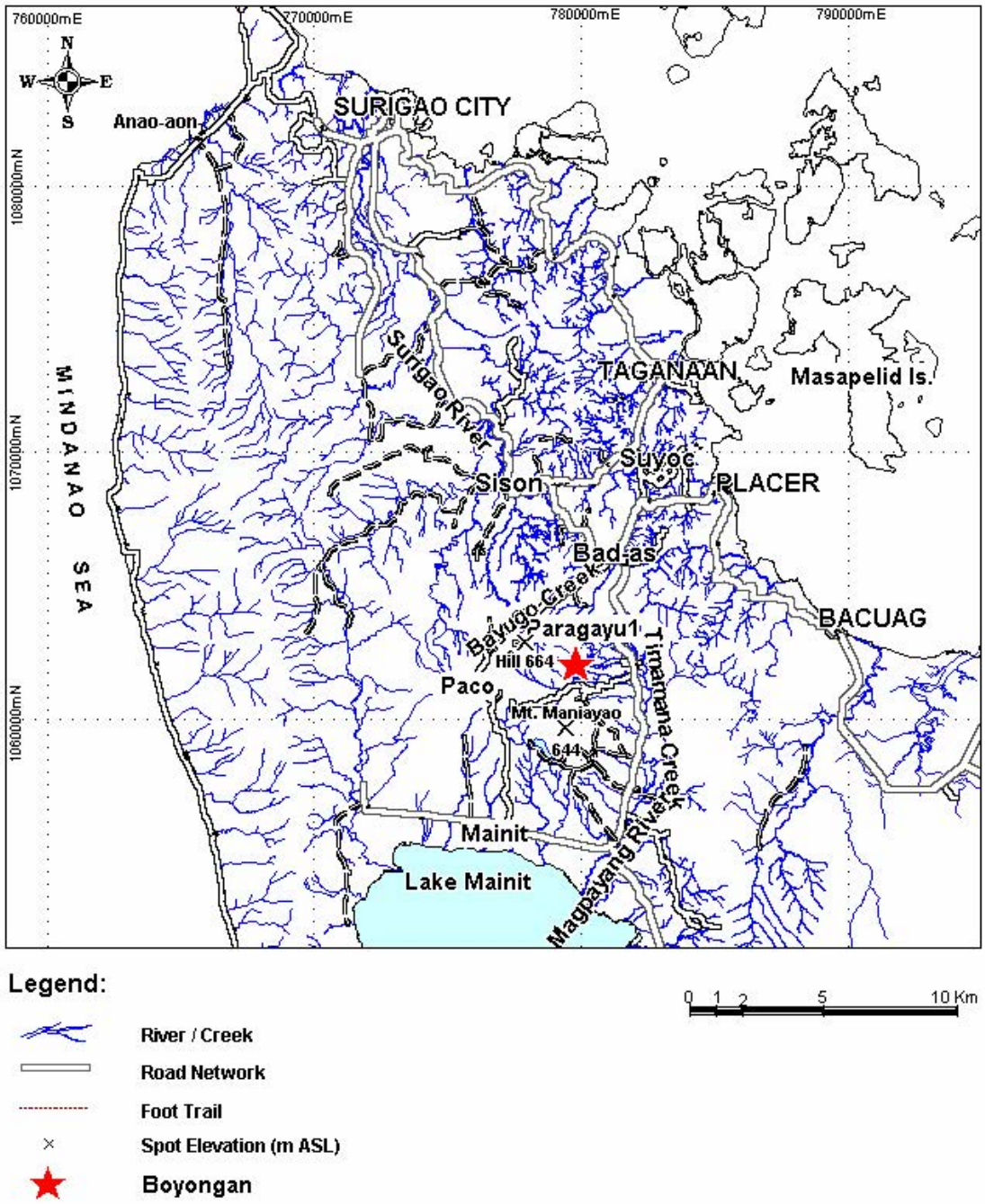

Fig. 1.2. Map showing creeks, rivers, roads, trails, and selected localities within the vicinity of Boyongan, Surigao del Norte, Norteastern Mindanao, Philippines

The United Nations Development Program (UNDP, 1987) conducted regional mapping and prospect definition in Surigao del Norte. They modified the regional stratigraphy of Surigao District proposed by Santos-Yñigo (1944) and recommended Boyongan and

Bagacay as areas worthy of follow-up investigations due to the presence of both mineralised and altered rocks and geochemical anomalies in stream sediments.

A reconnaissance geological and geochemical survey of tenements held by Philex Mining Corporation was conducted on January 1998 by AAEPI. This survey defined third order -80 mesh drainage anomalies at Boyongan to 225 ppb Au (Waters, et. al., 2001). Follow-up work on the drainage anomaly located mineralised diorite float with quartz stockworks, including samples with 2.49% Cu and 3.99g/t Au, and also 2.18% Cu and 0.64g/t Au. Detailed stream sediment sampling in conjunction with mineralised boulder sampling, soil geochemistry and detailed geological mapping was carried out over an area of 11 km^2 to determine the source of the mineralised boulders. The eleventh hole (TSD06) resulted in the discovery of the Boyongan deposit on August 2000. This hole intersected supergene copper mineralisation in potassic altered diorite breccia beneath 57 meters of post-mineral cover. The weighted average value of the intercept from 93 to 422 meters (329 meters) was 0.90% Cu and 2.07g/t Au (Waters, 2002). Waters et al. (2001) and Waters (2002) provide detailed descriptions of the methods employed in the discovery of Boyongan, and also document the current understanding of the local geology. Although Waters et al. (2001) and Waters (2002) described the supergene mineral assemblages in general, the spatial and temporal relationships of these assemblages has not been documented previously. This is the main topic of the current thesis.

The detailed information given in the following two chapters (Chapter 2 & 3), which discuss the geological setting and hypogene alteration/mineralisation, including regional/ prospect geological maps, geological cross-sections and plans, has been compiled from original work done by Anglo American geologists and consultants. These pre-existing data

provide the geological background upon which this thesis has been built. Chapters 4 to 7 on supergene alteration and mineralisation, metal zoning, carbon-oxygen isotope geochemistry and supergene ore genesis and implications to exploration are new and original work conducted by the author for the purposes of this Masters thesis.

CHAPTER 2

GEOLOGICAL SETTING

2.1 Introduction

This chapter reviews the tectonic setting of Surigao del Norte, and the regional and local stratigraphy at Boyongan, in order to better understand the controls of mineralisation of the Boyongan porphyry Cu-Au deposit.

2.2 Regional Tectonics

Surigao del Norte has a complicated regional geology and structural setting, which is a product of Miocene to Recent interaction of the Philippine Archipelago (southeastern portion of the Eurasian plate) and the Philippine Sea Plate. The Philippine trench marks the boundary between the Eurasian and Philippine Sea Plates (Fig. 2.1).

The Surigao gold district is located on the northern tip of the Eastern Mindanao Cordillera (Fig. 2.1 & 2.2). It is bounded to the east by the Philippine trench and to the west by the Philippine fault, two of the most active tectonic features in the Philippines (Fig. 2.2). The left-lateral strike-slip Philippine Fault accomodates oblique convergence of the Philippine Sea Plate and the Eurasian Plate. In northeastern Mindanao, there is a releasing bend in the Philippine fault where it changes from a NNW-strike in the north to N-striking in the south

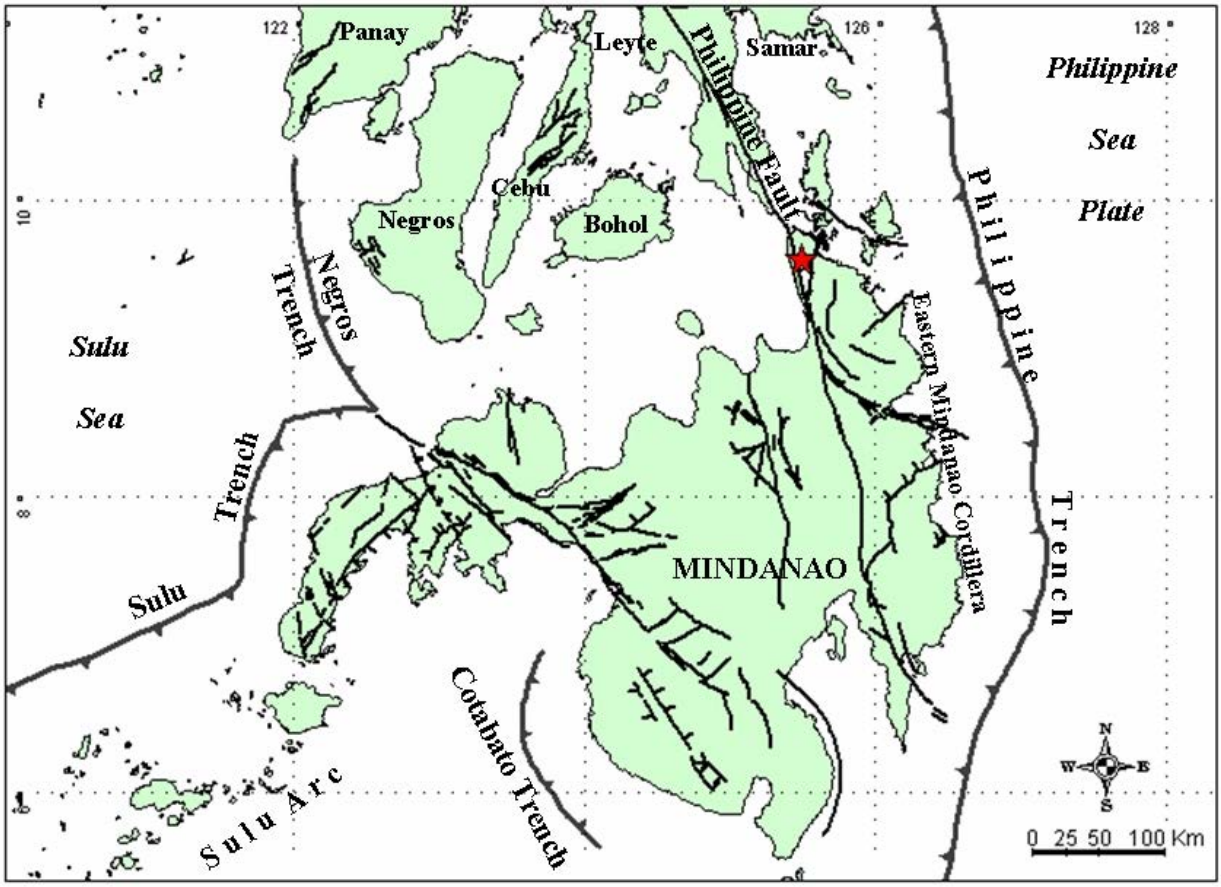

Fig. 2.1. The major tectonic features of Mindanao are the Philippine trench, the Philippine left-lateral strike-slip fault system, and the Cotabato Trench. Boyongan (marked by a red star) is located north of the Eastern Mindanao Cordillera, and occurs within the Philippine fault system

(Fig. 2.2). This releasing bend has induced local extension, with NE-trending extensional structures (horsts and grabens) developed within the Surigao district. The Pliocene Boyongan Porphyry Cu-Au deposit is located at the intersection between the NE-trending Placer and NW-trending Siana structures (Fig. 2.2) suggesting that the extensional fault architecture was important for localising magmatic-hydrothermal activity.

Lake Mainit (Fig. 2.2) occupies accommodation space created by a dilational jog or a pull-apart basin in the Philippine Fault system. It forms part of the Mainit Graben, whereas the western and eastern mountain ranges form the horst blocks (Fig. 2.2).

2.3 Regional & Local Stratigraphy

This section describes the regional and local geology of the Boyongan porphyry Cu-Au deposit. The stratigraphic sequences that occur in northern Surigao (Fig. 2.2) are in most cases observed locally at Boyongan (Fig. 2.4). Descriptions of the stratigraphic units are based mainly on the author's drillcore observations, coupled with petrographic studies from Sinclair Knight Merz (SKM, 2000-2003). No petrographic descriptions of the regional rock units were conducted as part of the current study.

2.3.1 Basement (Cretaceous-Paleogene)

In Surigao del Norte, the stratigraphic sequence ranges from Cretaceous to Quaternary (Fig. 2.2). The oldest rock units are **Cretaceous - Paleogene** serpentinized harzburgites, metasediments and schists of the Dinagat-Surigao Ophiolite and the Western Coastal Range (UNDP, 1987). At Boyongan, the Cretaceous ophiolitic and metamorphic rocks have not been intersected in drillhole.

2.3.2 Bacuag Formation (Oligocene-Miocene)

The Cretaceous basement is overlain unconformably by the **Oligocene-Miocene Bacuag Formation**, which consists of basalt flows, basaltic volcaniclastic rocks, and inter-bedded limestone, mudstones and calcareous mudstones (UNDP, 1987). The Bacuag Formation is well exposed in the eastern portion of the Surigao district (Fig. 2.2 & 2.3B). Calcareous beds within the Bacuag formation host gold mineralisation at the Siana deposit (Fig. 2.2). Relative ages of rock units have been obtained from fossil fauna in limestone, yielding ages of Upper Oligocene to Lower Miocene (UNDP, 1987). A K-Ar whole rock age of 23 ± 1.1 Ma has been obtained for a basalt flow (UNDP, 1987). This formation is estimated to be

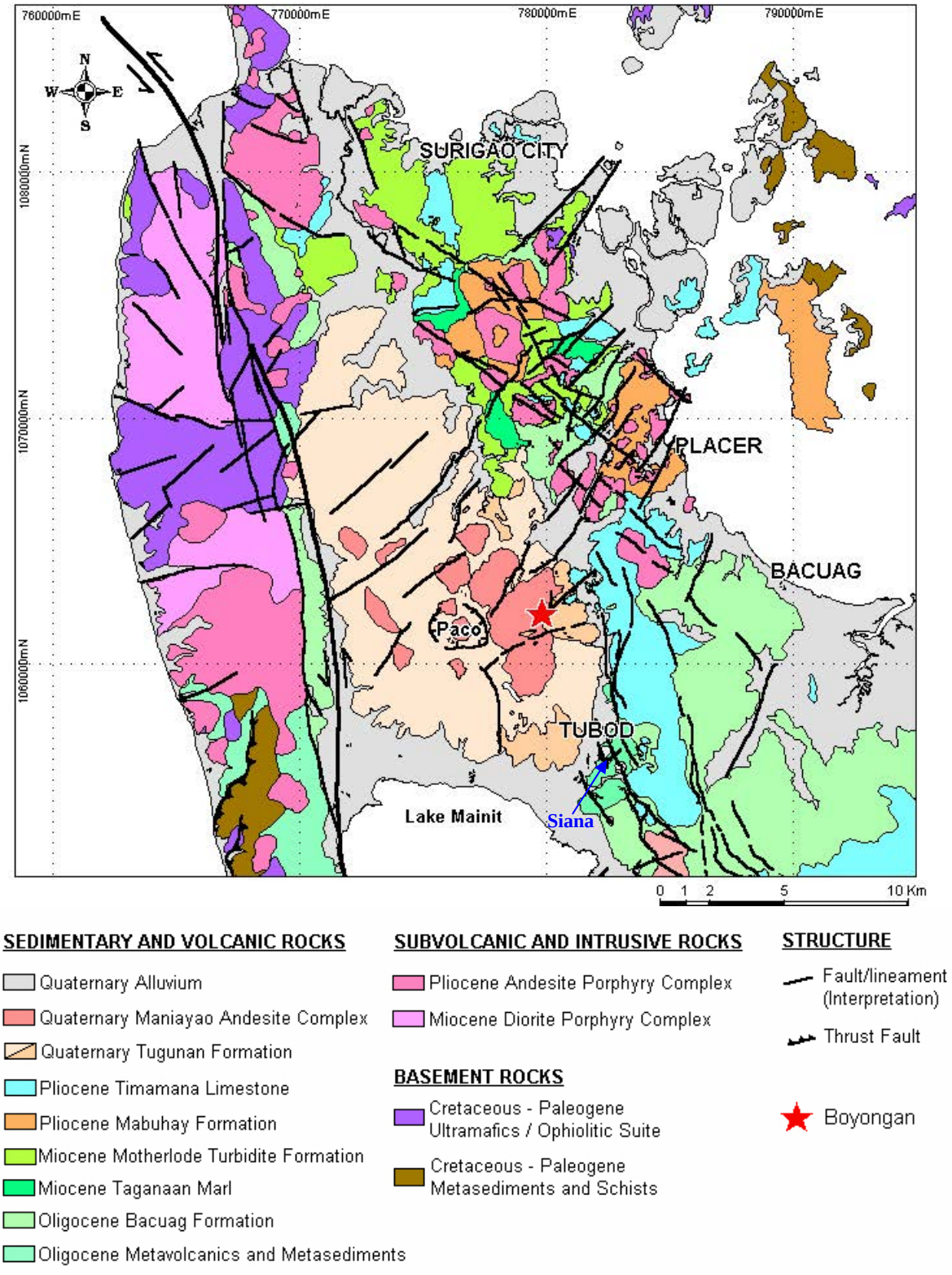

Fig. 2.2. Geology and structures of Surigao del Norte, Northeastern Mindanao, Philippines [modified and compiled from the Mines & Geosciences Bureau, UNDP (1987), Philex Corporation, Lithostructural interpretation of the Surigao area (Australian Photogeological Consultants Pty Limited, 1999), and from the regional mapping and detailed work of Anglo American Exploration (Philippines), Inc.]. The square surrounding Boyongan (marked by a red star) is the location of Fig. 2.5.

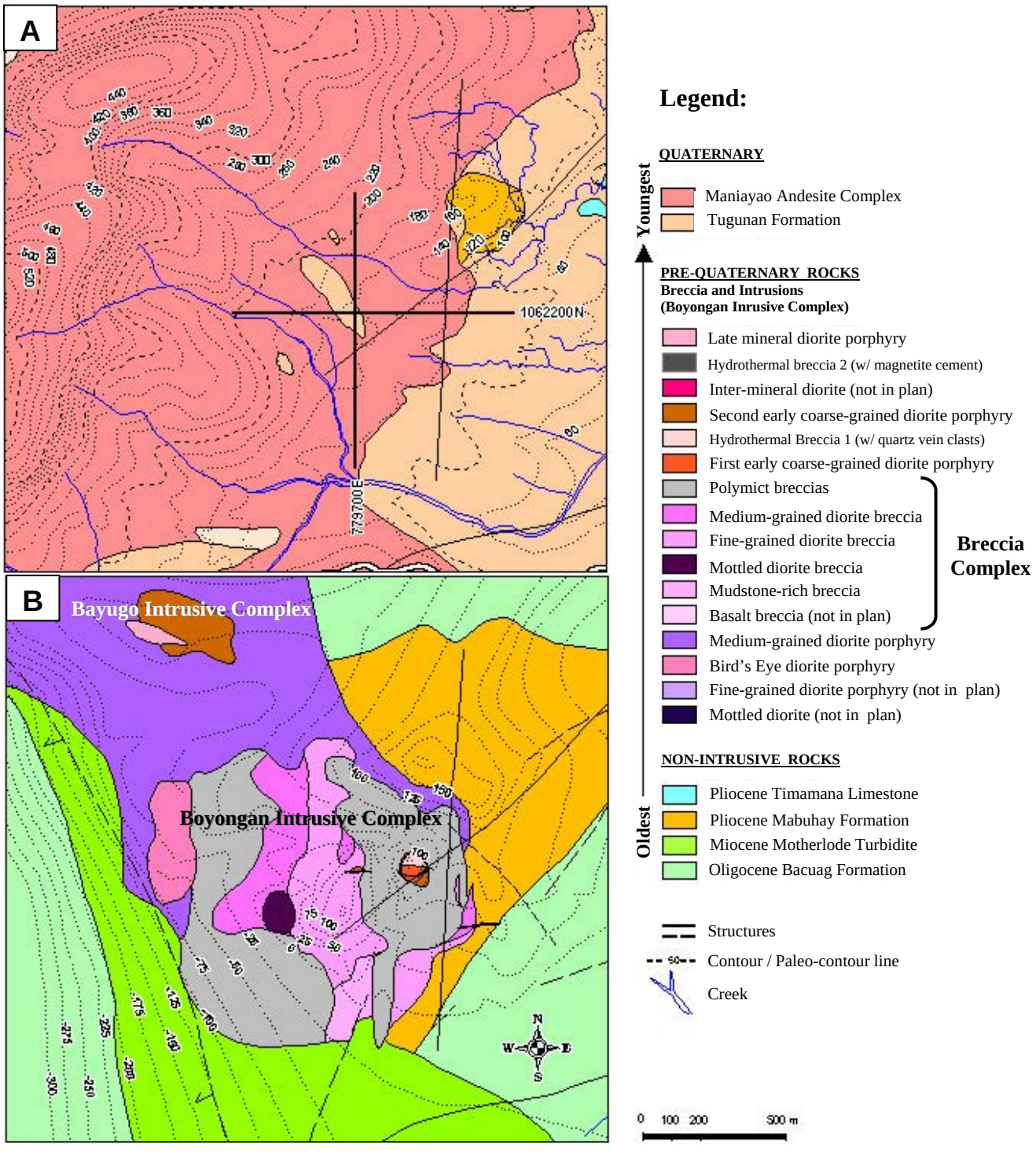

Fig. 2.3. **A.** Quaternary geologic map of Boyongan with 20-m contour elevation and structures. The Boyongan deposit is completely concealed by the Maniayao Andesite Complex and Tugunan Formation. Also shown here are section lines for 1062200N & 779700E. The geological cross-sections are shown on Fig. 2.6 and 2.8. **B.** Pre-Quaternary geological map of Boyongan with 25-m paleo-countour lines. This map shows the geology immediately beneath the Quaternary paleosurface, as determined by diamond drilling by Anglo American Exploration (Philippines), Inc. The 1-km circular breccia complex has intruded the non-intrusive wall-rocks and a pre-mineral medium-grained diorite porphyry that remains unbrecciated to the north. The breccia complex and other diorite intrusions are collectively known as the Boyongan Intrusive Complex. Two prominent peaks can be observed within the breccia complex with approximate elevations of 100m ASL. A steep slope is observed at the west of the breccia complex. The Bayugo Intrusive Complex is another porphyry Cu-Au system located approximately 500m NW of the breccia complex.

1,100 to 1,500m thick (UNDP, 1987).

The Bacuag Formation is the oldest rock package intersected through diamond drilling around Boyongan (Fig. 2.3B, 2.4, 2.5, 2.6, 2.7A & 2.8). It consists of basaltic flows and breccias (Fig. 2.7A). Some of the samples have been identified petrographically as altered basaltic hyaloclastite (SKM, 2001). The breccia texture in the hyaloclastites is inferred to have formed in response to thermal stress as the basaltic flow encountered cold water (SKM, 2001; McPhie, et al., 1992).

2.3.3 Motherlode Formation (Miocene)

The **Miocene Motherlode Formation** is exposed in the northern part of the Surigao gold district, where it unconformably overlies the Bacuag Formation (Fig. 2.2). The Motherlode Formation consists of sandstones, mudstones and siltstones and is known informally as the "Motherlode Turbidites". It includes a marl and limestone unit called the Taganan Marl (Fig. 2.2). Grading, cross-laminations, ripple marks, and convolute layers are preserved in some outcrops. The Taganaan Marl is interbedded with the Motherlode turbidites and has yielded a Lower to Middle Miocene in age from forams (UNDP, 1987). The maximum thickness of this formation is 700m (UNDP, 1987).

At Boyongan (Fig. 2.3B, 2.4, 2.5, & 2.8), the Motherlode Formation consists of dark gray to black, fine-grained laminated siltstone containing thin irregular calcite veinlets (Fig. 2.7B). Traces of pyrite have also been observed in drillcore. The Motherlode Formation is more indurated than the Tugunan Formation.

2.3.4 Mabuhay Formation (Pliocene)

The **Pliocene Mabuhay Formation** consists of sub-areal to shallow-marine andesitic pyroclastics, minor lavas, and calcareous siltstones. It unconformably overlies the Motherlode Formation (Fig. 2.2, 2.3 & 2.4). The Mabuhay Formation is the host to several epithermal gold and porphyry copper deposits in the Surigao district. This formation has an estimated age of Lower to Upper Pliocene (UNDP, 1987). At Boyongan, the Mabuhay Formation has been intruded by a diorite intrusive complex with ^{40}Ar-^{39}Ar dates of 2.58 ± 0.08 Ma to 2.39 ± 0.03 Ma (Waters, unpubl. data, 2001). A Mid-Pliocene age for the Mabuhay Formation is inferred. The maximum stratigraphic thickness of the Mabuhay Formation is estimated to be 200 meters (UNDP, 1987).

Around Boyongan (Fig. 2.3B, 2.4, 2.5, & 2.6), the Mabuhay Formation comprises pyroclastic including ignimbrite, tuffs, lapilli tuffs (Fig. 2.7C) have been intersected through drilling (SKM, 2000b).

2.3.5 Timamana Limestone (Pliocene)

The **Pliocene Timamana Limestone** is a massive, coralline, and buff-colored limestone. It occurs as prominent scarp ridges to the east of Boyongan. The limestone also crops out along a NNW-trend as a few isolated occurrences to the north (Fig. 2.2). The limestone unit unconformably overlies the Oligocene-Miocene Bacuag Formation and Miocene Motherlode turbidites (Fig. 2.3B & 2.4). An Upper Pliocene to Lower Quaternary age is inferred based on the dating of the fossiliferous marl member, which yielded an age of Pliocene to Recent (UNDP, 1987). The maximum thickness of the Timamana Limestone is about 250 meters (UNDP, 1987).

The Timamana Limestone has been intersected in drillcore about 1.5 to 2.5 km south of Boyongan. The unit here is generally cream to dirty white, massive and locally contain fossils (Fig. 2.7D). Calcite occur as veinlets and cavity infills.

2.3.6 Tugunan Formation (Pleistocene)

The **Tugunan Formation** overlies the Boyongan porphyry copper deposit unconformably. It consists of volcanic-derived sedimentary rocks that are interbedded with plagioclase-biotite-hornblende andesites (Maniayao Andesite; Fig. 2.2). A K-Ar age

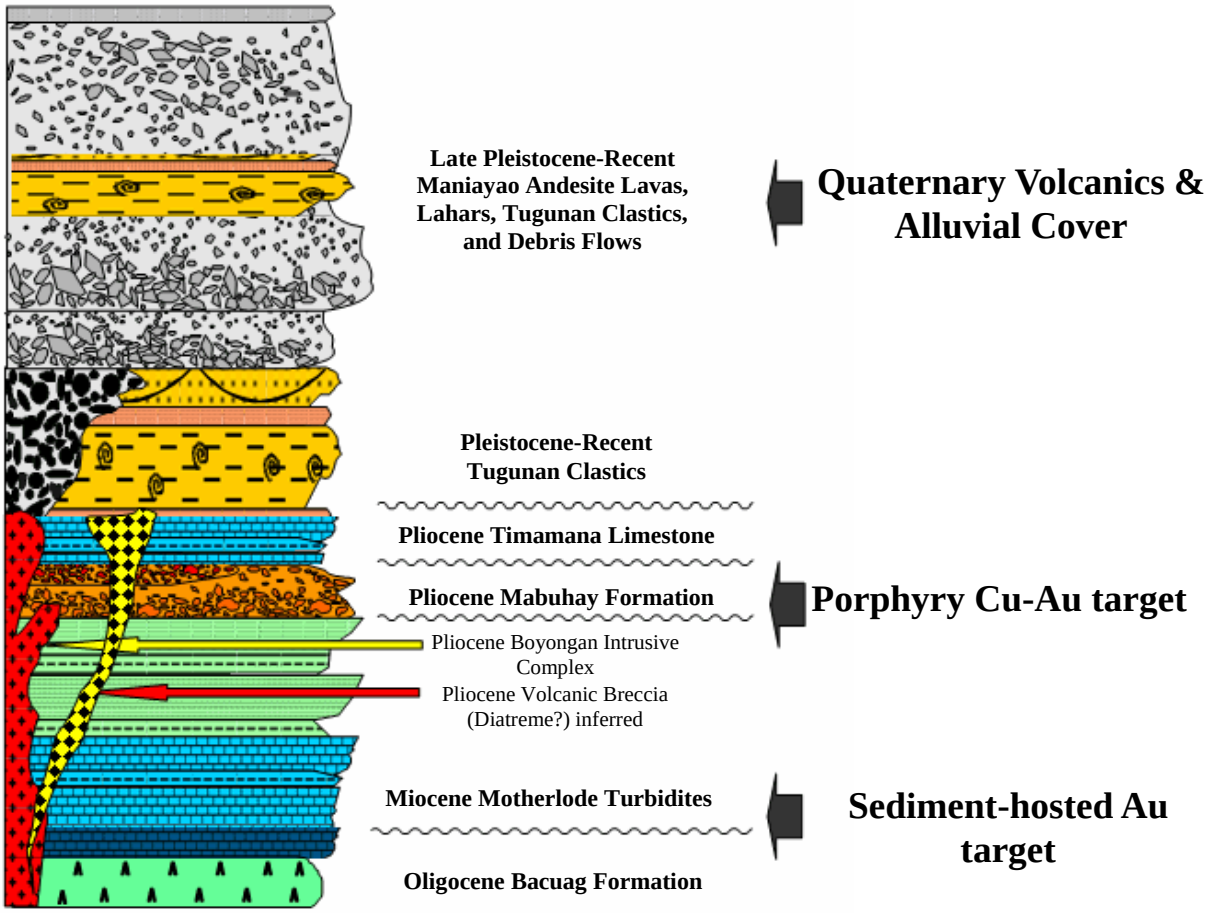

Fig. 2.4. Schematic graphic log for the Surigao gold district showing the stratigraphy of Boyongan and potentially favourble horizons with respect to mineral exploration (modified from Waters et.al., 2001)

determination for andesite from the Tugunan Formation on the eastern flank of Mt. Maniayao yielded an age of 0.3 ± 0.17 Ma (UNDP, 1987). The thickness of the andesite flows and clastics is highly variable. The maximum preserved thickness of the Tugunan Formation is estimated to be at least 600 meters (UNDP, 1987). The Tugunan Formation is believed to have formed in response to Pliocene-Pleistocene tectonism and magmatism accompanied by significant uplift in the Eastern Mindanao Cordillera (Waters, unpubl. data, 2001).

At Boyongan, the Tugunan Formation completely conceals the Boyongan Intrusive Complex and the altered and brecciated wallrocks to the porphyry deposit (Fig. 2.3A, 2.4, 2.5, 2.6, & 2.8). The Tugunan Formation is generally poorly consolidated and laminated, consisting of intercalated siltstones, carbonaceous mudstones, sandstones, debris flows, and polymictic conglomerate (Fig. 2.7E). The debris flow contains intensely clay- and pyrite-altered clast from the Boyongan Intrusive Complex or some other diorite intrusion. Drilling results show that the thickness of Tugunan Formation is highly variable, but generally thickens to the west of the Boyongan deposit, toward a deeply incised NNW-trending paleo-valley.

Some mudstones and sandstone beds in the Tugunan Formation contain bivalves, gastropods and tree branches. Carbon-14 dating results from tree branches suggests that the deposition of the Tugunan Formation spanned the period from Late Pleistocene (30,180 BP) to recent times (1,700 BP).

2.3.6.1 Maniayao Andesites

The Maniayao Andesites (Fig. 2.3A) are gray (pink when weathered), massive to flow

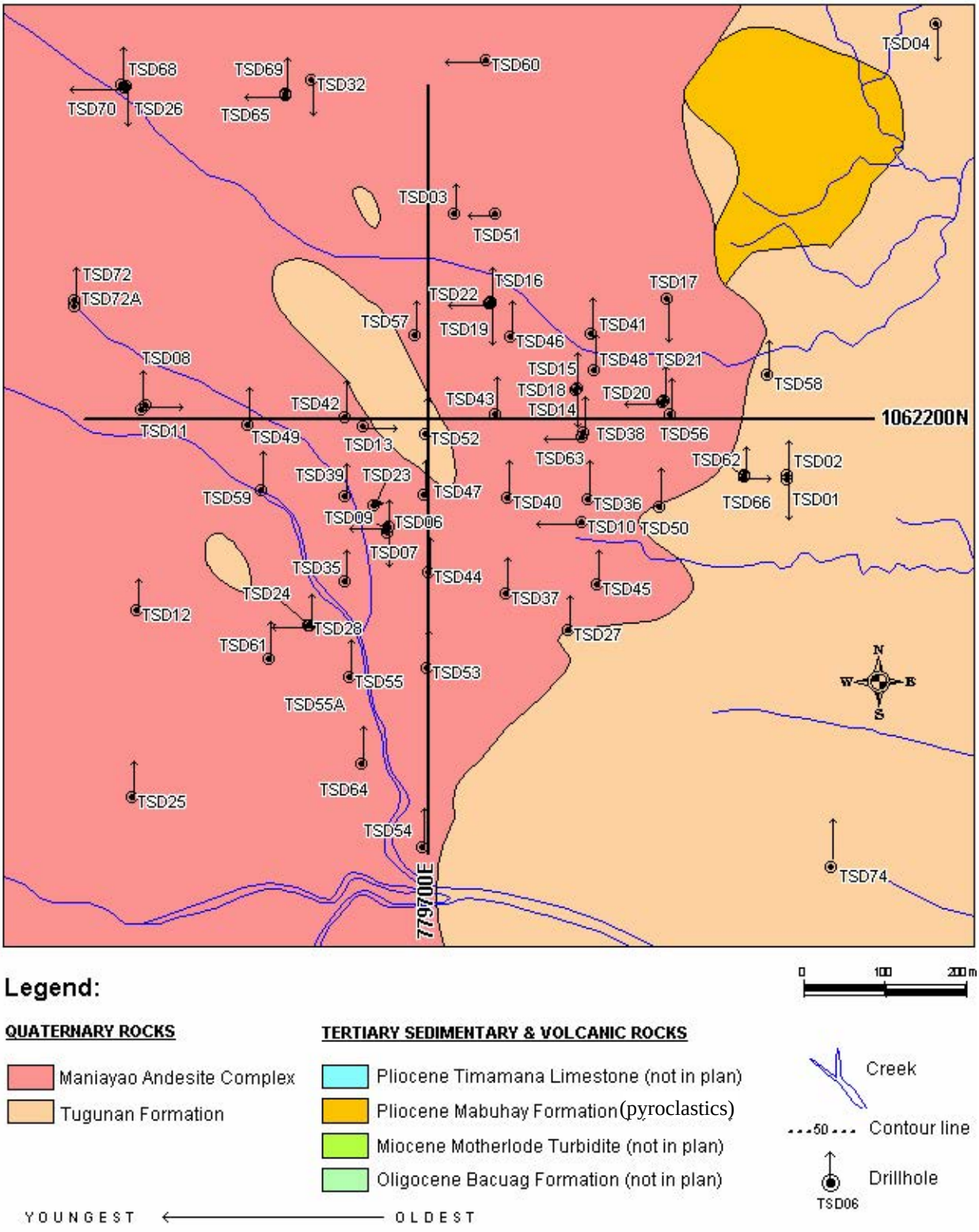

Fig. 2.5. Drillhole location at Boyongan. Dots at the center of circles and arrows represent the drillhole collar location and drillhole directions, respectively. Geological sections for 1062200N & 779700E are shown in Figs. 2.6 & 2.8.

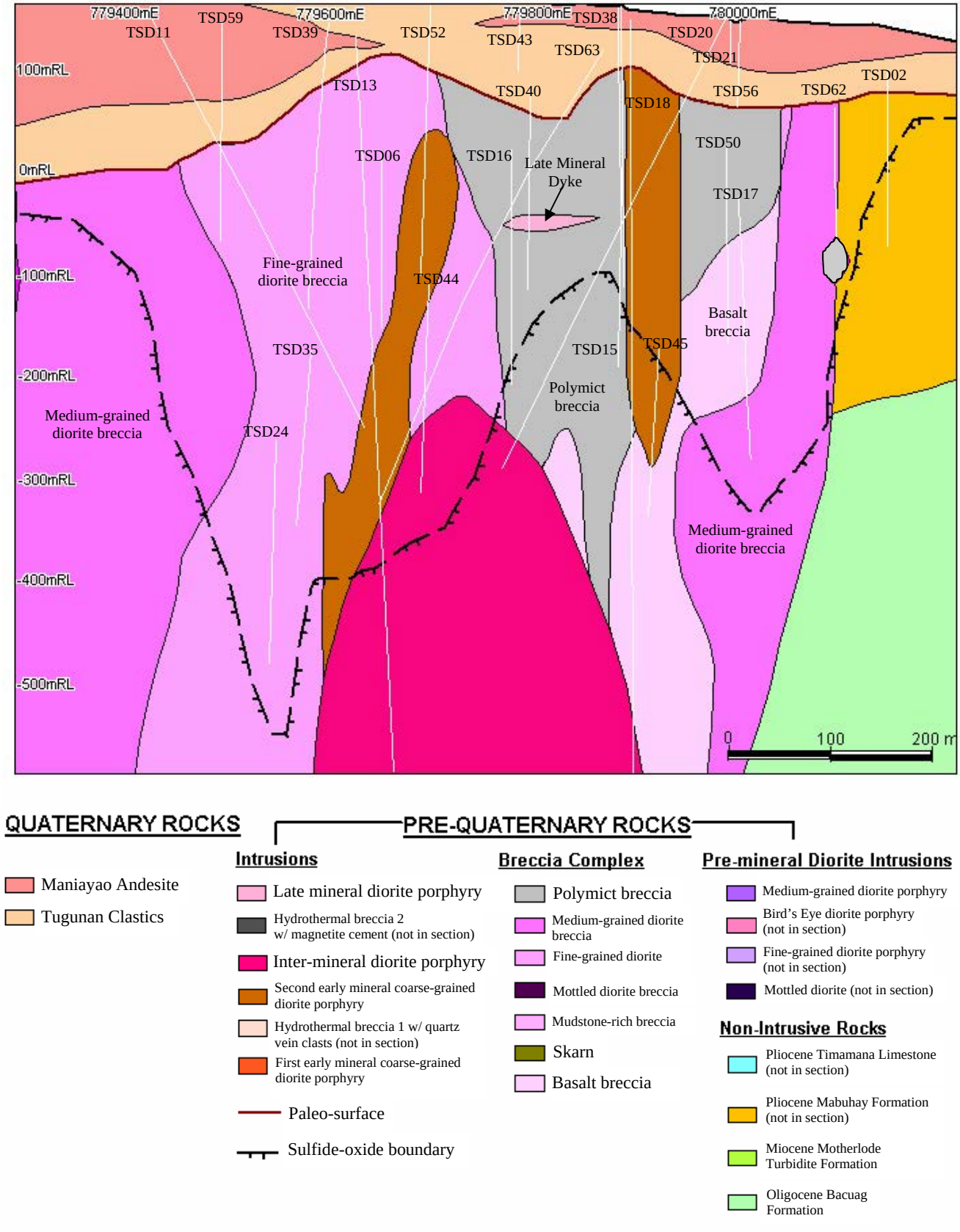

Fig. 2.6. Geological cross section along 1062200N (looking north). The geology was constrained using drillhole information. Drillholes traces are represented by solid white lines.

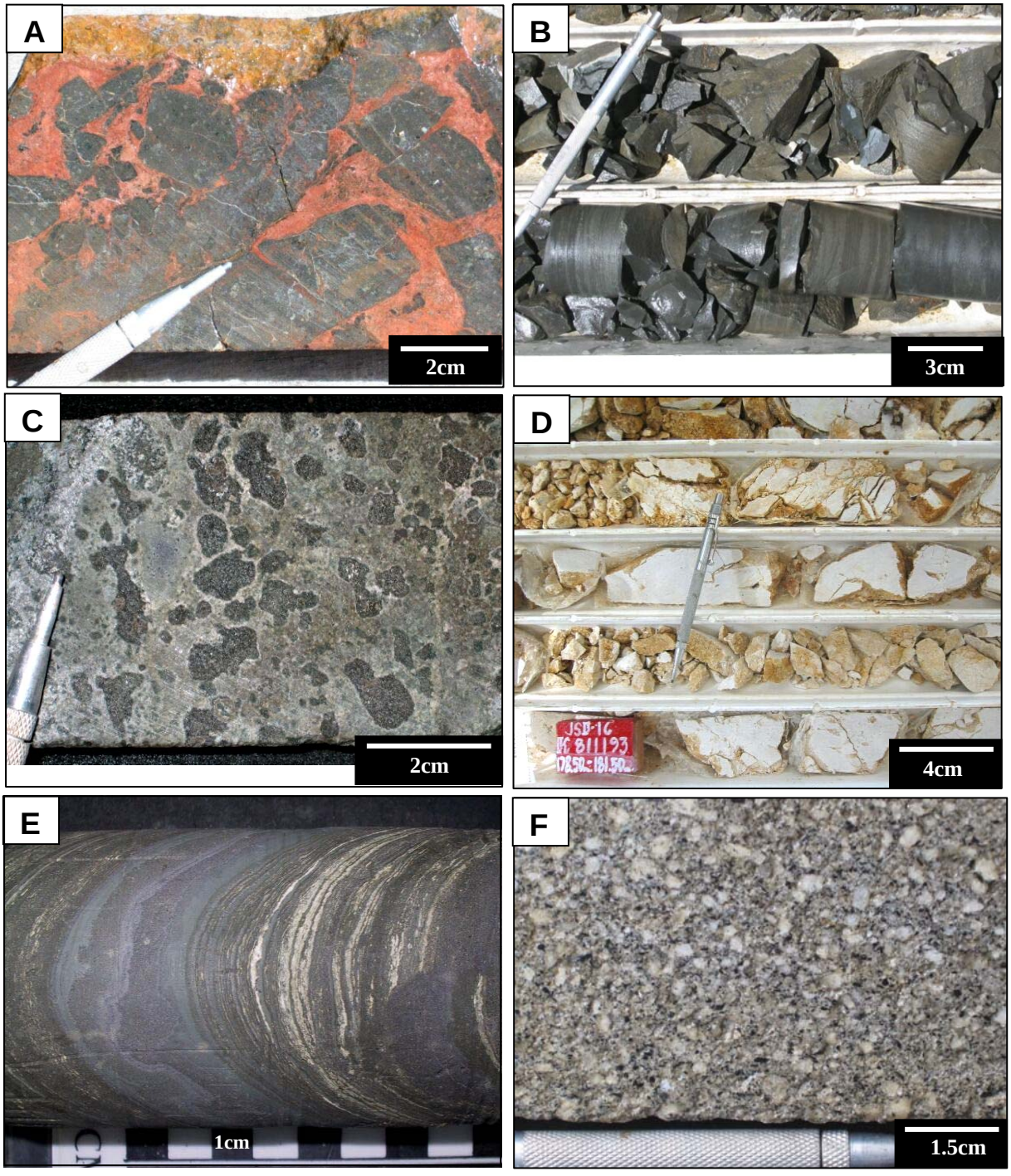

Fig. 2.7. A. Bacuag basalt breccia (part of the Bacuag Formation in TSD05 @ 97m). Clasts consists of fine-grained porphyritic basalt that are set in a hematite ± goethite-altered matrix, possibly due to weathering and/or thermal oxidation. Assay from 95.20 - 98.20m returned 0.015% Cu & 0.006 g/t Au. **B.** Dark gray to black, highly fractured siltstone with very thin calcite veinlets (part of Motherlode Formation in TD30 @ 182.00m). Assay from 179.90 – 182.90m in TSD30 returned 0.009% Cu & 0.009 g/t Au. **C.** Gray matrix-supported lapilli tuff (part Mabuhay Formation in TSD02 @ 234.70m) containing rounded to sub-rounded clasts of andesite to basalt in composition. Assay from 233 - 236m in TSD02 returned 0.169% Cu & 0.016g/t Au. **D.** Cream to dirty white, highly fractured, non-mineralised limestone (part of Timamana Limestone in JSD16 from 176 - 182m). **E.** Poorly consolidated laminated mudstone and siltstone (part of Tugunan Formation in TSD49 @ 200m). White calcareous laminations contain shell fragments. **F.** Porphyritic plagioclase-hornblende andesite (part of Maniayao Andesite in TSD12 @ 238.85m). bas = basalt, lst = limestone, plag = plagioclase, hbl = hornblende, hem = hematite

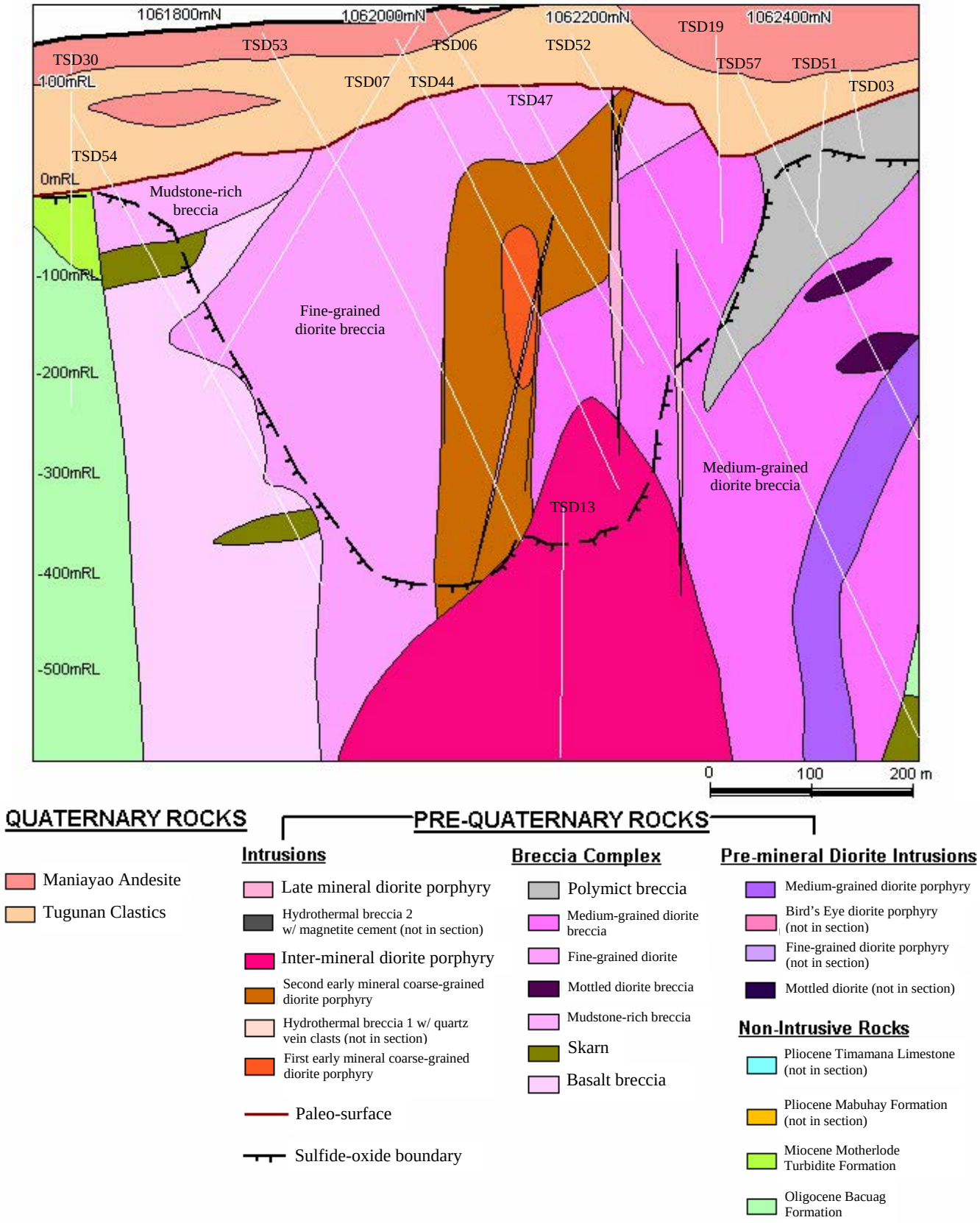

Fig. 2.8. Geological section along 779700E (looking west). The geology was constrained using drillhole information. Drillholes traces are represented by white solid lines.

banded andesite lavas which in some samples have distinctive glomeroporphyritic textures (McPhie, et al., 1992). They contain phenocrysts of plagioclase, hornblende, and biotite that are set in a fine-grained gray groundmass (Fig. 2.7F). Volcaniclastic facies occur in the southwestern portion of the district.

2.3.6.2 Paco Andesite (Quaternary)

The **Paco Andesite** (UNDP, 1987) is similar to the Maniayao Andesite and is included here as a member of the Tugunan Formation. It forms an almost intact, extinct volcano. The relict crater is two kilometers across with andesitic domes, lavas flows, and lahar deposits preserved in the vicinity of the volcano (Waters unpubl. data, 2001; Fig. 2.2). The crater and central cone at Paco (elevation of 524 meters) is still well-preserved, even though it is in an area of high rainfall and rapid erosion. This suggests that the **Maniayao Andesite** is probably no more than ~10,000 years old (UNDP, 1987). However, new K-Ar dating on the Maniayao Andesite by Prise (2001) yielded a range of ages from 0.15 to 0.57 Ma, which may reflect the actual crystallisation age of the rock (Braxton, pers. commun., 2003).

2.3.7 Sediments (Recent)

Recent conglomerates are exposed in the Surigao district, consistent with continued uplift through the Quaternary (Waters unpubl. data, 2001). Recent alluvium and colluvium occupy the principal drainages (Fig. 2.2).

2.4 Boyongan Intrusive Complex

The Bacuag, Motherlode, and Mabuhay Formation have been intruded by a series of

diorites and breccias, which are referred to here collectively as the Boyongan Intrusive Complex (Fig. 2.3B, 2.4, 2.6 & 2.8). The Boyongan copper-gold deposit is mainly hosted in the Boyongan Intrusive Complex. At least nine intrusive phases have been identified during core logging by Anglo American geologists in collaboration with R. Sillitoe (Sillitoe, 2001 & 2002). These phases include:

1. Mottled diorite
2. "Bird's Eye" diorite porphyry
3. Medium-grained diorite
4. Fine-grained diorite
5. Microdiorite
6. First early coarse-grained diorite porphyry
7. Second early coarse-grained diorite
8. Inter-mineral diorite porphyry
9. Late diorite porphyry

The first four porphyries (mottled diorite, "Bird's Eye" diorite porphyry, medium-grained diorite, & fine-grained diorite) occur as clasts within the breccia complex, and are interpreted to be pre-mineral intrusives. The microdiorite intruded the pre-mineral intrusives and occurs as breccia cement. The first and second early coarse-grained diorite porphyries are interpreted to have been the main mineralising intrusions (Sillitoe, 2001). The Boyongan Intrusive Complex intruded basaltic flows of the Oligocene to Miocene Bacuag Formation and andesitic pyroclastics of the Mabuhay Formation. Although the wallrocks are strongly altered, they are only weakly mineralised. Part of the andesitic pyroclastics are exposed at the northeastern part of the deposit at Paragayu Hill. The Boyongan Intrusive Complex and surrounding wallrocks underlie the Tugunan Formation and Maniayao Andesite). The descriptions of the individual phases of the intrusive complex provided below are mainly based on personal drill core observations, combined

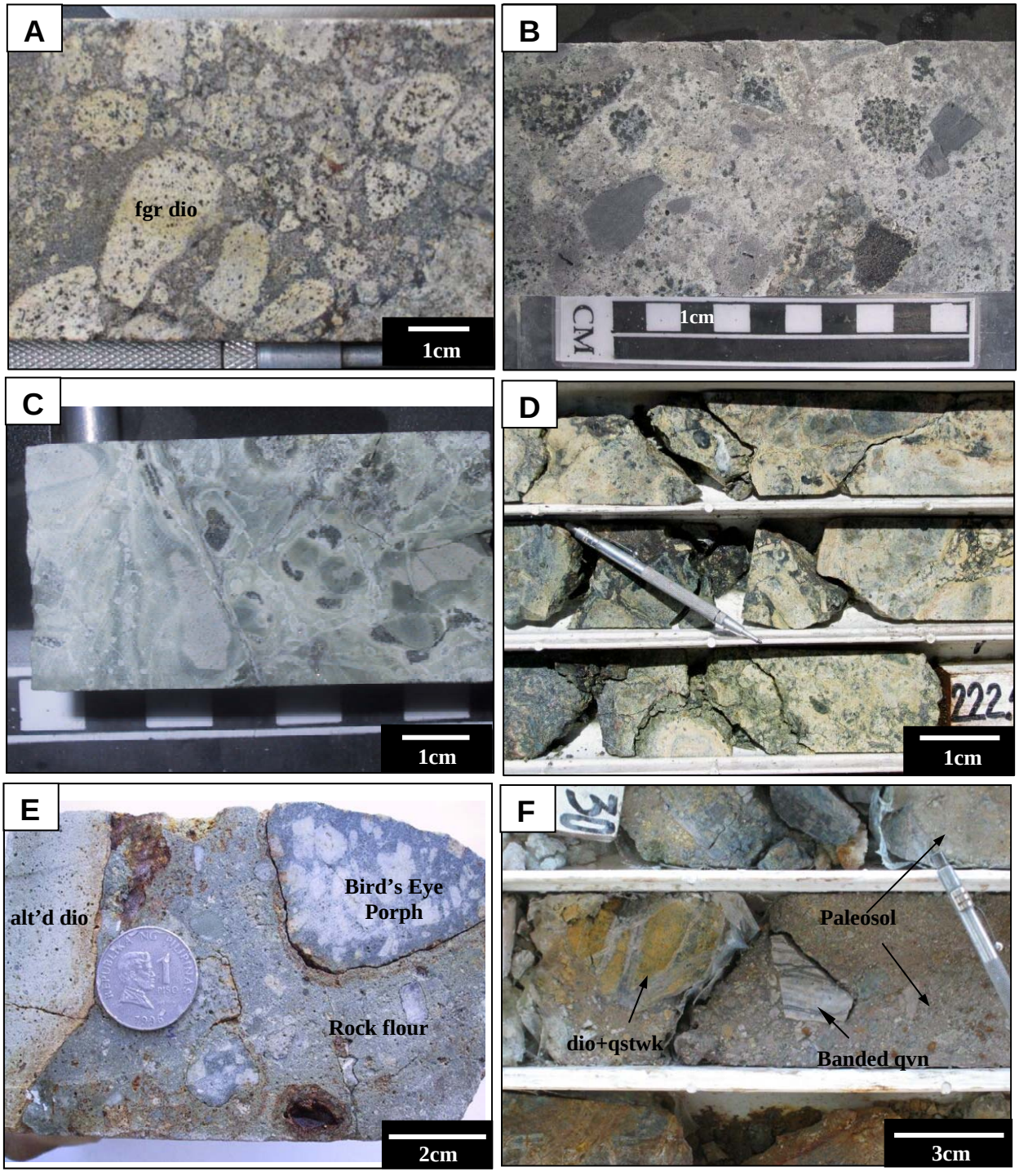

Fig. 2.9. A. Fine-grained diorite breccia with sub-rounded fine-grained diorite clasts (fgr dio) set in microdiorite matrix (TSD16 @ 347.20m). Assay from 345.20 - 348.20m in TSD16 returned 0.251% Cu & 0.388g/t Au. **B.** Polymict breccia containing various diorite and silicified fragments (TSD51 @ 272.90m). Assay from 270.65 - 273.65m in TSD51 returned 0.142% Cu & 0.094g/t Au. **C.** Mudstone-rich breccia or hydrothermal or phreatomagmatic(?) breccia (SKM, January 2003) in TSD54 @ 169.25. The concentric structures are lapilli which may have been formed by the accumulation of fine-material in a wet environment (SKM, January 2003). Assay from 168.10 – 171.10m in TSD54 returned 0.04% Cu & 0.033g/t Au. **D.** Brecciated skarn (chlorite+epidote+calcite+magnetite±garnet) in TSD54 @ 221m. Assay from 219.55 – 221.55m in TSD54 returned 0.362% Cu & 0.284g/t Au. **E.** Diatreme float sample from Paragayu creek consisting of various sub-rounded diorite fragments set in a rock flour matrix. **F.** Paleosol with altered diorite + quartz vein stockwork fragments with occasional quartz vein fragments (TSD63 @ 127.50m). Assay from 125.95 – 129m in TSD63 returned 3.29% Cu & 4.18g/t Au. dio = diorite, fgr = fine-grained, porph = porphyry, alt'd = altered, qvn = quartz vein, qstwk = quartz vein stockwork

with supplementary petrographic studies from Sinclair Knight Merz (2000-2003):

2.4.1 Breccias

At least six facies of pre-mineral breccias have been identified in the breccia complex (Fig. 2.3, 2.6 and 2.8). These include:

- Basalt breccias
- Mottled diorite breccia
- Medium-grained diorite breccia
- Fine-grained diorite breccia
- Polymict breccia 1 and 2
- Mudstone-rich breccia

These breccias were identified on the basis on the dominant clast types and probably reflect the local country rocks to the breccia. Overall, the breccia complex consists of various clasts of diorite that are set in a microdiorite matrix (Fig. 2.9A), and was described as a microdiorite intrusion breccia by Sillitoe (2001). It forms a circular body approximately 1km in diameter (Fig. 2.3B). The gray to white coloured breccia matrix is derived primarily from the diorites. The breccias locally have intensely milled textures, with clasts strongly comminuted and containing abundant rock flour (SKM, 2001).

The polymict breccias (Fig. 2.3B, 2.6 and 2.8) consists of various types of clasts of diorite (mottled, “Bird’s Eye”, medium-grained and fine-grained diorite porphyries), basalt from the Bacuag Formation, possible sediments from the Motherlode Formation, and minor quartz vein clasts (Fig. 2.9B). The western and eastern margins of the breccia complex are in general defined by N-trending, upward flaring polymict breccias.

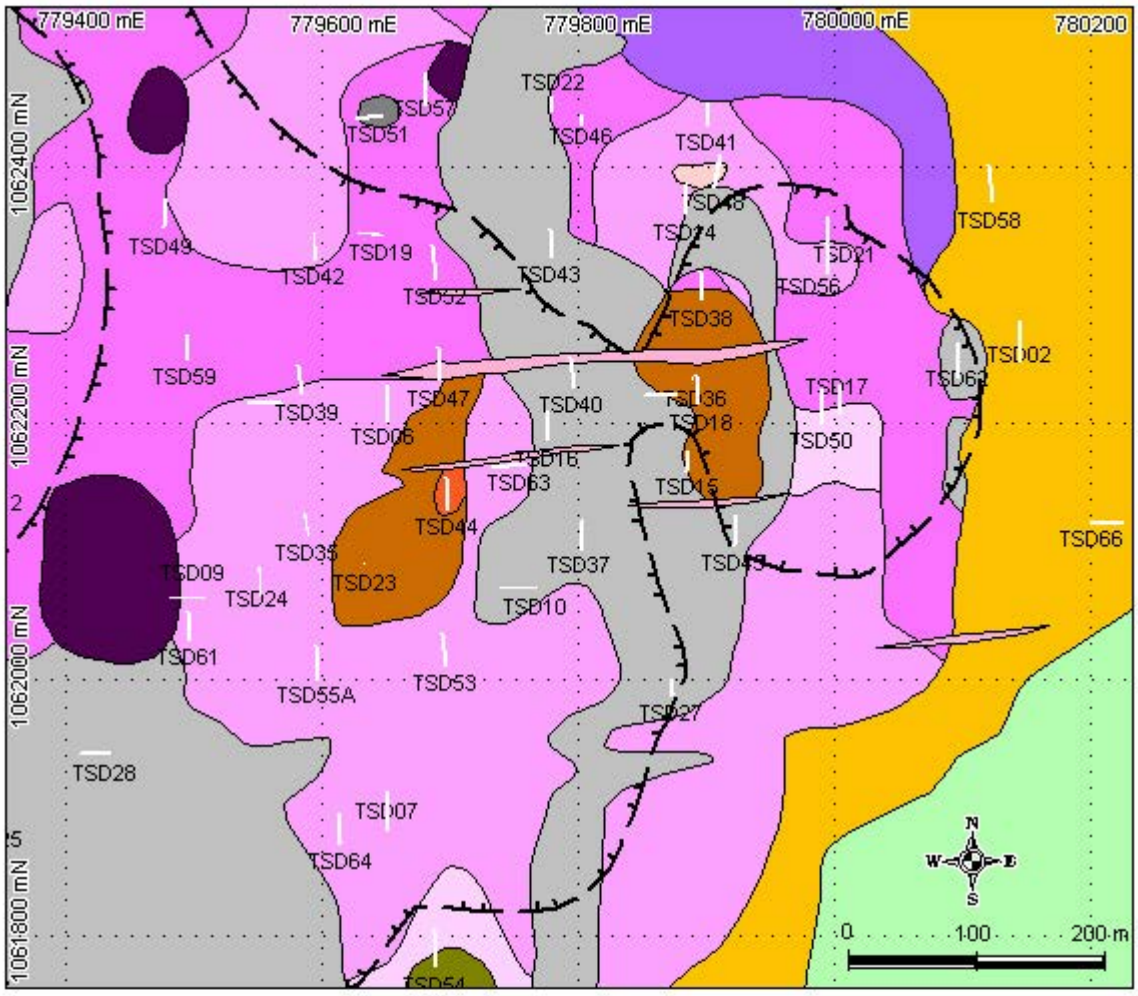

PRE-QUATERNARY ROCKS

Intrusions

- Late mineral diorite pophyry
- Hydrothermal breccia 2 w/ magnetite cement
- Inter-mineral diorite porphyry
- Second early mineral coarse-grained diorite porphyry
- Hydrothermal breccia 1 w/ quartz vein clasts
- First early mineral coarse-grained diorite porphyry

Sulfide-oxide boundary

Breccia Complex

- Polymict breccia
- Medium-grained diorite breccia
- Fine-grained diorite breccia
- Mottled diorite breccia
- Mudstone-rich breccia
- Skarn
- Basalt breccia

Pre-mineral Diorite Intrusions

- Medium-grained diorite porphyry
- Bird's Eye diorite porphyry (not in plan)
- Fine-grained diorite porphyry (not in plan)
- Mottled diorite (not in plan)

Non-Intrusive Rocks

- Pliocene Timamana Limestone (not in plan)
- Pliocene Mabuhay Formation (pyroclastics)
- Miocene Motherlode Turbidite Formation (not in plan)
- Oligocene Bacuag Formation (basalt)

Fig. 2.10. Geological plan along –100mRL. The geology shown here is focussed on the Boyongan Intrusive Complex which has intruded the non-intrusive wallrocks of the Mabuhay and the Bacuag Formations. The second early coarse-grained diorite porphyry on the east intrudes the polymict breccia while the other second early diorite porphyry on the west intrudes a package of fine-grained diorite breccia. EW-trending late-mineral diorite dykes cut the Boyongan Intrusive Complex.

Mudstone-rich breccia was intersected in one of the drillholes (Fig. 2.8). This light green to gray polymictic breccia contains subangular to subrounded pebble clasts of mudstone and siltstone from the Motherlode Formation(?), together with minor clasts of fine-grained diorite, pyroclastic rock fragments with possibly accretionary lapilli set in a clastic matrix derived from the diorites (Fig. 2.9C).

An inferred volcanic breccia (possibly a diatreme) has cut through the Boyongan Intrusive Complex. It occurs only as floats along Paragayu Creek (Fig. 2.9E).

2.4.2 Intrusions

The criteria used to discriminate different intrusive phases of Boyongan are: phenocyrst size, phenocryts composition, mineralisation, and density of quartz stockwork. Different clast types in the breccia complex provide evidence for multiple intrusions. At least nine intrusive phases have been identified during logging.

2.4.2.1 Pre-mineral Intrusions

Mottled diorite is interpreted to be the oldest intrusive unit at Boyongan prospect. It is inferred to be a pre-mineral intrusion. It has an estimated age of ~8Ma based on a U/Pb zircon age determination (Camacho, 2001). This unit has a “mottled” or “leopard” spot texture (Fig. 2.11A). Phenocrysts range from 1.5 to 2.0mm. Both biotite and hornblende phenocrysts are present, and they range from 0.5 to 2.0mm, and are set in a fine-grained groundmass of feldspars. This occur exclusively as clasts in the breccia complex (Fig. 2.3B & 2.8). In thin section, the crowded porphyritic texture is defined by subhedral to euhedral plagioclase (andesine) phenocrysts, which are up to 3.5mm long (average 1.5mm). Most of

the plagioclase phenocrysts are albiltised or flecked with secondary biotite. Relict primary hornblende has been recognised locally. The texture of the groundmass is not well preserved, but was likely to have been very fine-grained and granular (SKM, 2000).

Bird's Eye diorite porphyry has a "peanut brittle" texture, where prominent feldspar phenocrysts (up to 10mm across) and hornblende phenocrysts (2 - 5mm) are set in fine-grained groundmass (Fig. 2.11B). The Bird's Eye diorite porphyry mainly occurs as minor clasts in the Boyongan Intrusive Complex. The first in-situ Bird's Eye porphyry intrusive

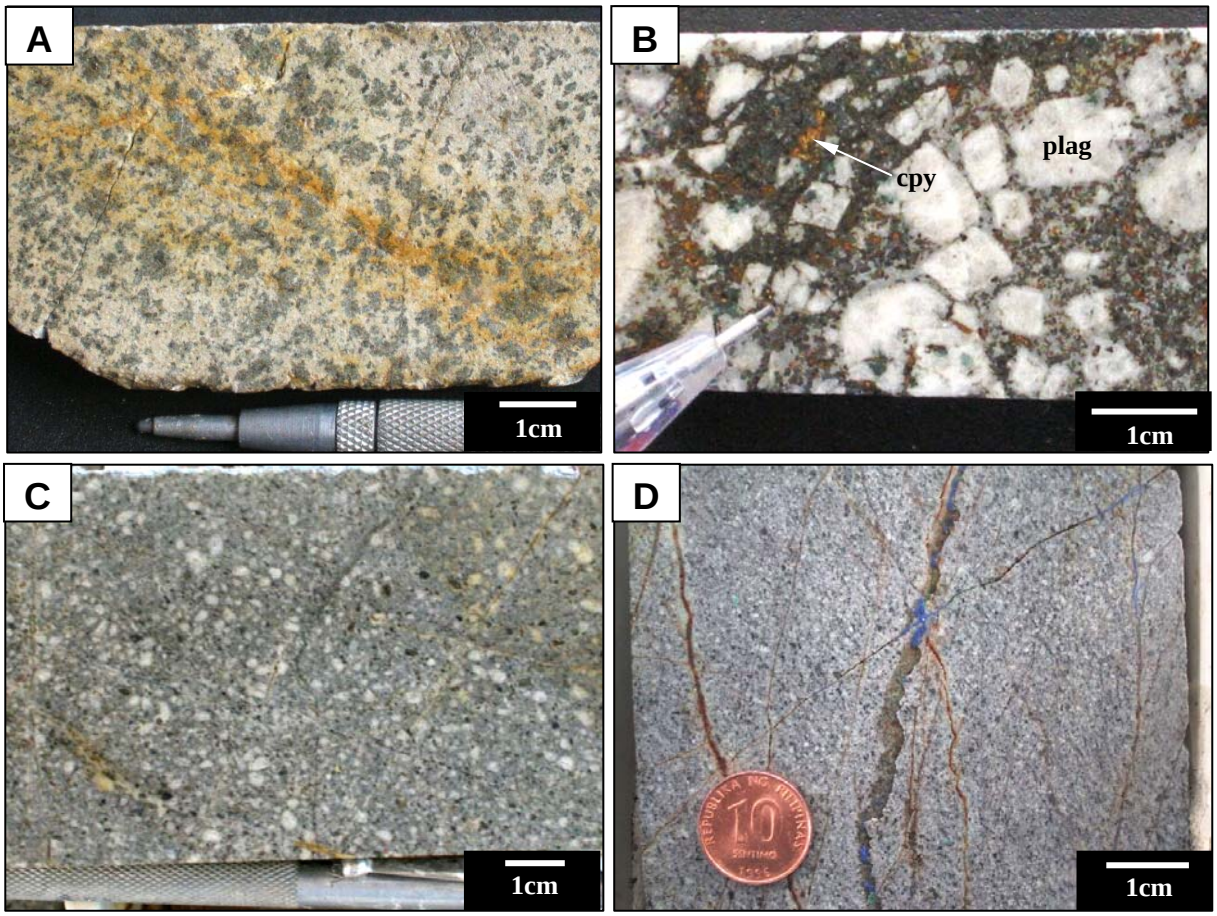

Fig. 2.11. A. Mottled diorite (TSD09 @ 340.10m). Assay from 339 - 342m in TSD09 returned 0.324% Cu & 0.693g/t Au. **B.** Plagioclase-phyric diorite porphyry ("Bird's Eye" porphyry; TSD67 @ 810.55m). Assay from 807.70 – 810.70m in TSD67 returned 0.336% Cu & 0.249g/t Au. **C.** Medium-grained diorite with seriate texture (TSD52 @ 346.60m). Phenocyrsts of plagioclase and hornblende set in fine-grained feldspar groundmass. Assay from 345.30 – 348.30m in TSD52 returned 0.366% Cu & 0.350g/t Au. **D.** Fine-grained diorite with azurite and limonite along fractures (TSD23 @ 113.40m). Assay from 111.80 – 114.80m in TSD23 returned 0.910% Cu & 1.33g/t Au. plag = plagioclase, cpy = chalcocpyrite

was intersected in TSD67, approximately 200m west of the main Boyongan Intrusive Complex (Fig. 2.3B). In thin section, prominent andesine phenocrysts are medium to coarse-grained and subhedral. They contain flecks of sericite and minor secondary albite and K-feldspar. The mafic phenocrysts and groundmass have been replaced by fine-grained secondary biotite and opaques, which have in turn been partially altered to sericite and chlorite. Relict primary biotite and hornblende have been recognised (SKM, 2004).

Medium-grained diorite occurs as both clasts and wall rock to the Boyongan Intrusive Complex, which remain unbrecciated to the north (Fig. 2.3B, 2.6 & 2.8). As for the mottled diorite, it is also considered to be pre-mineral intrusive. It generally displays seriate texture and it consists of plagioclase (1.5 to 3mm), hornblende (0.5-1.5mm), and biotite (1-2mm) phenocrysts set in a fine-grained groundmass (Fig. 2.11C).

Fine-grained diorite occurs only as clasts within the breccia complex (Fig. 2.3B, 2.6, & 2.8). It is generally gray to green coloured with 0.5 to 1mm diameter plagioclase and hornblende phenocrysts set in a fine-grained groundmass (Fig. 2.11D). In thin section, it has a crowded porphyritic texture with relict zoned plagioclase phenocrysts, together with obscured mafic (hornblende?) phenocrysts. The plagioclase has been partly albitised, and also altered to illite, quartz and kandite. Hornblende has been replaced by secondary biotite, opaques and quartz. Much of the rock consists of complex intergrowth of quartz, K-feldspar, and opaques with secondary biotite (SKM, 2000).

Microdiorite intruded the pre-mineral intrusives and served as a matrix to the breccia complex (Fig. 2.3B, 2.6, 2.8). It is gray to white in colour with a tuffaceous appearance (Fig. 2.9A). In thin section, the rock show intense milling and comminution and displays a

rock flour breccia texture (SKM, 2001).

2.4.2.2 Early-mineral Intrusions

The **first early coarse-grained diorite porphyry** (Fig. 2.3B) occurs as a remnant intrusion at the top of the **second early coarse-grained diorite porphyry**, and has been intersected in drillholes TSD14, 15, 18, and 38 (Fig. 2.5). Both diorites have intruded the breccia complex. Based on its location, the first early diorite porphyry most likely has been partly eroded. The first early diorite porphyry is characterised by intense alteration, unusual high grade mineralisation (>2% Cu & >5 g/t Au), and intense development of a quartz stockwork (Fig. 2.12A). In hand specimen, phenocrysts of plagioclase and hornblende range from 0.5 to 2.0mm in diameter. In thin section, the original rock has been totally replaced. Outlines of phenocrysts suggest the original presence of plagioclase and hornblende that have been replaced by a mixture of illite-smectite and kaolinite. The diorite is associated with a hydrothermal breccia which contains clasts of fine-grained diorite and quartz vein fragments.

The **second early coarse-grained diorite porphyry** (Fig. 2.3B, 2.5, 2.6, & 2.8) occurs as a series of dyke-like intrusions intercepted by drillholes TSD18 (east) and 23 (west). These dykes have a NNE-strike, parallel to the long axis of the first early diorite porphyry. They range from 2 to 45 meters in width (Sillitoe, 2001). Copper and gold grades within the dykes are moderate (0.75% to 1% Cu & 0.75 to 4 g/t Au) but this phase is believed to have contributed some ore to the strongly mineralised first early diorite porphyry (Sillitoe, 2001). The deeper exposures of second early diorite porphyry contain an intensely developed quartz vein stockwork that is poorly mineralised. In hand specimen, plagioclase phenocrysts range from 1.5 to 3.0mm and hornblende phenocrysts vary from 1.5 to 2mm

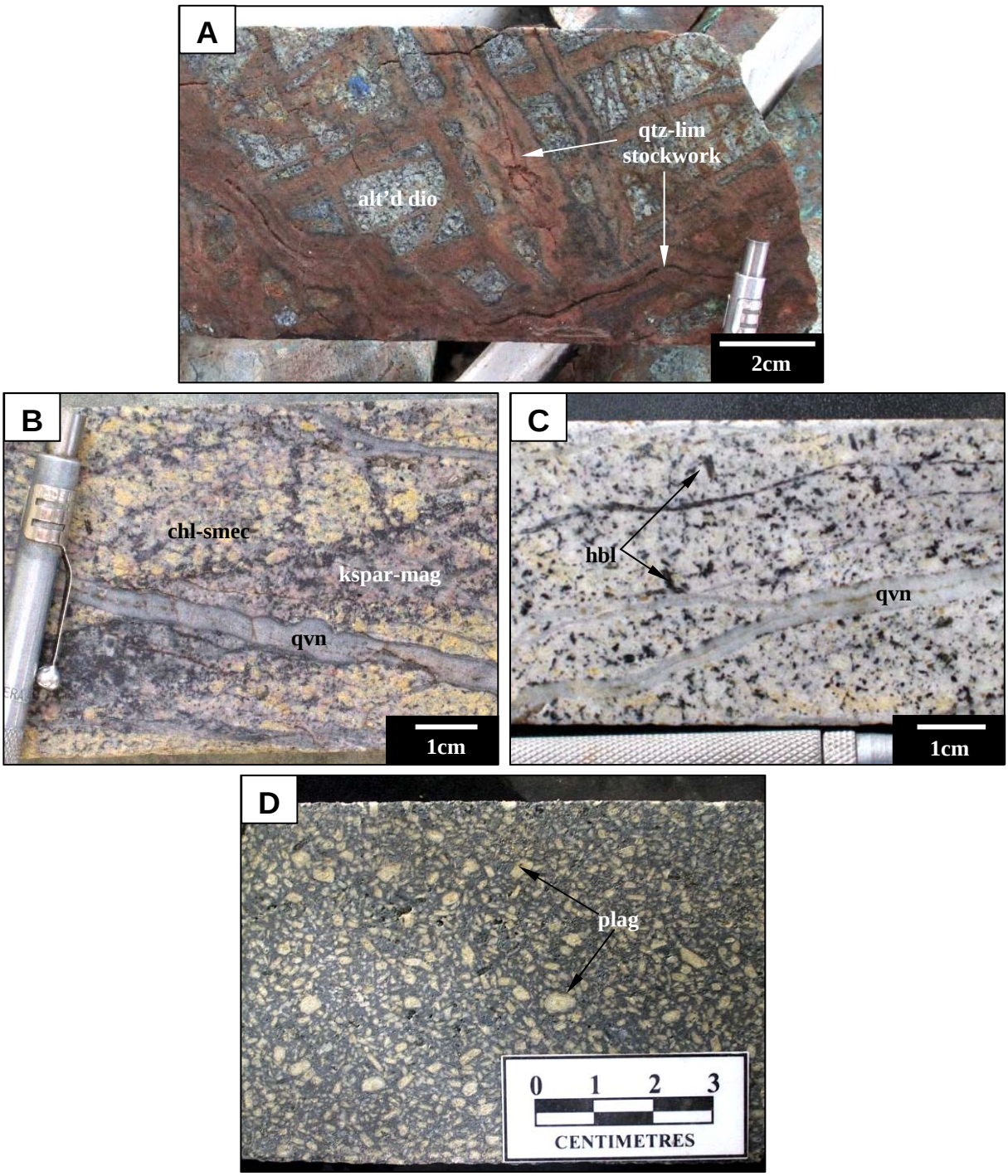

Fig. 2.12. A. First early coarse-grained diorite porphyry (TSD15 @ 87.40m), which has been intensely altered and quartz veined. Quartz veins are intensely limonite stained. The original porphyry texture can still be recognised. Assay from 85 - 88m in TSD15 returned 1.74% Cu & 6.18g/t Au. **B.** Second early coarse-grained diorite porphyry with K-feldspar--magnetite+chlorite+smectite alteration (TSD18 @ 361.20m). This is cut by quartz-magnetite veins. Assay from 360 - 363m in TSD18 returned 0.141% Cu & 0.720g/t Au. **C.** Inter-mineral diorite porphyry consisting of plagioclase and hornblende phenocrysts that are cut by quartz and magnetite veinlets (TSD13 @ 696.60m). Assay from 695.45 – 698.45m in TSD13 returned 0.015% Cu & 0.076g/t Au. **D.** Late diorite porphyry consisting of sub-rounded plagioclase and hornblende phenocrysts set in a dark-gray, fine-grained gray groundmass (TSD45 @ 339.40m). Assay from 338.90 – 341.60m in TSD45 returned 0.039% Cu & 0.039g/t Au. alt'd dio = altered diorite, qtz-lim = quartz-limonite, kspar-mag = K-feldspar-magnetite, chl-smec = chlorite-smectite, qvn = quartz vein, plag = plagioclase, hbl = hornblende

(Fig. 2.12B). Strong K-feldspar and magnetite alteration is common, and there is a yellow clay-alteration overprint immediately below the base of oxidation, which has overprinted the quartz-magnetite stockwork. In thin section, fine to medium subhedral grained plagioclase and outlines of hornblende and biotite phenocrysts occur in a very fine-grained equigranular groundmass. Plagioclase is locally altered to orthoclase, and also to late sericite or chlorite-smectite which has imparted a yellow color to the sample. The primary mafic phenocrysts have been altered to secondary biotite that has been partially altered to chlorite-smectite. The groundmass has been altered to fine-grained granular quartz and opaques (SKM, 2001).

2.4.2.3 Inter-mineral Intrusion

At depths below –300m RL, the second early diorite porphyry and the diorite breccia complex have been intruded by an inverted, conical-shaped **inter-mineral diorite porphyry** (Fig. 2.6 & 2.8). The inter-mineral diorite porphyry is approximately 300 meters in diameter at –600m RL. Radiometric age determination of hornblende and biotite phenocrysts range from 3.10 ± 0.06 to 2.39 ± 0.03 Ma (Prise, 2002). In hand specimen, plagioclase (2-3mm) and hornblende (1-2mm) phenocrysts are set in a fine-grained gray groundmass (Fig. 2.12C). This intrusion contains a weak quartz stockwork (0.5 to 5%) with weakly developed K-feldspar-secondary biotite-magnetite alteration. In thin section, the subhedral phenocrysts of plagioclase and hornblende have been partly altered. The plagioclases contain flecks of sericite whereas the hornblende has been replaced mostly by secondary biotite, and partially by smectite in some places. In the vicinity of quartz veins, plagioclase has been altered to orthoclase. The groundmass consists of equigranular, fine-grained secondary(?) quartz and primary magnetite (SKM, 2001).

2.4.2.4 Late-mineral Intrusion

Late diorite porphyries occur as sub-vertical dykes (Fig. 2.8) that are 3-10 meters wide which have cut the inter-mineral diorite porphyry and all older rocks. In plan view, these porphyries have an east-west elongation axis (Fig. 2.3). In hand specimen, the late diorite porphyry has a crowded porphyritic texture where plagioclase (1-3mm) and hornblende (1-2mm) are set in a fine-grained gray groundmass (Fig 2.12D). The dykes are weakly altered (minor chlorite-secondary biotite±K-feldspar) and some samples contain minor quartz stockwork veins and fracture-fillings of chalcopyrite and bornite. In thin section, medium-grained subhedral to euhedral, oscillatory zoned andesine plagioclase is abundant, and has been partially altered to sericite. Some strongly sericitised grains have also been albitised. Fine-medium grained hornblende and biotite have been altered to chlorite and opaques. Remnant biotite has been observed locally. Phenocrysts are set in a very fine-grained felsic groundmass which is altered to quartz and minor sericite (SKM, 2001).

2.4.3 Paleosol

Weathering and erosion of the altered and mineralised Pliocene Intrusive complex has resulted in the formation of a reddish brown to orange paleosol at the unconformity surface (Fig 2.9F). The paleosol varies from 0.5 to 12 meters thick and formed intense oxidation and weathering of the underlying rocks. The paleosol locally contains mineralised diorite porphyry and quartz vein fragments demonstrating that the mineralised porphyry was uplifted and eroded before it was covered by the Tugunan Clastics and andesite lava flow deposits.

2.5 Faults

Although Boyongan is situated in a very active tectonic terrain within the Philippine fault zone, there is no appreciable offset or juxtaposition of geological units that has been observed in drillcore. Nonetheless, a strong NNE-trending structural control of the early progenitor intrusives is apparent (Sillitoe, 2001). A tensional fault is inferred to have controlled early intrusion and mineralisation. A major, possibly structurally controlled, NW-trending paleovalley has been delineated through paleosurface contour interpretations by Anglo American geologists. This paleovalley extends west of the breccia complex (Fig. 2.3B) to Siana in the southeast. This NW-trending palaeographical feature may have controlled the emplacement of medium-grained diorite and the diorite breccia complex, prior to the main stage of hypogene mineralisation at Boyongan.

2.6 Summary

The major points of relevance from this chapter to the supergene enrichment zone at Boyongan are as follows. Boyongan is located in the northern tip of the Eastern Mindanao Cordillera. It is bound to the east by the Philippine trench and to the west by the Philippines fault, two of the most active tectonic features of the Philippines. Extensional fault architecture was important in localising magmatic hydrothermal activity.

Volcanic and sedimentary rocks in Surigao del Norte consists of basaltic flows (Bacuag Formation), andesitic pyroclastics (Mabuhay Formation), and clastic sediments (Motherlode Formation). These are all part of the basement sequence in Boyongan. Volcanic and sedimentary textures suggest that these rocks were deposited both in submarine and subaerial environments.

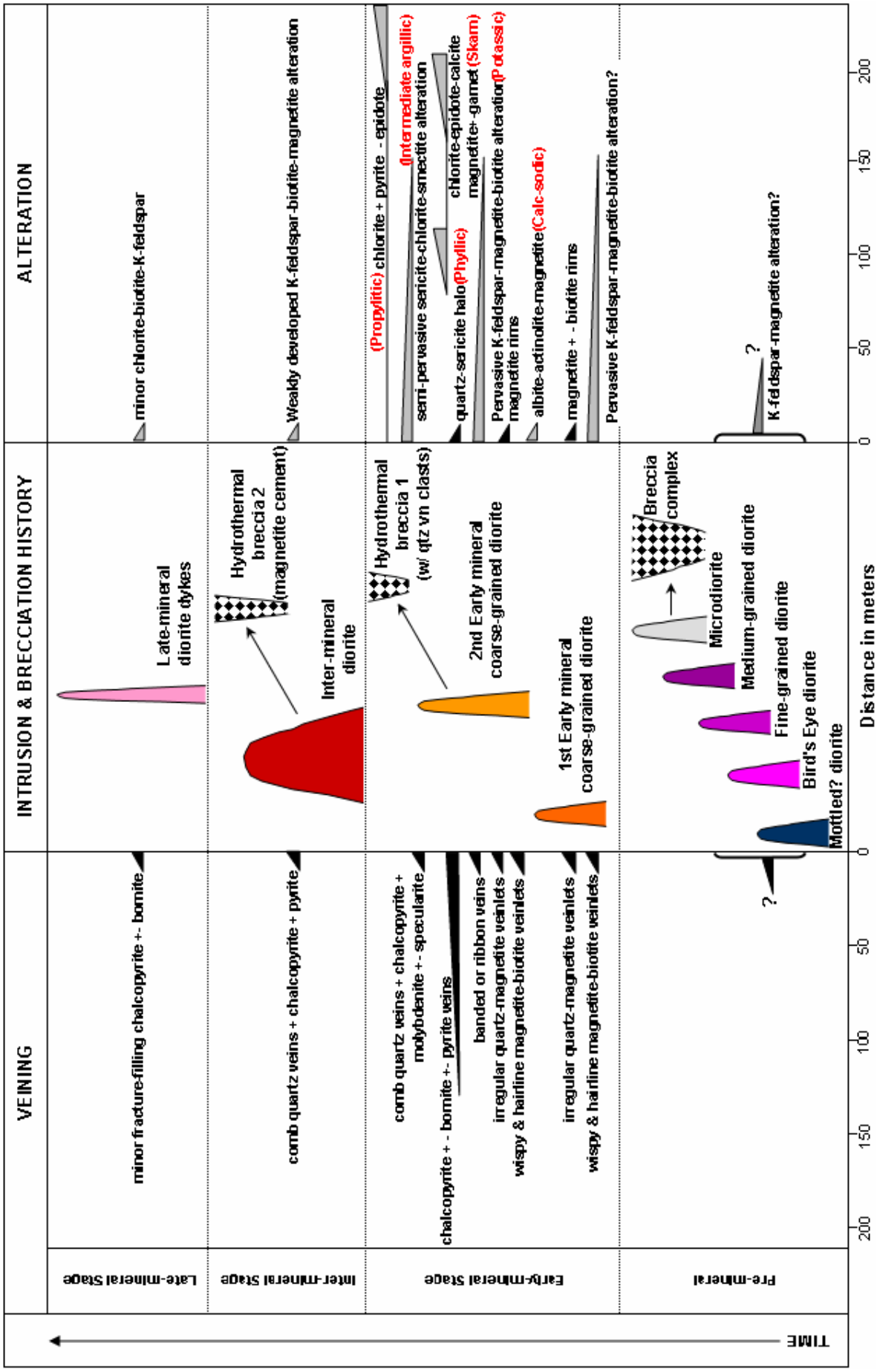

Fig. 2.13. Schematic space-time diagram of alteration and vein stages relative to the intrusive history of the Boyongan Intrusive Complex. Pervasive styles of alteration unrelated to a specific vein stage are filled with gray, whereas hydrothermal alteration assemblages that are related to a vein stage have a black fill. The distance from the Boyongan Intrusive Complex is based on the distribution of veins and alteration assemblages on sections 1062200N, 779700E, and –100mRL.

The basement sequence has been disrupted by a series of diorites and breccias that probably took place two to three kilometers beneath the present surface. These diorite intrusions and breccias are referred collectively as the Boyongan Intrusive Complex. Nine intrusive phases were identified in the Boyongan Intrusive Complex. The pre-mineral intrusions consists of the successive emplacement of diorite stocks (mottled diorite, "bird's Eye", medium-grained, & fine-grained diorite porphyries). Microdiorite intruded the pre-mineral intrusions and occurs as breccia cement. Pre-mineral phases now occur as clasts within breccia complex.

The emplacement of breccia complex preceeded the intrusion of high grade porphyries (first & second early coarse-grained diorite porphyries; Fig. 2.13). The first early diorite porphyry occur as a remnant intrusion at the top of second early diorite porphyry that occur as a series of dykes that have a NNE-strike, parallel to the long axis of the first early diorite porphyry. Both intrusions are characterized by intense alteration and quartz vein stockwork. However, the first early diorite porphyry is higher in grade (>2% Cu & >5g/t Au) compared to the second early diorite porphyry (0.75% to 1% Cu & 0.75 to 4 g/t Au). The deeper exposure of second early diorite porphyry however is poorly mineralised. Mineralisation probably took place during the Pliocene to Pleistocene.

The second early diorite porphyry and the breccia complex have been intruded by a low-grade, inverted, conical-shaped inter-mineral coarse-grained diorite. Late-mineral diorite porphyries occur as sub-vertical dykes which have cut the inter-mineral diorite porphyry and all overlying rocks.

Post-mineral events at Boyongan include rapid uplift and exposure of the mineralised intrusions to weathering and oxidation. These have produced the unique supergene profile at Boyongan which is one of the deepest in the world (Chapter 4). Poorly consolidated sediments and andesite lavas (Tugunan Formation & Maniayao Andesite) completely conceals the Boyongan Intrusive Complex and surrounding wallrocks, suggesting that Boyongan subsided in a pull-apart basin and have been subsequently been buried by lake sediments. During this time, the Maniayao and Paco andesite lavas have helped to bury the Boyongan porphyry deposit.

CHAPTER 3

HYPOGENE ALTERATION & MINERALISATION

3.1 Introduction

This chapter describes Boyongan's hypogene alteration assemblages and veins briefly, based on results of core logging during the current study, and fluid inclusion studies by consultants to Anglo American. This information is provided as background to the subsequent descriptions of supergene mineralisation and alteration (Chapter 4). The hypogene features of the Boyongan deposit are currently the subject of a PhD investigation by David Braxton (University of Tasmania).

3.2 Hydrothermal Alteration

Hydrothermal alteration assemblages at Boyongan are similar to other porphyry copper deposits in island arc settings (e.g. Sillitoe & Gappe, 1884). Potassic, propylitic intermediate argillic, phyllic, advanced argillic and calc-sodic assemblages have been recognised, and are described briefly below. The timing of alteration in relation to veining, intrusion and brecciation history of Boyongan is presented in Fig. 2.13.

3.2.1 Potassic Alteration

Hypogene Cu-Au mineralisation at Boyongan is spatially and temporally associated with a

potassic alteration assemblage, which is characterised by secondary biotite, K-feldspar, magnetite, and specularite (Fig. 3.1A, 3.1B & 3.2A). Secondary biotite has replaced primary ferromagnesian minerals in the quartz diorite intrusions and volcanic wallrocks. K-feldspar had replaced plagioclase and has locally flooded groundmass of intrusions and clasts in the breccia complex. Secondary magnetite occurs as disseminations and discontinuous hairline veinlets (Fig. 3.2A). Fluid inclusion analyses of veins associated with potassic alteration have revealed high salinity (>20wt% NaCl), high temperature (>500ºC) fluids (SKM, 2000). The hypogene grades associated with the potassic alteration range from <0.1 to 8 % Cu and <0.1 to 34 g/t Au.

3.2.2 Propylitic Alteration

Potassic alteration grades outward to a chlorite-pyrite± epidote assemblage that defines the propylitic zone. A pyrite halo, which is a common feature in porphyry copper deposits, also characterises this alteration assemblage (Fig. 3.1A & 3.1B). The propylitic assemblage occurs on the periphery of the Boyongan deposit, and has affected the intrusions, breccia complex, and volcanic wallrocks. Chlorite has replaced primary hornblende ± biotite, and epidote has altered both plagioclase and ferromagnesian minerals. Propylitic alteration is associated with grades ranging from <0.1 to 0.3 % Cu and <0.1 to 0.2 g/t Au.

3.2.3 Intermediate Argillic Alteration

Within the core of the Boyongan deposit, the potassic alteration assemblage has been overprinted by an intermediate-argillic alteration assemblage, which consists of sericite, chlorite, and smectite. Although Boyongan is extensive weathered and oxidized, this alteration assemblage is still preserved in the deeper portions of the deposit (Fig. 2.12B). Sericite has replaced secondary orthoclase and chlorite has replaced secondary biotite. It is

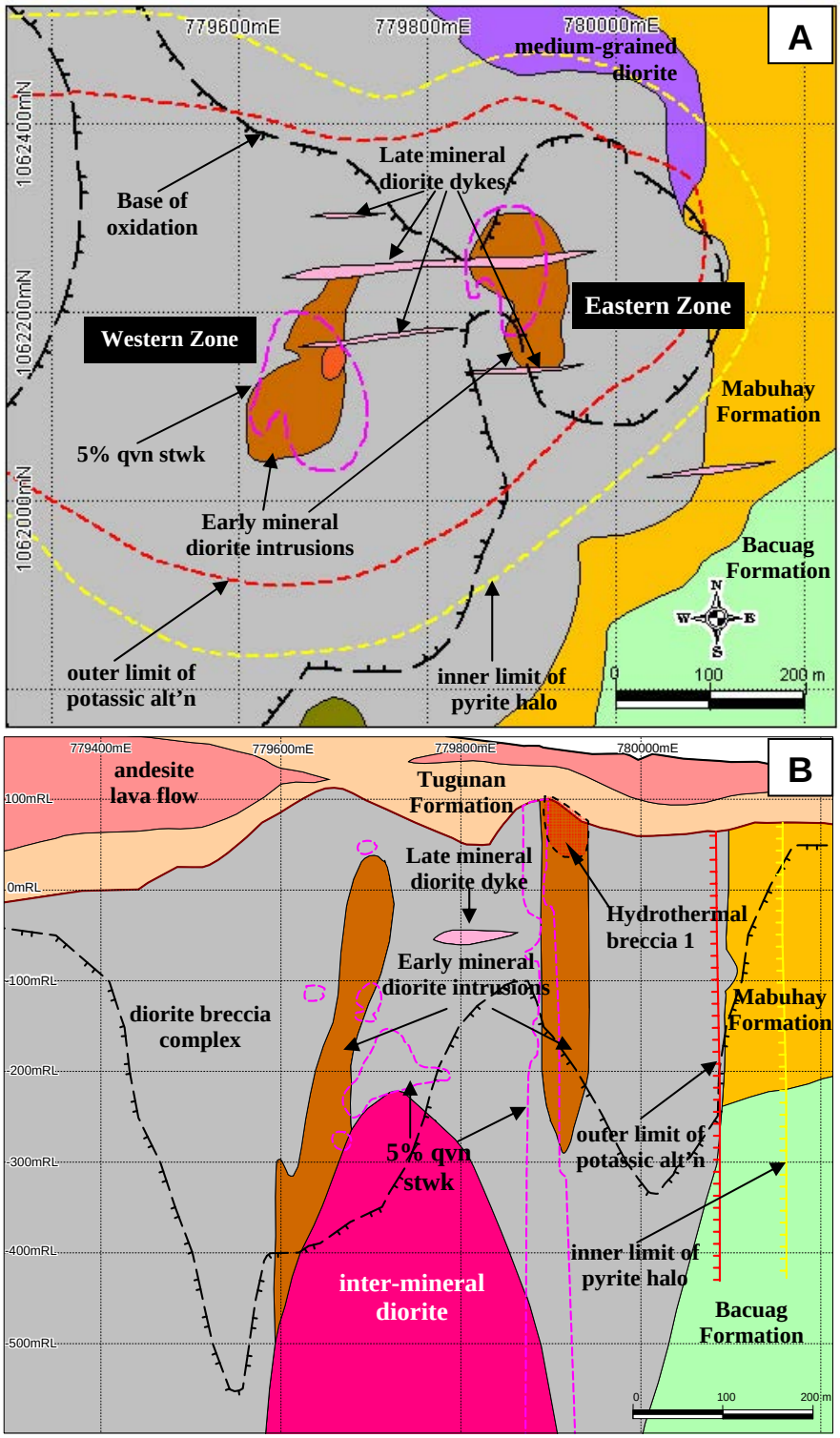

Fig. 3.1. Plan -100RL (**A**) and section 1062200N (**B**) showing areas that contain more than 5% quartz vein stockwork (pink broken lines). Also shown are the outer limit of potassic zone (broken red line) and inner limit of pyrite halo (broken yellow line) which is part of the propylitic zone. Highly mineralised hydothermal breccia 1 with characteristic diorite and quartz vein clasts is projected from section 1062250N. Wallrocks consists of Bacuag Formation (green colour), Mabuhay Formation (yellow colour), and medium-grained diorite (purple) that remain unbrecciated to the north (**A**). Wallrocks are intruded by diorite breccia complex (gray colour) and consequently intruded by the early mineral diorite intrusions (brown and orange colour), inter-mineral diorite (dark pink), and EW-trending diorite dykes. Skarn alteration (**A**) affected the breccia complex. Wallrocks, breccia complex, diorite intrusions are overlain by Tugunan Formation (light brown colour) and andesite lava flow (medium pink) in Figure 3.1B. qvn = quartz vein, stwk = stockwork

not known at this stage whether hypogene grade of Boyongan has been upgraded by intermediate argillic alteration.

3.2.4 Phyllic Alteration

Quartz, sericite and pyrite define the phyllic alteration assemblage at Boyongan, which has overprinted all earlier-formed alteration assemblages. It occurs as a halo to both quartz and sulfide veins (Fig. 3.2B). Illite is indicative of near neutral pH fluids and temperatures greater than 230ºC (Corbett & Leach, 1998; SKM, 2000). This type of alteration is very localised and has partially preserved the original rock textures.

3.2.5 Calc-Sodic Alteration

Albite-magnetite-actinolite alteration of the diorites (Fig. 3.2C) has occurred at depths of 600 meters below the paleosurface in drillhole TSD18. Albite has flooded the groundmass of the second early diorite porphyry and is associated with needles of actinolite and disseminated magnetite.

3.2.6 Advanced Argillic Alteration

One clast of intensely veined and altered diorite has been observed within the paleosol in TSD06 at 61.50m. This clast has been altered to a sericite-pyrophyllite mineral assemblage, typical of deep level advanced argillic alteration zones (e.g. Moore & Masterman, 2002). This clast may represent a remnant of a now eroded advanced argillic cap to the Boyongan system.

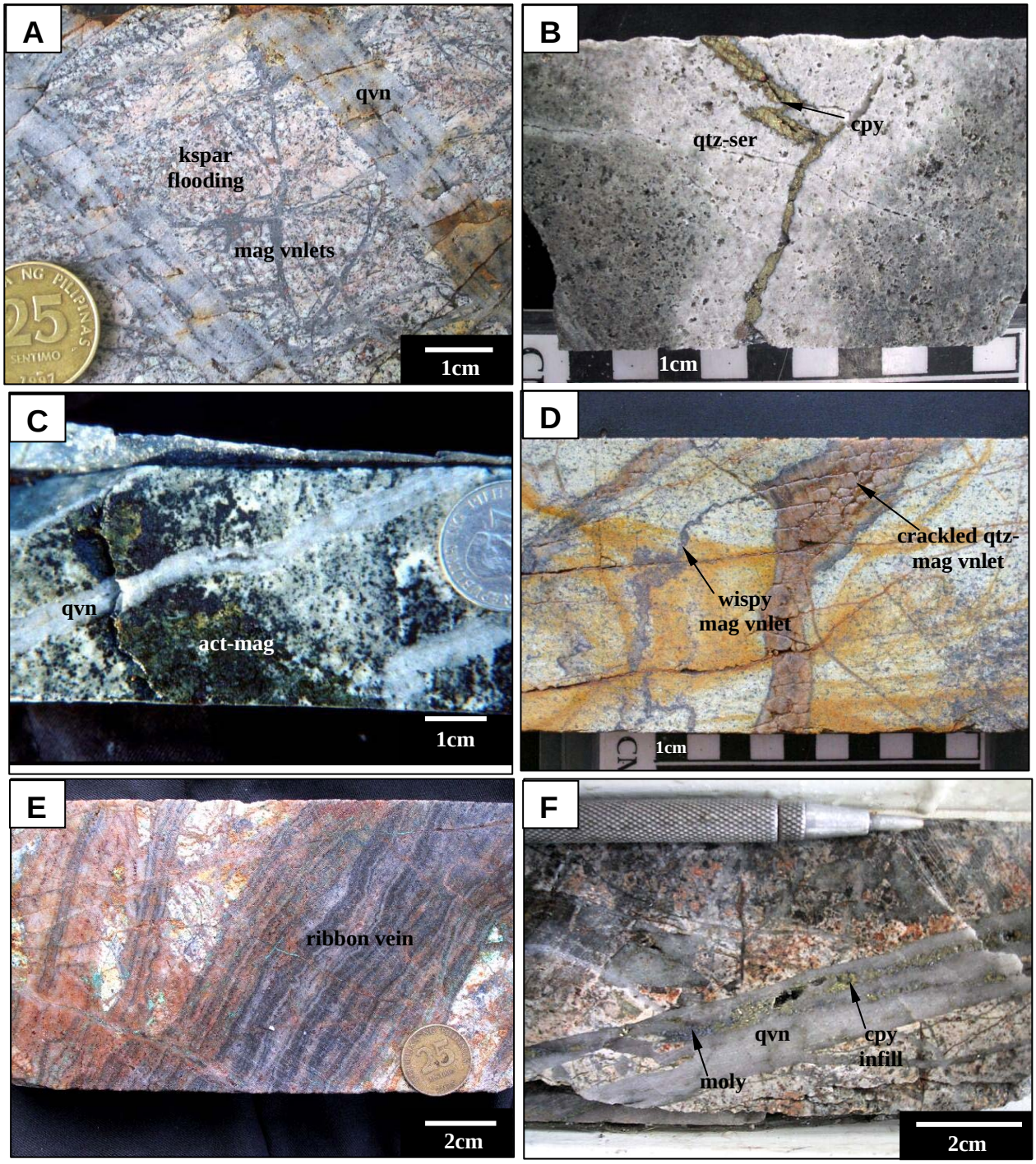

Fig. 3.2. A. Potassic alteration manifested as K-feldspar flooding of the groundmass, plus secondary biotite replacements of primary hornblende, and veinlets and dissemination of magnetite in the first early coarse-grained diorite porphyry (TSD44 @ 297.30m). Assay from 295 - 298m in TSD44 returned 0.323% Cu & 0.361g/t Au. **B.** Quartz-sericite halo on chalcopyrite vein in medium grained diorite porphyry (TSD52 @ 440.35m). Assay from 438.70 - 441.70m in TSD52 returned 0.344% Cu & 0.279g/t Au. **C.** Early actinolite-magnetite alteration with albite flooding in second early coarse-grained diorite porphyry cut by comb quartz vein (TSD18 @ 770.00m). Assay from 768 - 771m in TSD18 returned 0.163% Cu & 0.324g/t Au. **D.** Wispy magnetite (Stage 1 vein) and quartz-magnetite veinlets (Stage 2 vein) in second early coarse-grained diorite (TSD18 @ 181.20m). Assay from 180.20 - 183.20m in TSD18 returned 0.304% Cu & 0.267g/t Au. **E.** Banded or ribbon quartz veins (Stage 3) in first early coarse-grained diorite (TSD14 @ 91.25m). Assay from 88.45 - 91.45m in TSD14 returned 3.99% Cu & 5.17g/t Au. **F.** Comb quartz vein with chalcopyrite, pyrite and molybdenite (Stage 4 vein) cutting hydrothermal breccia (TSD18 @ 502.20m). Assay from 499.40 – 502.40m in TSD18 returned 0.32% Cu & 0.259g/t Au. qvn = quartz vein, kspar = K-feldspar, qtz-ser = quartz-sericite, act-mag = actinolite-magnetite, mag vnlet = magnetite veinlet, cpy = chalcopyrite, moly = molybdenite

3.2.7 Calc-Silicate Alteration

Yellow to green coloured skarns were intersected in TSD54 (Fig. 2.5 & 3.1A). They consist of chlorite+epidote +calcite+magnetite±brown garnet with disseminated pyrite and minor chalcopyrite that occur in both the breccia complex and the surrounding wallrocks (Fig.2.9D). Epidote skarn was intersected in the same hole and contains calcite, garnet, and clinopyroxene together with abundant epidote (SKM, 2003a). These skarns, together with other skarns intersected in drillholes TSD 42, 52, and 57 (Fig. 2.5, 2.8, & 3.1A), probably formed when magmatic hydrothermal fluids reacted with and replaced basalt and calcareous clasts in the host volcano-sedimentary sequence. Current drilling shows that these skarns are small and occur as irregular lenses. No large coherent body of skarn has been discovered as yet.

3.3 Veins

Potassic alteration at Boyongan is associated with hairline magnetite veinlets and multiple generations of cross-cutting quartz veinlets, which have formed a complex vein stockwork in and around the diorite porphyries (Fig. 3.2A). The intensity of quartz veining generally decreases away from the centre of the Boyongan deposit. Most of the veins are related to the early stage diorite intrusions. Earlier veins have been broken and now occur as clasts within highly mineralised hydrothermal breccia (Fig. 3.1B & 3.3C; section 3.4). Weak to moderate veining has been observed in the inter-mineral intrusions and the breccia complex. The generalised vein paragenesis for Boyongan is as follows:

Stage 1: The earliest-formed veins at Boyongan are the hairline, wispy, discontinuous **magnetite-biotite veinlets** that contain minor chalcopyrite (Fig. 3.2D). These has been cut

by all later vein generations.

Stage 2: Stage 1 veinlets have been cut by stage 2 **irregular quartz-magnetite veins** (quartz veins with magnetite rims) similar to the A veins described from El Salvador by Gustafson and Hunt (1975). Some stage 2 veins have a distinctive "crackled" texture (Fig. 3.2D). Sulfides locally occupy the fractures that define the crackled texture.

Stage 3: Stage 2 veins are cut by stage 3 **banded or "ribbon" texture veins** (Fig. 3.2E). Assay data indicates that most of the high grade hypogene copper and gold is associated with stage 3 veins. These veins may have re-opened several times to produce the composite banded veins.

Stage 4: Stage 3 banded veins are locally cut by stage 4 **comb quartz veins**. These veins are characterised by centre lines with local void space, where euhedral quartz crystals have terminated after growing inwards from the vein margins (Fig. 3.2F). Stage 4 quartz veins contain minor chalcopyrite±bornite±molybdenite±specularite.

Five stage 4 vein samples (quartz+magnetite+chalcopyrite±bornite±hematite) were submitted to Sinclair Knight Merz for fluid inclusion analyses (SKM, 2003). Laboratory results indicate vein formation from high salinity (50-69 wt% NaCl) and high temperature fluids with measured homogenisation temperatures from 400-800ºC. Some of the primary fluid inclusions are vapour-rich, and many are three-phase, containing cyrstals that appear to be halite, as well as liquid and vapour. In addition to halite, other minerals observed in these inclusions were sylvite, anhydrite, and hematite (SKM, 2003). These are typical of fluid inclusions in porphyry copper deposits (Reynolds and Beane, 1985; Cooke, et al., 1998; Hedenquist and Richards, 1998; Sillitoe, 2000).

Stage 5: The final stage of hypogene vein mineralisation are the **massive sulfide veins**, which consists of pyrite ± chalcopyrite ± bornite (Fig 3.3A). These are comparable to the D veins described from El Salvador by Gustafson and Hunt (1975). They are locally associated with quartz-sericite alteration halos.

3.4 Hydrothermal Breccias

In the eastern high grade zone intersected by drill holes TSDs 14, 18, 38 and 48 (Fig. 2.5), the exceptionally high grade 'hydrothermal breccia 1' occurs. It is spatially associated with

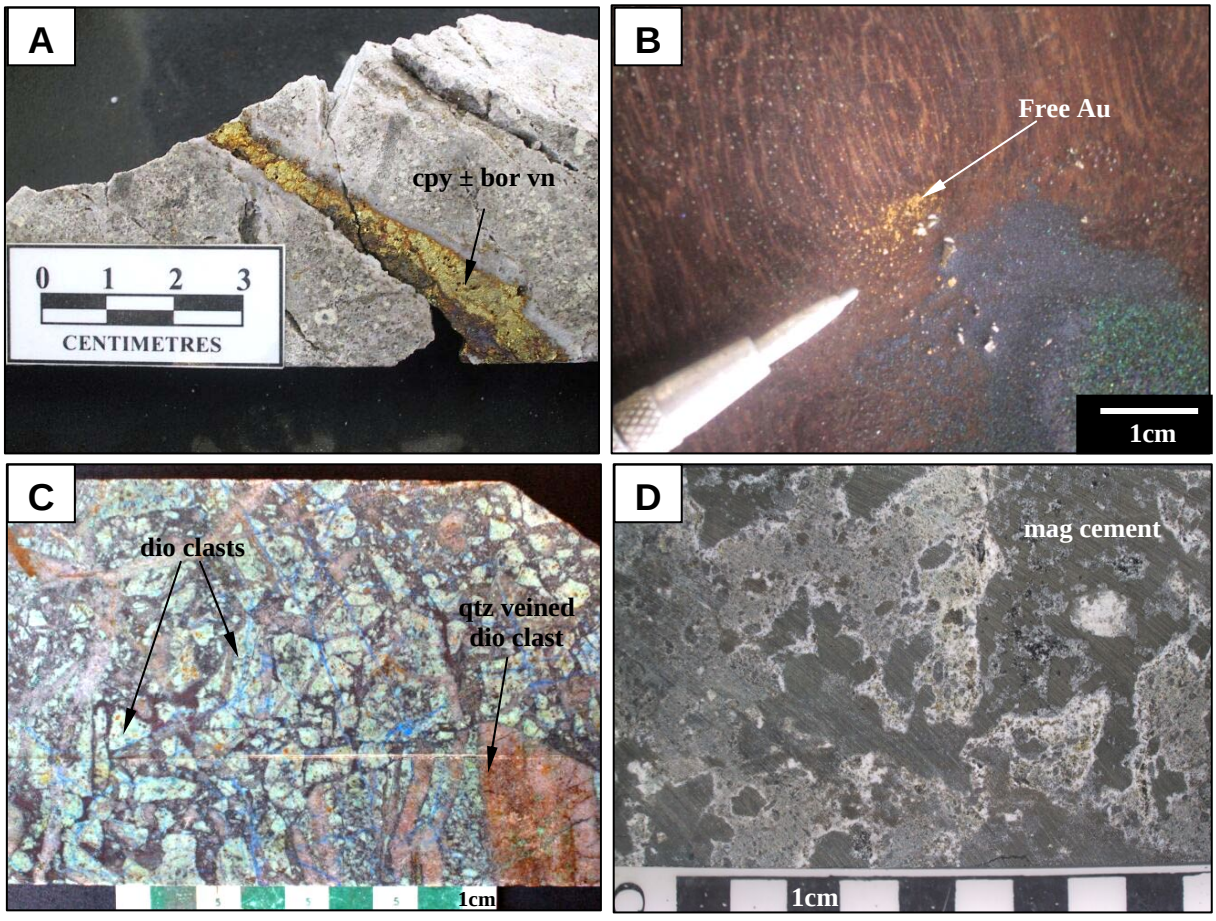

Fig. 3.3. A. Chalcopyrite ± bornite stage 5 vein in fine-grained diorite breccia (TSD45 @ 359.50m). Assay from 398.60 – 401.60m in TSD44 returned 0.762% Cu & 1.41g/t Au. **B.** Free gold from panned rock saw cuttings (TSD38 from ~100 - 120m) **C.** Highly silicified hydrothermal breccia 1 containing sub-angular to angular diorite and quartz vein fragments (TSD38 @ 84.25m). Assay from 84 – 87m in TSD38 returned 6.83% Cu & 9.74g/t Au. **D.** Hydrothermal breccia 2 (Hbr2) with magnetite ± chalcopyrite (TSD51 @ 360.25). Assay from 359.20 – 360.95m in TSD51 returned 0.159% Cu & 0.151g/t Au. cpy = chalcopyrite, bor = bornite, mag = magnetite, dio = diorite, qtz = quartz, vn = vein, Au = gold

the second early coarse-grained diorite. The breccia has a cup-shaped geometry. It is approximately 90 meters across and 150 meters in length from top to bottom (Fig. 3.1B). This breccia is highly silicified with characteristic sub-angular to angular diorite and quartz vein clasts (Fig.3.3C). The presence of clasts with truncated quartz veins indicates that this breccia formed after the initial phases of mineralisation at Boyongan. The margins of the clasts have been altered to secondary magnetite that has in turn been altered to hematite and quartz. Later mineralised stage 4 quartz veins have cut the breccia.

Hydrothermal Breccia 2 is magnetite-cemented. It has been intersected in TSD14, 38 and 51 and is spatially related to the inter-mineral diorite (not shown on the sections). This breccia has been described as black coloured with clasts of fine-grained diorite, mottled diorite and silicified rocks set in a magnetite cement (Fig. 3.3D).

3.5 Hypogene Mineralisation

Hypogene copper-iron sulfides and gold occurs primarily in stage 3 and 4 quartz veins at Boyongan. The sulfides are dominated by chalcopyrite with lesser bornite and pyrite. Sulfides occur as fracture-fill, vug-fill, disseminations, and veinlets in quartz veins, and locally as replacements in the altered wallrocks (Fig. 3.4). Massive chalcopyrite ± bornite veins have been observed. Molybdenite is very minor and appear to be associated with stage 4 veins comb quartz veins. The abundance of pyrite increases away from the main Cu orebody, forming a pyrite halo typical of most porphyry copper deposits (Lowell and Guilbert, 1970; Sillitoe and Gappe, 1984). Below the zone of oxidation, hypogene copper grades vary from <0.1 to 0.5% and gold from 0.1 to 1 g/t.

Hypogene mineralisation is intimately associated with quartz veining, which appears to

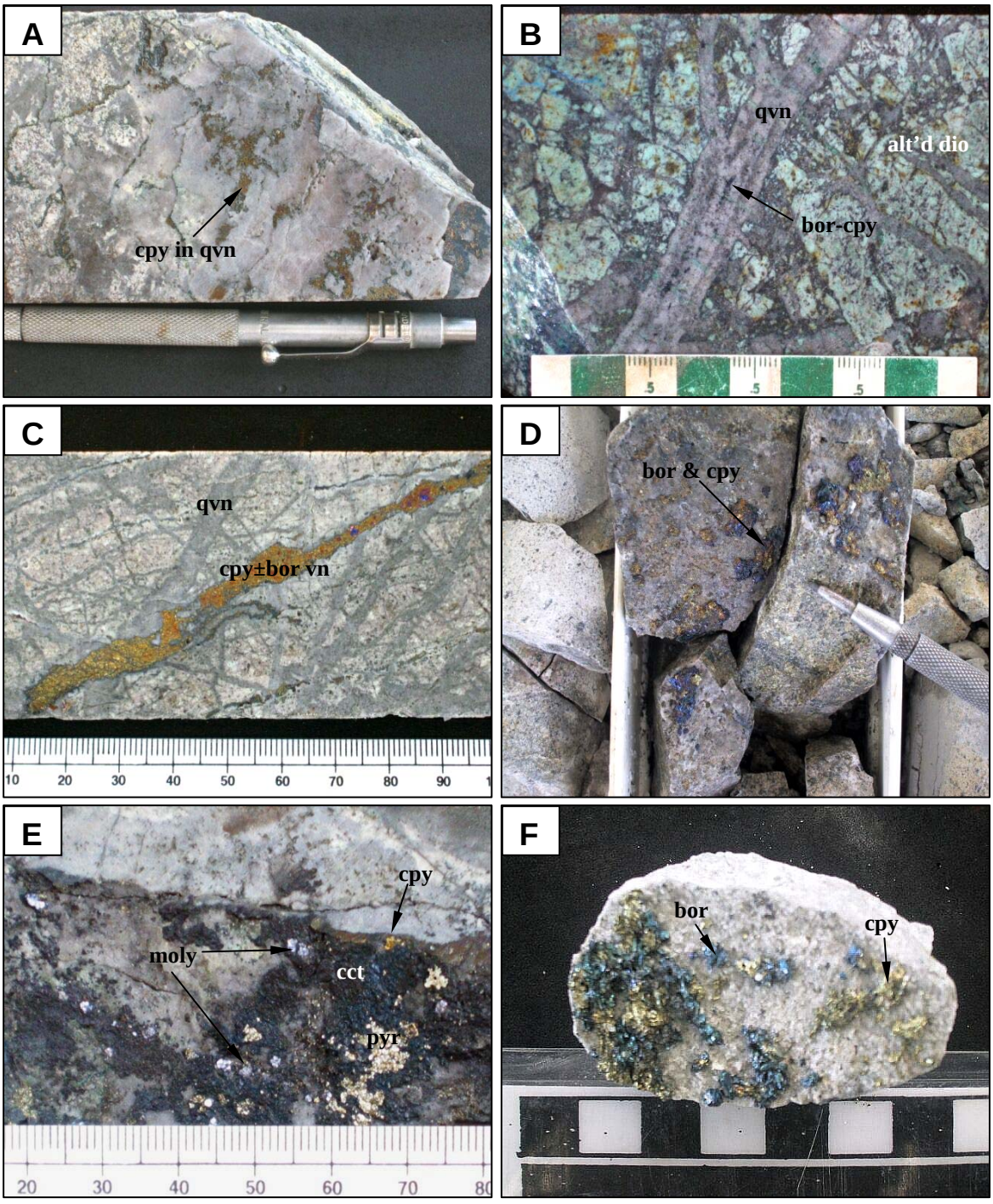

Fig. 3.4. Photographs of hypogene sulfide occurrences at Boyongan. **A.** Chalcopyrite ± bornite in stage 3 quartz vein in TSD38 @ 262.60m. **B.** Fine bornite and chalcopyrite in stage 4 quartz vein that has cut hydrothermal breccia 1 in TSD38 @ 84.50m. **C.** Stage 5 chalcopyrite ± bornite vein cutting stage 4 quartz veins in TSD20 @ 301.95m. **D.** Fracture-filling bornite and chalcopyrite in TSD45 @ 372.40m. **E.** Fracture-filling pyrite, chalcopyrite ± molybdenite being replaced by supergene chalcocite in TSD20 @ 298.20m. F. Fracture-filling chalcopyrite, bornite and covellite(?) in TSD49 @ 690.10m. cpy = chalcopyrite, bor = bornite, pyr = pyrite, cct = chalcocite, moly = molybdenite, alt'd dio = altered diorite, qvn = quartz vein, vn = vein

have been related primarily to the intrusion of the early coarse-grained diorite. However, some quartz veins are not mineralised, especially in the deeper portions of the deposit. It could be that the deeper parts of the system were too hot, preventing copper and gold from precipitating because their solubilities were too high (Sillitoe, 2001). These barren quartz veins define the low grade core of the Boyongan deposit.

Visible gold has been observed both in drillcore and in thin section. Sub-millimetre gold grains have been recovered from panned rock saw cuttings (Fig. 3.3D) especially for samples from high grades zones where intense quartz stockwork has developed. Gold has been observed within the bornite, and as isolated free grains within quartz veins.

3.6 Summary

- Potassic alteration occurred during the formation of an intense quartz, stockwork which contains the bulk of hypogene sulfide and gold mineralisation at Boyongan. The potassic assemblage has been overprinted by a sericite-chlorite-smectite (intermediate argillic) alteration assemblage, and is surrounded by an outer propylitic alteration halo.

- Hypogene sulfide mineralisation at Boyongan is dominated by chalcopyrite± bornite± pyrite±molybdenite

- The copper-iron sulfides occur as fracture-fill, vug-fill, disseminations, and veinlets in quartz veins, and locally as replacements in the altered wallrocks.

- Gold occurs within bornite and also as isolated grains in quartz veins.

- A hydrothermal breccia, which is associated with the first early coarse-grained diorite porphyry contain abundant chalcopyrite and bornite.

CHAPTER 4

SUPERGENE MINERALISATION & ALTERATION

4.1 INTRODUCTION

This chapter describes the different supergene minerals of Boyongan, the spatial distribution of supergene minerals, and how they evolved through time.

4.2 SECONDARY COPPER SULFIDE MINERALISATION

Supergene mineralisation in Boyongan has formed via the oxidation and weathering of pre-existing hypogene minerals (section 3.5). Remnant hypogene and supergene sulfides have been observed throughout the core logging, indicating that sulphide oxidation has not proceeded to completion. The supergene profile at Boyongan is therefore inferred to be immature (Fig. 4.1). The supergene copper sulfides observed during the current study are chalcocite, digenite, and pseudo-covellite.

4.2.1 Chalcocite

Chalcocite (Cu_2S) is the most common supergene sulfide, occurring as partial to complete replacements of bornite and chalcopyrite (Fig. 4.1A, B, & D). It is black, occasionally sooty, and has a shiny metallic luster under polished surface. It has been replaced by cuprite

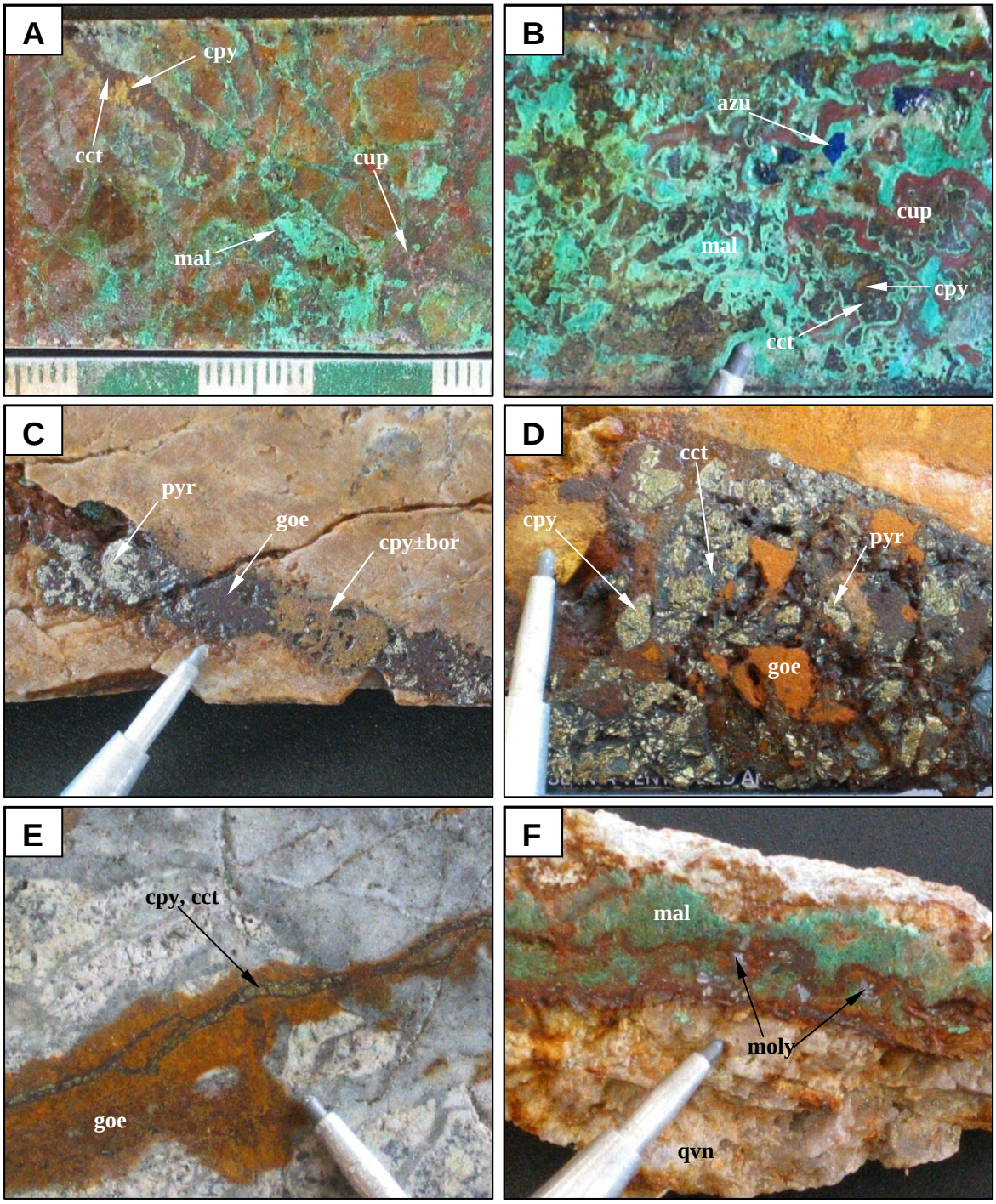

Fig. 4.1. A series of photographs showing remnant sulfides in the oxide zone at Boyongan. **A.** Remants of chalcopyrite have been partially replaced by chalcocite, malachite and cuprite in TSD38 @ 78.40m. **B.** Remants of chalcopyrite and bornite have been replaced by chalcocite, malachite, and cuprite in TSD14 @ 135.95m (tip of scriber for scale) **C.** Chalcopyrite, bornite + pyrite have been partially replaced by chalcocite and goethite (scriber for scale). **D.** Chalcopyrite, bornite, and pyrite have been replaced by chalcocite and goethite (scriber for scale). **E.** Chalcopyrite and chalcocite in fracture fringed with limonite (scriber for scale). **F.** Pyrite, chalcopyrite, molybdenite have been replaced by goethite and malachite in quartz vein in TSD20 @ 258.70m (scriber for scale). cpy = chalcopyrite; bor = bornite; moly = molybdenite; pyr = pyrite; cct = chalcocite; cup = cuprite; mal = malachite; goe = goethite; qvn = quartz vein

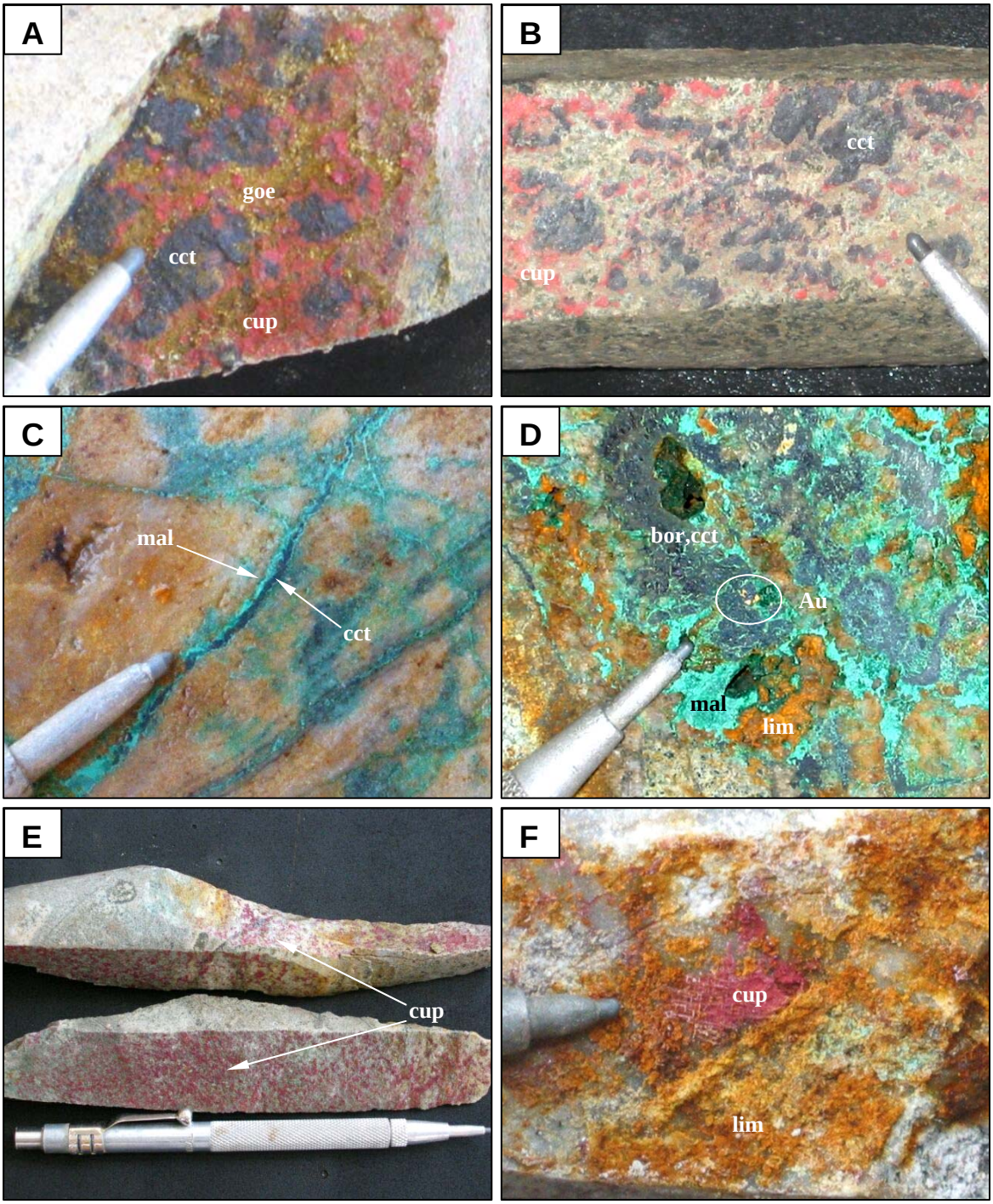

Fig. 4.2. Styles of supergene mineralisation. **A.** Chalcocite replaced by cuprite in TSD52 @ 277.90m (scriber for scale). **B**. Chalocite replaced by cuprite in TSD62 @ 280.90m (scriber for scale) **C.** Chalcocite replaced by malachite in TSD18 @ 70.55m **D**. Bornite with gold (in circle) replaced by chalcocite and malachite in TSD38 @ 107.40m (scriber for scale). **E.** Fracture-fill -± dissemination of cuprite in TSD53 @ 245.90m (scriber for scale). **F.** Mesh or neddles of cuprite associated with limonite in TSD18 @ 308.90m (scriber for scale). bor = bornite; cct = chalcocite; cup = cuprite; mal = malachite; goe = goethite; lim = limonite; Au = gold

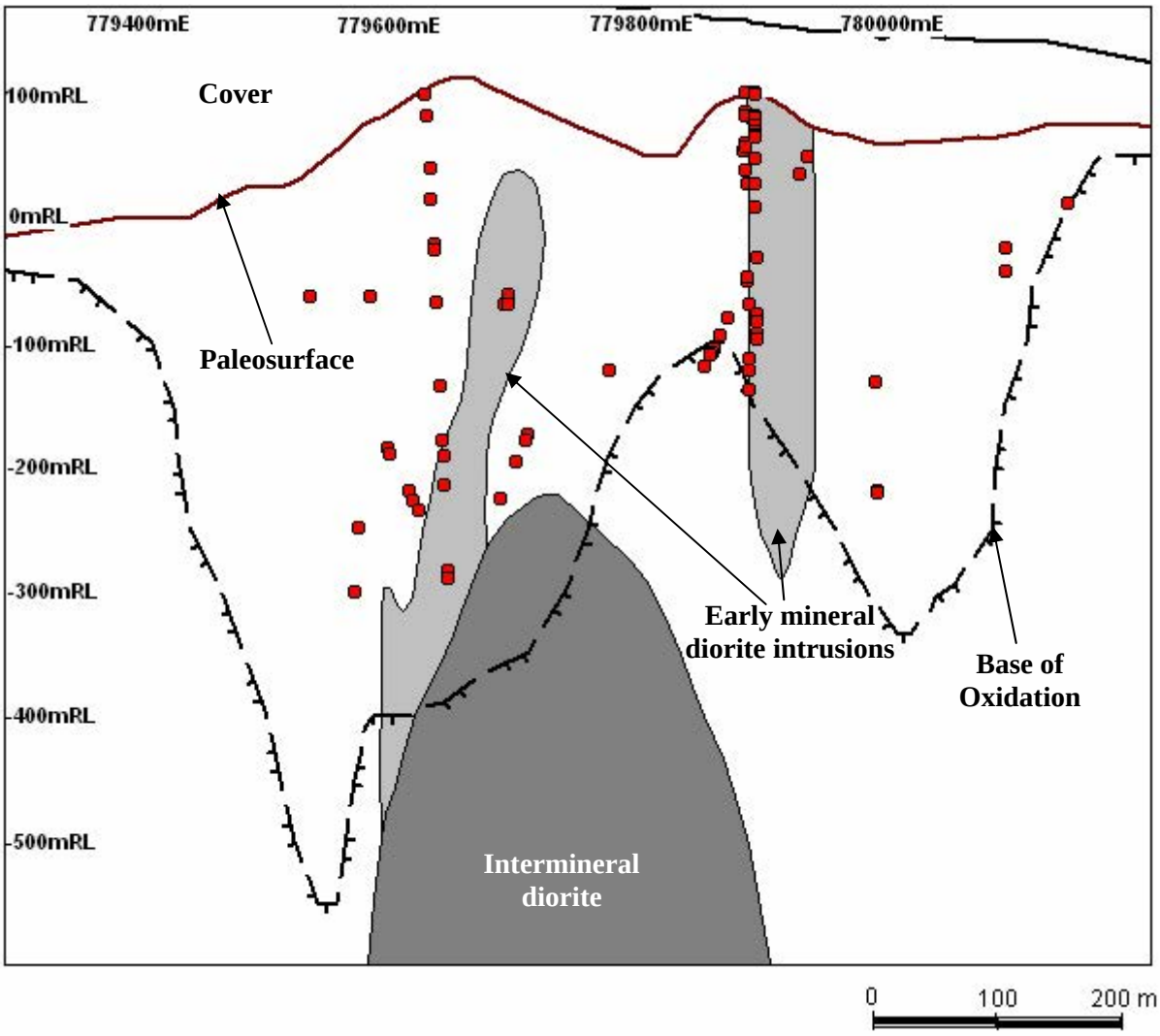

Fig. 4.3. Ore microscopy sample locations along section 10622000N (looking north). Most samples were collected from the eastern zone, whereas remnant hypogene sulfides are preserved within the oxide zone. Both megascopic and ore microscopic observations were used to establish the supergene mineral paragenesis at Boyongan.

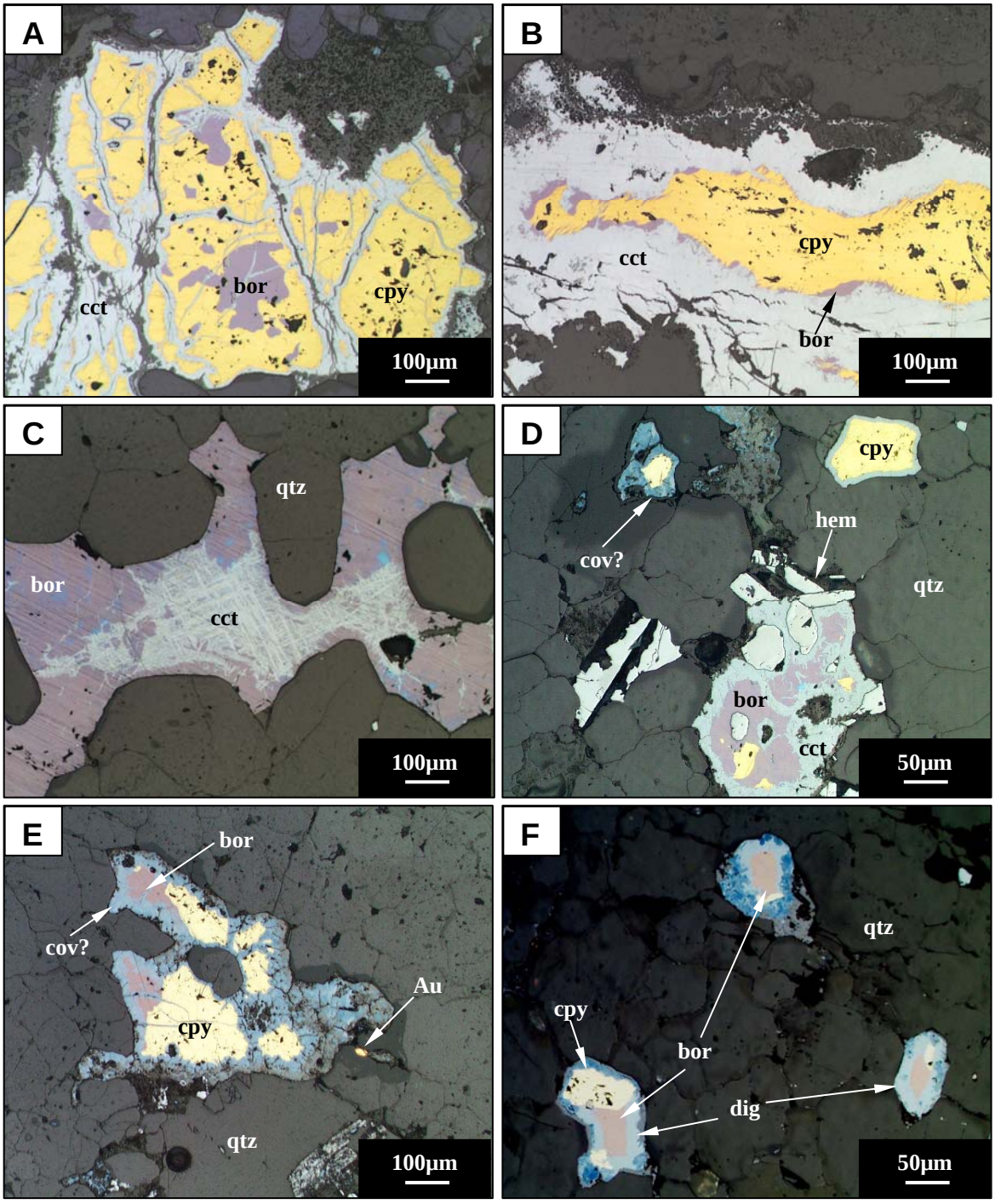

Fig. 4.4. **A.** Chalcopyrite and bornite, partially replaced by chalcocite in TSD38 @ 74.80m (field of view or FOV: 1.10mm; Reflected light or RL). **B.** Chalcopyrite intergrown with bornite, partially replaced by chalcocite in TSD13 @ 482.90m (FOV: 1.10mm; RL). **C.** Supergene chalcocite, replacement of bornite on exsolution lamellae(?) in TSD38 @ 271.20m; sulfides occur between quartz grain boundaries (FOV: 1.10mm; RL). **D.** Chalcopyrite rimmed by covellite (upper left); bornite & chalcopyrite (bottom and upper right) have been partially replaced by chalcocite in TSD38 @ 138.15m; sulfides occur between quartz grain boundaries (FOV: 0.55mm; RL). **E.** Chalcopyrite and bornite partially replaced by covellite in TSD38 @ 138.15m; sulfides occur between quartz grain boundaries; Gold grain at the right side of photo (FOV: 1.10mm; RL). **F.** Digenite has partially replaced chalcocite; chalcocite have replaced pre-existing sulfides (bornite and chalcopyrite) in TSD38 @ 253.60m; sulfides occur between quartz grain boundaries (FOV: 0.55mm; RL). cpy = chalcopyrite; bor = bornite; cct = chalcocite; cov = covellite; dig = digenite; qtz = quartz; Au = gold; hem = hematite

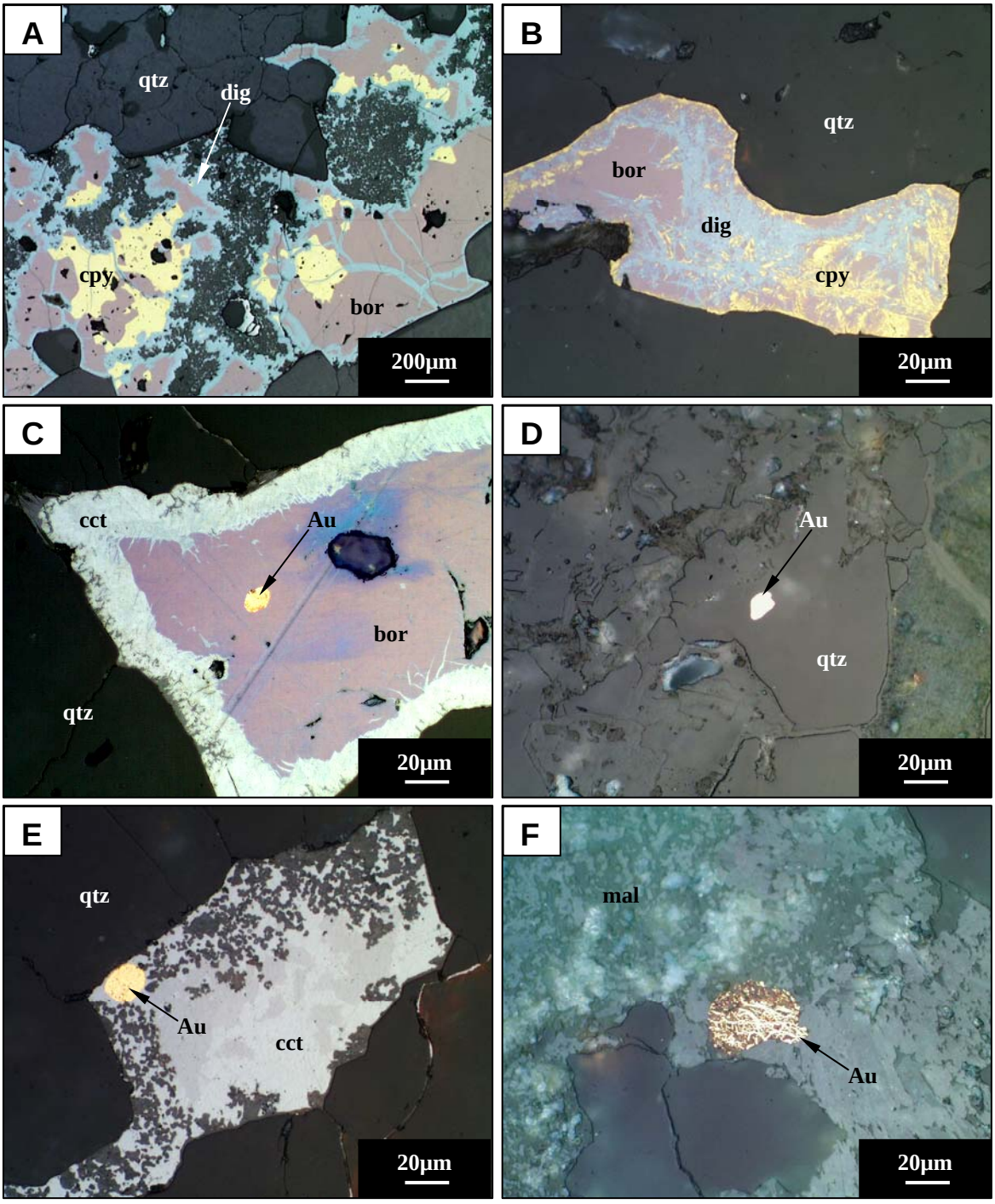

Fig. 4.5. A. Supergene digenite has partially replaced bornite and chalcopyrite in TSD38 @ 84.85m; quartz vein host (field of view or FOV: 2.20mm; reflected light or RL). **B** Supergene(?) or hypogene(?) digenite replacement of bornite and chalcopyrite in TSD38 @ 276.80m; quartz vein host (FOV 0.22mm; RL). **C.** Hypogene gold in bornite in TSD38 @ 138.15m; bornite replaced by chalcocite (FOV 0.22mm; RL). **D.** Hypogene gold in quartz vein in TSD13 @ 216.70m (FOV 0.22mm; RL). No microprobe results are available for hypogene gold. **E.** Supergene gold in chalcocite in TSD18 @ 116.20m; electron microprobe results (Appendix 3) show that this mineral contains 97.67wt% Au, 1.80wt% Ag, and 2.82wt% Cu (FOV 0.22mm; RL). **F.** Supergene Au in malachite ± goethite in TSD13 @ 216.70m (FOV 0.22mm; RL). cpy = chalcopyrite; bor = bornite; cct = chalcocite; dig = digenite; mal = malachite; qtz = quartz; Au = gold

(Fig. 4.2A & B) and malachite locally (Fig. 4.2C & D). Chalcocite occurs as fracture-fill and microfractures within quartz veins. Minor chalcocite was observed to coat pyrite crystals (Fig 4.15A, B, & C) suggesting that the copper was exotic (Blanchard, 1968). This texture is interpreted to indicate that pyrite acted as a local reductant during weathering (Einaudi, 1995). Replacement textures of gray chalcocite rimming sulfides are readily evident under the microscope (Fig. 4.4A, B, C, & D).

4.2.2 Digenite

Digenite (Cu_9S_5) is the second most abundant supergene sulfide observed at Boyongan. It is blue in colour and non-pleochroic under the microscope (Spry and Gedlinske, 1987). Like chalcocite, it was observed to replace bornite and chalcopyrite (Fig. 4.5A & B).

4.2.3 Pseudo-covellite

Pseudo-covellite occurs as minor replacements of chalcopyrite, bornite, chalcocite, and digenite at Boyongan (Fig. 4.4E & F). It is distinguished from covellite under the petrographic microscope because it displays strong indigo-blue pleochrism when the microscope stage is rotated (Ixer, 1990; Spry and Gedlinske, 1987).

The occurrence of chalcocite, digenite, and pseudo-covellite at Boyongan suggest that primary sulfides were progressively oxidized during weathering, because of the progressively higher oxidation states for copper (Boyle,1996).

4.3 SECONDARY COPPER OXIDES & NATIVE COPPER MINERALISATION

4.3.1 Cuprite

The most common copper oxide mineral is cuprite (Cu_2O). It usually occurs both as acicular needles of chalcotrichite (Fig. 4.2E & F) and as euhedral cuprite crystals (Fig. 4.6D). Fresh examples are deep pinkish red or pure red in colour, whereas the more oxidised varieties are orange to yellow orange coloured. Cuprite can also be identified not only by its colour and form but through an acid test (Fig. 4.12F), where a copper plate is left when cuprite is mixed with cold dilute hydrochloric acid on a steel knife or plate. At Boyongan, cuprite usually occurs along fractures and as minor disseminations that have preferentially replaced plagioclase phenocrysts (Fig. 4.7E). Cuprite is associated with chalococite, native copper (Fig. 4.6C), copper carbonates such as malachite and azurite (Fig. 4.7D), and goethite.

4.3.2 Native Copper

Native Copper (Cu^0) occurs along fractures (Fig. 4.6C & E) with cuprite (Fig. 4.7A). Dentritic forms are common (Fig. 4.7C). Native copper is also associated with chalcocite (Fig. 4.7B). Native copper can be difficult to recognise when it is mixed with goethite. Under the microscope, native copper has been observed to have been partially replaced by euhedral crystals of cuprite (Fig. 4.6C)

4.3.3 Malachite

Malachite [$Cu_2(CO_3)(OH)_2$] is green in colour and typically occurs in fractures (Fig. 4.7F)

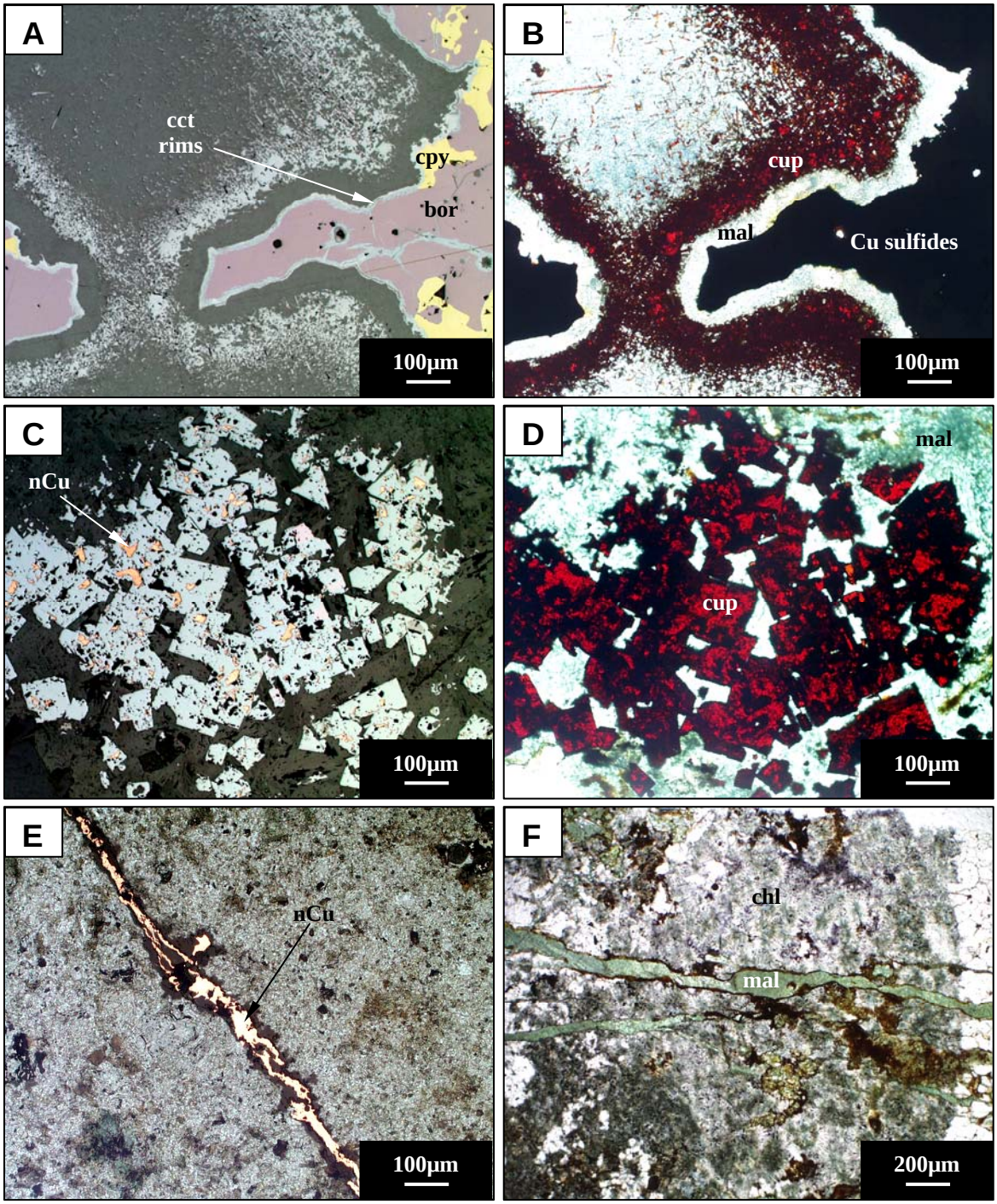

Fig. 4.6. A. Bornite intergrown with chalcopyrite, and replaced by chalcocite in TSD14 @ 135.95m (Field of view or FOV: 1.10mm; reflected light or RL). **B.** Same as A; bornite, chalcopyrite, and chalcocite have been replaced by malachite and then overgrown by needles of cuprite in TSD14 @ 135.95m (FOV: 1.10mm; same as A but viewed under transmitted light or TL). **C.** Native copper replaced by cuprite in TSD18 @ 132.30m (FOV: 1.1mm; RL). **D.** Euhedral crystals of cuprite surrounded by malachite in TSD18 @ 132.30m (FOV: 1.10mm; same as C but viewed under TL). **E.** Fracture-filling native Cu in TSD47 @ 356.00m (FOV: 1.10mm; RL). **F.** Fracture-filling malachite rimmed by goethite and surrounded by chlorite in TSD38 @ 114.90m (FOV: 2.2mm; TL). cpy = chalcopyrite; bor = bornite; cct = chalcocite; cup = cuprite; nCu = native copper; mal = malachite; chl = chlorite

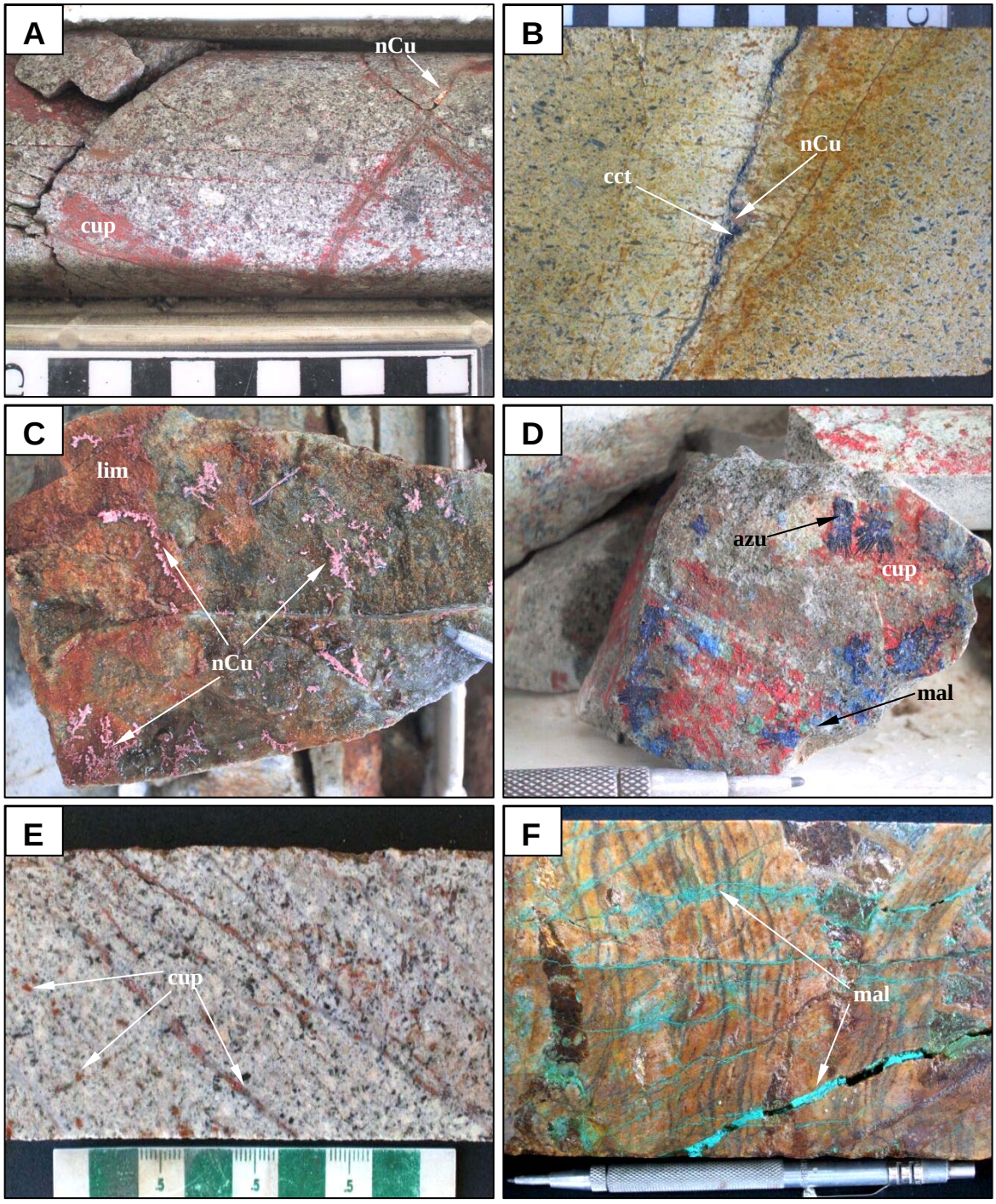

Fig. 4.7. Styles of supergene mineralisation **A.** Cuprite associated with native Cu in TSD50 @ 379.20m (cm card for scale). **B.** Pyrite replaced by chalcocite then by native Cu in TSD18 @ 216.30m (cm card on top for scale). **C.** Dentritic native Cu in TSD45 @ 304.40m (tip of scriber on the right for scale)**. D.** Complex intergrowth of cuprite, azurite ± malachite in fracture in TSD24 @ 215.20m (scriber for scale). **E.** Selective copper staining (cuprite) on plagioclase in TSD53 @ 386.30m. **F.** Fracture-filling malachite cutting limonitic, banded or "ribbon" quartz veins in TSD38 @ 60.20m (scriber for scale). cct = chalcocite; nCu = native copper; cup = cuprite; mal = malachite; azu = azurite; lim = limonite

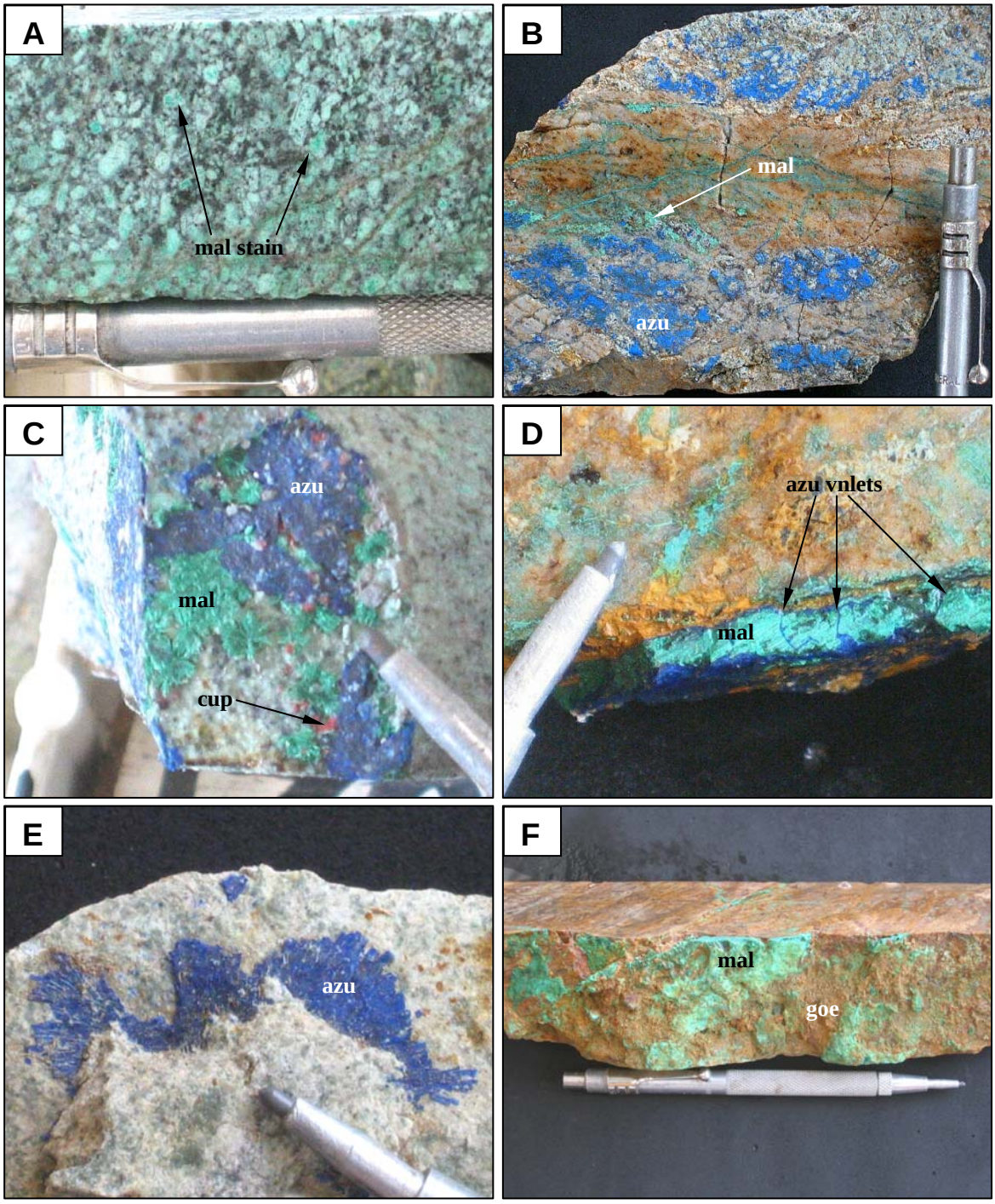

Fig. 4.8. Styles of supergene mineralisation. **A** Selective copper staining (malachite) on plagioclase in diorite within TSD44 @ 231.80m (scriber for scale). **B.** Fracture-filling malachite in quartz vein and disseminated azurite in groundmass of diorite in TSD38 @ 56.20m (scriber for scale). **C.** Cuprite overgrown by malachite then by azurite in TSD44 @ 133m (tip of scriber for scale). **D.** Azurite cutting and rimming malachite in TSD38 @ 107.60m (scriber for scale). **E.** Radiating crystals of azurite in fracture in TSD11 @ 397.20m (tip of scriber for scale). **F.** Malachite associated with limonite in fracture in TSD18 @ 65.30m (scriber for scale). cup = cuprite ; mal = malachite; azu = azurite; goe = goethite

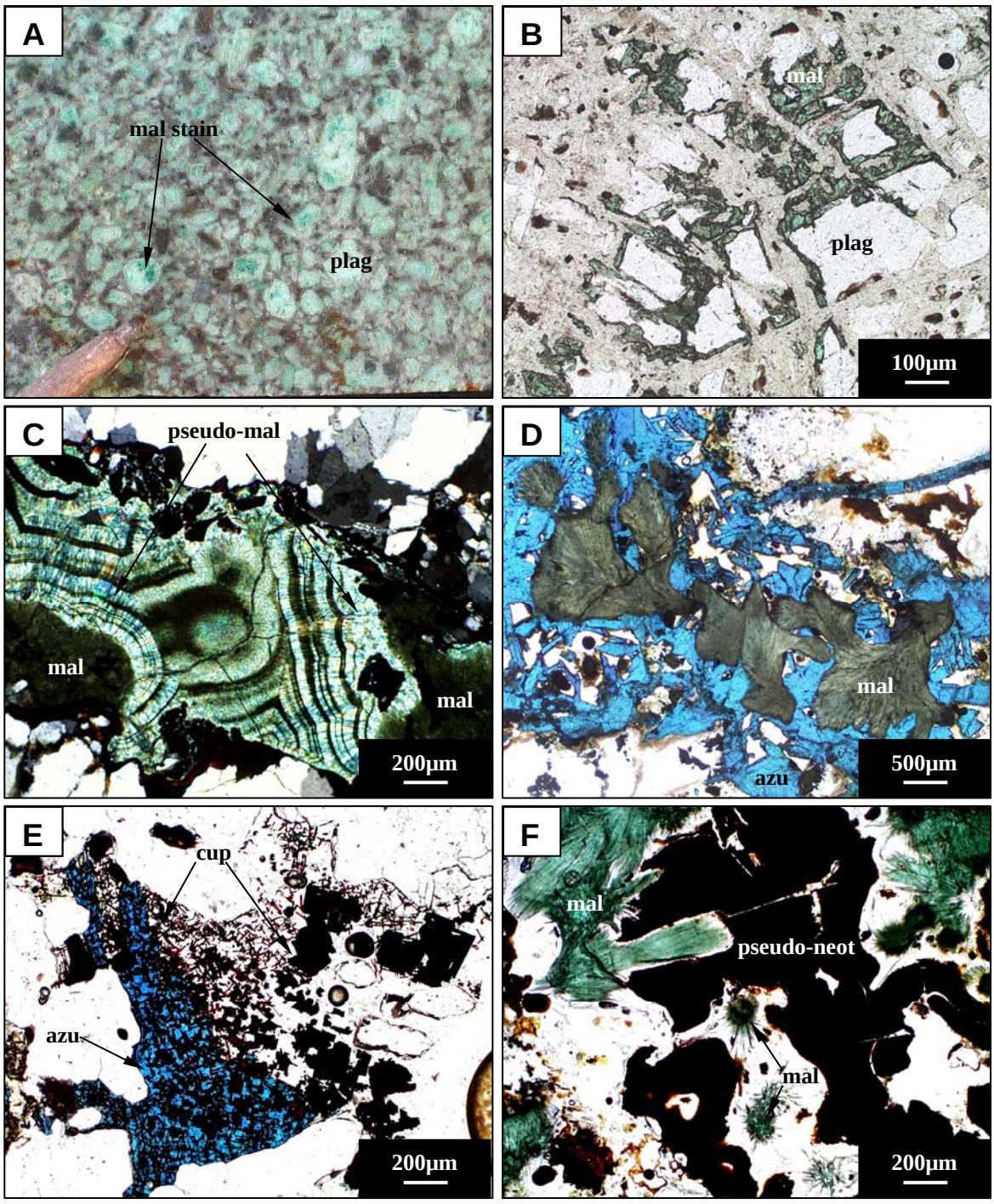

Fig. 4.9. A. Preferential replacement of plagioclase with malachite in TSD18 @ 88.70m (tip of scriber for scale). **B.** Same as A observed under the petrographic microscope in TSD18 @ 88.70m (field of view or FOV: 1.10mm; transmitted light or TL) **C.** Pseudo-malachite or "copper phosphate" intergrown with malachite; electron microprobe results show that it contains 69wt% CuO, 7.5wt% CO_2, & 23wt% P_2O_5 in TSD18 @ 132.30m (FOV: 2.20mm; TL with crossed-polars); **D.** Malachite overgrown by azurite in TSD38 @ 95.25m (FOV: 5.50mm; TL). **E.** Cuprite overgrown? or replaced by azurite in TSD11 @ 526.40m (FOV: 2.20mm; TL). **F.** Elongated & fibrous (upper left corner), and round & radiating crystals (center) of malachite overgrown by pseudo-neotocite (identified as neotocite in logs) in TSD38 @ 86.35m (FOV: 2.20mm; TL). cup = cuprite; mal = malachite; azu = azurite; neot = neotocite; plag = plagioclase

and as stains and/or disseminations on or within plagioclase phenocrysts in diorite intrusions (Fig. 4.8A, 4.9A & 4.9B). Malachite is associated with cuprite, azurite, copper phosphate, a chrysocolla-like mineral, goethite, and remnant hypogene sulfides. Malachite has been observed to occur as rims around cuprite (Fig. 4.6D). Complex radiating fibers of malachite has also been observed (Fig. 4.9D) suggesting multiple cycles of the growth of malachite. Other microscopic forms of malachite are fibrous and elongated, and round with radiating crystals (Fig. 4.9F).

4.3.4 Pseudo-malachite

Pseudo-malachite [$Cu_3(PO4)_2$] has a characteristic mamillary texture (Fig. 4.10A) similar in appearance to malachite but does not effervesce in acid. Under the microscope, it displays strong green pleochroism (Fig. 4.9C & 4.10B). Results from EPMA (Appendix 4) show that pseudo-malachite is composed mainly of copper and phosphate with a small amount of carbonate.

4.3.5 Azurite

Azurite [$Cu_3(CO_3)_2(OH)_2$] is blue in colour, and has a similar mode of occurrence to malachite, occurring commonly along fractures and as minor disseminations. Some azurite are characterised by radiating needles (Fig. 4.7D & 4.8E). Azurite is associated with malachite, cuprite, a chrysocolla-like mineral, and goethite. Azurite seem to be late in the supergene paragenetic sequence, beacause it has been observed to cut and rim malachite (Fig.4.8D) and cuprite (Fig. 4.9E)

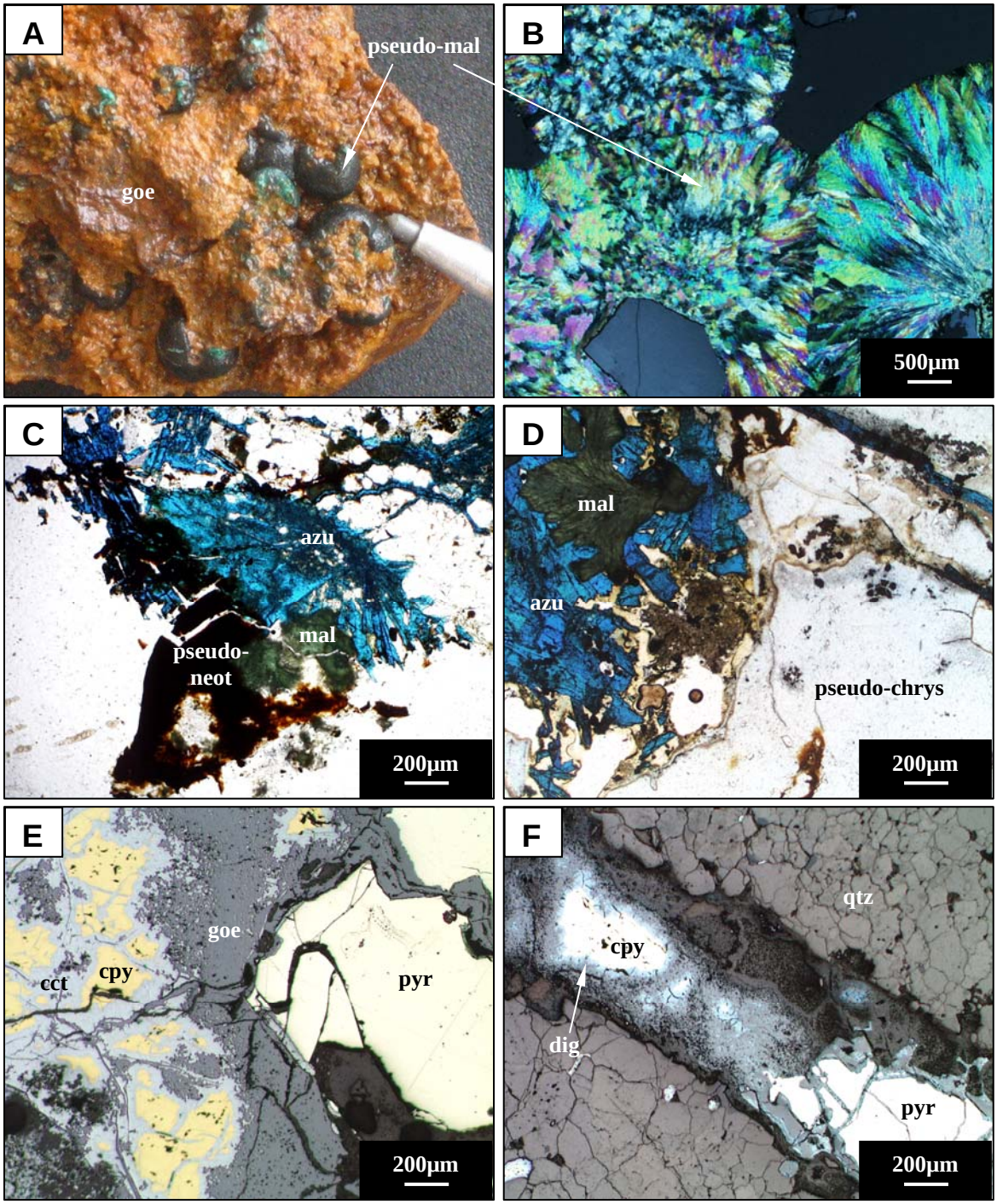

Fig. 4.10. A. Mamillary pseudo-malachite intergrown with goethite in TSD11 @ 383.70m (tip of scriber for scale). **B.** Photomicrograph of pseudo-malachite; electron microprobe results (Appendix 5) show that this mineral contains 69wt% CuO, 6.9wt% CO_2, and 23wt% P_2O_5 (field of view or FOV: 5.50mm; crossed polars). **C.** Dark brown to black pseudo-neotocite (identified using electron microprobe; Appendix 4 & 5) has partially replaced malachite and azurite in TSD38 @ 86.35m (FOV: 2.20mm; transmitted light or TL) **D.** Pseudo-chyrsocolla (identified by probe analysis; Appendix 4 & 5; lower right hand corner) associated with malachite and azurite in TSD38 @ 95.25m (FOV: 2.20mm; TL). **E.** Chalcopyrite partially replaced by chalcocite, and pyrite partially replaced by goethite in TSD11 @ 576.55m; in-situ development of chalcocite (FOV: 2.20mm; reflected light or RL). **F.** Chalcopyrite replaced partially by digenite, and pyrite replaced by goethite in TSD18 @ 286.25m; in-situ development of digenite (FOV 2.20mm; RL). cpy = chalcopyrite; pyr = pyrite; cct = chalcocite; dig = digenite; mal = malachite; azu = azurite; chrys = chrysocolla; goe = goethite

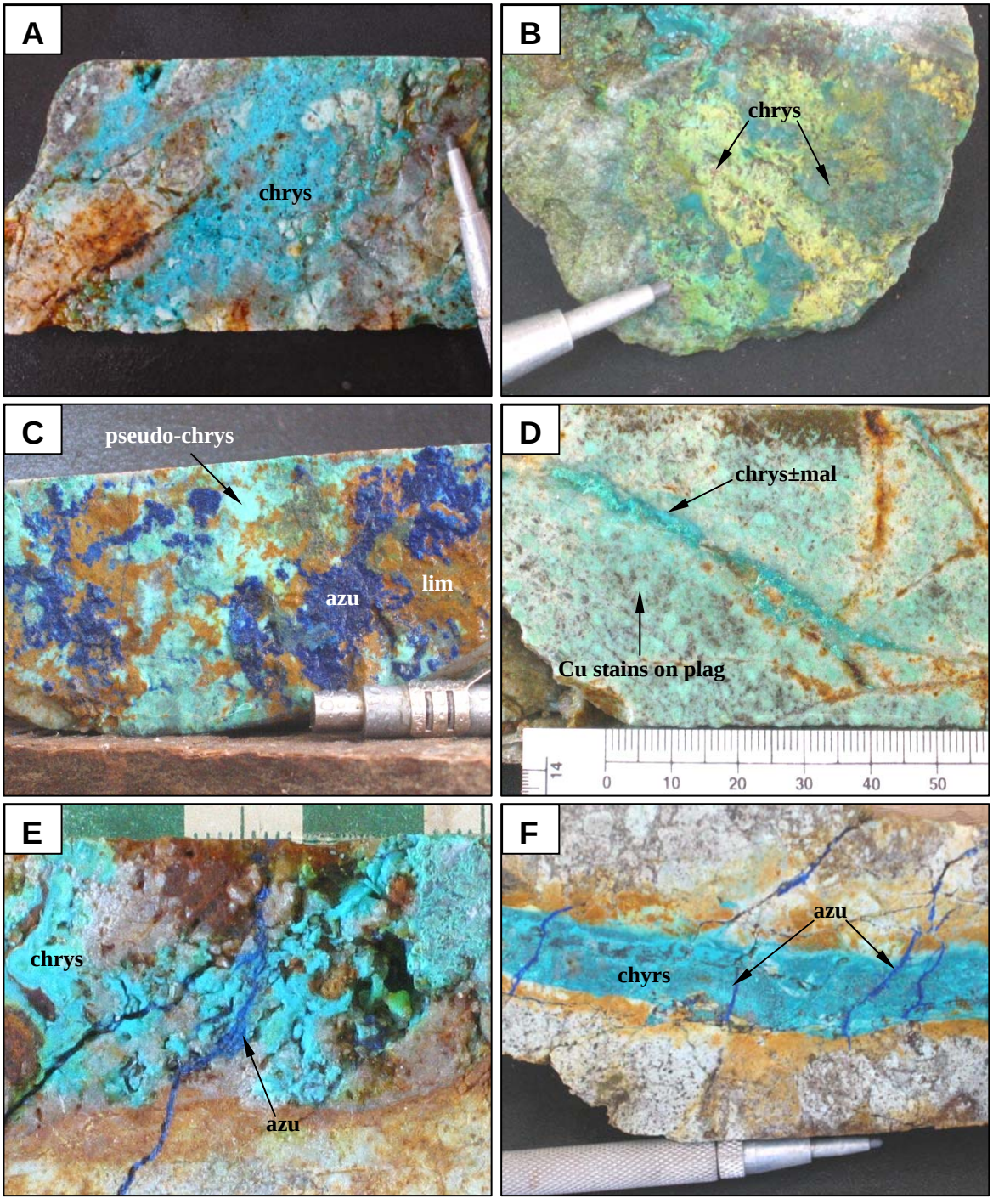

Fig. 4.11. Styles of supergene mineralisation at Boyongan. **A.** Chrysocolla in quartz vein; speck of gold observed at tip of scriber associated with limonite in quartz vein, in TSD17 @ 458.30m (scriber for scale). **B.** Blue to yellow green coloured chrysocolla in TSD47 @ 378.30m (scriber for scale). **C.** Chrysocolla ± malachite associated with azurite in TSD38 @ 95.25m (scriber for scale). **D.** Chrysocolla ± malachite in fracture; copper stains (green) on plagioclase in TSD20 @ 273.20m. **E.** Fracture-filling azurite cutting and chrysocolla in TSD53 @ 288.25m. **F.** Chrysocolla in quartz vein cut by azurite in TSD53 @ 205.00m (scriber for scale). chrys = chrysocolla; azu = azurite; mal = malachite; lim = limonite;

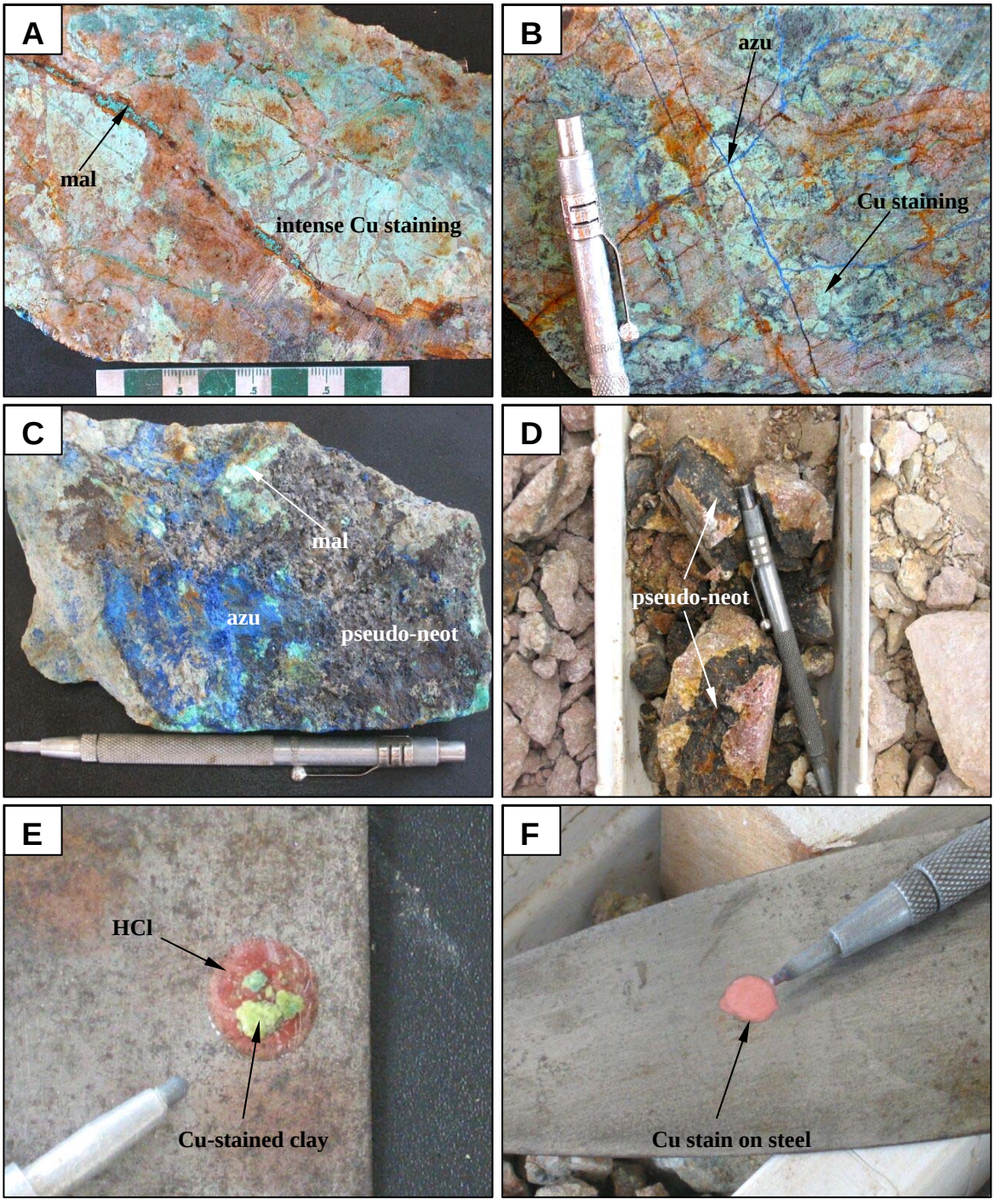

Fig. 4.12. Styles of supergene mineralization from Boyongan. **A.** Pervasive green secondary copper staining (chrysocolla?) in TSD38 @ 91.70m. **B.** Fracture-filling azurite in an intensely copper stained rock in TSD38 @ 89.20m (scriber for scale). **C.** Black pseudo-neotocite associated with azurite and minor malachite in TSD38 @ 86.35m (scriber for scale). **D.** Pseudo-neotocite in fractures associated with limonite in TSD20 @ 91.00m (scriber for scale). **E.** Results of acid test on copper-stained clay in TSD17 @ 397.60m, native copper has precipitated indicating the presence of copper in the clay (tip of scriber for scale). **F.** Similar to E, results of acid test on cuprite in TSD20 @ 189.80m produced copper-plating on steel (scriber for scale). mal = malachite; azu = azurite; neot = neotocite; HCl = hydrochloric acid (dilute)

4.3.6 Chrysocolla

Chrysocolla ($CuSiO_3nH_2O$) is an amorphous (non-crystalline) sky blue coloured copper mineraloid (Anderson, 1982). Since it is a silicate, it does not effervesce in dilute cold hydrochloric acid.

4.3.7 Pseudo-chrysocolla

Pseudo-chrysocolla [$Cu_3(CO_3)_2(OH)_2$-$Al_2Si_2O_5(OH)_4$] is similar to chrysocolla except that its colour is more similar to turquoise, in that it is sky blue or blue green in colour (Fig. 4.11) and effervesces in acid. It has a faint blue colour when viewed under plane polarized light (Fig. 4.10D). It occurs in fractures as well as pervasive copper staining (Fig. 4.12A & B) which probably is a result of the mixing of copper and supergene kaolinite. This mineral is found associated with malachite and azurite (Fig. 4.10D). Samples collected for EPMA show that this amorphous mineral is mainly composed of copper, carbonate, aluminium, and silica (Appendix 4 & 5). Its composition seems to be a mixture of azurite [$Cu_3(CO_3)_2(OH)_2$], chrysocolla [$CuSiO_3nH_2O$], and possibly kaolinite [$Al_2Si_2O_5(OH)_4$].

4.3.8 Pitch Limonite/ Cuprous Goethite

Pitch limonite [$H(Fe,Cu)O_2$] or cuprous goethite (Fig. 4.13C & 4.13E) has formed via the oxidation of pre-existing chalcopyrite and/or bornite. The copper is residual, have co-precipitated with limonite (Anderson, 1982). The presence of pitch limonite suggests incomplete leaching of copper during supergene oxidation and weathering (Blachard, 1968; Einaudi, 1995). Identifying the presence of pitch limonite when mixed with goethite can be difficult, especially when the limonite is very fine-grained. One of the ways to test for the

presence of residual copper is through an acid plate test similar to Figure 4.12F.

4.3.9 Pseudo-neotocite

Pseudo-neotocite [$(Mn,Cu)_2CO_{3;}$] is dark brown to black in colour and has a characteristic brownish to black coloured streak (Fig. 4.12C & 4.12D). This can be distinguished from non-cuprian manganese oxides through an acid test. It leaves minor to moderate copper plating on steel knife or plate. When viewed under the petrographic microscope, pseudo-neotocite has replaced malachite and azurite (Fig. 4.10C). Electron microprobe analysis has shown that this mineral is mainly composed of Mn, Cu, and carbonate (Appendix 4 & 5), distinguishing it from neotocite, which has a chemical formula of $(Cu,Fe,Mn)SiO_2$.

4.4 SUPERGENE IRON OXIDES

Goethite [FeO(OH)] is the most common variety of limonite at Boyongan. Abundant amount of goethite, together with minor hematite (Fig. 4.13F), occurs in the uppermost portions of the weathered zone. Goethite has formed via the oxidation of pyrite (Fig. 4.13D, 4.14A & B) and copper sulfides (chalcopyrite and/or bornite; Fig. 4.14D & E). The weathering of hornblende and biotite in the diorite intrusions may have contributed to the production of goethite locally.

Fine cellular boxwork textures (<1.5mm) are common in Boyongan (Fig. 4.13A; Blanchard, 1968) suggesting in-situ oxidation of primary sulfide minerals. This texture has developed during weathering where thin webs of limonite have progressively penetrated along cleavage and fracture pattterns within hypogene sulfides. The cellular pattern is sub-angular to rounded, and cell walls are rigid and well joined to one another (Fig. 4.14C;

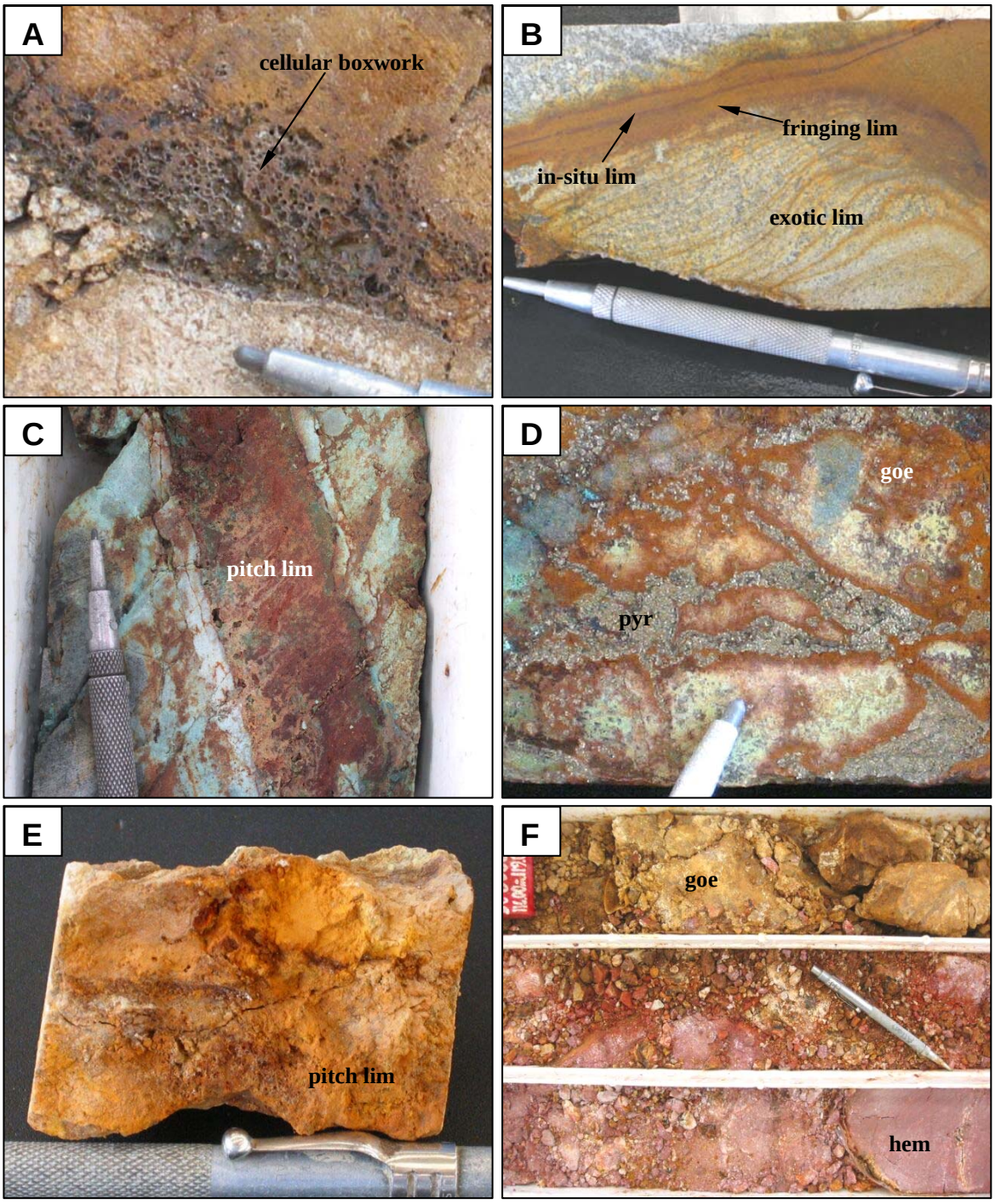

Fig. 4.13. **A.** Cellular texture of pitch limonite in TSD44 @ 188.00m (scriber for scale). **B.** In-situ (with minor cellular texture), fringing and exotic limonite in TSD53 @ 240.20m (scriber for scale). **C.** Pitch limonite (formerly chalcopyrite) with partially fringing copper staining on quartz-sericite alteration in TSD13 @ 214.25m (scriber for scale). **D.** Pyrite oxidised to goethite in TSD39 @ 271.90m (scriber for scale). **E.** Pitch limonite (like sponge) in TSD20 @ 170.40m (scriber for scale). **F.** Hematite-goethite in TSD47 @ 117.00m (scriber for scale). pyr = pyrite; lim = limonite; goe = goethite; hem = hematite

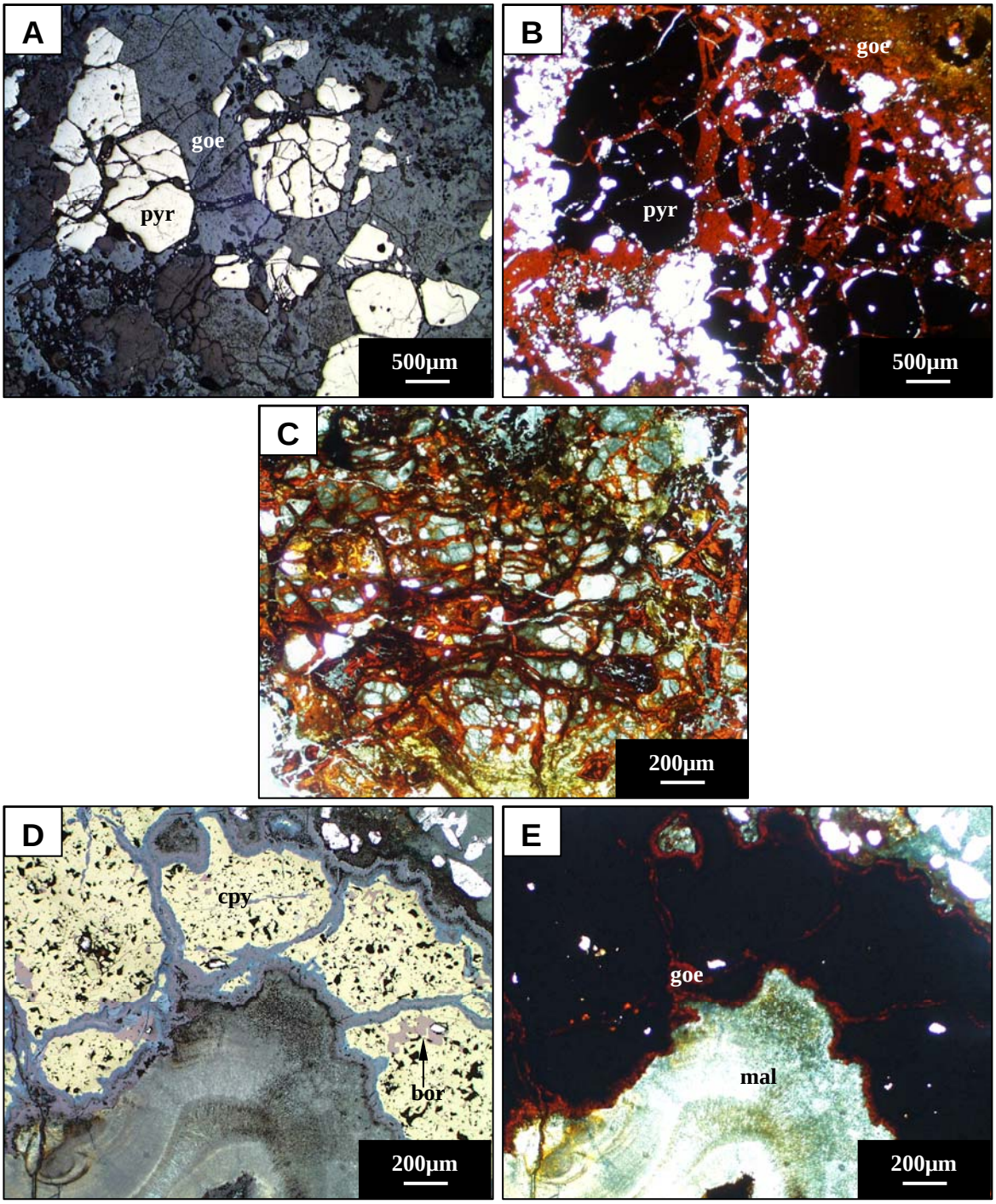

Fig. 4.14. A. Broken, euhedral pyrite in TSD18 @ 225.00m (FOV 5.5mm; RL); **B.** Same as A; goethite has partially replaced pyrite in TSD18 @ 225.00m (FOV 5.5mm; transmitted light or TL). **C.** Cellular texture in goethite with malachite in TSD38 @ 114.90m (FOV: 2.20mm; TL). **D.** Chalcopyrite intergrown with bornite oxidised to goethite and then to malachite in TSD14 @ 135.95m (FOV 2.20mm; reflected light). **E.** Same as D; goethite has replaced copper sulfides, and goethite is overgrown by malachite in TSD14 @ 135.95m (FOV: 2.20mm; TL). cpy = chalcopyrite; bor = bornite; pyr = pyrite; mal = malachite; geo = goethite

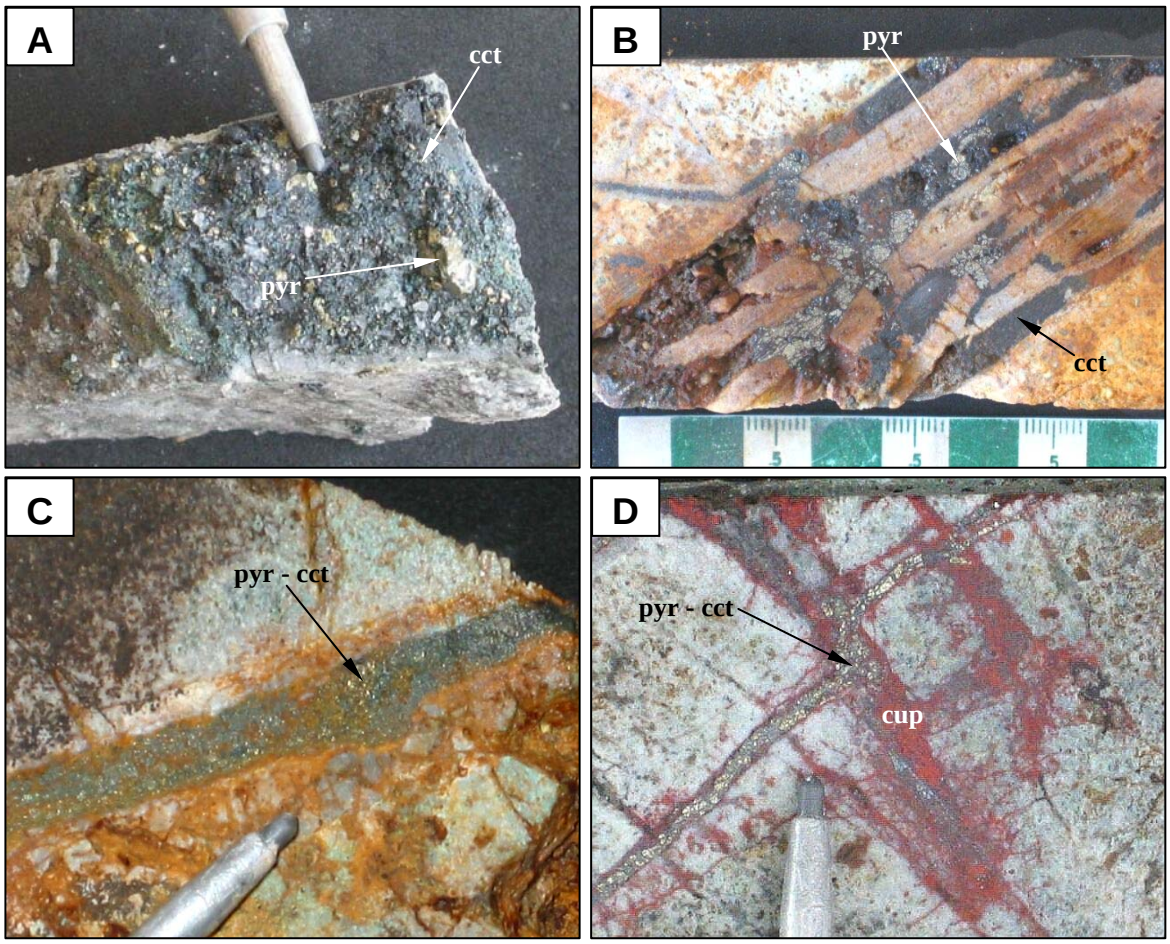

Fig. 4.15. Evidence for copper remobilisation. **A**. Chalcocite coatings on pyrite ± chalcopyrite in TSD47 @ 430.30m (scriber for scale). **B.** Pyrite ± chalcopyrite replaced by chalcocite in fracture in TSD53 @ 414.50m. **C.** Pyrite replaced by chalcocite in TSD2 @ 141.40m (scriber for scale). **D.** Pyrite ± chalcopyrite replaced by chalcocite, then by cuprite in TSD50 @ 396.00m (scriber for scale). pyr = pyrite; cct = chalcocite; cup = cuprite

Blanchard, 1968). Cellular sponges are also common, and individual cells within these are more rounded (Fig. 4.13E). Fringing and exotic limonite varieties are also common (Fig. 4.13B; Blanchard, 1968). Exotic goethite has been observed commonly at the hand-specimen scale. Overall, on the deposit scale, goethite is mostly indigenous (in that it developed in-situ within the deposit).

4.5 SUPERGENE GOLD

Supergene gold has been observed during the current study in chalcocite (Fig. 4.2D), chrysocolla, goethite and malachite both during logging and petrographically. The gold may have been liberated from hypogene sulfides such as bornite or chalcocpyrite during supergene oxidation (Fig. 4.4E). When analysed using the electron microprobe (Appendix 3), the supergene gold was found to contain 97.67wt% Au and 1.80wt% Ag in TSD18 (116.20m). Gold grains are <100μm in diameter, generally sub-rounded, bright brass-yellow colour (Fig. 4.5C & E) and sometimes dendritic (Fig. 4.5F). Microprobe analyses for hypogene gold was not conducted and cannot be compared with the results of supergene gold.

4.6 SPATIAL DISTRIBUTION OF COPPER OXIDES AND SULFIDES

Anglo American's geological database, compiled during drill core logging has been used to confirm the distribution of various minerals within the supergene zone. Anglo American geologists provided visual estimates (vol%) of the abundance of secondary mineral species for every 3-meter sampling interval (Campbell, 2002). However, the visual estimates are somewhat subjective, so the volume percent for each mineral were converted to a proportion of copper (PCu) in the sample, contributed by each of the minerals (Campbell, 2002; Corpuz, 2003 pers. commun.). Volume estimate (vol%), concentration of copper in the copper mineral (%Cu), and specific gravity (SG) was used to determine the contribution or proportion of a specific copper mineral to the overall copper grade in a 3-meter sample. The PCu or proportion of copper in a sample from each mineral is equal to the product of the vol% times %Cu times SG divided by the total proportion or contribution of copper

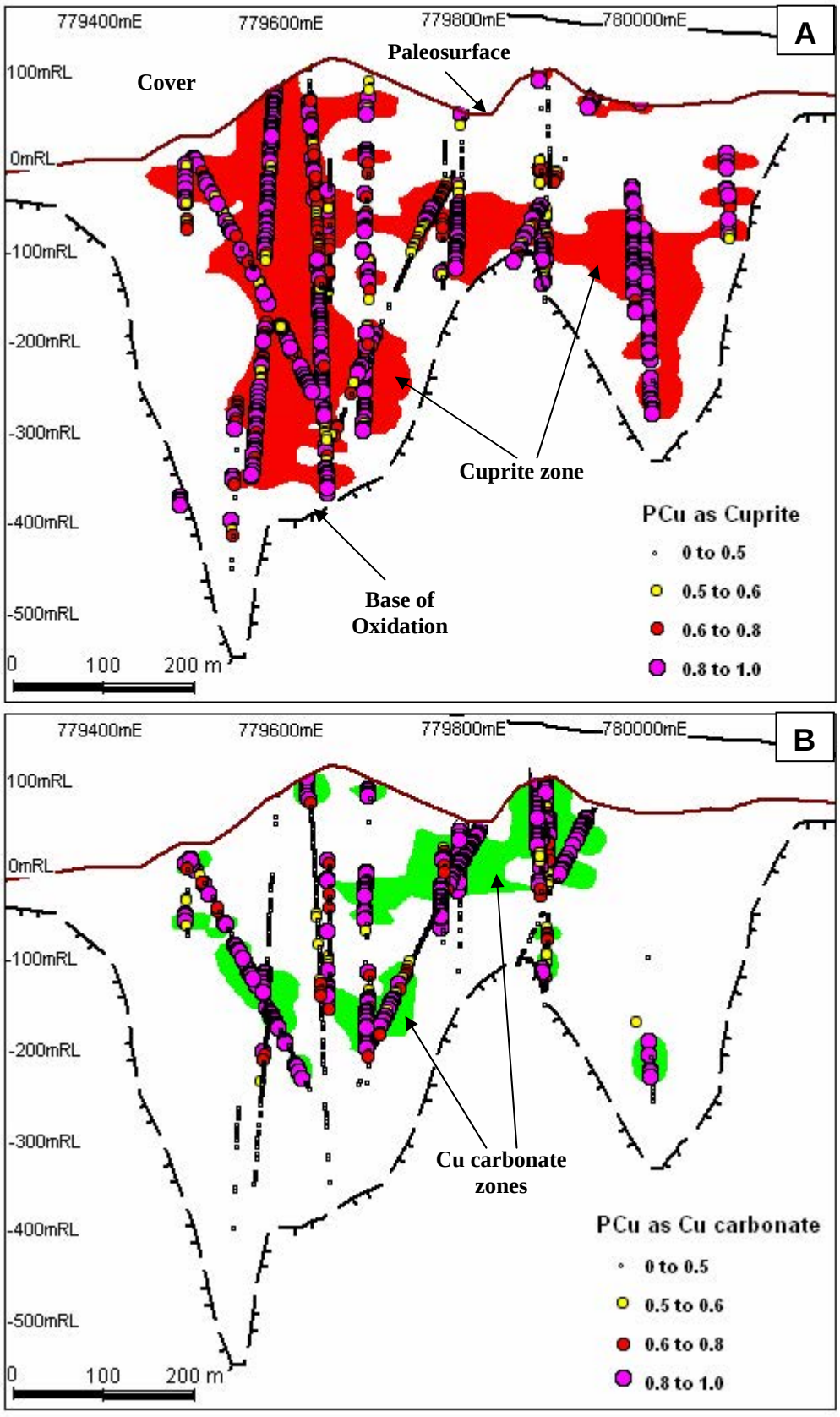

Fig. 4.16. Section 1062200N (looking north). **A.** Cuprite zone (red) generated based on downhole plot of proportion of copper as cuprite. **B.** Copper carbonate zone (green) generated based on downhole plot of proportion of copper as copper carbonate (malachite and azurite combined). A proportion cut-off of 0.5 was used in generating zones. PCu = proportion of copper

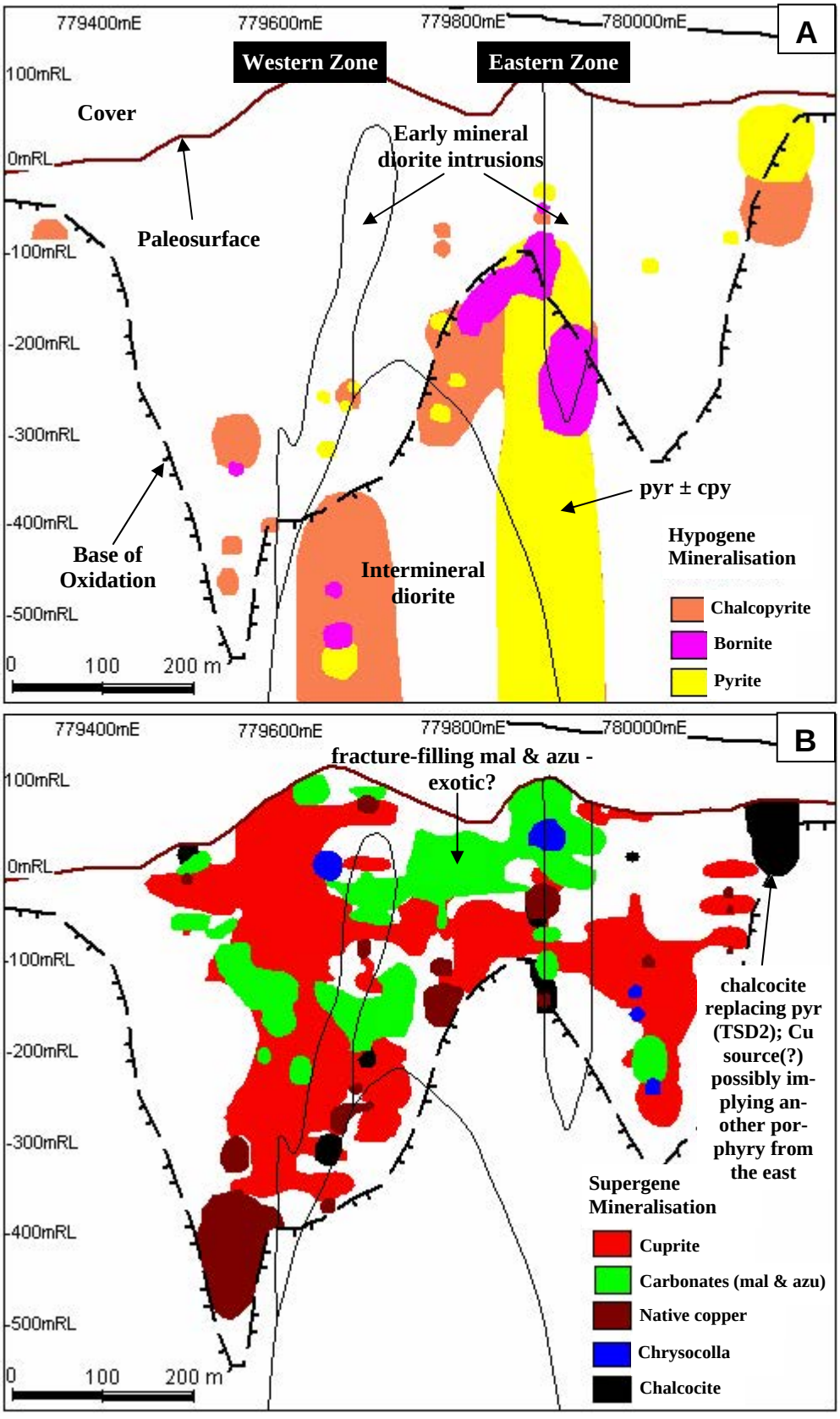

Fig. 4.17. Section 1062200N (looking north). Note the early mineral and intermineral diorite intrusions for reference. **A.** Hypogene sulfide mineral assemblages composed of chalcopyrite, bornite, and pyrite. **B.** Spatial distribution of supergene minerals, cuprite is dominant, followed by copper carbonates, native copper, chrysocolla, and chalcocite. Note that the oxidation of the western zone is deeper compared to the eastern zone. cpy = chalcopyrite; pyr = pyrite; mal = malachite; azu = azurite

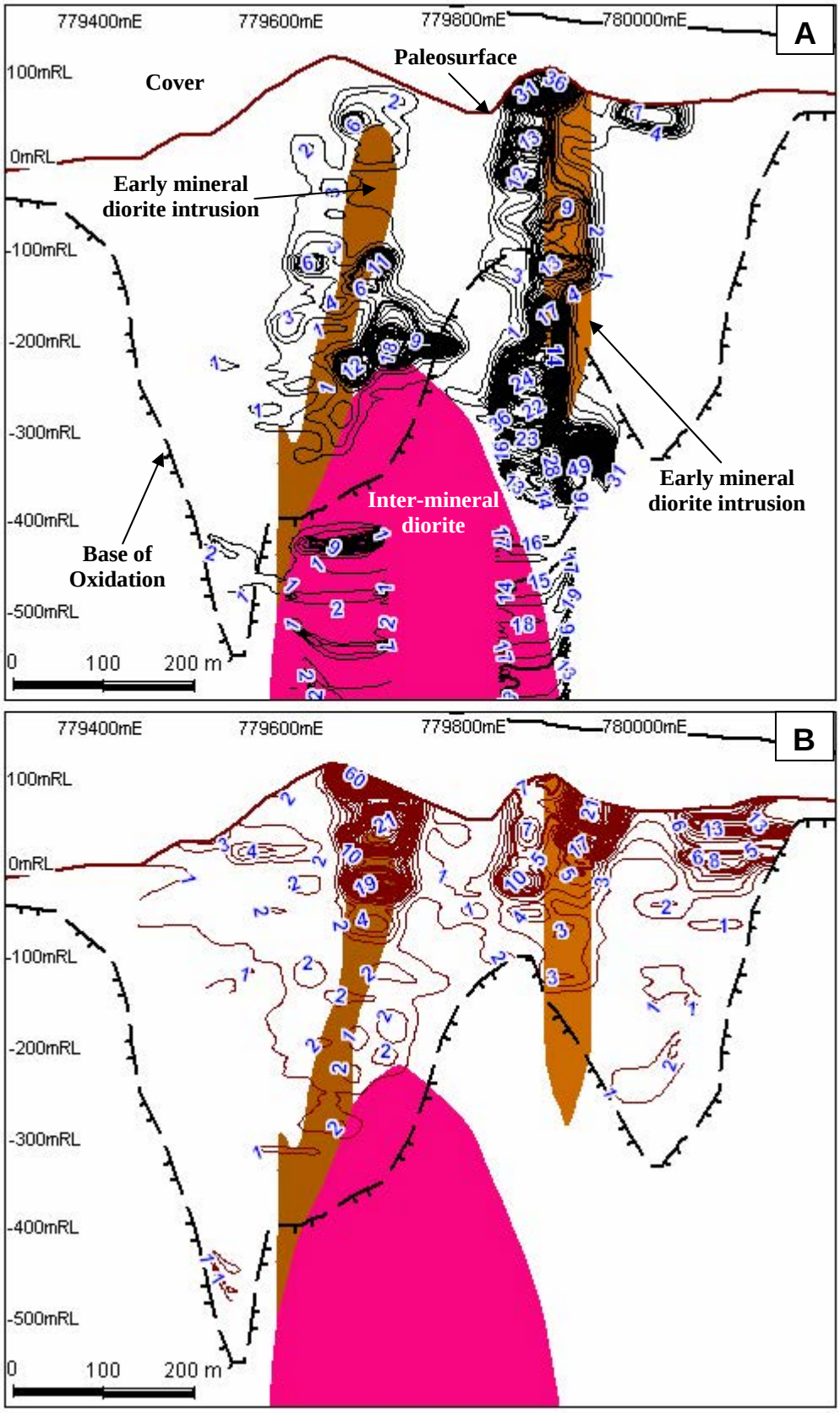

Fig. 4.18. Section 1062200N (looking north). Note the early mineral and intermineral diorite intrusions for reference. **A.** Quartz stockwork contour. Stockwork zone in the eastern zone is more confined or restricted compared to a more diffused zone on the western zone. Veining density on the eastern zone is greater compared western zone. **B.** Limonite contour. Note that limonite (dominantly geothite) is concentrated at the uppermost portion of the early mineral intrusions.

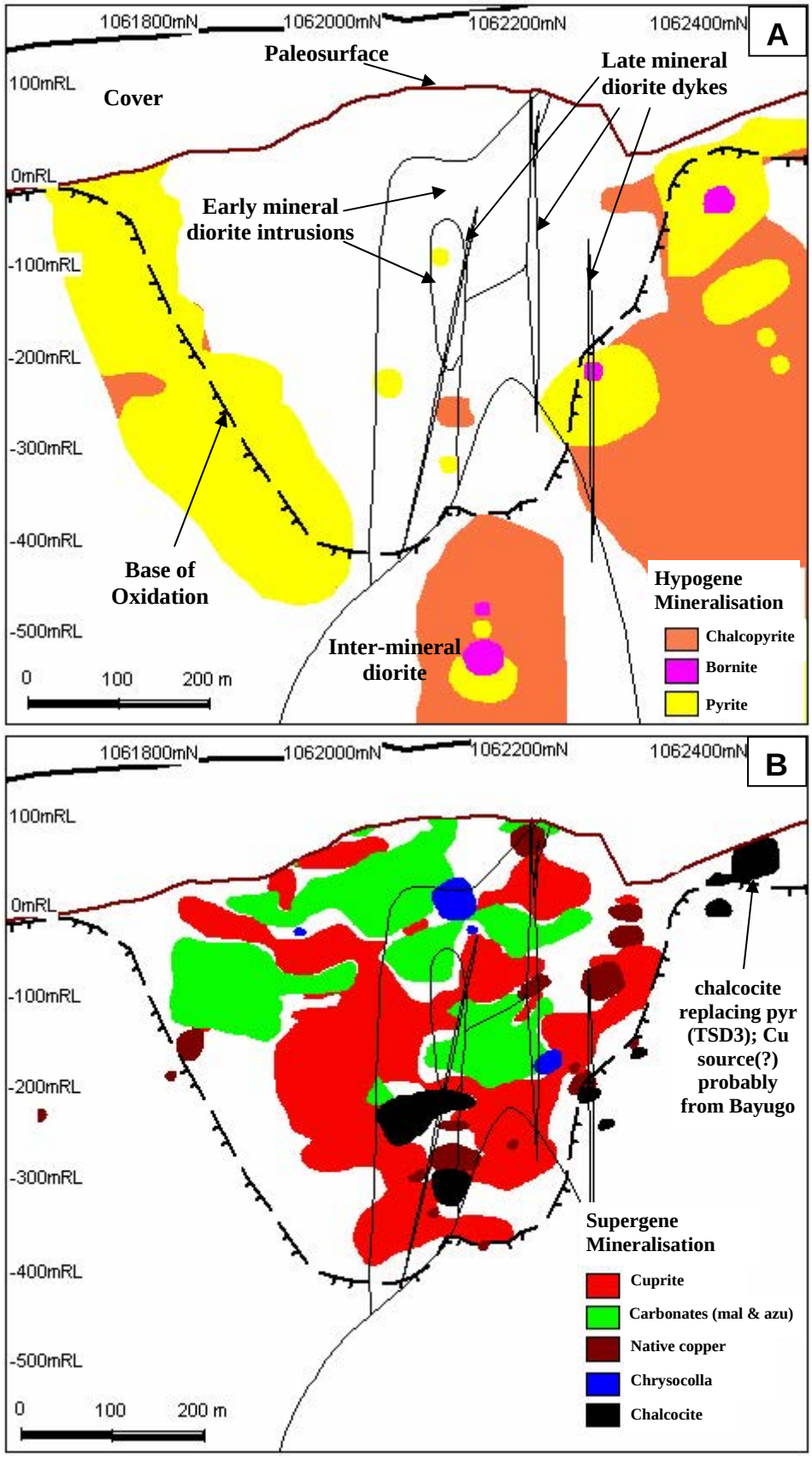

Fig. 4.19. Section 779700E (looking west). Note the early mineral, intermineral, and late mineral diorite intrusions for reference. **A.** Hypogene mineral assemblages composed of chalcopyrite, bornite, and pyrite. **B.** Supergene mineral assemblages and zonation. The supergene ore is dominanted by cuprite, followed by malachite & azurite, native copper, chalcocite, and chrysocolla.

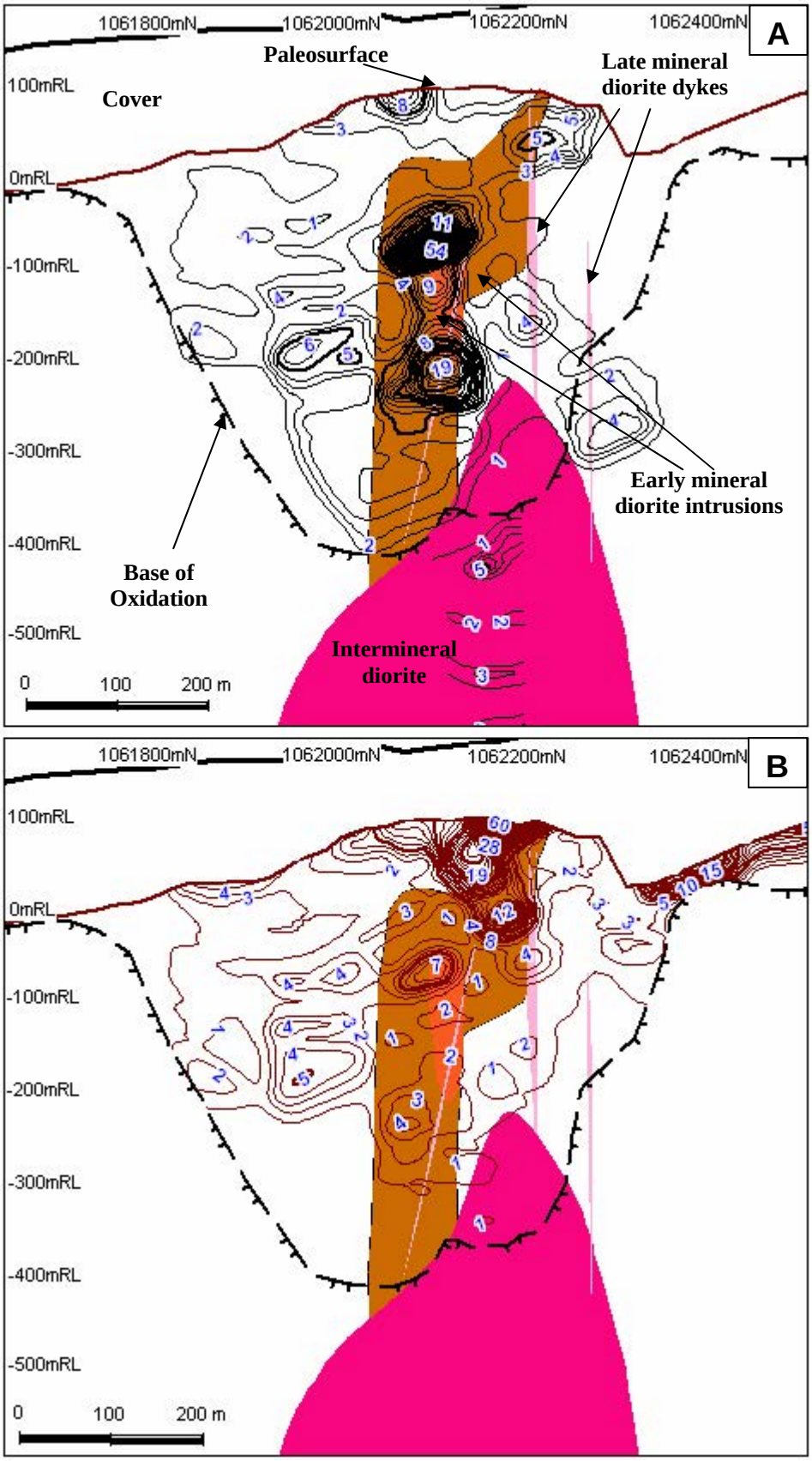

Fig. 4.20. Section 779700E (looking west). Note the early mineral, intermineral, & late mineral diorite intrusions for reference. **A.** Quartz stockwork density contour. **B.** Limonite contour. Note that limonite (dominantly geothite) is concentrated at the uppermost portion of the early-mineral intrusion.

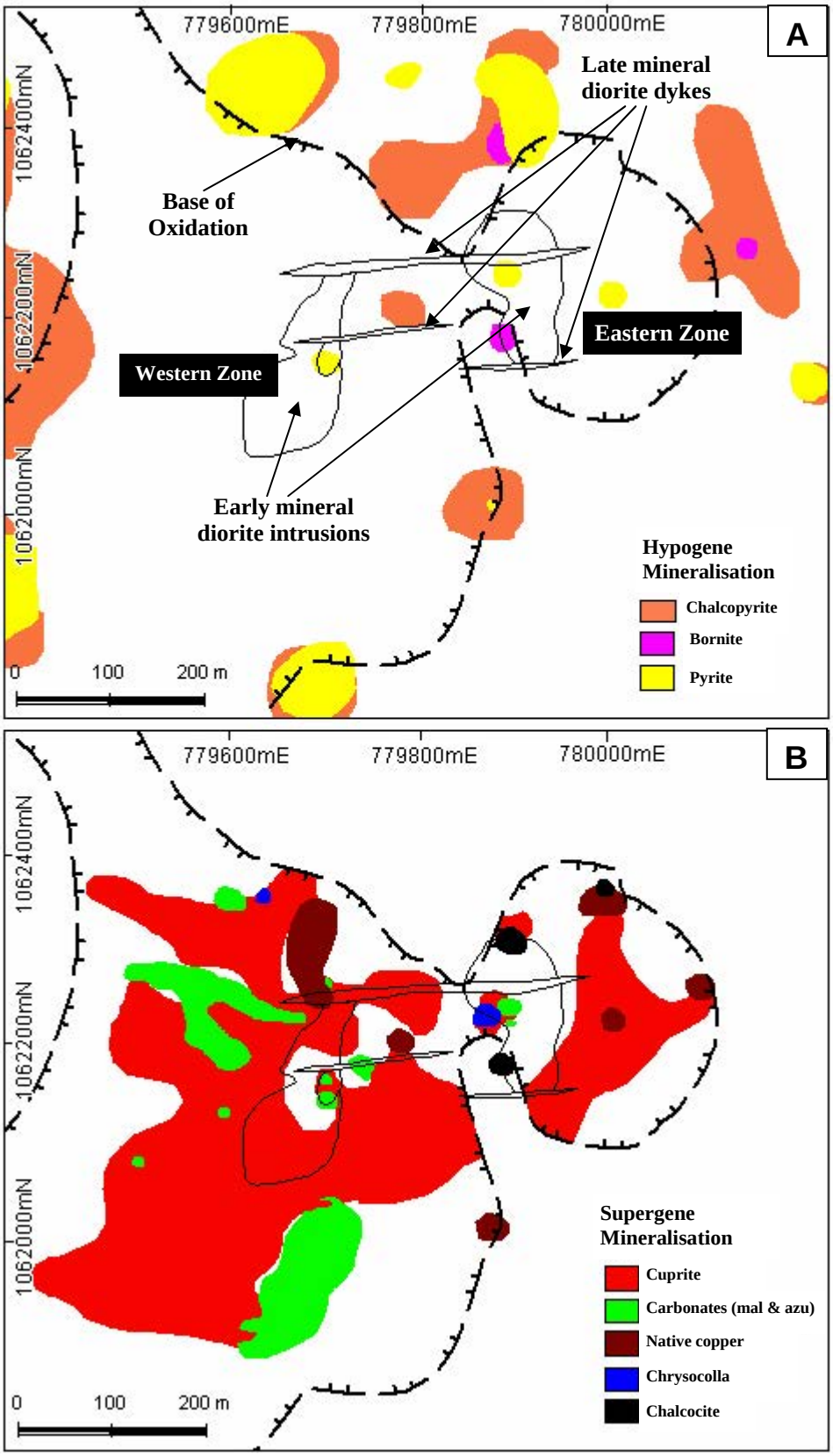

Fig. 4.21. Geological plan of Boyongan at –100RL. Broken line with teeth marks the base of oxidation. **A.** Plan showing hypogene sulfide distribution. Remant hypogene sulfides were observed within the supergene zone. **B.** Distribution of supergene cuprite, malachite and azurite, native copper, chrysocolla and chalcocite

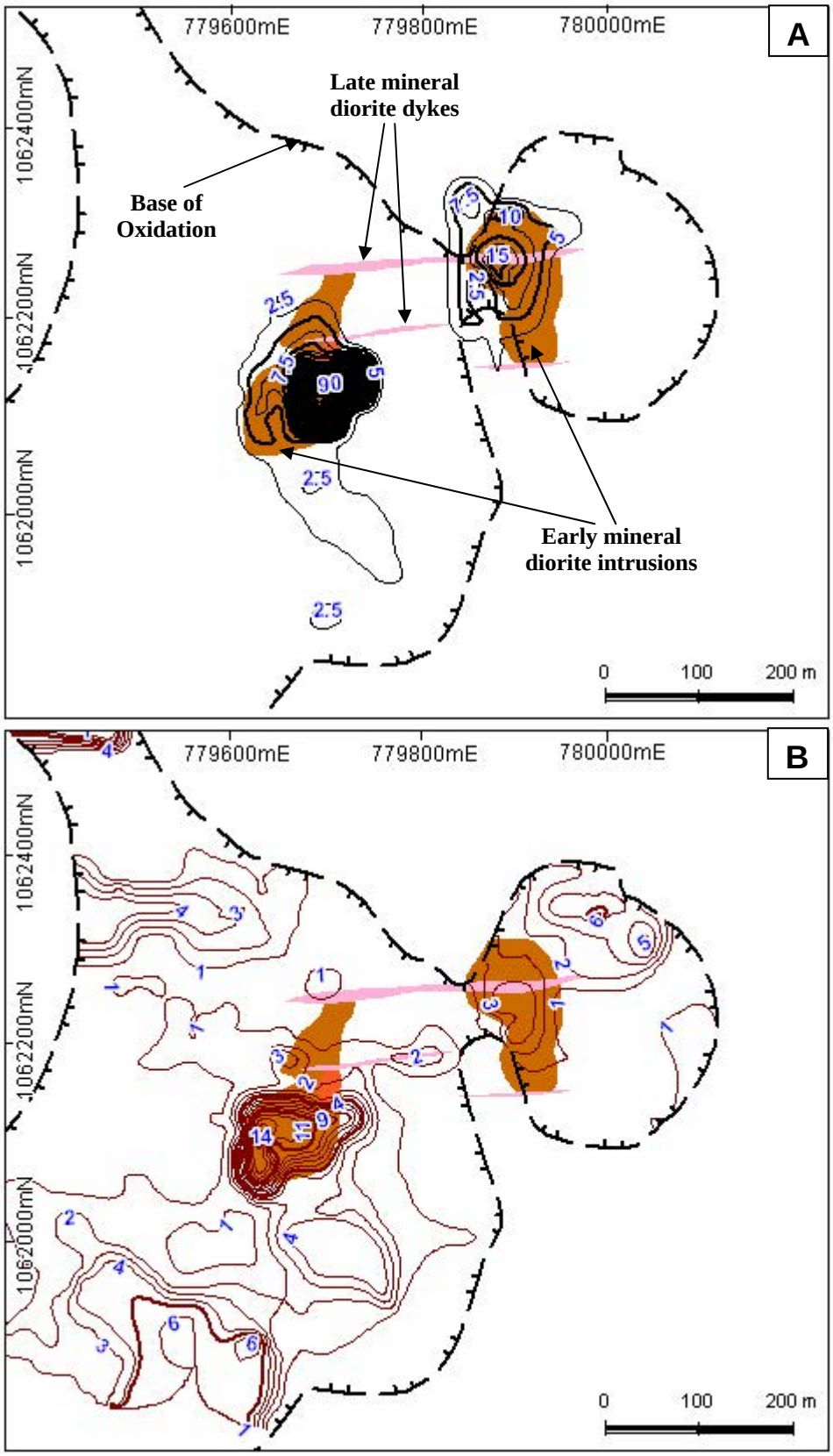

Fig. 4.22. Geological plan of Boyongan at –100RL. Broken line with teeth marks the base of oxidation. **A.** Quartz stockwork density contour. Quartz stockwork veining is closely related with the early mineral intrusions. **B.** Limonite contour. Abundant limonite (up to 14 volume %) can be observed in the western zone.

minerals (PCu_{total}). This can be represented in the formula PCu = [(vol%) x (%Cu) x (SG)] / (PCu_{total}). PCu_{total} is equal to the $\sum$ (vol% x %Cu x SG) for each for the copper minerals or, PCu_{total} = (vol%cpy*34.6*4.2) + (vol%bor*63.3*5.1) + (vol%cov*66.4*4.6) + (vol%cct*79.80*5.6) + (vol%nCu*100.0*8.9) + (vol%cup*88.8*6.1) + (vol%mal*57.4*3.9) + (vol% azu*55.3*3.8) + (vol%chrys*38.0*2.2) [note: cpy = chalcopyrite; bor = bornite; cov = covellite; cct = chalcocite; nCu = native copper; cup = cuprite; mal = malachite; azu = azurite; chrys = chrysocolla].

Calculated proportions of copper (values ranging from 0 to 1) by each supergene mineral with a proportion cu-off of 0.5 were used in generating the supergene mineral zonation sections (Fig. 4.16, 4.17, 4.19, & 4.22). Only the major mineral species/groups (cuprite, carbonates, chrysocolla, native copper, and chalcocite) are shown on Figures 4.17B, 4.19B, 4.22B). Hypogene minerals (chalcopyrite, bornite, and pyrite) are also shown (Fig. 4.17A, 4.19A, 4.22A). These diagrams highlight zones of overlap between supergene minerals and hypogene sulfides, consistent with textures observed in hand sample and under the microscope.

Deep oxidation has developed a complex supergene mineralogy and zonation patterns at Boyongan. The sequence of supergene copper mineralisation is as follows: supergene sulfide (chlacocite, digenite, and pseudo-covellite), native copper, and supergene copper oxides [cuprite (occurring as acicular and euhedral crystals called chalcotrichite), malachite, pseudo-malachite, azurite, chrysocolla, pseudo-chrysocolla, and pseudo-neotocite] (Figs. 4.17B, 4.19B, 4.21B). The supergene minerals generally occur as fracture-fill and disseminations, and are more abundant closer to the diorite intrusions. Remnant hypogene sulfides (chalcopyrite, pyrite, and bornite) occur in the oxide zone (Fig. 4.17A, 4.19A, 4.21A) especially where sulfides have been tightly encapsulated in quartz vein stockwork.

There is no chalcocite enrichment zone. Instead, chalcocite generally occurs wherever there are remnant hypogene sulfides. There is a subtle vertical zonation of supergene copper minerals, where carbonates (malachite and azurite) are underlain by cuprite and then by native copper (Fig. 4.17B), consistent with progressively more reducing conditions with depth (Markl, et al., 1997). This pattern is largely controlled by Eh and pH (Anderson, 1982; Sillitoe, 2002b). The dominance of cuprite over carbonates in the western zone may be explained by more reducing conditions.

Limonite (goethite) is intensely developed at the apex of the early-mineral coarse-grained diorite porphyries (Fig. 4.18B, 4.20B, & 4.22B). This most likely relate to the re-opening intervals occurring in fractures associated with the quartz stockwork zone (Fig. 4.18A, 4.20A, & 4.22A). The shallow base of oxidation in the eastern zone (200m along 779900E to 400 meters along 780000E) coincides with a domain of intense quartz veining (up to 50%). Fractures in this area are very tight and it may be that supergene-, low temperature-, oxygenated fluids were not able to permeate to great depths as compared to the western zone (650 meters along 779500E). Fracturing, together with topography, has controlled the present shape of the supergene profile at Boyongan.

There is evidence of minor supergene copper remobilisation (exotic copper). Chalcocite occurs as coatings on pyrite ± chalcopyrite at several localities (Fig. 4.15A, B, & C; 4.17B; 4.19B; & 4.21B). Some copper oxide minerals (e.g. malachite and azurite), have filled “clean” fractures, or fractures that show no evidence of prior mineralisation typical of exotic copper (Fig. 5.1A, Chavez, 2000).

4.7 WALLROCK ALTERATION (Clay Mineralogy)

A total of 259 drillcore samples were analysed using PIMA during the current study.

Samples of varying sizes were generally collected every 20 meters depth from a representative cross-section (1062200N) through the deposit. The PIMA was calibrated before making measurements. Each sample was held on the PIMA window for about 30-60 seconds. The Spectral Geologist or TSG software package was used to process spectral data (Merry et al, 1999). This software was used for rapid spectral interpretations. It has a module called the TSA (The Spectral Assistant) that automatically assesses the likely mineral contributors to a spectrum (Pontual & Merry, 1995). TSG attempts to identify the

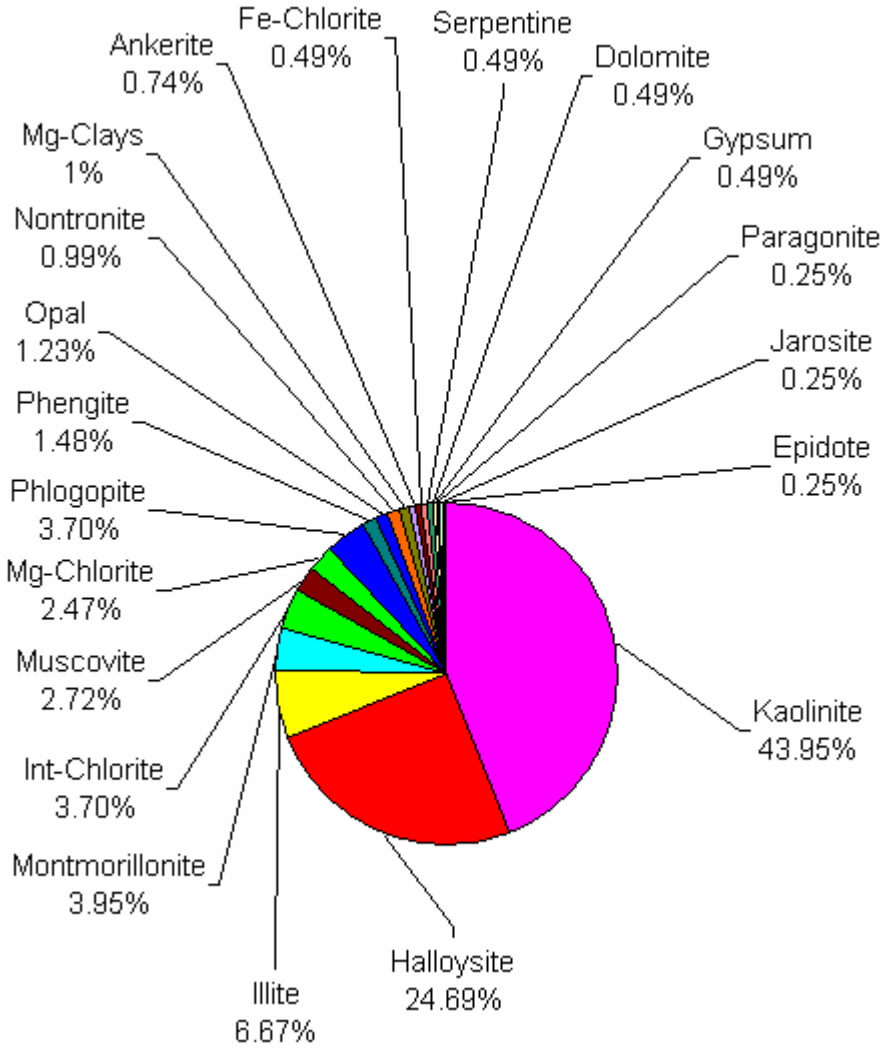

Fig. 4.23. Pie Chart showing the abundance of various types of clays in Boyongan. The three most abundant clays are kaolinite and halloysite which can be classified under the group of kandites. Minor components include illite, montmorillonite, chlorite, etc. This pie chart has been generated from 241 data points which is less than 250 TSA error. TSA reports a goodness-for-fit (or error) measure for each match. There is a range within which TSA results should be taken seriously. In general, a TSA Error of 250 or below should be considered viable (Merry et. al, 1999). Int = Intermediate; Mg = Magnesium; Fe = Iron

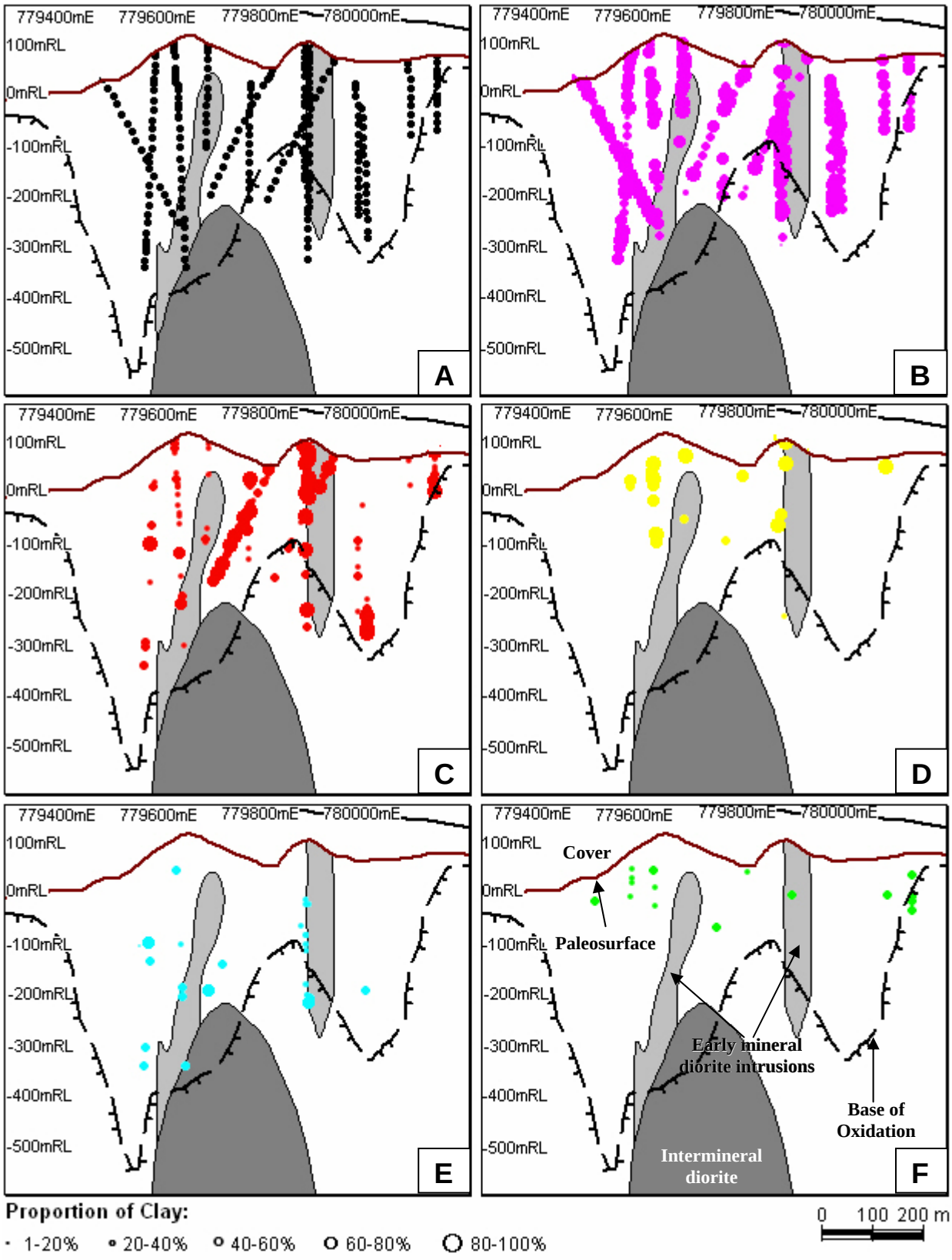

Fig. 4.24. Series of sections along 1062200N (looking north) showing core sample locations, types and proportions of clays identified using PIMA. The paleosurface, base of oxidation, early mineral, and inter-mineral diorite intrusions are shown (Fig. 4.2E). **A.** Core sample locations for SWIR analysis. A total of 159 core samples of various sized were collected **B.** Down-hole plot showing proportion of clay as kaolinite. **C.** Downhole plot showing proportion of clay as halloysite. **D.** Downhole plot showing proportion of clay as illite. **E.** Downhole plot showing proportion of clay as montmorillonite. **F.** Downhole plot showing proportion of clay as chlorite. Note that kaolinite, halloysite, and montmorillonite persists below the zone of oxidation.

mineral phases using raw reflectance spectra, although absorption troughs are better viewed using the hull quotient (Appendix 1a; Fig. A1a).

A total of 309 PIMA readings were taken from 259 drillcore samples (Appendix 1b). Some samples had 2 or more readings. However, only 241 readings were acceptable based on the TSA error values. TSA reports a goodness-for-fit (or error) measure for each match. This value is saved as the TSA error. There is a range that TSA results should be taken seriously. In general, a TSA Error of 250 or below should be considered viable (Merry et. al, 1999).

The following clay species, arranged in decreasing abundance, have been identified at Boyongan by PIMA analyses: kaolinite, halloysite, illite, montmorillonite, intermediate chlorite, muscovite, and Mg-chlorite. The abundance of minor clays such as phlogophite, phengite, opal, nontronite, and magnesium clays are also shown in Figure 4.1. The spatial distribution of the most common clay phases on section 1062200N is shown in Figure 4.23. The percentages shown in Figure 4.23 represent the frequency within the 241 spectral readings. Kaolinite, illite and montmorillonite are common in hypogene argillic, and intermediate-argillic alteration zones (Pontual & Merry, 1995; Thompson, 2002; Sillitoe, 2000), and in weathered parts of porphyry copper systems (Thompson, 2002; Merry et al., 1999). Halloysite is characteristic of the weathering zone (Merry et al., 1999). A brief description of the Boyongan clays and their chemical compositions are presented below:

- **Kaolinite** $\{Al_2Si_2O_5(OH)_4\}$ is common in weathered zones, but also occurs in argillic and advanced argillic hypogene alteration zones. At Boyongan, it is mixed with goethite and copper oxides, suggesting a supergene origin.

- **Halloysite** $\{Al_2Si_2O_5(OH)_4 \cdot 4H_2O\}$ is a hydrated version of kaolinite, common in the

weathering zones.

- **Illite** $\{K_{2-X}Al_4(Si^{6+X}Al_{12-X})O_{20}(OH)_4\}$ can occur in hypogene phyllic or argillic alteration zones (Hedenquist, et al., 1998) and also in the weathering zone. At Boyongan, it occurs in fractures (weathering?) as well as soapy selvages to limonite veins.

- **Montmorillonite** $\{(Ca,Na)_{0.67}Al_4(Si,Al)_8O_{20}(OH)_4 \cdot nH_2O\}$ is a common smectite mineral.

- **Intermediate Chlorite** $\{(Mg,Al,Fe)_{12}[(Si,Al)_8O_{20}](OH)_{16}\}$ is part of the chlorite solid solution as composition between Fe-chlorite and Mg-chlorite. It is of hypogene origin, and is most common in the propylitic alteration zone peripheral to hydrothermal mineral deposits. Minor amounts of chlorite occur within the main mineralised zone of Boyongan.

- **Muscovite** $\{K_2Al_4(Si_6Al_2)O_{20}(OH)_4\}$ occurs widely in felsic igneous and pelitic metamorphic rocks. It also occurs as a main constituent in various hydrothermal alteration systems (e.g. in Boyongan), especially the phyllic alteration zone of porphyry copper-gold deposits (Meyer and Hemley, 1967). Sericite is a textural term commonly used to describe fine-grained white micas (muscovite, phengite and/or illites) developed in hydrothermally altered rocks. In Boyongan, it appears as white silky clays especially along fractures.

- **Phlogophite** $\{K_2(Fe^{2+},Mg)_6(Si_6A_{l2})O_{20}(OH)_4\}$as well as its Fe-rich counterpart biotite, is commonly present in igneous and regional metamorphic rocks. In plutonic rocks, the Mg:Fe value of phlogopite may vary and increase from andesitic to ultramafic rocks. Phlogopite readily decomposes during weathering. It occurs rarely in potassic alteration zones (e.g. Lihir; Carman, 2002).

- **Phengite** $\{K_2(Al,Mg,Fe)_4(Si_{6-X},Al_{2-X})O_{20}(OH)_4\}$ common in hydrothermally altered rocks (Hermann, et al., 2002).

- **Nontronite** $\{(Ca,Na)_{0.66}Fe_{3+4}(Si,Al)_8O_{20}(OH)_4 \cdot nH_2O\}$ is a common smectite mineral which commonly occurs in which probably hydrothermal in origin.

- Two types of **chlorite**: **(1) Mg-Chlorite** $\{(Mg,Al,Fe)_{12}[(Si,Al)_8O_{20}](OH)_{16}\}$ where absorption features are 2250nm and 2330-2340nm (asymmetric); and **(2) Fe-Chlorite**

{$(Mg,Al,Fe)_{12}[(Si,Al)_8O_{20}](OH)_{16}$}where absorption features were observed at 2260nm and 2350nm (symmetric), (Merry, et al., 1999).

• **Magnesium Clays** $[(Na,Ca)_{0.67}(Mg,Li)_6Si_8O_{20}(OH)_4{\cdot}nH_2O]$ which is formed by the weathering of low-temperature hydrothermal alteration assemblages in intermediate to mafic rocks (Merry, et al., 1999).

Acidic solutions seem to persist below the zone of weathering as evidenced by the presence of kaolinite, halloysite and montmorillonite beneath the base of oxidation (Fig. 4.24B, C, & E).

Another technique to identify minerals is the use of XRD (X-Ray Diffraction). Like PIMA, it can identify specific types of clays. The process however involves laborious sample preparation and the cost is expensive. Braxton (in prep.) has used this technique to determine other types of clays at Boyongan that have not been detected using the PIMA. The preliminary results of Braxton's work show that the three most abundant clays present in the weathering zone at Boyongan are illite, chlorite, and smectite. These clays are also among five clays most commonly identified using PIMA at Boyongan during the current study (Fig. 4.24). Braxton (pers. comm, 2003) noted that opal (15 spectral readings) had been identified through XRD but infers that it is in fact smectite.

4.8 SUPERGENE PARAGENESIS

The paragenetic sequence of copper sulfide and oxide minerals observed in oxidised copper-bearing deposits reveals that specific mineralogical changes take place during supergene oxidation (Chavez, 2000). This section discusses the supergene paragenesis at Boyongan based from mineralogical observations/associations and hostrock composition.

The supergene profile at Boyongan is a product of chemical weathering of sulfide minerals, which produced dominantly and highly acidic groundwaters (Blanchard, 1968; Anderson, 1982; Einaudi, 1995; Chavez, 2000). Minerals such as kaolinite and halloysite are interpreted to have formed through hydrolysis where hydrogen ions (H^+) or acids are consumed by the hostrock, and cations such as Na, K, Ca, Mg, and Fe are released into solution (Nelson, 2001). The most important source of hydrogen ions (H^+) come from sulfuric acid which is produced mainly from the oxidation of pyrite (Blanchard, 1968; Chavez, 2000). Other forms of acids are the carbonic acid (H_2CO_3) where CO_2 from air combines with H_2O in soil or rainwater (the chief natural acid involved in the chemical degradation of normal rocks exposed at the surface; Einaudi, 1995) and, however minor compared to sulfides, include magnetite and Fe-bearing silicates such biotite and amphiboles (Chavez, 2000).

Since hydrogen ions are consumed during weathering and oxidation, acids are therefore neutralised by the hostrocks at Boyongan and the mobility of metals during supergene oxidation and weathering may have been limited. At the Ray porphyry copper deposit in Arizona, the host rocks are similar to those at Boyongan. They contain abundant fresh plagioclase feldspar and mafic minerals. The wall rocks at Ray has a substantial capacity to neutralize oxygenated acidic solutions (Anderson, 1982; Chavez, 1999, 2000), and a similar scenario is envisaged for Boyongan. Aside from the acids being neutralised, Boyongan has a low concentration of pyrite (1-2%). The lower the concentrations of pyrite, the lower the production of acids during weathering, and the leaching and transport of metals are significantly reduced (Anderson, 1982; Sillitoe & Gappe, 1984; Einaudi, 1995; Chavez, 2000).

The amount of pyrite therefore is significant in determining the supergene sulfide and oxide mineralogy (Chavez, 2000). Moreover, the supergene mineral assemblage observed reflect the pH conditions at the time of supergene mineralisation. Figure 4.25 illustrates schematically the secondary iron minerals that can occur at different pH values, and as a function of hypogene pyrite:chalcopyrite ratios (Wilson, 2003). From Figure 4.25A, rocks

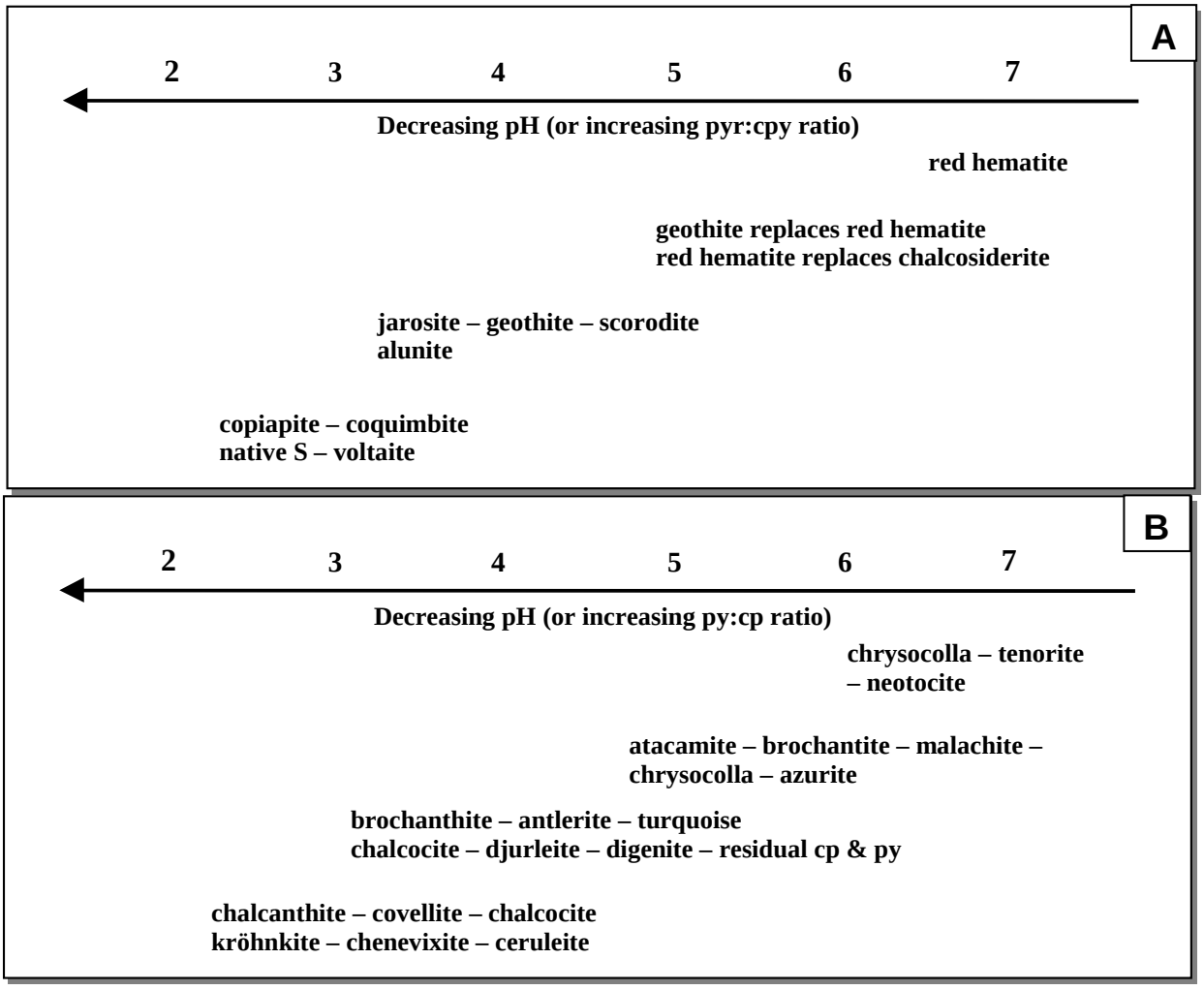

Fig. 4.25 A. Relative pH of formation of different secondary iron and related minerals developed in leached cappings: alunite $(K_3Al_3SO_4)_2(OH)_6$, chalcosiderite - $CuFe_6(PO_4)_4(OH)_8{\cdot}4H_2O$, copiapite –$(FeMg)Fe_4(SO_4)_8(OH)_2{\cdot}20H_2O$, coquimbite – $Fe_2(SO_4)_3{\cdot}9H_2O$, goethite – FeO(OH), hematite – Fe_2O_3, jarosite - $KFe_3(SO_4)_2(OH)_6$, scorodite $(FeAsO_4{\cdot}2H_2O)$, voltaite - $(K,Fe)_3Fe(SO_4)_{\cdot}4H_2O$. Based on the data from Chavez (1999); **B.** Relative pH formation of different secondary copper and related minerals developed in leached cappings: antlerite - $Cu_3(OH)_4SO_4$, atacamite - $Cu_2Cl(OH)_3$, azurite - $Cu_3(OH)_2(CO_3)_2$, brochantite – $Cu_4(OH)_6SO_4$, ceruleite - $CuAl_4(AsO_4)_2(OH)_8{\cdot}4H_2O$, chenevixite – $Cu_2Fe_2(AsO_4)_2(OH)_4{\cdot}H_2O$, chalcanthite – $CuSO_4{\cdot}5H_2O$, chrysocolla – $CuSiO_3{\cdot}nH_2O$, chalcocite – Cu_2S, covellite – CuS, digenite – Cu_9S_5, djurleite – $Cu_{31}S_6$, kröhnkite - $Na_2Cu(SO_4)_2{\cdot}H_2O$, malachite – $Cu_2(OH)_2CO_3$, neotocite – $(Cu,Fe,Mn)SiO_3$, tenorite – CuO, turquoise - $CuAl_6(PO_4)_4(OH)_8{\cdot}5H_2O$. Wilson (2003)

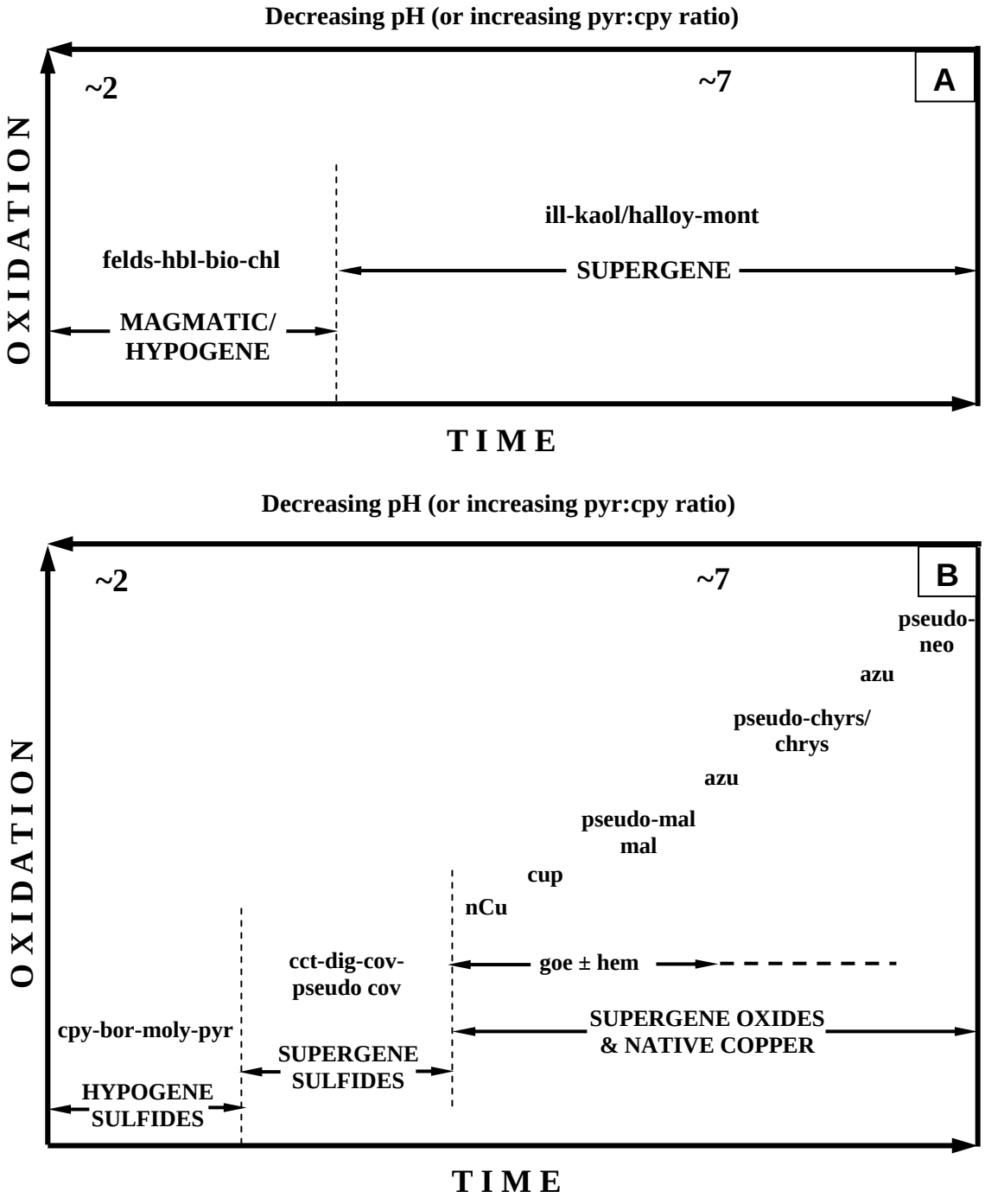

Fig. 4.26 Schematic summary of the timing, oxidation, and relative pH on the formation of supergene alteration and mineralistion in Boyongan: **A.** Hypogene and supergene alteration: feldspar (felds) - biotite (bio), hornblende (hbl), chlorite (chl), kaolinite (kaol) , halloysite (halloy), montmorillonite (mont), illite (ill). **B.** Hypogene and supergene copper mineralisation (± pyrite) : chalcopyrite (cpy) - $CuFeS_2$, bornite (bor) - Cu_5FeS_4, molybdenite (moly) - MoS_2, pyrite (pyr) - FeS_2, chalcocite (cct) - Cu_2S, digenite (dig) - Cu_9S_5, pseudo-covellite (pseudo-cov) - "bor-cov-dig" in composition, native Cu (nCu) - Cu^0, cuprite (cup) - Cu_2O, malachite (mal) - $Cu_2(CO_3)(OH)_2$, pseudo-malachite (pseudo-mal) - $Cu_3(PO_4)_2$, geothite (geo) - FeO(OH), azurite (azu) - $Cu_3(CO_3)_2(OH)_2$, chyrsocolla or pseudo-chrysocolla (chrys or pseudo-chrys) - $CuSiO3{\bullet}nH_2O$ or $Cu_3(CO_3)_2(OH)_2$-$Al_2Si_2O_5(OH)_4$, pseudo-neotocite (pseudo-neo) – $(Mn,Cu)_2CO_3$; it is useful to note that low temperature secondary iron, copper, and clay minerals can occur as a function of pH and as a function of pyrite/chalcopyrite ratio (based from Wilson, 2003 & Anderson, 1982). The more the pyrite in the deposit, the more acid the environment during supergene mineralisation.

with low acid generating capacity (e.g. low pyr:cpy ratio), should generate hematite as the principal iron oxide. However, at lower pH, the dominant iron oxide will change progressively from hematite to goethite, and then to jarosite. Therefore, it is expected that jarosite will develop in preference to geothite or hematite in rocks with high pyrite:chalcopyrite ratio. In rocks with high acid generating capacity, most of the iron will be removed from the system, leaving residual sulfates. In the case of Boyongan, the dominant iron oxide developed is goethite, suggesting lower pH conditions.

On the other hand, Figure 4.25B shows that copper oxides and silicates are the product of *in situ* oxidation of copper sulfide-bearing rocks by weakly acidic or even weakly alkaline waters (Anderson, 1982; Chavez, 2000; Wilson, 2003). This can be the case in areas of low pyrite:chalcopyrite ratio or in systems with a high acid neutralising capacity (e.g. El Abra & Mantos Blancos, Chavez, 2000). With increasing pyrite:chalcopryite (or chalcocite) ratio, the production of higher quantity of acid results in more efficient leaching of copper mineralisation and associated development of secondary chalcocite (e.g. Chuquicamata, Chavez, 2000). The supergene copper mineral assemblages (chalcocite, pseudo-covellite, digenite, native copper, cuprite, malachite, pseudo-malachite, azurite, chrysocolla, pseudo-chyrsocolla, and pseudo-neotocite) developed at Boyongan are most likely a product of in situ oxidation of pre-existing hypogene copper sulfides that formed in a near neutral to neutral pH environment (Wilson, 2003). Nonetheless, evidences of remobilised copper (exotic copper) can still be observed (e.g. chalcocite replacing pyrite; Fig. 4.15).

Figure 4.26 shows the general sequence of supergene mineral deposition at Boyongan. The initial stages of supergene mineralisation is the replacement of hypogene sulfides such as chalcopyrite, bornite by chalcocite, digenite, and pseudo-covellite. In some places, chalcocite replaces pyrite. Goethite is generally derived from pyrite, chalcopyrite, bornite,

and chalcocite.

Cuprous ion (Cu^{2+}) that is released in solution precipitates in native form (native Cu). Native copper also replaces chalcocite (e.g. native Cu overgrowing chacocite in TSD18 @ 216.30m). Native copper marks the depth of the paleowater table (Anderson, 1982). Native copper later oxidised to form cuprite or the acicular and euhedral crystals of chalcotricite. It is also possible that cuprite may have formed formed from Cu^{2+} in solution and when chalcocite reacts with oxygenated groundwaters.

Malachite replaced chalcocite and/or Cu^{2+} when it encountered CO_2-bearing oxygenenated groundwaters. Pseudo-malachite has replaced malachite, and may have been formed when phosphate ions (PO_4^{3-}) replaced carbonate ions in malachite to form copper phosphate. Phosphate may have come from the mineral apatite, which is probably an accessory mineral of the diorite intrusions. Apatite is generally considered to be a fairly stable mineral but is soluble in acids and could be dissolved by supergene solutions. It could therefore serve as a source of phosphate ions in the formation of supergene minerals (Peterson, 1947). Another possible source of phosphate ions is from organic material in soil. Malachite and pseudo-malachite been overgrown by azurite and then by pseudo-chrysocolla and/or chrysocolla. Pseudo-chrysocolla may be a mixture of azurite, chrysocolla and kaolinite. Moreover, supergene solutions may have also been high in dissolved silica when the chrysocolla and/or pseudo-chrysocolla was formed (Anderson, 1982). Azurite has overgrown, rimed, and cut malachite, cuprite and pseudo-chyrsocolla. Pseudo-neotocite replaced malachite and azurite and is considered to be the latest in the paragenetic sequence. Manganese, which is a major component of pseudo-neotocite is commonly present as an admixed impurity of limonite (Blanchard, 1968).

4.9 SUMMARY

The complex supergene mineralogy at Boyongan has formed via the oxidation and weathering of pre-existing hypogene minerals (pyrite+chalcopyrite±bornite). Remnant hypogene and supergene sulfides have been observed, indicating that sulphide oxidation has not proceeded to completion. The supergene profile at Boyongan is inferred to be immature. Boyongan is generally a low-pyrite porphyry copper system. Low pyrite contents would mean insufficient supergene acid generated during supergene oxidation and weathering. Most of the supergene mineral assemblages at Boyongan may have formed in-situ and may have developed in a near neutral to neutral pH environment (Anderson, 1982).

Deep oxidation at Boyongan has developed a complex supergene mineralogy consisting chalcocite, digenite, pseudo-covellite, pitch limonite/cuprous goethite, native copper, cuprite, malachite, pseudo-malachite, azurite, chrysocolla, pseudo-chrysocolla, and pseudo-neotocite. This supergene mineralogy is more or less paragenetically arranged from earliest (chalcocite) to latest (pseudo-neotocite). Goethite is the most common variety of limonite at Boyongan. Oxidation and the development of supergene minerals is mainly controlled by fracturing and the availability of reduced sulfur or hypogene sulfides. Fine gold (<100μm) is observed in goethite, chalcocite, chrysocolla, and malachite.

Although the supergene mineralisation in Boyongan is generally in-situ, there is still some evidence that shows minor copper remobilisation (exotic copper), including chalcocite and cuprite coatings on pyrite. Moreover, some copper oxide minerals (such as malachite and azurite) were observed to fill “clean” fractures or fractures that show no evidence of prior mineralisation.

Clays identified at Boyongan through the use of PIMA dominated by kaolonite and halloysite with minor illite ± montmorillonite that are largely produced from weathering of diorite hostrock. Other minor clays are chlorite ± muscovite ± phlogophite ± phengite ± nontronite ± Mg-clays. These are dominantly hydrothermal in origin, but are partially preserved in the weathering zone.

CHAPTER 5

METAL ZONING

5.1 INTRODUCTION

This chapter documents the copper and gold zonation at Boyongan, and relates the distribution of these metals to the supergene mineral profile. Copper and gold grade contour data have been plotted on sections 1062200N (Fig. 5.1A & B), 779700E (Fig. 5.2A & B), and plan –100mRL (Fig. 5.3A & B) in order to illustrate how copper and gold are distributed at Boyongan. Copper-gold ratios have also plotted and see if they are related at least in part to the observed supergene mineral assemblages (Fig. 5.7)

5.2 COPPER & GOLD DISTRIBUTION

There are two distinct high-grade copper (>1%) and gold (>1g/t) zones (east and west zones) at Boyongan (Fig. 5.1A & B, 5.3A & B). They are spatially and mostly likely genetically related to the early mineral diorite intrusions within the diorite breccia complex (Sillitoe, 2002a; Fig. 2.6). A very high-grade copper and gold zone (>2% and 2 g/t, respectively) occurs in the eastern zone (Fig. 5.1C & D). It is related to the hydrothermal breccia which contains distinctive quartz vein clasts. Although the metal distribution is related primarily to hypogene geological elements, the mineralisation itself is primarily

supergene. Only remnant hypogene mineralisation was observed within the quartz stockwork zones. Based on detailed logging at available drillholes, it is estimated that 80% of copper mineralisation in the deposit is supergene, while only 20% is hypogene.

The 0.5% Cu and 0.5g/t Au contours for copper and gold are mostly confined within the supergene or oxidised zone (Fig 5.1A & B, 5.2A & B, & 5.3A & B). Copper is generally more dispersed or erratic in distribution compared to gold which is spatially more restricted or confined within and adjacent to the early mineral diorite intrusions (Fig. 5.1A & B, 5.3A & B). Copper grades in the cuprite-dominant western zone (Fig. 5.4 & 5.5) generally decrease with depth toward zones of patchy native copper. A copper carbonate-dominated blanket, consisting of malachite and azurite, overlies the cuprite zone (Fig. 5.4 & 5.5) and contains high copper and gold (>1% & >2 g/t, respectively). Patchy zones of chalcocite replacing pyrite (Fig. 5.4 & 5.5) are generally low in copper and gold (<0.5% & <0.5 g/t, respectively). However, in zones where chalcocite has partially replaced pre-existing copper sulfides such as chalcopyrite and gold-bearing bornite (Fig. 4.5C), copper and gold values are elevated (>0.5% Cu & >1g/t Au; Fig. 5.4 & 5.6). Minor patchy zones of chrysocolla and/or pseudo-chrysocolla are generally confined within high copper and gold zones (>0.5% & >1g/t, respectively). Copper and gold grades below the base of oxidation that are related to the hypogene sulfides are generally below 0.5% Cu and 0.5 g/t Au.

5.3 METAL ZONING

Sections 1062200N (looking north; Fig. 5.1C & D), 779700E (looking west; Fig. 5.2C & D), and -100mRL (plan; Fig 5.3C & D) illustrates the current understanding of metal zoning at Boyongan. Metal zones were created from contours generated from downhole assay data.

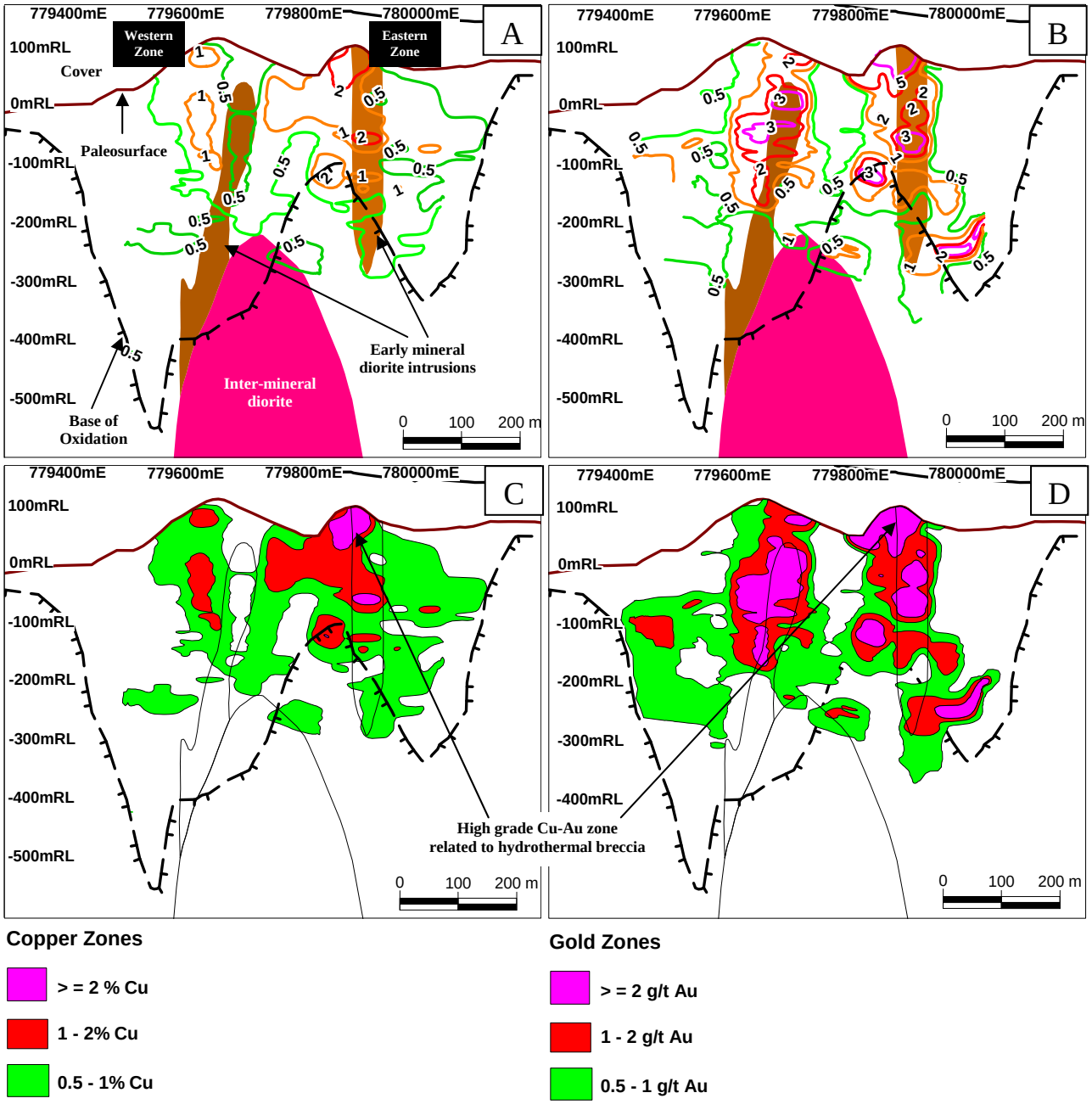

Fig. 5.1. Section along 1062200N (looking north) showing the early-mineral and inter-mineral diorite intrusions for reference. Also shown here are the paleosurface (solid brown line) and base of oxidation (dashed black line with teeth). **A.** Copper grade contour (weight percent). **B.** Gold grade contour (g/t). **C.** Copper metal zonation. **D.** Gold metal zonation.

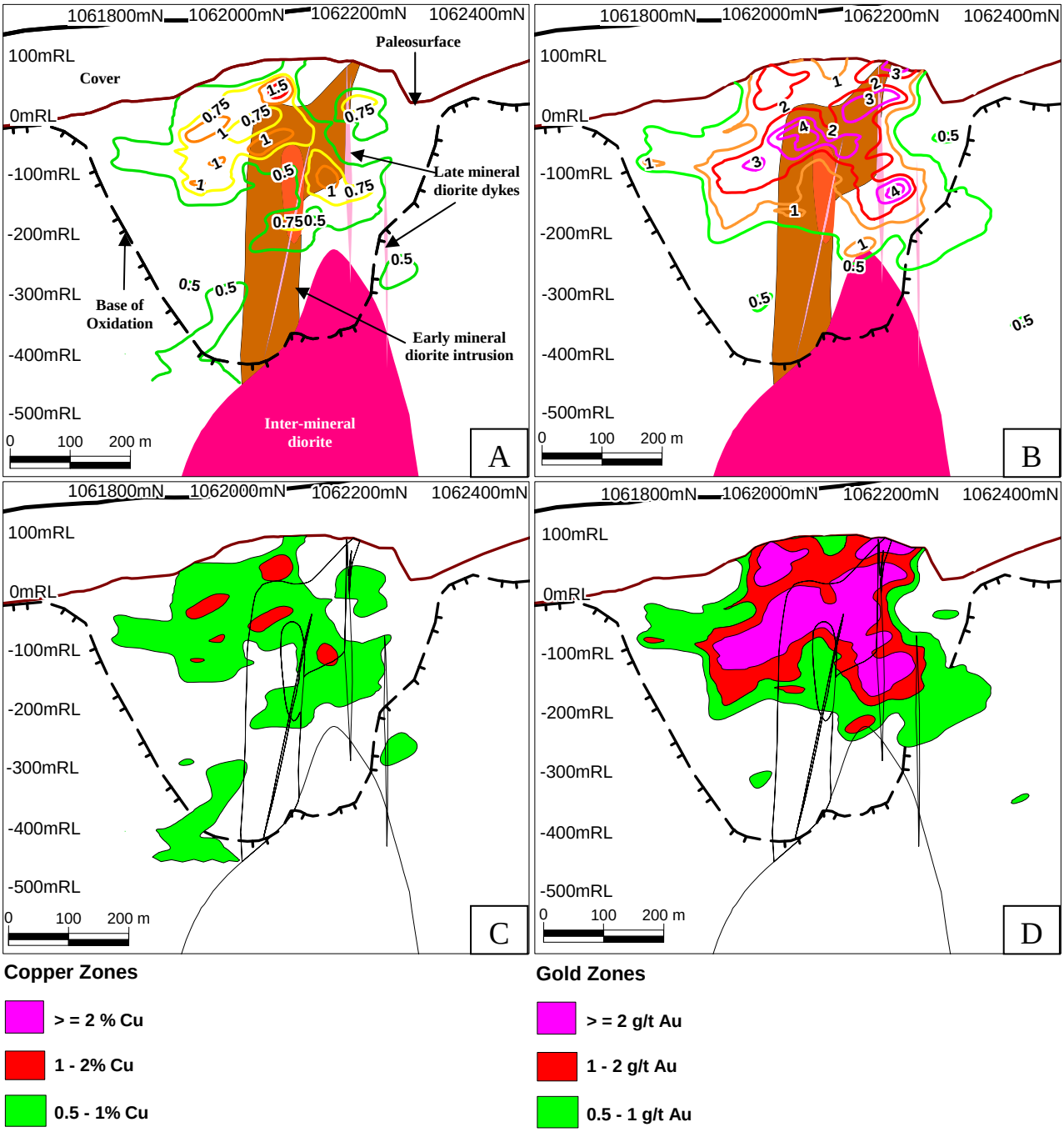

Fig. 5.2. Section along 779700E (looking west) showing the early-mineral and inter-mineral diorite intrusions for reference. Also shown here are the paleosurface (solid brown line) and base of oxidation (dashed black line with teeth). **A.** Copper grade contour (weight percent). **B.** Gold grade contour (g/t). **C.** Copper metal zonation. **D.** Gold metal zonation.

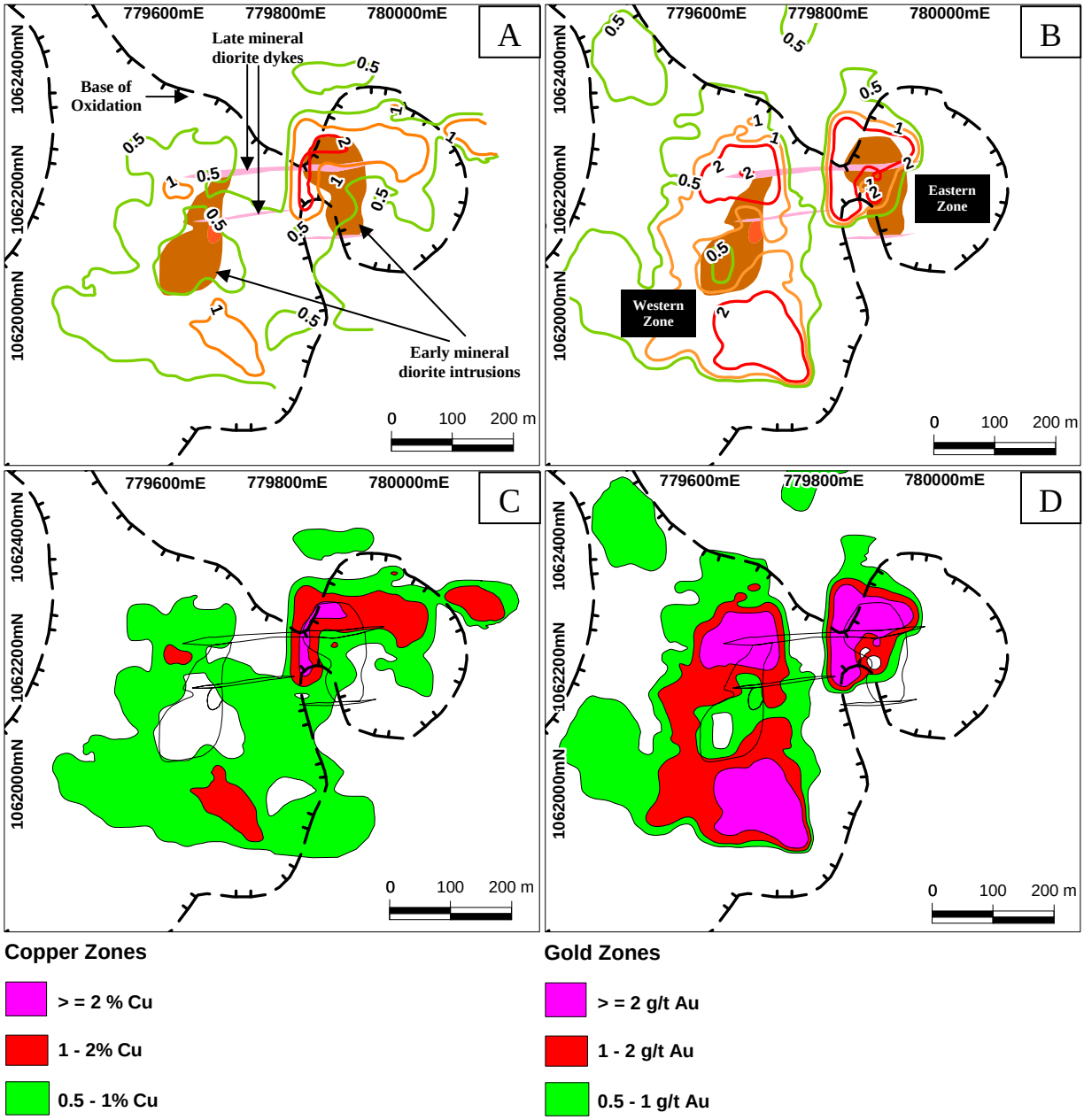

Fig. 5.3. Geological plan at –100mRL showing the early-mineral and inter-mineral diorite intrusions for reference. Also shown here are the paleosurface (solid brown line) and base of oxidation (dashed black line with teeth). **A.** Copper grade contour (weight percent). **B.** Gold grade contour (g/t). **C.** Copper metal zonation. **D.** Gold metal zonation.

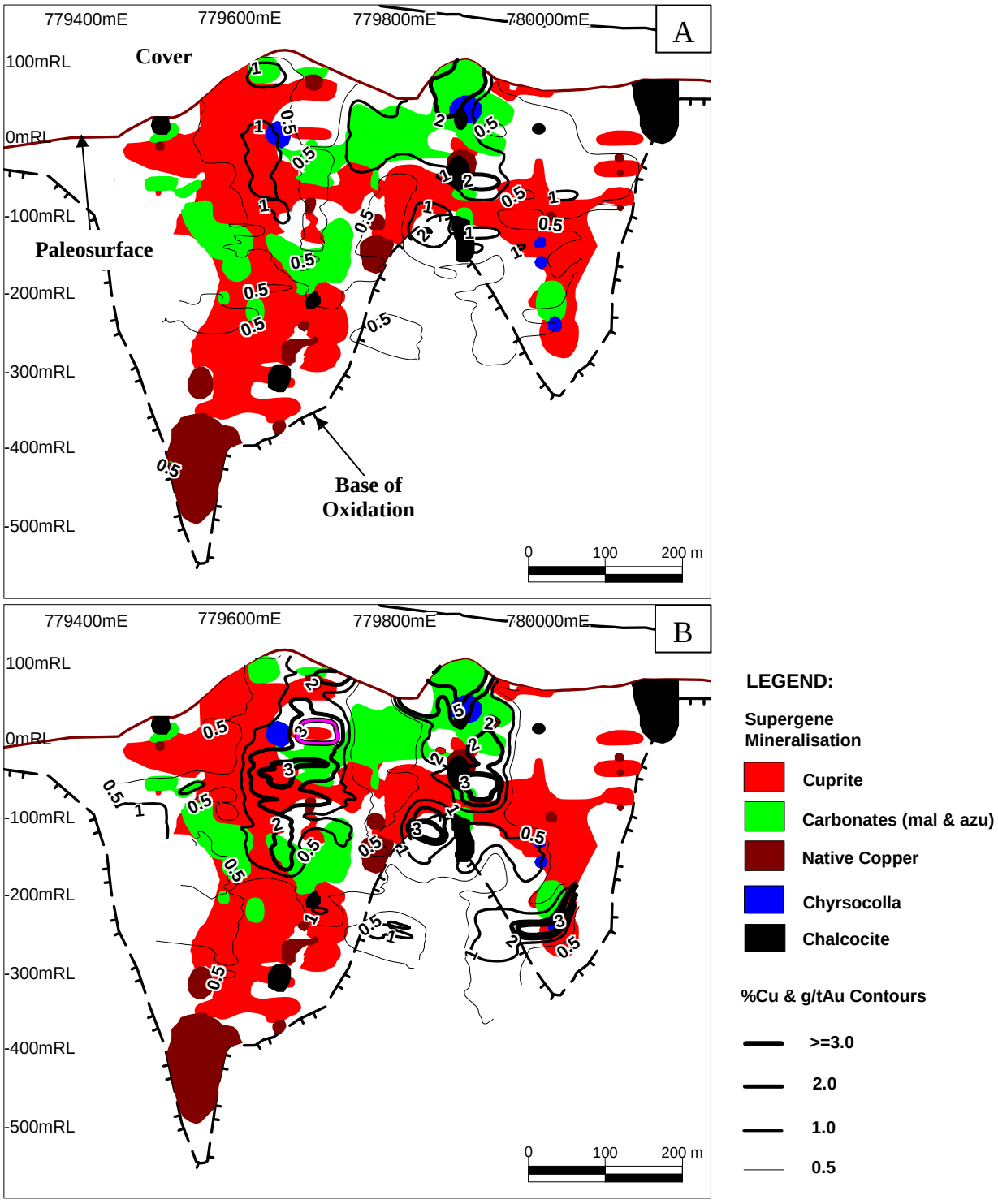

Fig. 5.4. Section along 1062200N (looking north). Note paleosurface and base of oxidation for reference. A. Spatial distribution of supergene mineral assemblages with copper grade contour (weight percent). B. Spatial distribution of supergene mineral assemblages with gold grade contour (g/t).

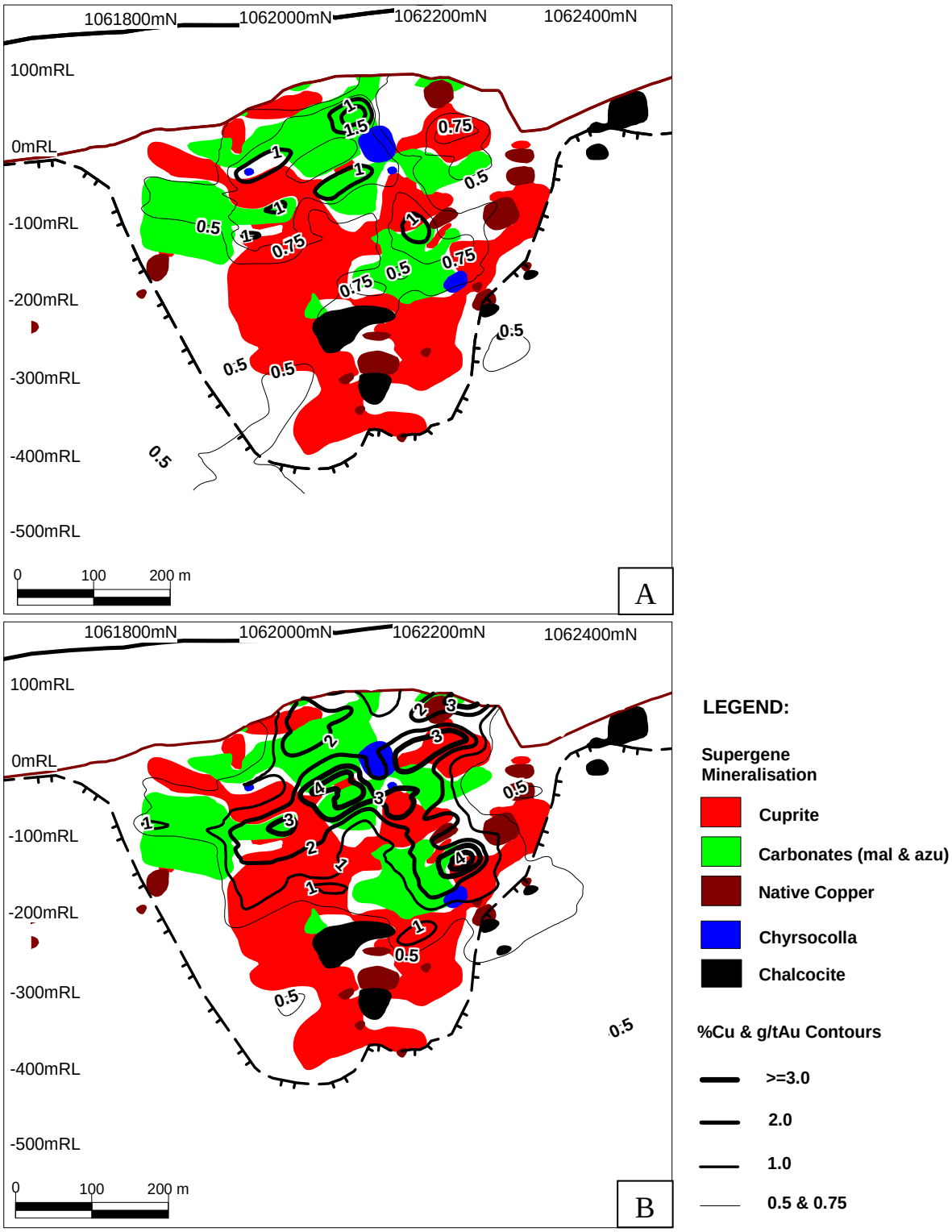

Fig. 5.5. Section along 779700E (looking west). Note paleosurface and base of oxidation for reference. A. Spatial distribution of supergene mineral assemblages with copper grade contour (weight percent). B. Spatial distribution of supergene mineral assemblages with gold grade contour (g/t).

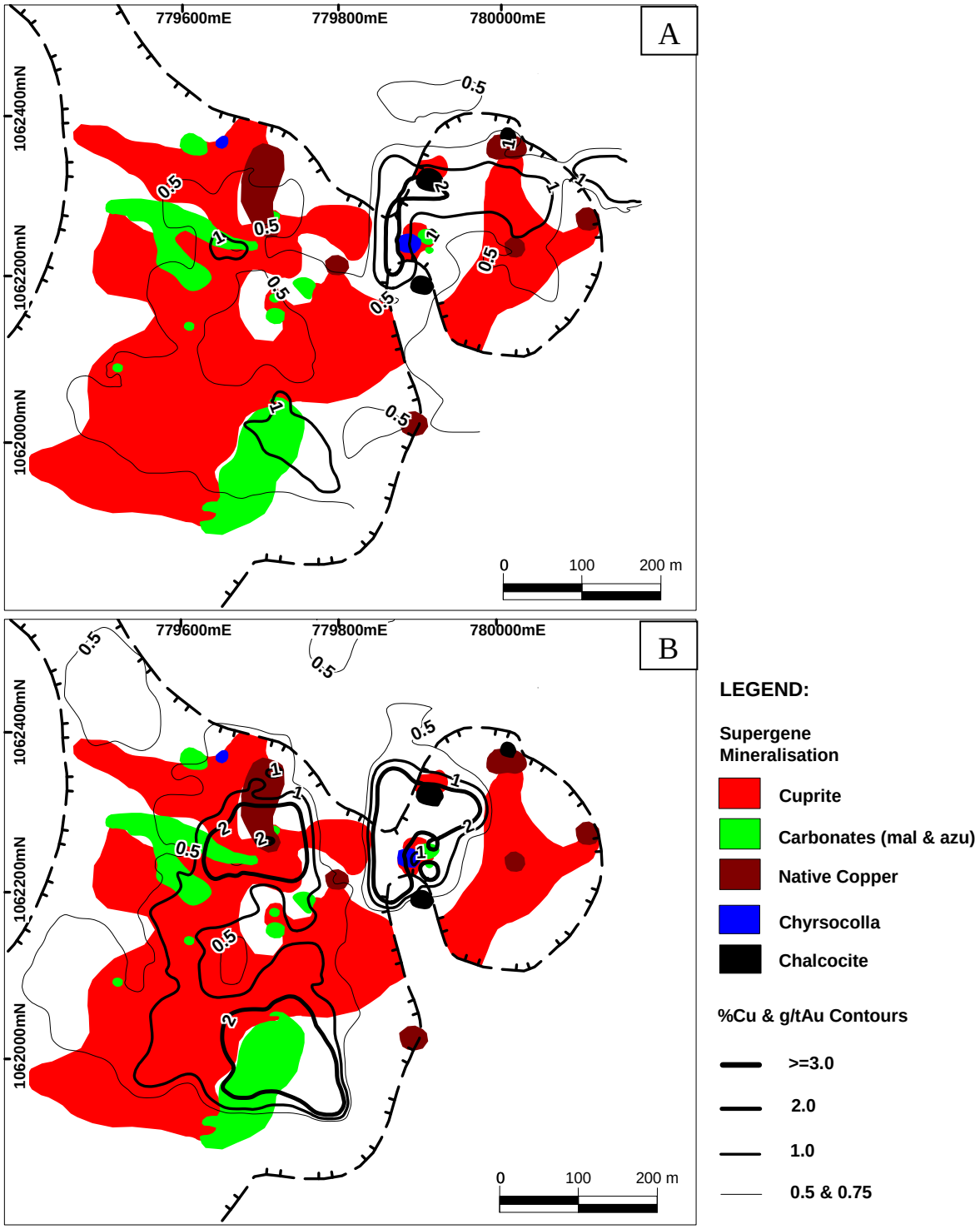

Fig. 5.6. Geological plan of Boyongan at –100RL. Note paleosurface and base of oxidation for reference. A. Spatial distribution of supergene mineral assemblages with copper grade contour (weight percent). B. Spatial distribution of supergene mineral assemblages with gold grade contour (g/t).

Zones were colour-coded with respect to grade ranges.

Generally, both copper and gold grades decrease away from the intrusions. Grades likewise decrease with depth. The 0.5% Cu envelop has an irregular shape but generally almost completely surrounds the two early mineral diorite intrusions (Fig. 5.1C & 5.2C). In plan, subtle NE- and ENE-trends can be observed within the 0.5% Cu envelope (Fig 5.3C). Moreover, NS– and EW-trends can be observed in the high grade copper zones (1% & 2% envelopes; Fig. 5.3C). These trends may be structurally related. Gold assay data defines two vertically elongated zones that decrease in grade both outwards and downwards (Fig. 5.1D). This spatial distribution is strong evidence that gold is genetically related to the two early mineral diorite intrusions. The highest grade gold zone (> 2 g/t) is umbrella-shaped (Fig. 5.2D) and caps the early mineral intrusion. In plan, high grade gold zones occur on the margins of the early mineral diorite intrusions (Fig. 5.3D).

5.4 DISCUSSION

The spatial distribution of high-grade copper may have been similar to gold prior to supergene mineralisation. However, there is not much evidence at depth to support this as grades dramatically decrease at depth. Changes appear to have occurred during weathering and uplift of the Boyongan deposit which resulted in the irregularly-shaped copper zones. This may suggest that copper may have been partly remobilised during supergene mineralisation. Evidence to support supergene redistribution of copper includes the copper-staining of plagioclase in diorite (Fig. 4.9A & B), chalcocite and cuprite coating pyrite (Fig. 4.15), and some copper oxide minerals filling “clean” fractures. Copper may have been transported from a few meters to several tens of meters. Boyongan is very much similar to

the El Abra porphyry system in northern Chile where the copper oxides were developed generally in-situ and there was no copper grade enhancement in the oxide zone (Chavez, 1999 & 2000). Like El Abra, chalcocite has been developed erratically.

The U-shaped copper-only zone at Boyongan (Cu/Au ratio >2; Fig. 5.7A & C) that occurs between the two early mineral porphyries is interpreted here to be a domain of transported or exotic copper (definitions of Blanchard, 1968) consisting of malachite and azurite. In this area, supergene minerals occupy "clean" fractures, including fractures that show no evidence of prior hypogene mineralisation (Chavez, 2000). The copper in this zone may have come from both the eastern and western zones. The copper-only zone (dominantly cuprite) on the east at 780000E (Fig. 5.4B & 5.7C) may also be dominantly exotic as it occurs on the fringe of the main copper-gold zone (Fig. 5.1C & D, 5.3C & D). The zones that are inferred to be exotic or transported have copper-gold ratios greater than 2.0 (Fig. 5.7).

Plots of copper-gold ratios show large copper-dominated zones in the eastern zone (Fig. 5.7C & D). These may be exotic in origin, either originating from the early mineral diorite intrusions or it may have come from other porphyry copper centres.

Although supergene gold was observed in chalcocite, chrysocolla and goethite during core logging, the regular shape of the gold zones (Fig. 5.1D, 5.2D & 5.3D) and its proximity to the early mineral diorite intrusions may suggest that gold may only been slightly remobilised by supergene processes as compared to copper. Supergene gold was generally developed in-situ.

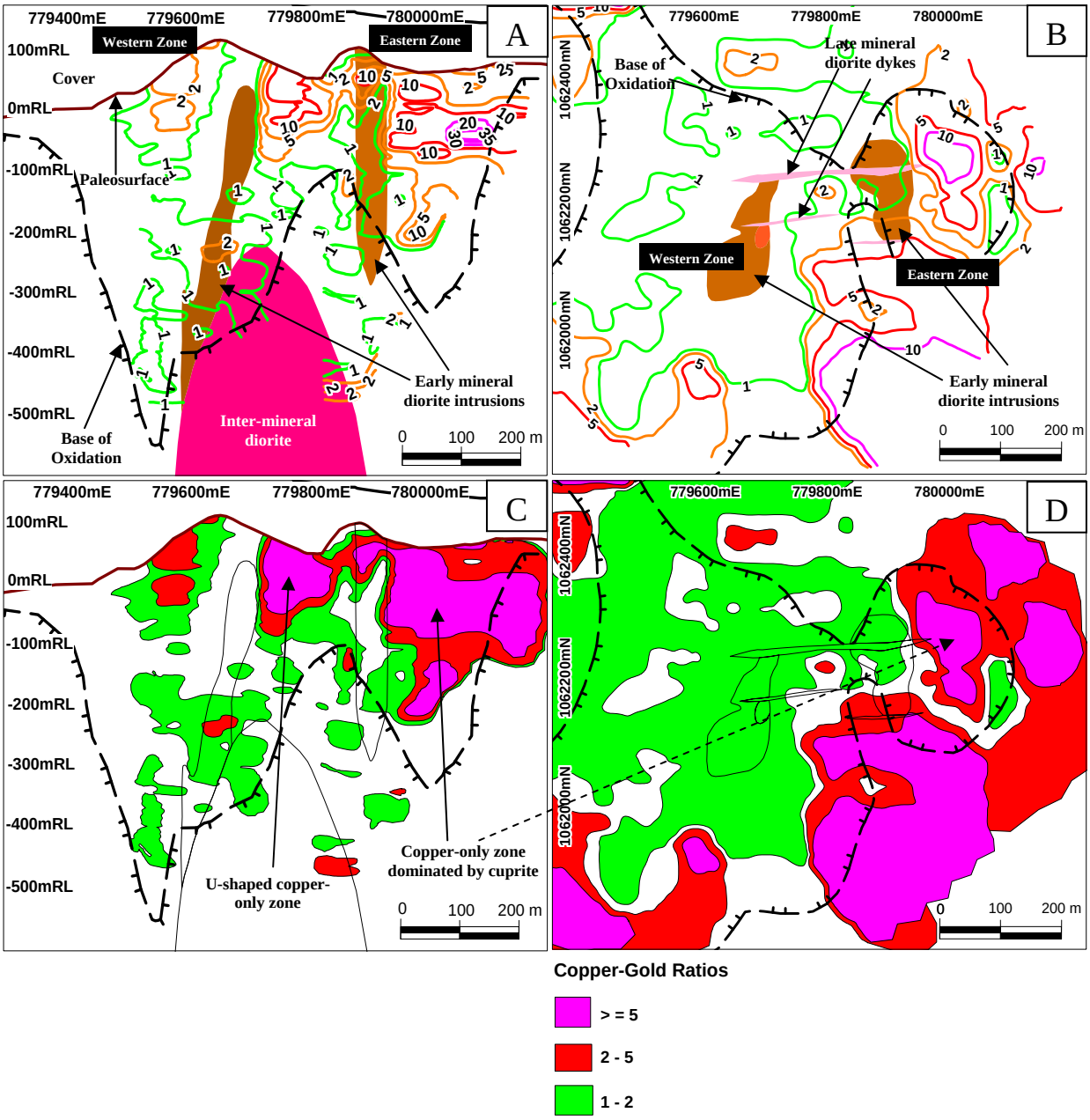

Fig. 5.7. Section and plan showing copper-gold ratios. **A.** Copper-gold ratio contour along 1062200N. **B.** Copper-gold ratio contour at –100mRL (plan). **C.** Copper-gold ratio zonation along 1062200N. **D.** Copper-gold ratio zonation at –100mRL (plan).

5.5 SUMMARY

Copper contours show that copper generally has a more dispersed or erratic distribution compared to gold (Fig. 5.1, 5.2 & 5.3). The latter is restricted spatially to, within and adjacent to the early mineral diorite intrusions. Copper grades in the cuprite-dominated zone in the west generally decrease with depth toward zones of patchy native copper (Fig. 5.4 & 5.5). The copper carbonate-dominated blanket above the cuprite zone contains both high grade copper and gold (>1% & >2 g/t, respectively; Fig. 5.4 & 5.5). Chalcocite zones that have partially replaced hypogene copper sulfides have higher grades compared to zones of chalcocite replacing pyrite (Fig. 5.4 & 5.5). Chrysocolla and/or pseudo-chrysocolla is confined to zones that contain high copper and gold grades (>0.5% & >1 g/t, respectively; Fig. 5.4 & 5.5).

Both copper and gold grades decrease with distance away from the early mineral diorite intrusions (Fig. 5.1, 5.2 & 5.3). Grades likewise decrease with depth. High-grade copper zones are irregular in shape and have subtle NE-trends that may be structurally controlled (Fig. 5.3C). On the other hand, high-grade gold defines two elongated and regular vertical zones that cap and/or fringe the early mineral diorite intrusions (Fig. 5.1C, 5.2C & 5.3C).

Although the development of supergene copper in Boyongan has occurred largely in-situ, some copper may have been partly remobilised during supergene mineralisation, based on the irregular distribution of copper mineralisation, metal zoning patterns (Fig. 5.1C, 5.2C & 5.3C) and physical evidence observed during core logging (e.g. selective copper-staining of plagioclase; chalcocite and cuprite replacing pyrite; copper oxides occupying “clean” fractures, etc.). Supergene copper may have been transported from a few meters to several

tens of meters. In contrast, supergene gold was generally developed in-situ and appears not to have been remobilised during supergene mineralisation. Consequently, copper zones that are inferred to have formed due to deposition of transported (exotic) copper have copper-gold ratios greater than 2.0. These ratios could therefore be used as a vector to search for hypogene porphyry copper-gold mineralisation within supergene mineralised zones similar to Boyongan.

CHAPTER 6

CARBON AND OXYGEN ISOTOPE GEOCHEMISTRY

6.1 INTRODUCTION

This chapter presents the results of a reconnaissance stable isotope study of carbonate minerals and organic detritus from Boyongan. This work has been conducted in order to help evaluate the genesis of supergene copper carbonate mineralisation.

6.2 Methodology

Carbon-oxygen isotope analyses were performed on three samples of malachite and two azurite samples from Boyongan. Data has also been generated from four shells from the Quaternary Tugunan Formation, three Pliocene Timamana limestone samples, and four Oligocene Bacuag limestone samples. Carbon isotopes were analysed from two wood samples from the Quarternary Tugunan Formation. A total of eighteen samples were collected (Fig. 6.1). Samples were prepared using a diamond drill. Powdered samples was placed in small vials and submitted to the Central Science Laboratory (CSL), University of Tasmania for C-O Isotope analysis. At the CSL, powdered samples were digested in acid, and the gas produced was analysed by a VG Micromass Optima SIMS instrument (Stable

Isotope Mass Spectrometer). Results are presented in Appendix 6 as delta 13C PDB (per mil), delta 18O PDB (per mil), and delta 18O SMOW (per mil). SMOW means Standard Mean Ocean Water. PDB is a standard derived from the belemnite *Belemnita americana,* from the Pee Dee Formation in South Carolina, USA. SMOW and PDB values are related by the equation $\delta^{18}O = 1.03091 \times \delta^{18}O_{PDB} + 30.01$. SMOW and PDB values are presented as per mil (‰) or parts per thousand. A value of $\delta^{18}O = 10‰$, for example, signifies that a sample has 10‰ more ^{18}O than the standard. Increasing isotopic values are referred to as *positive* or *heavier* values, and decreasing values are referred to as *lighter* or *negative* values (Davidson, 2003).

6.3 Results

The $\delta^{18}O$ values of malachite fall within the range of +26 to +28‰ SMOW. Likewise, the $\delta^{13}C$ values of malachite fall between -18 and -20‰ PDB (Fig. 6.2).

Moreover, the measured $\delta^{18}O$ values for azurite from Boyongan fall within the range of +28‰ to +30‰ SMOW. The $\delta^{13}C$ values of azurite at Boyongan fall between 0‰ and +6‰.

6.4 Discussion

The $\delta^{18}O$ values of malachite is probably dominantly controlled by $\delta^{18}O$ values of ambient meteoric water and the surface temperatures (Melchiorre, 1999). Likewise, the $\delta^{13}C$ values of malachite may reflect a vegetation-respired soil CO_2 (Melchiorre, 1999). A carbonate-rock derived carbon is unlikely as adjacent carbonate rocks (e.g. Timamana and

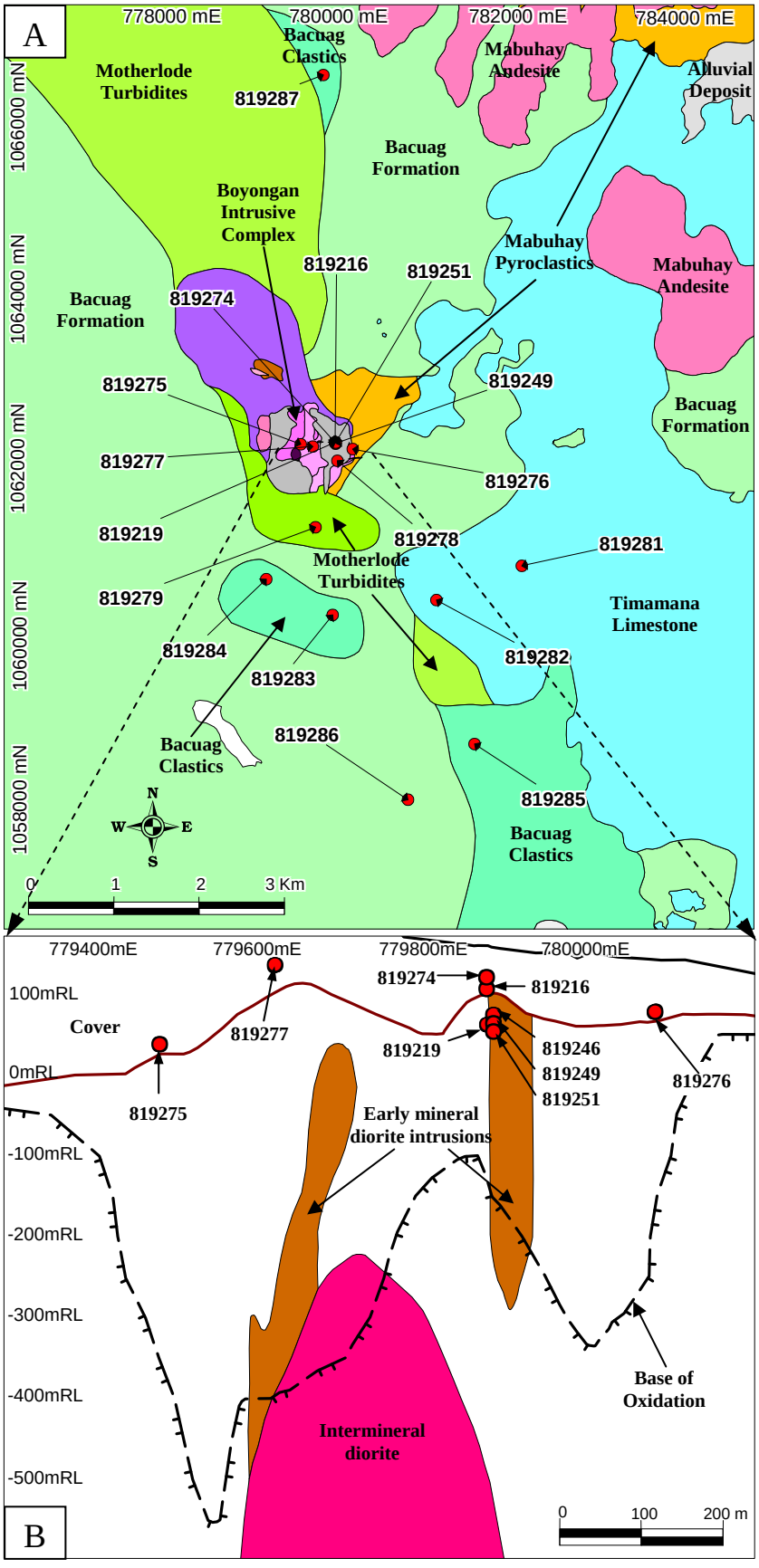

Fig. 6.1. A. Carbon and oxygen sample locations on pre-Quarternary geological plan. **B.** Carbon and oxygen sample locations along section 1062200N (looking north) as projected from Fig. 6.1A. List of samples and analytical results are described in Appendix 6.

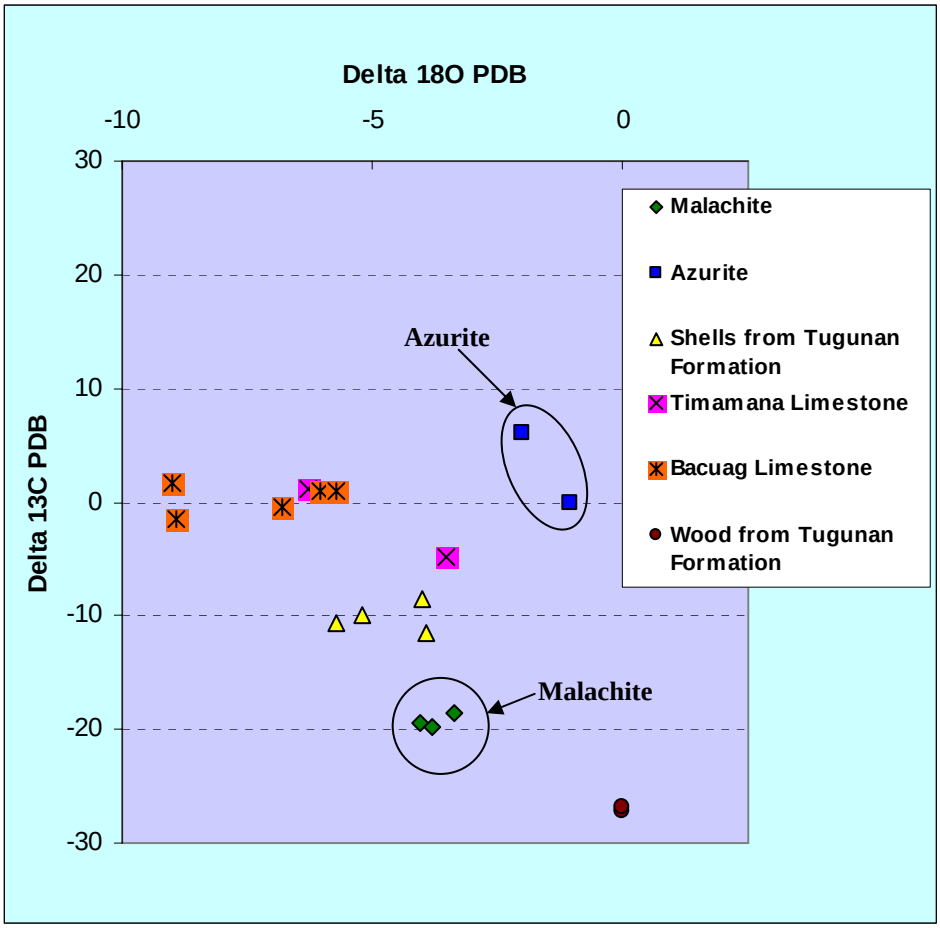

Fig. 6.2. Carbon and oxygen isotope signatures of carbonate and wood samples from Boyongan. Note that delta 13C PDB for malachite is lighter compared to azurite which may suggest different carbon sources.

Bacuag limestones) have different isotopic signatures (Fig. 6.2). It is possible that malachite formed when Boyongan was uplifted and exposed to the atmosphere in order to explain the soil CO_2- and/or meteoric water-signature of the malachite. Uplift may have been accompanied by a drop in water table and capillary waters (Anderson, 1982) may have been largely involved in the development or formation of malachite.

The measured $\delta^{18}O$ values for azurite are consistent with deposition from low temperature waters that have low $\delta^{18}O$ compositions, appropriate for meteoric waters (Melchiorre, 2000). SMOW and PDB values are higher or more positive compared to that of malachite. The

lower $\delta^{13}C$ value of azurite (-0.014‰) may suggests that a soil CO_2 component is inferred (Melchiorre, 2000) or carbon may also be bacterial in origin (Melchiorre, 2001 & 2003). Sulfide-oxidising bacteria (*Thiobacillus ferrooxidans*) may have also contributed indirectly to copper carbonate deposition within the oxide zone by providing free carbon (Melchiorre, 2001 & 2003). Moreover, it is also possible that some of the carbon in azurite has a seawater source. The heaviest $\delta^{13}C$ measured for azurite (+6.062 ‰, PDB) may result from the incorporation of aqueous carbonate species in equilibrium with atmospheric CO_2, or CO_2 liberated from other secondary carbonates that have been re-dissolved by a rising water table, or a combination of these (Melchiorre, 2000). In order to account for a soil CO_2 or bacterial component as a source of carbon for the azurite, Boyongan would need to have still been exposed when azurite formed. Some or all of the azurite may have formed when the water table began to rise as the deposit began to subside, probably in a pull-part basin, associated with the formation of Lake Mainit beside the Philippine Fault (Fig. 2.2). Another mechanism of azurite formation may have involved groundwaters intersecting pockets of high P_{CO2}, possibly produced by sulfide oxidation by supergene-related bacteria above the water table (Melchiorre, 2003). In summary, the mechanism of azurite formation remains uncertain, and more data are needed to resolve the various possible explanations.

Overall, malachite and azurite may have different sources of carbon which suggests that there copper carbonates could have formed at different times. This is consistent with the established and observed supergene mineral paragenesis at Boyongan (Fig 4.8C & D, 4.9D) where azurite has rimmed and cut malachite.

6.5 Stable Isotope Geothermometry

Detailed studies on the carbon and oxygen isotopic compositions of both natural and synthetic malachite and azurite has resulted in the development of the malachite-H_2O (Melchiorre et. al, 1999) and the azurite-H_2O isotope geothermometers (Melchiorre et. al, 2000). Melchiorre et. al (1999, 2000, 2001 & 2003) used these isotope geothermometers and has effectively measured temperatures of the formation of copper carbonates.

Using the malachite-H_2O thermometer [formula given as: 1000 *ln* α Oxygen mal-water = 2.66 ($10^6/T^2$) + 2.66; where T is in kelvins, mal represent the CO_2 liberated by acidification of malachite corrected as total calcite oxygen, and alpha (α) is the fractionation factor which is calculated as $\alpha = (1000+\delta^{18}O_{malachite}/1000+\delta^{18}O_{H2O})$; Melchiorre, 1999], the temperatures of formation for the three samples of fracture-filling malachite are 19˚C, 16˚C, and 18˚C, with an average of 18˚C for the three malachite samples. This contrasts with higher temperatures calculated for other malachite-bearing rocks (e.g. 58˚C at Broken Hill, NSW Australia) recorded by Melchiorre (1999) which reflected exothermic oxidation of concentrated sulfides. Note, however, that the calculated temperature of malachite formation at Boyongan should be considered with caution since a $\delta^{18}O$ = -7.5 ‰ SMOW for meteroic water has been used. This is the average value of $\delta^{18}O$ from 20 isotope measurements from creeks, springs, groundwater wells, and rainwater from Palimpinon, Negros (Rae, 2002). A more accurate temperature could be calculated using $\delta^{18}O$ values Boyongan water samples, but such data are not available at this time. Melchiorre et al. (2003) showed that in the Morenci District, Arizona, temperatures of malachite deposition coincided with areas of higher copper grades. Additional stable isotope analyses at Boyongan are required to evaluate whether a similar relationship occurs.

There is a high malachite concentration in the eastern ore zone at Boyongan, where remnant hypogene sulfides (chalcopyrite, bornite and pyrite) are present. The spatial correlation between abundant malachite and remnant sulfides is consistent with most of the malachite forming from in-situ oxidation of copper sulfides.

Using the azurite-H_2O thermometer [formula given as: 1000 *ln* α Oxygen $azu_{(CO3)}$-water = 2.67 $(10^6/T^2)$ + 4.75; where T is in kelvins, $azurite_{(CO3)}$ denotes the CO_2 liberated by acidification of azurite and corrected to calcite standards, and alpha (α) is the fractionation factor which is calculated as $\alpha = (1000+\delta^{18}O_{azurite}/1000+\delta^{18}O_{H2O})$; Melchiorre, 2000] and a $\delta^{18}O$ = -7.5 ‰ SMOW for meteroic water (Rae, 2002), the temperatures of formation for the two fracture-filling azurite samples from Boyongan are 15˚C and 20˚C, with an average of 18˚C for the two azurite samples.

Calculated low temperatures for malachite and azurite are consistent with Boyongan being a low-sulfide porphyry system. Higher pyrite contents would probably have led to greater degrees of sulfide oxidation. Given that pyrite oxidation is an exothermic chemical reaction, higher groundwater temperatures would also be expected when pyrite oxidation is widespread (e.g. Broken Hill; Melchiorre, 1999).

6.6 Summary

The measured $\delta^{18}O$ values of malachite from Boyongan are consistent with deposition from meteoric water at surface temperature conditions. The $\delta^{13}C$ values of malachite may reflect vegetation respired CO_2 (Melchiorre, 1999) suggesting that malachite may have formed in a subareal setting when Boyongan was uplifted and exposed.

The measured $\delta^{18}O$ values of azurite from Boyongan are consistent with near-isotopic equilibrium with waters having low $\delta^{18}O$, appropriate for meteoric waters. Measured $\delta^{18}C$ values of azurite could be derived from soil CO_2, sea-water carbonates, and/or CO_2 liberated from carbonates dissolved as the water table rose during burial (Melchiorre, 2000). Azurite may have been formed during the final stages of uplift as well as during subsidence. Moreover, fluids may have intersected high pockets of P_{CO2} produced by supergene-related bacteria above the water table (Melchiorre, 2003).

Low temperatures of formation have been calculated for malachite and azurite (average of 17.48˚C and 17.57˚C, respectively). These low temperatures are consistent with Boyongan being a low-sulfide porphyry system.

CHAPTER 7

SUPERGENE ORE GENESIS & IMPLICATIONS FOR EXPLORATION

7.1 SUPERGENE ORE GENESIS

The weathering environment at Boyongan (Fig. 7.1) can be divided broadly into two principal geochemical domains (Chavez, 2000): the oxide and sulfide-stable zones. A third domain, known as the leached zone, is typically very minor in the uppermost portions of weathered porphyries (Chavez, 2000) and is included here in the oxide zone.

Metals were accumulated and partially removed from the oxide zone at Boyongan. Some hypogene sulfides have survived oxidation, forming areas of perched sulfides especially in zones that have been encapsulated tightly within quartz veins. The sulfide-stable zone comprises pre-oxidation mineral assemblages or minerals that were not affected by oxidation. The well-developed copper oxide zone in Boyongan appears to have developed through in-situ oxidation of pre-existing hypogene sulfides similar to systems such as El Abra and Mantos Blancos in northern Chile (Chavez, 2000). Deep oxidation was developed along zones of intense fracturing, resulting in significant variations in thickness and intensity of the oxide zone. Minor exotic copper mineralisation occurs on the fringe of the high-grade copper-gold zone, suggesting lateral transport of copper, mostly from the eastern zone (Fig. 7.1).

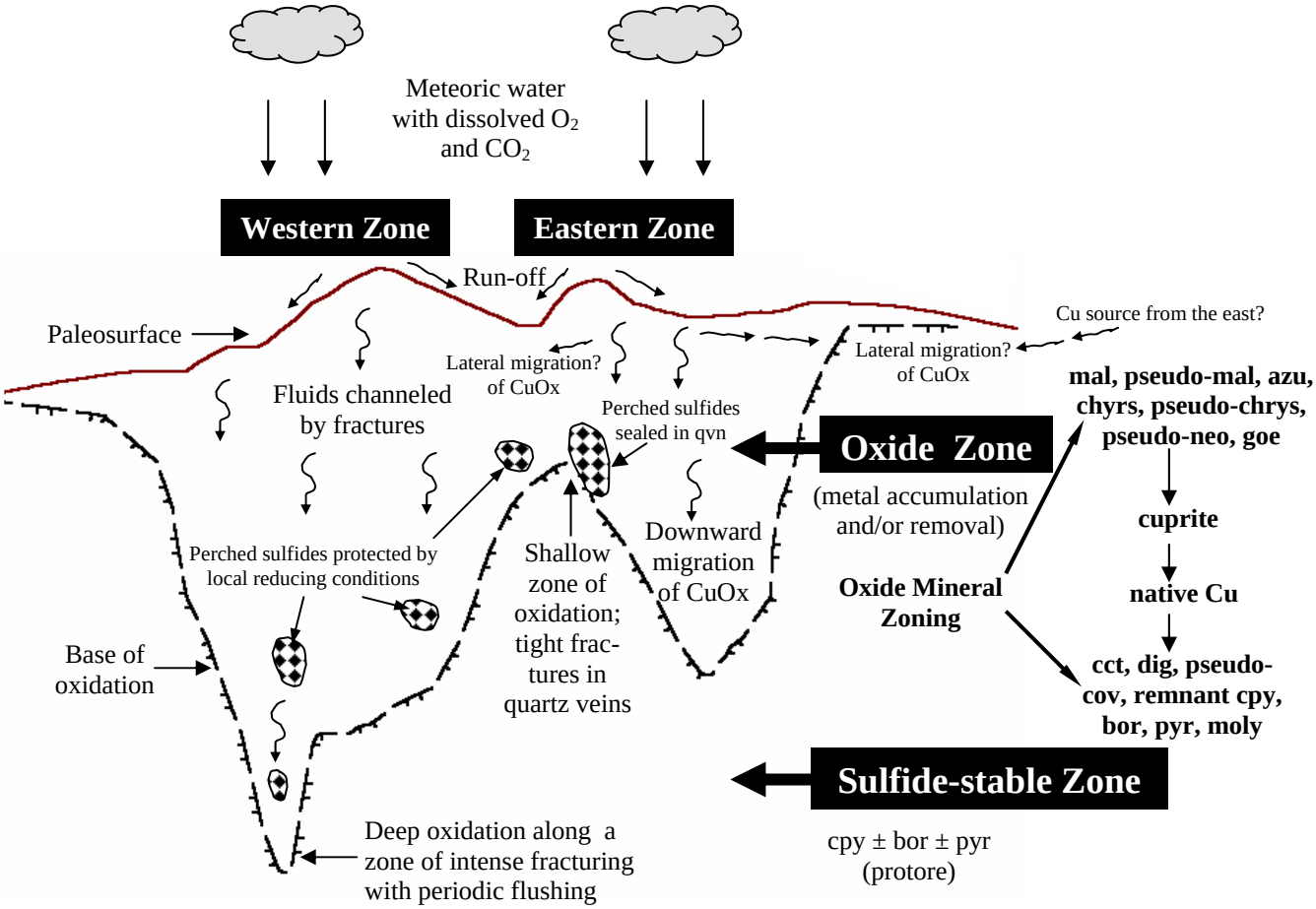

Fig. 7.1 Schematic diagram showing the weathering environment at Boyongan prior to the deposition of post-mineral sediments and volcanics. Curved arrows are movement of groundwater fluids within fractures. Oxide and sulfide zones with mineral assemblages characteristic of both zones are displayed on the right of the diagram (based on Chavez, 2000). CuOx = copper oxide; mal- = malachite; azu = azurite; chrys = chrysocolla; neo = neotocite; goe = goethite; cct = chalcocite; dig = digenite; cov = covellite; cpy = chalcopyrite; bornite = bornite; pyr = pyrite; moly = molybdenite

A genetic model for Boyongan is proposed here based on Anderson's (1982) genetic model for supergene mineralisation. An initial first cycle of oxidation occurred without leaching and enrichment (Fig. 7.2B). This continued until most of the primary sulfides were completely oxidised above the water table. The second cycle (subsequent oxidation; Fig. 7.2C & D) was then caused by progressive lowering of groundwater table, exposing additional sulfides to the oxidising environment. The second cycle stopped when complete oxidation of sulfides had occurred above the new groundwater table. The presence of pitch limonite at Boyongan suggests incomplete leaching of copper during supergene oxidation

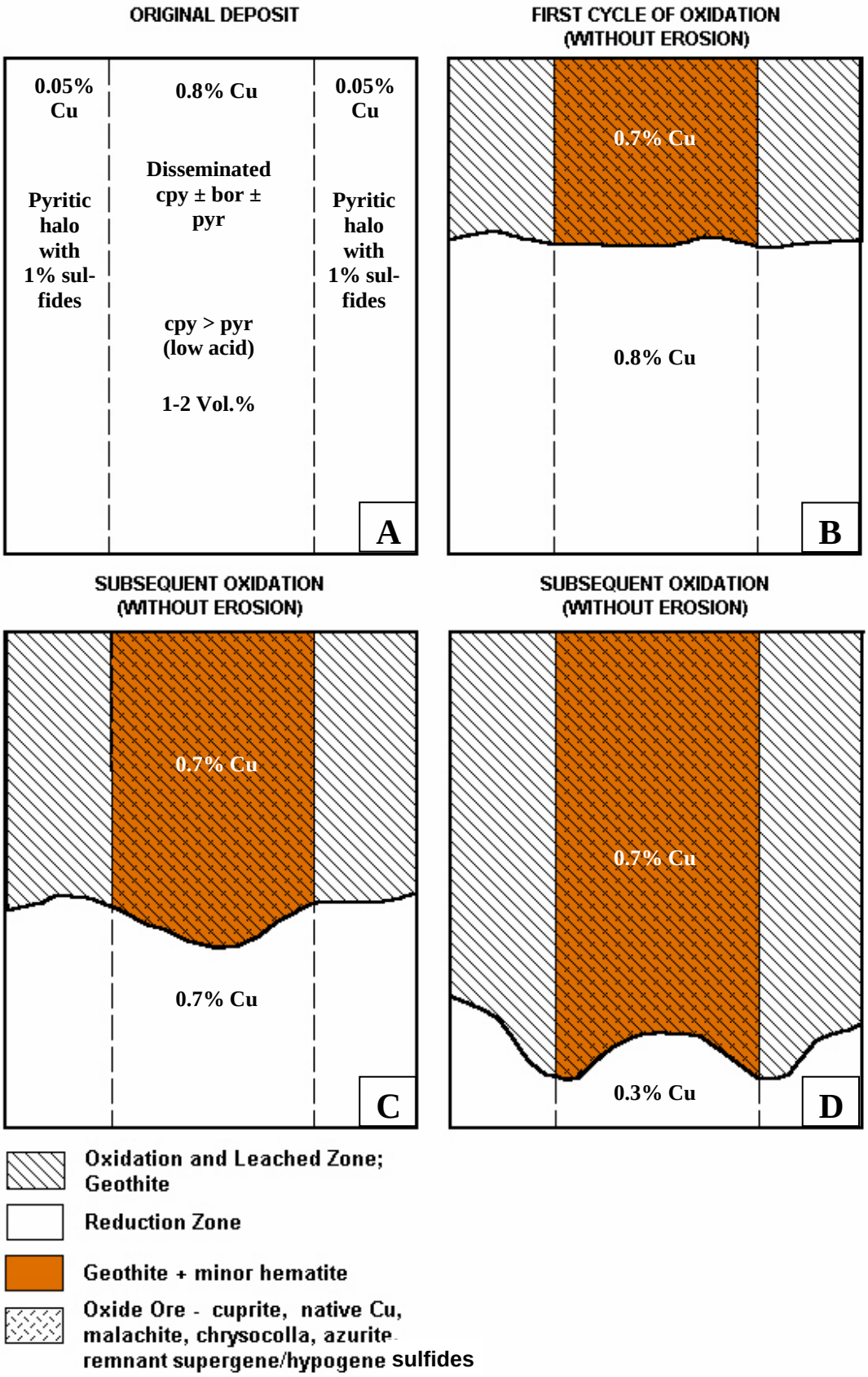

Fig. 7.2 Idealised cross-sections showing oxidation and leaching of Boyongan porphyry copper deposit, assumed here to contain an average hypogene grade of of 0.8% Cu and 1-2 volume percent total sulfide (modified from Anderson, 1982). The decrease in grade (C & D) may suggest copper enrichment, however no significant copper enrichment was observed. The downward decrease of copper grades may be explained by an increase in temperature (Sillitoe, 2000b). cpy = chalcopyrite; bor = bornite; pyr = pyrite.

and weathering (Fig. 4.13C; Einaudi, 1995), as does the presence of remnant hypogene sulfides in the oxide zone.

The supergene copper-sulfide, oxide mineralisation as well as the clay mineralogy in Boyongan provides insights into the pH of the groundwaters (Anderson, 1982; Chavez, 2000; Wilson, 2003). Initial pH conditions have been low enough to form kaolinite (pH<~4). However, as the acids were consumed by reactive diorite hostrocks, pH increased and the mobility of metals was significantly reduced. Goethite is the dominant limonite species, suggesting a near-neutral pH environment (Anderson, 1982; Chavez, 1999). Supergene mineralisation at Boyongan is therefore concluded to have generally formed in-situ. This conclusion is supported by the presence of fine-cellular boxwork textures in limonite that are <1.5mm in size (Fig. 4.13A; Blanchard, 1968).

The distribution of goethite and minor hematite at Boyongan provides insights into the hypogene sulfide distribution of the system prior to oxidation (Chavez, 2000; Wilson, 2003). Goethite is most abundant in the uppermost portions of the porphyry (Fig. 4.18B & 4.20B), and this part of the system is inferred to have been the most sulfide-enriched prior to oxidation.

Copper leaching in Boyongan appears to have been very inefficient, as the residual copper content in the goethite capping (up to ~50,000 ppm Cu) is very high compared to leached caps in South America, where a large percentage of copper has been leached out (e.g. <100ppm Cu at La Escondida, Chile; 300-700ppm Cu at Cuajone, Peru; Chavez, 2000). This is consistent with the preservation of remnant sulfides in the goethite cap at Boyongan. Leaching may have been more efficient in the pyrite halo or localised phyllic zones at

Boyongan where more abundant pyrite would have potentially provided a greater volume of sulphuric acid.

7.2 SUMMARY

Boyongan is a porphyry Cu-Au deposit that formed during the late Pliocene. It was uplifted, eroded, and then buried beneath lacustrine sediments and lava flows in the Pleistocene (Fig. 2.3 & 2.4). Hypogene porphyry-style alteration and mineralisation is hosted in the Boyongan Intrusive Complex which consists of multiphase diorite intrusions and breccias. Hypogene mineralisation is centered on two early mineral coarse-grained diorite porphyries (Fig. 3.1).

Hypogene K-feldspar-biotite-magnetite (potassic) alteration is associated with an intensely developed quartz vein stockwork. This alteration assemblage has been overprinted by sericite-chlorite-smectite (intermediate argillic) alteration. Quartz-sericite (phyllic) alteration occur as alteration selvedges to sulphide-rich veins. Albite-magnetite-actinolite (calc-sodic) alteration occurs at a depth of 600m below the Pleistocene paleosurface (Fig. 3.2). Irregular and small lenses of chlorite+epidote+calcite+magnetite± garnet skarns occur in the breccia complex and surrounding wallrocks (Fig. 2.9D).

Hypogene sulfides (chalcopyrite, pyrite, bornite and minor molybdenite) occur as fracture-fill, disseminations within the quartz vein stockwork, sulfide-rich D veins, and locally as replacements in altered wallrocks (Fig. 3.4). Hypogene gold has been observed in bornite and as free grains within quartz veins (Fig. 4.5C & D).

Post-hypogene mineral events at Boyongan include rapid uplift and exposure of the mineralised intrusions, which promoted extensive weathering and oxidation. These have produced the unique supergene profile at Boyongan, which is one of the deepest in the world (up to 650m thick).

Deep oxidation at Boyongan has developed a complex copper supergene mineralogy consisting of chalcocite, digenite, pseudo-covellite, pitch limonite/cuprous goethite, native copper, cuprite, malachite, pseudo-malachite, azurite, chrysocolla. pseudo-chrysocolla and pseudo-neotocite (Chapter 4). Supergene copper mineralisation generally occurs as fracture-fillings and disseminations. It is estimated that up to 80% of the mineralisation at Boyongan is supergene, whereas only 20% of relict hypogene mineralisation is preserved. Most of the supergene mineral assemblages at Boyongan appear to have formed in-situ. Fine supergene gold (<100μm) has been observed in goethite, chalcocite, chrysocolla, and malachite during logging and ore-microscopy (Fig. 4.5E & F).

The most common variety of limonite at Boyongan is goethite. Fine cellular boxwork texture in goethite has been observed (Fig. 4.13A) suggesting in-situ sulfide oxidation (Blanchard, 1968). The shallow depth of the base of oxidation in the eastern zone (200-400m) is mainly due to intense quartz veining (up to 50%) in this region forming a comparatively impermeable rockmass. Fractures in this area are very tight, and it appears that oxidising fluids were not able to permeate to great depths. In contrast, sulfide oxidation in the western zone extended to depths of 650m in rocks that were less intensely quartz veined that in the eastern zone.

The initial stages of supergene mineralisation involved the replacement of hypogene sulfides such as chalcopyrite and bornite by chalcocite, digenite, and pseudo-covellite (Fig.

4.4). In some places, chalcocite has replaced pyrite (Fig. 4.15). Goethite is generally derived from pyrite, chalcopyrite, bornite, and chalcocite (Fig. 4.13 & 4.14). This is inferred to be as a consequence of decreasing acidity, when weakly acidic ground waters mixed with neutral groundwater (Einaudi, 1995) and released Cu^{2+} in solution.

Cuprous ion (Cu^{2+}) that was released into solution could have precipitated in native metal form (native Cu). Native copper marks the depth of the paleowater table (Anderson, 1982). Native copper has replaced and overgrown chalcocite (Fig. 4.7B). Native copper later oxidised to form cuprite, and also formed acicular and euhedral crystals of chalcotricite (Fig. 4.6C). Some cuprite may have precipitated directly from Cu^{2+} in solution, and also in places where chalcocite reacted with oxygenated groundwaters.

Late stage supergene copper mineralisation was dominated by copper carbonates and phosphates. Malachite replaced chalcocite, and may have also precipitated directly from solution (Fig. 4.2C). Pseudo-malachite then partially replaced malachite (Fig. 4.9C). Both malachite and pseudo-malachite have been overgrown and cut by azurite (Fig. 4.9D), followed by chrysocolla and/or pseudo-chrysocolla (Fig. 4.10D). Azurite has also overgrown and replaced cuprite (Fig. 4.9E) and pseudo-chrysocolla (Fig. 4.11C). Pseudo-neotocite has replaced malachite and azurite and appears to have been the last copper-bearing mineral precipitated at Boyongan (Fig. 4.10C).

Supergene clays identified by at Boyongan PIMA are kaolinite, halloysite, illite and montmorillonite (Fig. 4.24). Kaolinite, halloysite and montmorillonite are weathering products and are interpreted to have been formed through hydrolysis, where hydrogen ions (H^+) were consumed by the host rock. Some illite is inferred to be supergene, specifically

where found within fractures together with limonite, whereas other illite are interpreted to be hypogene in origin if found in relatively less oxidised rocks.

Copper generally has a more dispersed or erratic distribution compared to gold (Fig. 5.1, 5.2 & 5.3). Gold is restricted spatially to the early mineral intrusions. Copper grades in the cuprite-dominated zone in the west generally decrease with depth toward zones of patchy native copper (Fig. 5.4 & 5.5). The copper carbonate-dominated blanket above the cuprite zone contains both high grade copper and gold (>1% & >2 g/t, respectively; Fig. 5.4 & 5.5). Chalcocite zones that have partially replaced hypogene copper sulfides have higher grades compared to zones of chalcocite replacing pyrite (Fig. 5.4 & 5.5). Chrysocolla is confined to zones that contain high copper and gold grades (>0.5% & >1 g/t, respectively; Fig. 5.4 & 5.5).

Both copper and gold grades decrease away from the early mineral diorite intrusions (Fig. Fig. 5.1, 5.2 & 5.3) and also with increasing depth. Copper zones are irregularly shaped and have a subtle NE-trend (Fig. 5.3C) while gold shows two elongated and regular vertical zones (Fig. 5.1D). Supergene copper is partly remobilised from a few meters during supergene mineralisation. Copper-gold ratios greater than 2.0 may infer exotic copper zones (Fig. 5.7).

The $\delta^{13}C$ values of malachite may reflect vegetation respired CO_2 (Melchiorre, 1999) suggesting that malachite may have formed in a subareal setting when Boyongan was uplifted and exposed. Measured $\delta^{18}C$ values of azurite could be derived from soil CO_2, sea-water carbonates, and/or CO_2 liberated from carbonates dissolved as the water table rose during burial (Melchiorre, 2000). This suggest that azurite may have been formed during the final stages of uplift as well as during subsidence. Alternatively, azurite may have been

produced by supergene-related bacteria above the water table (Melchiorre, 2003).

Low temperatures of formation have been calculated for malachite and azurite (average of 17.48˚C and 17.57˚C, respectively). These low temperatures are consistent with Boyongan being a low-sulfide porphyry system. Higher pyrite contents would probably have led to greater degrees of sulfide oxidation as well as higher groundwater temperatures (e.g. Broken Hill; Melchiorre, 1999).

A genetic model for Boyongan is hereby proposed. An initial first cycle of oxidation occurred without leaching and enrichment (Anderson, 1982; Fig. 7.2B). This continued until most of the primary sulfides were completely oxidised above the water table. The second cycle (subsequent oxidation; Fig. 7.2C & D) was then caused by progressive lowering of groundwater table, exposing additional sulfides to the oxidising environment. The second cycle stopped when complete oxidation of sulfides had occurred above the new groundwater table. Initial pH conditions have been low enough to form kaolinite (pH<~4). However, as the acids were consumed by reactive diorite hostrocks, pH increased (near-neutral) and the mobility of metals was significantly reduced (Anderson, 1982; Chavez, 2000; Wilson, 2003).

The well-developed copper oxide zone in Boyongan developed through in-situ oxidation of pre-existing hypogene sulfides similar to systems such as El Abra and Mantos Blancos in northern Chile (Chavez, 2000). Deep oxidation was developed along zones of intense fracturing, resulting in significant variations in thickness and intensity of the oxide zone.

Poorly consolidated sediments and andesite lavas (Tugunan Formation & Maniayao Andesite) completely conceals the Boyongan Intrusive Complex and surrounding wallrocks,

and the associated hypogene and supergene ores. It appears likely that Boyongan subsided in a Pleistocene pull-apart basin, and was buried by lake sediments. During this time, andesitic volcanism resulted an eruption of the Maniayao and Paco andesite lavas, further concealing the Boyongan porphyry system.

7.3 IMPLICATIONS FOR EXPLORATION

Exploring for blind deposits like Boyongan is a very challenging task. The only surface indications of mineralisation discussed at Boyongan were mineralised porphyry float samples along creeks north and east of the deposit (Waters, 2002), a molybdenum stream sediment anomaly along Paragayu creek, elevated Au-Ag-Cu-Mo in soil on the eastern slope of Boyongan which is sourced from windows of Mabuhay and Tugunan sediments within the Maniayao Andesites (Fig. 2.3A) , and a “false” I.P. anomaly that is being masked by carbonaceous Tugunan sediments (Waters, 2002). Molybdenite is a very important pathfinder for copper and/or gold mineralisation because it is not readily mobilised during supergene weathering. It remains as molybdenite and/or ferrimolybdenite and is tied with goethite (Wilson, 1965). These geological, geochemical and geophysical indicators gave Anglo American sufficient encouragement to drill Boyongan.

Drilling at Boyongan initially revealed the presence of limonite and copper oxides. Based on the results of drilling at Boyongan, copper oxide and metal zoning patterns could be used to target the centre of hypogene mineralisation, allowing targeting of underlying sulfide mineralisation. At Boyongan, deep drilling intersected uneconomic sulfide mineralisation, with the bulk of mineralisation found to be located within the oxide profile. It is possible that other systems with a similar geological history could have a more substantial hypogene ore zone.

Successful application of interpretation of leached caps and/or copper oxide zones guides drilling and finds porphyry copper orebodies (Wilson, 2003). In the case of Boyongan being a blind deposit, the leached cap interpretation should be integrated with structural interpretations, alteration mapping, rock geochemistry, and plenty of geological imagination (Wilson, 1965) in order to make exploration even more successful.

Careful logging of supergene mineralisation and limonite in addition to any remnant sulfides can aid in the reconstruction or pre-oxidation sulfide distribution of the system. Within the oxide zone at Boyongan, remnant chalcopyrite, pyrite, minor molybdenite and bornite were observed. Boyongan is dominated by goethite and minor hematite suggesting that it is a pyrite-poor and chalcopyrite-dominated system. This study has shown that contour maps or sections of limonite content aid in the visualisation of sulfide distribution, and similar approaches should be taken for other supergene mineralisation in the Philippines. Moreover, mapping and/or logging the distribution of copper oxide and copper sulfide minerals, and determining the paleo-geomorphology has provided useful information in assessing the geologic history at Boyongan. This type of information helps to assess the economic potential of an exploration target, and allows for similar targets to be identified in a given province.

During the fieldwork, acid testing and copper plating on stainless steel has been very important for identifying copper minerals (e.g. cuprite, malachite, chrysocolla, pitch limonite, etc.). This should be a routine logging practice in supergene mineralisation. The electron probe microanalyser (EPMA) has proven to be a very useful tool in the laboratory for identifying supergene copper minerals, and their complex chemical compositions.

The analysis of the C-O isotopic compositions of supergene carbonates has provided insights in the conditions of supergene ore formation and fluid sources (e.g. Melchoirre, 1999, 2000, 2001, 2003). Oxygen isotope geothermometry may have potential for predicting the abundance of pre-oxidised sulfides (i.e. sulfide-rich or low-sulfide system), and has some potential for helping to determine whether supergene mineralisation was in-situ or exotic.

Similar types of deposits to Boyongan may exist elsewhere in the Surigao district. The Bayugo deposit, which is located to the northwest of Boyongan, was discovered in part by the recognition of exotic chalcocite that has replaced pyrite in TSD29. Minor chalcocite coatings were likewise observed in TSD3 (immediately north of Boyongan porphyry; Fig. 4.19B) and may have come from Bayugo rather than Boyongan. Boyongan is generally a low pyrite system and sulfuric acid generated is not enough to produce a chalcocite enrichment blanket. East or northeast of drillhole TSD2 (east of Boyongan; Fig. 4.17B), there is some potential of another porphyry system based on the recognition of minor exotic chalcocite (replacing pyrite) intersected in TSD2.

The supergene profile at Boyongan is a mixture of green copper oxides, cuprite and native which makes the deposit metallurgically complex and difficult to process. Exploration for similar systems should attempt to locate more pyrite-enriched systems which have greater potential for developing thick chalcocite enrichment blankets.

REFERENCES

Anderson, J.A., 1982, Characteristics of Leached Capping and Techniques of Appraisal, in Titley S.R., ed., Advances in Geology of the Porphyry Copper Deposits, Southwestern North America: Tucson, Arizona, The University of Arizona Press, p. 275-296.

Armstrong, Richard, 2001, C-14 dating. E-mail to Paddy Waters dated June 14, 2001 from the Australian National University Research School of Earth Sciences, Canberra, Australia. 1 p. (unpublished report)

Australian Photogeological Consultants Pty Ltd, 1999, Lithostructural Interpretation of the Surigao Area, NE Mindanao, Philippines, for Minorco Exploration (Philippines), Inc., Job No. 746M, p. 1-12. (unpublished report)

Blanchard, R., 1968, Interpretation of Leached Outcrops, Nevada Bureau of Mines Bulletin 66, 196 p.

Bogie, I., **2000**, Petrology report on 24 samples from Buyongan and Bagacay, Surigao, Report for Anglo American Exploration Philippines, Inc. Sinclair Knight Merz Report No. P1260009 M1108 June 2000, Auckland, New Zealand., 40 p. (unpublished report)

Boyle, D.R., **1996,** Supergene base metals and precious metals: in Geology of Canadian Mineral Deposit Types, (ed.) O.R. Eckstrand, W.D. Sinclair, and R.I. Thorpe; Geological Survey of Canada, Geology of Canada, no. 8, p. 92-108 (also Geological Society of America, The Geology of North America, v. P-1).

Bureau of Mines and Geosciences, 1981, Geology and Mineral Resources of the Philippines, vol.1, 406 p.

Camacho, A, 2001, Ar-Ar age determinations of hornblende samples from Mindanao, Report R01-190 for Anglo American Exploration (Philippines), Inc., PRISE, Research School of Earth Sciences, The Australian National University, Canberra, Australia, 50 p. (unpublished report)

Campbell, D., Waters, P., Estaris, M., Brand, N., Gushee, G., Corpuz, M., 2002, Boyongan Copper-Gold Project: Mineral Resource Evaluation and Exploration Potential, Anglo American Exploration Philippines, Inc. Internal Report, 142 p. (unpublished report)

Camus, F., 2002, Andean Porphyry Systems, in Cooke, D.R., Pongratz, J., eds., Giant Ore Deposits: Characteristics, Genesis and Exploration, Centre for Ore Deposit Research, Special Publication No. 4, p. 5-21.

Carman, G.D., 2003, Geology, Mineralization, and Hydrothermal Evolution of the Ladolam Gold Deposit, Lihir Island, Papua New Guinea, in Simmons, S.F. and Graham, I., eds, Volcanic, Geothermal, and Ore-Forming Fluids: Rulers and Witnesses of Processes within the Earth: Society of Economic Geologist, Special Publication 10, p. 247-284

Chavez, W.X., 1998, Weathering-Related Metals Mobility in Copper Systems: Examples of Copper-Grade Enhancement as Oxide and Sulfide Assemblages from Chile, Minerals & Environmental Engineering Department, New Mexico School of Mines, Abstracts from http://www.dregs.org/abs1998.html

Chavez, W.X., 1999, Preliminary Petrographic Documentation of Iron and Copper Oxide Assemblages with reference to weathering-derived metals mobility and hypogene and supergene mineral-lithology associations: Minerals and Environmental Engineering Department New Mexico School of Mines, Socorro, New Mexico, USA 87801, 17 p. (unpublished report)

Chavez, W.X., 2000, Supergene Oxidation of Copper Deposits: Zoning and Distribution of Copper Oxide Minerals, SEG Newsletter, No. 41, p. 10-21.

Cooke, D.R., Heithersay, P.S., Wolfe, R., and Losada-Calderon, A., 1998, Australian and Western Porphyry Cu-Au deposits, Australian Geological Survey Organisation Journal of Geology and Geophysics, 17 (4), p. 97-104.

Corbett, G.J, and Leach, T.M., 1998, Southwest Pacific rim gold-copper systems: Structure, alteration and mineralization: SEG Special Publication No. 6, 236 p.

Davidson, G., 2003, Ore Deposit Geochemistry, Hydrology, and Geochronology Vol. 1. Course Notes, University of Tasmania, Hobart, Australia. 41 p. (unpublished report)

Downing, B.W., 2003, Acid Rock Generation/Drainage in Mineral Deposit Throughout Time (Kemess Case Study), 9 p.

Dunlap, J., 2002, Ar-Ar Age determination for Boyongan Minerals: Amphiboles 800631 and 800633, Biotites 800630 and 800632, Report AP1/7-02 for Anglo American Exploration (Philippines), Inc., PRISE, Research School of Earth Sciences, The Australian National University, Canberra, Australia, 5 p. (unpublished report)

Einaudi, M.T., 1995, Topics in porphyry copper-gold and related deposits: Workshops and Field visits conducted for Western Pacific Exploration Group, Newmont, 67 p. (unpublished report)

Gilmour, P., 1994, A field Guide to Leached Capping Interpretation, in Bolm, J.G., and Pierce, F.W., Porphyry copper deposits of the American Cordillera: Tucson, Arizona Geolgical Society Digest 20, p. 69-179.

Gustafson, L.B., and Hunt, J.P., 1975, The porphyry copper deposit at El Salvador, Chile: ECONOMIC GEOLOGY, v.70, p.857-912.

Hedenquist, J.W., and Richards, J.P., 1998, The influence of geochemical techniques in the development of genetic models for porphyry copper deposits: Reviews in ECONOMIC GEOLOGY, v.10, p. 235-256.

Herrmann, W., Blake, M., Doyle, M., Huston, D. L., Kamprad, J., Merry, N. , and Pontual, S., 2001, Short Wavelength Infrared (SWIR) Spectral Analysis of Hydrothermal Alteration Zones Associated with Base Metal Sulfide Deposits at Rosebery and Western Tharsis, Tasmania, and Highway-Reward, Queensland, ECONOMIC GEOLOGY vol. 96, no. 5, pp. 939-956

Ixer, R.A., 1990, Altas of opaque and ore minerals and their associations, Society for Mining, Metallurgy and Exploration: US, 208 p.

Lowell , J.D., and Guilbert, J.M., 1970, Lateral and vertical alteration-mineralisation zoning in porphyry ore deposits: ECONOMIC GEOLOGY, v. 65, p. 373-408.

Markl, G., and Bucher, K., 1997, Reduction of Cu^{2+} in mine waters by hydrolysis of ferrous sheet silicates, European Journal of Mineralogy, v. 9, p. 1227-1235.

McPhie, J., Doyle, M., Allen, R., 1993, Volcanic Textures: A guide to the interpretation of textures in volcanic rocks: Centre for Ore Deposit Research, University of Tasmania, 196 p.

Melchiorre, E.B., Criss, R.E., and Rose, T.P., 1999, Oxygen and carbon isotope study of natural and synthetic malachite: ECONOMIC GEOLOGY, v. 94, p. 245-259.

Melchiorre, E.B., Criss, R.E., and Rose, T.P., 2000, Oxygen and carbon isotope study of natural and synthetic azurite: ECONOMIC GEOLOGY, v. 95, p. 621-628.

Melchiorre, E.B., Williams, P.A., 2001, Stable isotope characterization of the thermal profile and subsurface biological activity during oxidation of the Great Australia Deposit, Cloncurry, Queensland, Australia: ECONOMIC GEOLOGY, v. 96, p. 1685-1693.

Melchiorre, E.B., and Enders, M.S., 2003, Stable isotope geochemistry of copper carbonates at the northwest extension deposit, Morenci District, Arizona: Implications for conditions of supergene oxidation and related mineralisation: ECONOMIC GEOLOGY, v. 98, p. 607-621.

Merry, N., Pontual, S., and Gamson, P., 1999, The Spectral Geologist User Manual v2.0. AusSpec International Pty Ltd., 146 p.

Meyer, C., and Hemley, J, 1967, Wallrock alteration, in Barnes, H.L., ed., Geochemistry

of Hydrothermal Ore Deposits, p. 166-235

Moore, R.L., and Masterman, G.J., 2002, The corporate discovery history and geology of the Collahuasi district porphyry copper deposits, Chile, in Cooke, D.R., and Pongratz, J. eds.,Giant Ore Deposits: Characteristics, genesis and exploration, Centre for Ore Deposit Research, Special Publication No. 4, Hobart, Australia, p. 23-50

Municipality of Placer, province of Surigao del Norte, Philippines, Climate: http://202.90.139.50/placer, climate

Nelson, S., 2001, Clay Minerals, Geology 211 (Mineralogy), Tulane University, 4 p. (unpublished report)

Ney, C.S., Cathro, R.J., Panteleyev, A., and Rotherham, D.C., 1976, Supergene Copper Mineralisation, CIM special volume 15, pp. 72-78.

Peterson, N.P., 1947, Phosphate minerals in the castle dome copper deposit, Arizona, American Mineralogist, v.63, p. 574-582

Philex Gold Inc., 2004, Second Quarter Report for 2004, Toronto, Canada, 17 p. (unpublished report)

Pontual S., and Merry N., 1995, PIMA WORKSHOP 2: Practical Implementation of the PIMA in Exploration and Mining, AusSpec International Pty Ltd., 38 p. with accompanying Spectral Library, 40 p.

Rae, A., 2002, Porphyry and Geothermal systems of Southern Negros, Philippines, Unpublished Ph.D. thesis, University of Tasmania, Hobart, Australia, 243 p.

Reynolds, T.J., and Beane, R.E., 1985, Evolution of hydrothermal fluid characteristics at the Santa Rita, New Mexico, Porphyry Copper Deposit, ECONOMIC GEOLOGY, 80: 1328-1347.

Santos-Ynigo, L., 1944, Geology of the Surigao Gold District. 91 p. (unpublished report)

Sillitoe, R. H. & Gappe, I.M., 1984, Philippine Porphyry Copper Deposits: Geologic setting and characteristics, CCOP/TP14, RAS/81/120, UNDP Technical support for regional offshore prospecting in East Asia: United Nations Development Program, 89 p.

Sillitoe, R.H., 2000, Gold-rich porphyry deposits: Descriptive and genetic models and their role in exploration and discovery: Reviews in ECONOMIC GEOLOGY, v. 13, pp. 315-345.

Sillitoe, R. H. 2001, Preliminary geological model of the Boyongan porphyry copper-gold prospect, Mindanao, Philippines. Unpublished report for Anglo American Exploration (Philippines), Inc., August 2001. Surigao City, Philippines. 10 p.

Sillitoe, R. H. 2002a, Additional modelling of the Boyongan porphyry copper-gold prospect, Mindanao, Philippines. Unpublished report for Anglo American Exploration (Philippines), Inc., March 2002. Surigao City, Philippines. 13 p.

Sillitoe, R. H. 2002b, Further commnents on the the Boyongan porphyry copper-gold deposit and Nearby Exploration Potential, Mindanao, Philippines. Unpublished report for Anglo American Exploration (Philippines), Inc., December 2002. Surigao City, Philippines. 9 p.

Sinclair Knight Merz (SKM), 2000a, Petrology report on 24 samples from Boyongan and Bagacay, Surigao, RP, Unpublished final report M1108 for Anglo American Exploration (Philippines), Inc., June 2000, Auckland, New Zealand.

Sinclair Knight Merz (SKM), 2000b, Petrology of 40 Drillcore samples from Boyongan Prospect, Surigao, Philippines, Unpublished final report for Anglo American Exploration (Philippines), Inc., December 2000, Auckland, New Zealand.

Sinclair Knight Merz (SKM), 2001, Petrology of 30 samples from Boyongan, Surigao, Philippines. Unpublished final report no. M1125 for Anglo American Exploration (Philippines), Inc., December 2001, Auckland, New Zealand.

Sinclair Knight Merz (SKM), 2003a, Petrology report of 26 samples from Boyongan, Surigao. Unpublished final report no. P1134 for Anglo American Exploration (Philippines), Inc., January 2003, Auckland, New Zealand.

Sinclair Knight Merz (SKM), 2003b, Petrology report of 6 samples from Boyongan, Surigao. Unpublished final report no. P1135 for Anglo American Exploration (Philippines), Inc., March 2003, Auckland, New Zealand.

Spectral International, Inc, Alteration Systems, from http://pimausa.com/alt.html

Spry, P.G., and Gedlinske, B.L., 1987, Table for the Determination of Common Opaque Minerals, Department of Earth Sciences, 253 Science Hall I, Iowa State University, Ames, Iowa 50011. The Economic Geology Publishing Company, 52 p.

Surigao Page, source: Climate: http://www.xs4all.nl/~jwjgendt/surigao.html.

Thompson, A.J.B., 2002, Mapping alteration mineralogy with reflectance spectroscopy; Application to northern Sweden, PetraScience Consultants, Inc, 15 p.

Titley, S.R., Marozas, D.C., 1995, Processes and Products of Supergene Copper Enrichment, in Pierce, W., and Bolm, J.G., eds., Porphyry Copper Deposits of the American Cordillera: Arizona Geological Society Digest 20, p. 156-168.

United Nations, 1987, Geology and Gold Mineralisation of Surigao Del Norte, Technical Report No. 4, DP/UN/PHI-85-001/4, Manila, Philippines, 1987, 58p.

United States Geological Survey: Coastal and Marine Geology Division, X-Ray Diffraction Primer, USGS Open-File Report 01-041, http://pubs.usgs.gov/of/of01-041/htmldocs/xrpd.htm.

Waters, P.J., 2001, Geology And Mineralisation Of The Surigao Gold District, Unpublished report of Anglo American Exploration (Philippines), Inc., 12 p.

Waters, P.J., Comia, G.M., Estaris, M.S., Gonzales, R.I., Estacio, R.C., Briones, J.R., Cabrera, A.C., Ignacio, A.M., Briola, O.A., 2001, The Geology of the Boyongan Porphyry Copper-Gold Deposit. A report prepared for the 14th Annual Geological Convention of the Geological Society of the Philippines (GEOCON 2001), 5-7 December, 2001, Mapua Institute of Technology, Manila, Philippines, p. 1-17.

Waters, P.J., 2002, The Boyongan Cu-Au Porphyry deposit, Surigao Gold District, NE Mindanao Discovery, Journal on Environment, Energy, and Minerals, Vol v, No.1, Manila, Philippines, p. 36-39.

Wilson, A.J., 2003, Notes on Leached Cappings and Supergene Enrichment in Porphyry Copper Deposits, Center for Ore Deposit Research, University of Tasmania, 10 p. (unpublished report)

Wilson, J.C., 1965, Use of alteration, capping appraisal, and rock geochemistry in exploration: Kennecott Copper Corporation, Exploration Services, Geologic Research Division, Salt Lake City, Utah, 50 p. (unpublished report)

World Mining News - Item [59909]: News Release, 2004, Philex Gold Reports Boyongan Inferred Mineral Resource 14 June 2004, http://www.mbendi.co.za/a_sndmsg/news_view.asp?I=9909&PG=15

APPENDIX 1

PIMA ANALYSES

Appendix 1a
Introduction to Infrared Spectroscopy

Infrared spectrometry is a technique used to identify phyllosilicate, clay, carbonate, and selected sulphate minerals. This technique has been applied successfully to mineral exploration in many different environments using a field-portable instrument (Thompson, 2002). For the current study, a PIMA II (Portable Infrared Mineral Analyser) was used on site at Boyongan in order to identify the mineralogy of the fine-grained clay minerals. This instrument provided rapid information on alteration mineralogy and was the primary basis for clay alteration mapping (Pontual & Merry, 1995). No sample preparation was required. Each measurement takes 30-60 seconds, and the spectra can be viewed instantly on the computer screen.

PIMA analyses the spectra of rocks and minerals in the short wavelength infrared (SWIR), from 1300 to 2500nm. It measures the reflected radiation from the surface of hand samples (Pontual & Merry, 1995). A typical spectrum consists of several characteristic features including the hull (background), wavelength position, feature depth and width (Thompson, 2002). The reflectance hull or curvature observed in figure A1.A may be a result of out-of range absorptions such as ferrous iron (around 1000mn) or strong water & carbonate absorptions (around 2700mn). This tends to distort the spectral absorption features and make determinations of the wavelength difficult, particularly on the steepest parts of the reflectance spectrum. To enhance the spectral absorption, a hull quotient is used where the hull and the reflectance spectra are ratioed (Fig. A1.B & C). This lessens the distortion of the spectrum (Pontual & Merry, 1995).

Appendix 1a
Introduction to Infrared Spectroscopy

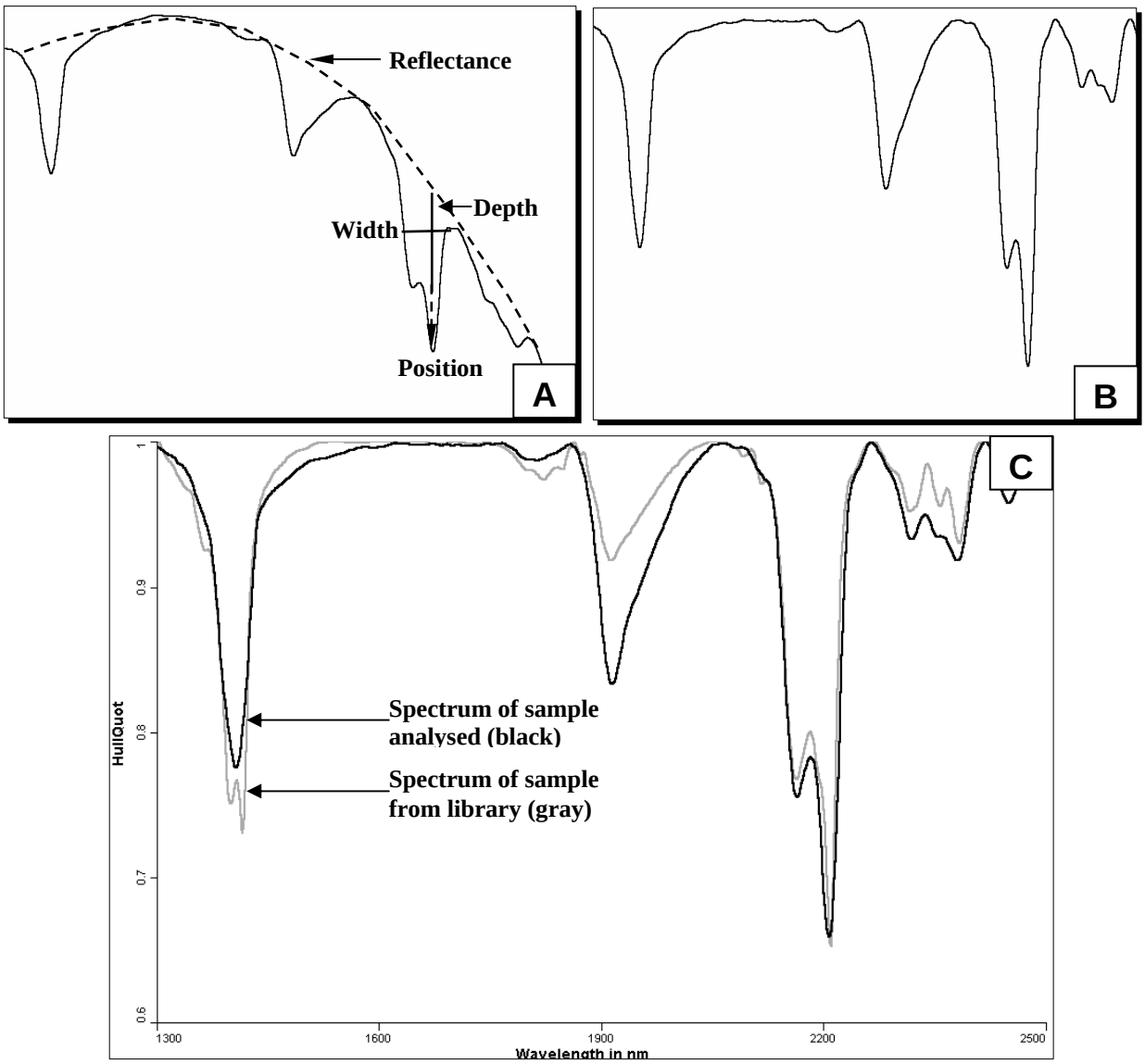

Fig. A1 a. Example of a reflectance spectra (of kaolinite) with its characteristic features; outline of reflectance hull is shown in curved dashed line (modified from Thompson, 2002) **b.** Kaolinite spectrum. Similar to Fig. A1.A but enhanced by Hull Quotient. Note depth of troughs are greatly improved and reflectance hull or curvature is removed. **C.** An example of a spectral match (for Kaolinite). Note depth of troughs has been enhanced and reflectance hull or curvature is removed.

Appendix 1a
Introduction to Infrared Spectroscopy

Mineral identification is based on feature positions, intensity and shape and absorption troughs and the overall shape of the entire spectrum (Thompson, 2002). Subtle spectral variations, such as wavelength shifts and variations in the shapes of the absorption features may be observed within the spectra from a mineral group. These may be attributed to variations in crystallinity, composition and mineral orientation (Pontual & Merry, 1995). Mixed spectrums are common suggesting the presence of two or more minerals.

Appendix 1b
PIMA Results

ID	SampNo	HoleID	From	To	TSA_Min1	TSA_Wt1	TSA_Min2	TSA_Wt2	TSA_Error	Comments
1	Tsd02_01	TSD02	68.000	68.000	Halloysite	1	NULL	NULL	167.663	
2	Tsd02_02	TSD02	84.300	84.300	Kaolinite	0.602	Halloysite	0.398	33.571	
3	Tsd02_03	TSD02	101.100	101.100	Kaolinite	0.672	Halloysite	0.328	43.119	
4	Tsd02_04	TSD02	107.800	107.800	Kaolinite	0.735	Halloysite	0.265	66.712	
5	Tsd02_05	TSD02	121.100	121.100	Halloysite	0.58	IntChlorite	0.420	192.939	
6	Tsd02_07	TSD02	140.000	140.000	Halloysite	0.722	Muscovite	0.278	51.973	
7	Tsd02_08	TSD02	160.800	160.800	Halloysite	1	NULL	NULL	186.085	
8	Tsd02_09	TSD02	167.300	167.300	IntChlorite	0.546	Kaolinite	0.454	191.505	
9	Tsd02_10	TSD02	181.400	181.400	Kaolinite	0.556	IntChlorite	0.444	205.535	
10	Tsd02_11	TSD02	200.200	200.200	IntChlorite	0.52	Kaolinite	0.480	228.703	
11	Tsd02_12	TSD02	219.600	219.600	Kaolinite	0.601	MgChlorite	0.399	249.35	
12	Tsd02_13	TSD02	240.600	240.600	Kaolinite	0.66	Phlogopite2	0.340	241.741	
13	Tsd11_01	TSD11	280.100	280.100	Kaolinite	1	NULL	NULL	23.996	white
14	Tsd11_02	TSD11	300.000	300.000	Kaolinite	1	NULL	NULL	51.772	White
15	Tsd11_03	TSD11	320.400	320.400	Kaolinite	1	NULL	NULL	45.653	white cly +-lim
16	Tsd11_04	TSD11	339.400	339.400	Kaolinite	0.54	IntChlorite	0.460	87.654	
17	Tsd11_05	TSD11	360.800	360.800	Kaolinite	1	NULL	NULL	99.45	white to brown
18	Tsd11_06	TSD11	381.200	381.200	Kaolinite	0.572	Muscovite	0.428	62.241	cly in frac + lim
19	Tsd11_07	TSD11	381.201	381.201	Kaolinite	0.702	Phengite	0.298	35.305	cly in frac + lim
20	Tsd11_08	TSD11	400.000	400.000	Kaolinite	1	NULL	NULL	73.818	cly in frac
21	Tsd11_09	TSD11	421.000	421.000	Kaolinite	0.667	Phlogopite1	0.333	221.927	slightly limonitic
22	Tsd11_10	TSD11	440.800	440.800	Kaolinite	0.805	Montmorilloni te	0.195	67.376	
23	Tsd11_11	TSD11	460.000	460.000	Kaolinite	1	NULL	NULL	63.171	cly in frac-lim
24	Tsd11_12	TSD11	480.300	480.300	Kaolinite	1	NULL	NULL	91.936	White
25	Tsd11_13	TSD11	501.800	501.800	Kaolinite	1	NULL	NULL	141.698	
26	Tsd11_14	TSD11	521.500	521.500	Kaolinite	1	NULL	NULL	130.147	cly in frac
27	Tsd11_15	TSD11	540.400	540.400	Kaolinite	1	NULL	NULL	86.064	limonitic cly in frac
28	Tsd11_16	TSD11	560.350	560.350	Kaolinite	1	NULL	NULL	174.839	
29	Tsd11_17	TSD11	581.450	581.450	Kaolinite	0.824	Epidote	0.176	182.747	
30	Tsd11_18	TSD11	600.750	600.750	Kaolinite	0.743	Phlogopite2	0.257	152.848	White
31	Tsd13_01	TSD13	89.700	89.700	Kaolinite	0.524	Halloysite	0.476	62.72	with mal
32	Tsd13_02	TSD13	100.250	100.250	Kaolinite	0.574	Halloysite	0.426	44.564	
33	Tsd13_03	TSD13	110.500	110.500	Halloysite	0.59	Kaolinite	0.410	73.013	lim w/ cly selvedge
34	Tsd13_04	TSD13	119.700	119.700	Kaolinite	0.637	Halloysite	0.363	74.571	
35	Tsd13_05	TSD13	139.900	139.900	Illite	1	NULL	NULL	97.823	
36	Tsd13_06	TSD13	145.550	145.550	Illite	0.546	Opal	0.454	154.593	gn cly adj to chrys
38	Tsd13_08	TSD13	150.650	150.650	Kaolinite	0.587	Montmorilloni te	0.413	71.182	cly selvedge
39	Tsd13_09	TSD13	150.650	150.650	Kaolinite	0.572	IntChlorite	0.428	139.659	gr
40	Tsd13_11	TSD13	156.500	156.500	Illite	0.638	Nontronite	0.362	51.16	cly selvedge on lim
41	Tsd13_13	TSD13	156.500	156.500	Kaolinite	0.677	Halloysite	0.323	121.829	adj to cly selvedge - DBR
42	Tsd13_14	TSD13	159.800	159.800	Kaolinite	0.766	Nontronite	0.234	234.335	cly on rock
44	Tsd13_16	TSD13	169.250	169.250	Illite	0.754	Magnesium_ Clays	0.246	179.598	lt gn cly
45	Tsd13_17	TSD13	169.250	169.250	Illite	1	NULL	NULL	126.486	lt gn cly
46	Tsd13_19	TSD13	179.600	179.600	Kaolinite	0.775	Halloysite	0.225	46.738	
47	Tsd13_20	TSD13	185.950	185.950	Kaolinite	0.709	Halloysite	0.291	37.858	cly in frac
48	Tsd13_21	TSD13	185.960	185.960	Illite	0.755	Phengite	0.245	36.432	lt gn selvdge on lim

Appendix 1b
PIMA Results

ID	SampNo	HoleID	From	To	TSA_Min1	TSA_Wt1	TSA_Min2	TSA_Wt2	TSA_Error	Comments
49	Tsd13_22	TSD13	185.970	185.970	Kaolinite	0.723	Halloysite	0.277	26.291	wh cly in frac
50	Tsd13_23	TSD13	185.980	185.980	Kaolinite	0.676	IntChlorite	0.324	129.806	cly in rock
52	Tsd13_25	TSD13	186.010	186.010	Kaolinite	1	NULL	NULL	186.083	cly in rock
53	Tsd13_26	TSD13	200.600	200.600	Kaolinite	0.663	Halloysite	0.337	49.321	cly in rock
54	Tsd13_27	TSD13	214.150	214.150	Illite	0.668	Phengite	0.332	24.332	
55	Tsd13_29	TSD13	215.800	215.800	Illite	0.756	Nontronite	0.244	119.818	lt gn cly
57	Tsd13_31	TSD13	221.000	221.000	Kaolinite	0.772	IntChlorite	0.228	100.532	cly in lim (frac)
58	Tsd13_32	TSD13	221.010	221.010	Kaolinite	0.685	Halloysite	0.315	79.809	cly in rock
59	Tsd13_33	TSD13	236.100	236.100	Kaolinite	1	NULL	NULL	96.05	gn cly in frac
60	Tsd13_34	TSD13	236.110	236.110	Kaolinite	0.689	Halloysite	0.311	57.816	lt gn cly in rx
61	Tsd13_35	TSD13	240.700	240.700	Kaolinite	0.695	Halloysite	0.305	112.074	cly in rock
62	Tsd13_36	TSD13	259.250	259.250	Kaolinite	0.666	Halloysite	0.334	91.729	cly in rock
63	Tsd13_37	TSD13	280.800	280.800	Illite	1	NULL	NULL	40.653	cly in qtz selvedge
64	Tsd13_38	TSD13	280.810	280.810	Illite	0.767	Magnesium_ Clays	0.233	162.168	cly + lim
65	Tsd13_39	TSD13	299.300	299.300	Illite	0.673	Montmorilloni te	0.327	87.693	lt gn cly
66	Tsd13_40	TSD13	321.000	321.000	Halloysite	0.626	Phlogopite2	0.374	119.381	cly in rock
67	Tsd13_42	TSD13	360.600	360.600	Kaolinite	1	NULL	NULL	147.473	cly in frac
68	Tsd13_43	TSD13	360.610	360.610	Kaolinite	0.651	Halloysite	0.349	105.549	cly in rock
69	Tsd13_44	TSD13	383.650	383.650	Kaolinite	0.592	Montmorilloni te	0.408	213.413	cly adj to lim
71	Tsd13_46	TSD13	401.051	401.051	Halloysite	0.554	Montmorilloni te	0.446	137.586	cly in rock
73	Tsd13_50	TSD13	458.350	458.350	Kaolinite	0.705	MgChlorite	0.295	109.695	cly in rock
74	Tsd13_52	TSD13	501.000	501.000	Actinolite	0.601	Halloysite	0.399	399	clay-lim in frac
76	TSD16_01	TSD16	210.750	210.750	Halloysite	1	NULL	NULL	213.288	
77	TSD16_02	TSD16	220.200	220.200	Kaolinite	0.501	Halloysite	0.499	115.319	
78	TSD16_03	TSD16	240.000	240.000	Kaolinite	0.732	MgChlorite	0.268	80.174	
79	TSD16_04	TSD16	240.000	240.000	Kaolinite	1	NULL	NULL	193.948	
80	TSD16_05	TSD16	260.000	260.000	Kaolinite	0.552	Halloysite	0.448	93.693	
81	TSD16_06	TSD16	280.000	280.000	Halloysite	1	NULL	NULL	125.069	
83	TSD16_10	TSD16	340.300	340.300	Phlogopite2	0.526	Illite	0.474	165.122	
84	TSD16_12	TSD16	380.350	380.350	Kaolinite	0.737	Halloysite	0.263	26.982	
85	TSD16_15	TSD16	435.200	435.200	Kaolinite	0.766	Ankerite	0.234	175.557	LDP
86	Tsd17_01	TSD17	220.800	220.800	Kaolinite	0.646	Halloysite	0.354	54.622	
87	Tsd17_02	TSD17	240.600	240.600	Kaolinite	0.834	Ankerite	0.166	66.224	
88	Tsd17_03	TSD17	258.300	258.300	Kaolinite	1	NULL	NULL	152.516	
89	Tsd17_05	TSD17	301.800	301.800	MgChlorite	0.528	Kaolinite	0.472	183.521	
90	Tsd17_06	TSD17	320.300	320.300	Kaolinite	1	NULL	NULL	154.909	
91	Tsd17_07	TSD17	341.750	341.750	Kaolinite	0.674	Phlogopite1	0.326	146.702	
93	Tsd17_11	TSD17	420.600	420.600	Kaolinite	0.627	Halloysite	0.373	81.554	
94	Tsd17_12	TSD17	440.150	440.150	Kaolinite	0.59	Halloysite	0.410	68.374	
95	Tsd17_13	TSD17	458.500	458.500	Halloysite	1	NULL	NULL	112.505	
96	Tsd17_14	TSD17	480.150	480.150	Halloysite	1	NULL	NULL	231.741	
97	Tsd17_15	TSD17	493.000	493.000	Halloysite	1	NULL	NULL	191.078	
98	08073_01	TSD18	57.950	57.950	Paragonite	1	NULL	NULL	79.114	brown
99	08073_03	TSD18	71.600	71.600	Illite	0.708	Phengite	0.292	30.522	
100	08073_04	TSD18	75.400	75.400	Kaolinite	0.56	Halloysite	0.440	49.967	greenish
101	08073_05	TSD18	88.800	88.800	Halloysite	0.604	Opal	0.396	146.722	
102	08073_06	TSD18	101.800	101.800	Phengite	0.537	Halloysite	0.463	283.13	
103	08073_25	TSD18	111.300	111.300	Jarosite	1	NULL	NULL	225.564	white_cly
104	08073_07	TSD18	121.400	121.400	Halloysite	1	NULL	NULL	150.933	malachite

Appendix 1b
PIMA Results

ID	SampNo	HoleID	From	To	TSA_Min1	TSA_Wt1	TSA_Min2	TSA_Wt2	TSA_Error	Comments
105	08073_08	TSD18	138.100	138.100	Kaolinite	0.65	Muscovite	0.350	75.592	greenish
106	08073_09	TSD18	163.200	163.200	Kaolinite	0.559	Halloysite	0.441	55.538	
107	08073_10	TSD18	179.000	179.000	Halloysite	0.512	Kaolinite	0.488	62.919	brown
108	08073_11	TSD18	179.001	179.001	Halloysite	1	NULL	NULL	126.395	Brown cly in qtz
109	08073_12	TSD18	191.300	191.300	Kaolinite	0.74	Montmorilloni te	0.260	130.873	White cly in dio
110	08073_13	TSD18	201.000	201.000	Kaolinite	0.74	Montmorilloni te	0.260	130.873	
111	08073_14	TSD18	224.250	224.250	Illite	0.795	Nontronite	0.205	65.301	
112	08073_15	TSD18	224.251	224.251	Halloysite	1	NULL	NULL	191.256	
113	08073_16	TSD18	236.000	236.000	Kaolinite	1	NULL	NULL	231.59	
114	08073_17	TSD18	260.800	260.800	Kaolinite	0.67	Montmorilloni te	0.330	107.149	
115	08073_18	TSD18	281.800	281.800	Kaolinite	0.726	Montmorilloni te	0.274	75.084	
116	08083_37	TSD18	292.550	292.550	Halloysite	1	NULL	NULL	208.257	
117	08083_38	TSD18	292.551	292.551	Kaolinite	0.795	Montmorilloni te	0.205	49.012	
118	08073_26	TSD18	294.900	294.900	Kaolinite	0.627	Muscovite	0.373	54.56	yellow
119	08073_23	TSD18	305.700	305.700	Kaolinite	0.601	Halloysite	0.399	58.949	white_cly
120	08073_27	TSD18	320.300	320.300	Kaolinite	0.752	Magnesium_ Clays	0.248	83.027	yellow
121	08073_22	TSD18	333.400	333.400	Kaolinite	1	NULL	NULL	131.592	white
122	08073_28	TSD18	341.300	341.300	Kaolinite	0.576	Halloysite	0.424	64.965	yellow
123	08073_24	TSD18	345.700	345.700	Kaolinite	0.826	Gypsum	0.174	164.04	yellow
124	08073_29	TSD18	359.600	359.600	Kaolinite	0.666	Montmorilloni te	0.334	112.999	Yellow alt'n
125	08073_30	TSD18	380.800	380.800	Kaolinite	0.662	Montmorilloni te	0.338	161.758	yellow weathering
126	08073_20	TSD18	409.550	409.550	Halloysite	1	NULL	NULL	214.196	oxidised
127	08083_32	TSD18	420.450	420.450	Kaolinite	0.602	Illite	0.398	140.144	yellow
128	08083_35	TSD18	479.800	479.800	Muscovite	0.812	Kaolinite	0.188	63.708	yellow
129	08083_36	TSD18	502.800	502.800	Muscovite	0.752	Gypsum	0.248	220.76	
130	Tsd20_01	TSD20	83.100	83.100	Illite	1	NULL	NULL	50.377	
131	Tsd20_02	TSD20	95.750	95.750	Kaolinite	0.6	Halloysite	0.400	33.49	
132	Tsd20_03	TSD20	101.000	101.000	Kaolinite	0.6	Halloysite	0.400	33.49	
133	Tsd20_04	TSD20	121.600	121.600	Halloysite	1	NULL	NULL	95.537	
134	Tsd20_05	TSD20	140.200	140.200	Halloysite	0.556	Kaolinite	0.444	43.024	
135	Tsd20_06	TSD20	161.400	161.400	Halloysite	1	NULL	NULL	133.629	
136	Tsd20_07	TSD20	180.300	180.300	Kaolinite	0.529	IntChlorite	0.471	217.409	
137	Tsd20_08	TSD20	200.500	200.500	Kaolinite	0.763	Magnesium_ Clays	0.237	135.254	
138	Tsd20_09	TSD20	220.300	220.300	Kaolinite	0.721	Halloysite	0.279	59.28	
139	Tsd20_10	TSD20	239.900	239.900	Kaolinite	0.737	Halloysite	0.263	68.388	
140	Tsd20_11	TSD20	247.250	247.250	Kaolinite	0.672	Montmorilloni te	0.328	76.478	
141	Tsd20_12	TSD20	247.251	247.251	Illite	1	NULL	NULL	93.751	
142	Tsd20_13	TSD20	247.252	247.252	Illite	1	NULL	NULL	40.255	
143	Tsd20_14	TSD20	259.600	259.600	Kaolinite	1	NULL	NULL	102.62	
144	Tsd20_15	TSD20	282.600	282.600	Halloysite	0.507	Kaolinite	0.493	94.655	
145	Tsd20_16	TSD20	300.400	300.400	Kaolinite	0.562	Halloysite	0.438	93.037	
146	Tsd20_17	TSD20	321.300	321.300	Kaolinite	0.726	Phlogopite2	0.274	222.48	
147	Tsd20_18	TSD20	340.600	340.600	Kaolinite	1	NULL	NULL	149.341	
148	Tsd20_20	TSD20	381.800	381.800	Phlogopite2	0.648	Kaolinite	0.352	209.24	
149	Tsd20_21	TSD20	400.500	400.500	Phlogopite2	0.531	Kaolinite	0.469	146.101	
150	Tsd35_01	TSD35	379.600	379.600	Kaolinite	0.733	Halloysite	0.267	85.00	with lim

Appendix 1b
PIMA Results

ID	SampNo	HoleID	From	To	TSA_Min1	TSA_Wt1	TSA_Min2	TSA_Wt2	TSA_Error	Comments
151	Tsd35_03	TSD35	400.501	400.501	Kaolinite	1	NULL	NULL	122.952	
154	Tsd35_08	TSD35	461.300	461.300	Kaolinite	0.721	MgChlorite	0.279	246.677	
155	Tsd35_09	TSD35	481.000	481.000	Kaolinite	0.819	Serpentine	0.181	105.791	yellowish with cup
156	Tsd35_10	TSD35	500.200	500.200	Kaolinite	1	NULL	NULL	237.518	
157	Tsd35_14	TSD35	520.300	520.300	Kaolinite	0.703	MgChlorite	0.297	227.002	
158	Tsd35_15	TSD35	539.850	539.850	Kaolinite	0.694	Opal	0.306	218.471	
159	Tsd38_01	TSD38	52.500	52.500	Halloysite	1	NULL	NULL	104.86	light green
160	Tsd38_02	TSD38	54.400	54.400	Kaolinite	1	NULL	NULL	209.46	assoc w/ mal-azu
161	Tsd38_03	TSD38	64.300	64.300	Illite	1	NULL	NULL	101.029	qtz-lim-mal
162	Tsd38_04	TSD38	82.700	82.700	Halloysite	1	NULL	NULL	117.504	assoc w/ azu-mal
163	Tsd38_05	TSD38	91.350	91.350	Halloysite	1	NULL	NULL	179.712	lt gn cly w/ copper
164	Tsd38_06	TSD38	101.500	101.500	Halloysite	1	NULL	NULL	130.873	
165	Tsd38_08	TSD38	112.251	112.251	Illite	1	NULL	NULL	108.861	lim assoc w/ mal
166	Tsd38_09	TSD38	126.500	126.500	Kaolinite	0.82	Epidote	0.180	266.385	
168	Tsd38_11	TSD38	142.800	142.800	Halloysite	1	NULL	NULL	235.246	limonitic
169	Tsd38_12	TSD38	158.200	158.200	Halloysite	0.642	FeChlorite	0.358	228.262	light green
170	Tsd38_13	TSD38	169.000	169.000	Halloysite	1	NULL	NULL	141.402	light green
171	Tsd38_14	TSD38	178.250	178.250	Kaolinite	0.551	Opal	0.449	191.66	lt yl gn assoc w/ cup-neot(?)
172	Tsd38_15	TSD38	184.200	184.200	Halloysite	1	NULL	NULL	186.818	limonitic
173	Tsd38_16	TSD38	184.201	184.201	Halloysite	1	NULL	NULL	140.67	white
174	Tsd38_17	TSD38	200.800	200.800	Kaolinite	0.752	Montmorilloni te	0.248	88.932	limonitic
175	Tsd38_18	TSD38	221.550	221.550	Kaolinite	0.694	Halloysite	0.306	42.995	white
176	Tsd38_19	TSD38	237.350	237.350	Kaolinite	0.539	Halloysite	0.461	56.696	white
177	Tsd38_20	TSD38	261.650	261.650	Kaolinite	1	NULL	NULL	200.89	yellow
178	Tsd38_21	TSD38	280.000	280.000	Kaolinite	0.61	Phlogopite2	0.390	166.345	yellow-green
179	Tsd38_22	TSD38	300.600	300.600	Kaolinite	1	NULL	NULL	144.037	
180	Tsd38_23	TSD38	300.601	300.601	Kaolinite	1	NULL	NULL	85.385	greenish
181	Tsd38_24	TSD38	323.550	323.550	Kaolinite	1	NULL	NULL	161.74	pinkish green
182	Tsd38_25	TSD38	341.750	341.750	Kaolinite	0.812	Dolomite	0.188	232.358	greenish
184	Tsd39_01	TSD39	99.400	99.400	Kaolinite	0.69	Halloysite	0.310	58.328	
185	Tsd39_02	TSD39	114.000	114.000	Kaolinite	0.611	Halloysite	0.389	93.174	
186	Tsd39_03	TSD39	121.650	121.650	Kaolinite	0.837	Ankerite	0.163	93.654	
187	Tsd39_04	TSD39	141.800	141.800	Kaolinite	0.669	Phlogopite2	0.331	149.714	
189	Tsd39_06	TSD39	160.200	160.200	Kaolinite	0.682	IntChlorite	0.318	110.569	
190	Tsd39_08	TSD39	187.200	187.200	Illite	0.756	Halloysite	0.244	34.951	w/ lim
191	Tsd39_09	TSD39	187.201	187.201	Kaolinite	0.625	IntChlorite	0.375	143.61	
192	Tsd39_10	TSD39	196.750	196.750	Kaolinite	0.652	FeChlorite	0.348	97.725	near fracfill lim
194	Tsd39_12	TSD39	197.251	197.251	Halloysite	0.545	Illite	0.455	85.221	white
195	Tsd39_13	TSD39	217.600	217.600	Kaolinite	0.74	IntChlorite	0.260	177.445	w/ mal-azu-lim
196	Tsd39_14	TSD39	240.000	240.000	Kaolinite	0.819	Dolomite	0.181	199.678	
197	Tsd39_16	TSD39	280.100	280.100	Kaolinite	0.547	Halloysite	0.453	142.152	
198	Tsd39_17	TSD39	301.550	301.550	Kaolinite	0.532	Muscovite	0.468	62.213	
199	Tsd39_18	TSD39	320.900	320.900	Halloysite	1	NULL	NULL	203.403	
200	Tsd39_19	TSD39	320.901	320.901	Montmorillo nite	0.664	Kaolinite	0.336	224.002	
201	Tsd39_20	TSD39	341.650	341.650	Kaolinite	1	NULL	NULL	159.096	white
202	Tsd47_01	TSD47	89.500	89.500	Kaolinite	0.659	Halloysite	0.341	94.912	
203	Tsd47_02	TSD47	99.850	99.850	Kaolinite	0.669	Halloysite	0.331	43.66	
204	Tsd47_03	TSD47	116.700	116.700	Illite	1	NULL	NULL	45.544	selvdge to lim

Appendix 1b
PIMA Results

ID	SampNo	HoleID	From	To	TSA_Min1	TSA_Wt1	TSA_Min2	TSA_Wt2	TSA_Error	Comments
205	Tsd47_04	TSD47	116.701	116.701	Illite	0.793	Phengite	0.207	26.126	
206	Tsd47_05	TSD47	120.550	120.550	Kaolinite	1	NULL	NULL	56.038	hematitic
207	Tsd47_06	TSD47	136.850	136.850	Kaolinite	1	NULL	NULL	71.603	hematitic
208	Tsd47_07	TSD47	160.000	160.000	Kaolinite	0.732	Halloysite	0.268	23.496	yellow-brown
209	Tsd47_08	TSD47	160.001	160.001	Kaolinite	1	NULL	NULL	49.36	hematitic
210	Tsd47_09	TSD47	180.400	180.400	Kaolinite	1	NULL	NULL	112.274	Assoc with lim
211	Tsd47_10	TSD47	200.600	200.600	Kaolinite	0.734	Muscovite	0.266	72.496	Assoc with lim
213	Tsd47_12	TSD47	220.300	220.300	Kaolinite	1	NULL	NULL	122.126	
214	Tsd47_13	TSD47	239.900	239.900	Kaolinite	1	NULL	NULL	137.501	Assoc with azu-lim
215	Tsd47_14	TSD47	259.850	259.850	Illite	0.524	Muscovite	0.476	25.948	Yellow-cly near qtz-vn
217	Tsd47_16	TSD47	280.000	280.000	Muscovite	0.643	Halloysite	0.357	67.007	limonitic
218	Tsd47_17	TSD47	302.150	302.150	Kaolinite	0.515	Halloysite	0.485	117.339	slightly limonitic
219	Tsd47_18	TSD47	312.650	312.650	Kaolinite	0.679	Halloysite	0.321	71.455	
220	Tsd50_01	TSD50	130.000	130.000	Kaolinite	0.7	MgChlorite	0.300	116.946	
221	Tsd50_02	TSD50	140.800	140.800	Kaolinite	0.778	MgChlorite	0.222	126.591	
222	Tsd50_03	TSD50	159.500	159.500	Kaolinite	1	NULL	NULL	105.116	
223	Tsd50_04	TSD50	180.100	180.100	Kaolinite	1	NULL	NULL	127.19	
224	Tsd50_05	TSD50	200.800	200.800	Kaolinite	0.715	Phlogopite1	0.285	130.47	
225	Tsd50_06	TSD50	221.250	221.250	Kaolinite	0.793	MgChlorite	0.207	76.085	
226	Tsd50_08	TSD50	261.300	261.300	Kaolinite	0.574	Halloysite	0.426	36.762	
227	Tsd50_09	TSD50	281.650	281.650	Kaolinite	0.749	Halloysite	0.251	60.365	
229	Tsd50_11	TSD50	320.300	320.300	Kaolinite	0.7	Halloysite	0.300	56.697	
230	Tsd50_12	TSD50	340.800	340.800	Kaolinite	0.592	Halloysite	0.408	78.849	
231	Tsd50_14	TSD50	381.000	381.000	Kaolinite	1	NULL	NULL	161.461	
232	Tsd50_15	TSD50	394.600	394.600	Kaolinite	0.705	MgChlorite	0.295	179.286	
233	Tsd50_16	TSD50	405.900	405.900	Kaolinite	1	NULL	NULL	114.621	
234	Tsd50_17	TSD50	420.500	420.500	Kaolinite	0.658	Halloysite	0.342	89.536	
235	Tsd62_01	TSD62	86.300	86.300	Kaolinite	0.709	Halloysite	0.291	30.554	
236	Tsd62_02	TSD62	102.400	102.400	Illite	1	NULL	NULL	118.031	
237	Tsd62_03	TSD62	121.000	121.000	Kaolinite	0.747	Muscovite	0.253	63.122	
238	Tsd62_04	TSD62	140.100	140.100	Kaolinite	0.739	Halloysite	0.261	48.111	
239	Tsd62_05	TSD62	159.000	159.000	Kaolinite	0.529	IntChlorite	0.471	96.7	
240	Tsd62_06	TSD62	181.100	181.100	Kaolinite	0.694	Phlogopite1	0.306	129.464	
241	Tsd62_07	TSD62	200.800	200.800	Kaolinite	0.572	Phlogopite1	0.428	165.387	
242	Tsd62_08	TSD62	220.000	220.000	Kaolinite	0.686	Serpentine	0.314	242.368	
243	Tsd62_09	TSD62	242.600	242.600	Kaolinite	0.692	Phlogopite1	0.308	161.4	
244	Tsd63_01	TSD63	120.250	120.250	Kaolinite	0.643	Halloysite	0.357	100.071	
245	Tsd63_02	TSD63	134.250	134.250	Halloysite	0.639	IntChlorite	0.361	127.291	white selvdge to qtz-lim
246	Tsd63_04	TSD63	140.400	140.400	Kaolinite	1	NULL	NULL	122.396	
247	Tsd63_05	TSD63	146.700	146.700	Kaolinite	0.645	Halloysite	0.355	82.772	
248	Tsd63_06	TSD63	146.701	146.701	Illite	0.669	Phengite	0.331	31.939	selvedge to lim
249	Tsd63_07	TSD63	160.000	160.000	Kaolinite	0.587	Halloysite	0.413	69.988	
250	Tsd63_08	TSD63	181.900	181.900	Kaolinite	0.502	Halloysite	0.498	111.085	
251	Tsd63_09	TSD63	199.850	199.850	Kaolinite	1	NULL	NULL	164.137	
252	Tsd63_10	TSD63	199.851	199.851	Kaolinite	0.63	Halloysite	0.370	118.043	
253	Tsd63_11	TSD63	220.450	220.450	Kaolinite	1	NULL	NULL	115.774	
254	Tsd63_12	TSD63	241.650	241.650	Halloysite	1	NULL	NULL	227.959	
255	Tsd63_13	TSD63	261.000	261.000	Halloysite	0.587	IntChlorite	0.413	249.294	
256	Tsd63_14	TSD63	261.001	261.001	Kaolinite	0.618	Opal	0.382	225.485	fracture
257	Tsd63_15	TSD63	280.000	280.000	Kaolinite	0.528	Halloysite	0.472	91.834	

Appendix 1b
PIMA Results

ID	SampNo	HoleID	From	To	TSA_Min1	TSA_Wt1	TSA_Min2	TSA_Wt2	TSA_Error	Comments
258	Tsd63_16	TSD63	280.001	280.001	Halloysite	1	NULL	NULL	141.417	cly with cup
259	Tsd63_17	TSD63	300.700	300.700	Halloysite	1	NULL	NULL	144.948	
260	Tsd63_18	TSD63	300.701	300.701	Kaolinite	0.586	Halloysite	0.414	97.341	fracture
261	Tsd63_19	TSD63	320.700	320.700	Kaolinite	0.561	Halloysite	0.439	79.853	
262	Tsd63_20	TSD63	340.950	340.950	Kaolinite	0.542	Montmorilloni te	0.458	119.878	assoc with lim and chyrs
263	Tsd63_21	TSD63	340.951	340.951	Halloysite	1	NULL	NULL	153.17	
264	Tsd63_22	TSD63	360.800	360.800	Kaolinite	1	NULL	NULL	248.484	frac with lim
265	Tsd63_23	TSD63	360.801	360.801	Halloysite	1	NULL	NULL	172.369	

Abbreviations: TSA = The Spectral Analyst; Min = mineral; Wt = weight; dio = diorite; LPD = late diorite porphyry; lim = limonite; cly = clay; cup = cuprite; mal = malachite; azu = azurite; chrys = chrysocolla; neot = neotocite; qtz = quartz; vn = vein; lt = light; gn = green; yl = yellow; gr = gray; wh = white; frac = fracture; fracfill = fracture-fill(ing); assoc = associated; adj = adjacent

APPENDIX 2

SAMPLE DETAILS FOR ORE MICROSCOPY & ELECTRON PROBE MICROANALYSES (EPMA)

Appendix 2

Sample details for Ore Microscopy & EPMA

BHID	SampID	From	To	Objective1	Objective2	Description
TSD02	819295	141.40	141.40	Ore Microscopy	---	pyr + cct
TSD11	819235	383.00	383.00	Ore Microscopy	EPMA	mal with mamillary texture
TSD11	819236	520.90	520.90	Ore Microscopy	---	mag-hem + diss cup in FGD
TSD11	819237	526.40	526.40	Ore Microscopy	EPMA	cup, mal, azu in qvn frac
TSD11	819238	560.20	560.20	Ore Microscopy	---	pyr, cpy, rimmed by cct and goe in qtz-lim vn
TSD11	819239	567.60	567.60	Ore Microscopy	---	pyr vnlets oxidised to goe
TSD11	819240	576.55	576.55	Ore Microscopy	---	pyr + cpy rimmed by cct in qtz-lim vn
TSD13	819201	93.20	93.20	Ore Microscopy	---	interlocking xtals of azu, mal in fractures
TSD13	819202	109.20	109.20	Ore Microscopy	---	mal-azu in frac
TSD13	819203	152.10	152.10	Ore Microscopy	---	cup & lt gn cly in frac
TSD13	819204	176.95	176.95	Ore Microscopy	---	chyrs in frac
TSD13	819205	213.20	213.20	Ore Microscopy	---	lt gn clay_determine clay content
TSD13	819206	216.70	216.70	Ore Microscopy	EPMA	mal +- cct + Cu-bearing cly + azu
TSD13	819207	259.95	259.95	Ore Microscopy	---	lim with remnant sulfides
TSD13	819208	327.30	327.30	Ore Microscopy	---	limonite matrix, silicified clasts
TSD13	819210	372.20	372.20	Ore Microscopy	---	red and deep red cuprite in fractures
TSD13	819211	384.20	384.20	Ore Microscopy	---	pyr, cpy rp by cct and goe +- mal_boxwork goe
TSD13	819212	406.60	406.60	Ore Microscopy	---	pyr, bor to cct to goe
TSD13	819213	474.55	474.55	Ore Microscopy	---	pyr oxidised to goe in qvn
TSD13	819214	482.90	482.90	Ore Microscopy	EPMA	cpy-rp cct in lim-stained qvn
TSD14	819296	135.95	135.95	Ore Microscopy	---	cpy,bor,cct rimmed by mal, cup and then mal; azu late
TSD16	819288	363.45	363.45	Ore Microscopy	---	pyr-cct(?)-moly-goe
TSD18	819217	70.55	70.55	Ore Microscopy	---	cct-mal in frac
TSD18	819218	88.70	88.70	Ore Microscopy	---	mal preferentially on plag
TSD18	819218	88.70	88.70	Ore Microscopy	---	mal preferentially on plag
TSD18	819220	112.85	112.85	Ore Microscopy	---	qf cct with remnant cpy in qvn_cct to mal
TSD18	819221	112.80	112.80	Ore Microscopy	---	cpy rimmed by cct and mal_cup present
TSD18	819222	116.20	116.20	Ore Microscopy	EPMA	hem after cct
TSD18	819223	132.30	132.30	Ore Microscopy	EPMA	cup & mal in qvn
TSD18	819224	146.25	146.25	Ore Microscopy	EPMA	qf, ff mal & goe
TSD18	819226	225.00	225.00	Ore Microscopy	EPMA	ff goe with cct + pyr
TSD18	819227	242.60	242.60	Ore Microscopy	---	pyr-cpy in banded qtz vn with cct
TSD18	819229	285.60	285.60	Ore Microscopy	---	mal-spec-cpy
TSD18	819230	286.25	286.25	Ore Microscopy	EPMA	qvn with cpy-mag-pyr vn with cct-gn cly_copper staining
TSD18	819231	295.40	295.40	Ore Microscopy	---	bor-cpy-cct-goe_upper right_large slide
TSD18	819232	295.40	295.40	Ore Microscopy	---	left_pyr-cpy-cct-goe
TSD18	819234	309.70	309.70	Ore Microscopy	---	pyr rimmed by cct to cup cutting “A” vn_cct cut by frac containing cup above_large slide
TSD18	819233	309.05	309.05	Ore Microscopy	EPMA	pyr or cpy with bor @ center replaced by cct to cup to mal
TSD20	819258	115.40	115.40	Ore Microscopy	---	ff pitchlim in sil bx
TSD20	819259	129.55	129.55	Ore Microscopy	---	ff lim + mal_any remnant sulfides or Au
TSD20	819260	205.65	205.65	Ore Microscopy	---	remnant cpy +- pyr-cct-goe adj to qvn
TSD20	819261	221.60	221.60	Ore Microscopy	---	oxidised nat Cu-goe sil bx_large slide
TSD20	819262	258.70	258.70	Ore Microscopy	---	pyr-moly-cpy-goe-mal in qvn
TSD20	819263	273.10	273.10	Ore Microscopy	---	chyrs-mal_determine relationships
TSD20	819264	288.00	288.00	Ore Microscopy	---	cpy-pyr to goe to mal-chrys
TSD20	819264	288.00	288.00	Ore Microscopy	---	cpy-pyr to goe to mal to chrys
TSD20	819265	292.70	292.70	Ore Microscopy	---	pyr-goe-chyrs-mal
TSD20	819266	301.95	301.95	Ore Microscopy	---	upper right_cpy +- bor cutting qstwk
TSD35	819270	451.00	451.00	Ore Microscopy	---	azu-cup-mal-determine relationships
TSD35	819271	505.50	505.50	Ore Microscopy	---	cpy or goe
TSD38	819241	54.60	54.60	Ore Microscopy	---	mal-goe_close-up
TSD38	800916	55.20	55.20	Ore Microscopy	---	azu and mal in altered diorite
TSD38	819243	55.95	55.95	Ore Microscopy	---	mal-azu_determine intergrowth relationships
TSD38	819242	54.60	54.60	Ore Microscopy	---	mal-azu_close-up
TSD38	800917	59.35	59.35	Ore Microscopy	---	Quartz ("ribbon" or banded) veins with fracture filling malachite
TSD38	800918	77.20	77.20	Ore Microscopy	---	Quartz vein with malachite and chrysocolla(?)

Appendix 2

Sample details for Ore Microscopy & EPMA

BHID	SampID	From	To	Objective1	Objective2	Description
TSD38	800919	78.40	78.40	Ore Microscopy	---	Remants of chalcopyrite, rimmed by chalcocite, malachite, and chrysocolla
TSD38	819244	78.40	78.40	Ore Microscopy	---	cpy-cct-cup mal in vn
TSD38	819247	86.30	86.30	Ore Microscopy	---	azu-mal-neot_hand specimen
TSD38	800921	86.35	86.35	Ore Microscopy	EPMA	Brownish black sooty mineral - neotocite(?) or chalcocite(?)
TSD38	819245	84.85	84.85	Ore Microscopy	EPMA	qvn with bor-cct in HBR
TSD38	800920	91.30	91.30	Ore Microscopy	---	Green clay(?) or chrysocolla(?)
TSD38	819248	95.25	95.25	Ore Microscopy	EPMA	azu-chrys +- mal
TSD38	819250	98.75	98.75	Ore Microscopy	EPMA	cpy-cct-mal-cup in qvn_left side_close-up
TSD38	819252	114.90	114.90	Ore Microscopy	EPMA	cpy-cct-mal-goe
TSD38	800922	138.15	138.15	Ore Microscopy	---	Chalcopyrite, bornite, chalcocite, and malachite in quartz vein
TSD38	819253	161.00	161.00	Ore Microscopy	EPMA	cpy-bor-cup
TSD38	819254	253.60	253.60	Ore Microscopy	EPMA	cpy-cct in frac with fringing lim
TSD38	819255	262.60	262.60	Ore Microscopy	---	cpy-bor-cct in qvn_in a localised sulfide zone
TSD38	819256	271.20	271.20	Ore Microscopy	---	cpy-bor-cct
TSD38	819257	276.80	276.80	Ore Microscopy	EPMA	bor-cpy forming bands in qvn
TSD39	819273	271.90	271.90	Ore Microscopy	---	pyr to goe with minor chyrs
TSD47	800924	272.75	272.75	Ore Microscopy	---	Limonite, malachite; gold in limonite?
TSD50	819289	298.70	298.70	Ore Microscopy	EPMA	chyrs replacing goe
TSD50	819291	396.00	396.00	Ore Microscopy	---	pyr +- cpy replaced by cct then by cup
TSD50	819292	397.50	397.50	Ore Microscopy	---	cup replacing cct
TSD53	800927	239.00	239.00	Ore Microscopy	---	Limonite with chrysocolla with light green alteration halo
TSD53	800928	247.45	247.45	Ore Microscopy	---	Limonite and malachite in quartz vein with pale green(?) alteration halo
TSD53	800930	422.00	422.00	Ore Microscopy	---	Quartz vein with chalocopyrite, bornite +/- chalcocite in small vugs
TSD62	819293	177.65	177.65	Ore Microscopy	---	pyr coated with cct-goe; goe displaying boxwork texture
TSD62	819294	200.80	200.80	Ore Microscopy	EPMA	cct rp by cup
TSD63	819267	370.35	370.35	Ore Microscopy	---	cpy-bor + pyr rp by cct-hem
TSD63	819268	377.65	377.65	Ore Microscopy	---	pyr-cct-goe
TSD63	819269	395.40	395.40	Ore Microscopy	---	chrys like malachite_does not effervesce

Abbreviations: BHID = bore hole ID; SampID = sample ID; cpy = chalcopyrite; bor = bornite; pyr = pyrite; molybdenite = molybdenite; cct = chalcocite; cup = cuprite; nat Cu = native copper; azu = azurite; mal = malachite; chrys = chrysocolla; neot = neotocite; goe = goethite; lim = limonite; mag = magnetite; spec = specularite; hem = hematite; qvn = quartz vein; qtz = quartz; plag = plagioclase; qstwk = quartz stockwork; cly = clay; sil = silicified; xtals = crystals; frac = fracture; rp = replaced; qf = fracture in quartz vein; ff = fracture-fill(ing); adj = adjacent; lt = light; gn = green; HBR = hydrothermal breccia; bx = breccia

APPENDIX 3

EPMA RESULTS: COPPER SULFIDES & GOLD (Weight % & Atomic %)

Appendix 3
EPMA Results: Copper Sulfides & Gold

	S	Mn	Fe	Cu	Zn	As	Pb	Ag	Cd	Sb	Au	Te	Total	Sample No.
Weight%	25.99174	0.002409	11.65757	61.93316	-0.044243	0.011195	-0.252113	-0.000501	-0.004032	-0.01095	-0.147179	0.039752	99.63582	819214_1_bor1
Atomic%	40.70265	0.002202	10.47994	48.9312	-0.033974	0.007502	-0.061088	-0.000233	-0.001801	-0.004515	-0.037515	0.015641	100.1391	819214_1_bor1
Det Lim ppm	561	223	317	684	622	633	1168	363	395	505	1463	717	0	819214_1_bor1
Weight%	22.8253	-0.007175	0.046318	73.4348	1414.725	0.012553	-0.241501	0.017862	-0.002399	0.015506	-0.054679	0.066162	1511.144	819214_1_cct1
Atomic%	3.028788	-0.000556	0.003528	4.916202	92.05411	0.000713	-0.004958	0.000704	-0.000091	0.000542	-0.001181	0.002206	100.0068	819214_1_cct1
Det Lim ppm	562	217	270	696	242	866	1254	336	375	475	1462	681	0	819214_1_cct1
Weight%	21.58719	-0.002658	0.094061	78.05574	-0.023597	0.045849	-0.135825	0.006012	0.001008	0.003022	-0.014103	0.069186	99.86207	819214_2_cct1
Atomic%	35.37432	-0.002542	0.088485	64.53156	-0.018961	0.03215	-0.034439	0.002928	0.000471	0.001304	-0.003762	0.028486	100.0597	819214_2_cct1
Det Lim ppm	506	218	288	755	632	644	1104	367	396	509	1474	717	0	819214_2_cct1
Weight%	0.0854	-0.01981	0.000822	2.82636	-0.108697	0.05492	-1.771283	1.795745	-0.004351	-0.012096	97.6721	0.057134	102.4925	819222_1_electrum1
Atomic%	0.484184	-0.065544	0.002674	8.084501	-0.302194	0.13324	-1.553861	3.02598	-0.007036	-0.018059	90.13472	0.081387	101.9467	819222_1_electrum1
Det Lim ppm	521	343	452	608	733	500	2679	587	590	761	2029	1062	0	819222_1_electrum1
Weight%	21.26435	0.003803	0.016561	78.73352	-0.014165	0.056239	-0.222002	0.005983	-0.033874	-0.009026	-0.079692	0.071943	100.1524	819222_1cct-darker1
Atomic%	34.87328	0.003639	0.015591	65.1442	-0.011391	0.039467	-0.056334	0.002916	-0.015844	-0.003898	-0.021273	0.029644	100.1088	819222_1cct-darker1
Det Lim ppm	528	216	302	746	634	660	1105	358	410	512	1484	704	0	819222_1cct-darker1
Weight%	21.31149	0.007959	-0.004746	77.97297	-0.018319	-0.003313	-0.175525	0.015015	-0.004532	-0.003774	-0.145329	0.009423	99.31686	819222_1cct-lighter1
Atomic%	35.17016	0.007665	-0.004496	64.9202	-0.014825	-0.002339	-0.04482	0.007365	-0.002133	-0.00164	-0.039038	0.003907	100.1093	819222_1cct-lighter1
Det Lim ppm	544	215	298	737	636	677	1112	374	397	506	1503	732	0	819222_1cct-lighter1
Weight%	0.025557	0.008413	0.253858	84.46133	0.01608	0.015589	-0.00222	-0.017618	-0.006241	0.005593	-0.032175	0.006367	84.79279	819222_2_cup1
Atomic%	0.059722	0.011472	0.340548	99.5765	0.018426	0.015588	-0.000803	-0.012237	-0.004159	0.003442	-0.012238	0.003738	100.0294	819222_2_cup1
Det Lim ppm	347	199	254	754	605	764	853	351	381	474	1446	696	0	819222_2_cup1
Weight%	0.051227	-0.017764	0.06331	3.379538	-0.126142	0.020009	-1.668705	2.364913	-0.024518	-0.033487	96.77615	0.0129	102.668	819222_3_electrum1
Atomic%	0.285974	-0.057871	0.202892	9.518301	-0.345307	0.047798	-1.441385	3.923854	-0.039036	-0.049226	87.93592	0.018094	101.9328	819222_3_electrum1
Det Lim ppm	553	345	442	613	738	515	2633	596	596	778	2036	1085	0	819222_3_electrum1
Weight%	21.24139	-0.005152	0.100164	77.97523	-0.016487	0.036549	-0.168575	0.011279	0.015134	0.027596	-0.078296	-0.014898	99.40733	819222_3_cct1
Atomic%	35.04278	-0.00496	0.094862	64.90044	-0.013337	0.025802	-0.043031	0.00553	0.007121	0.011988	-0.021024	-0.006175	100.0885	819222_3_cct1
Det Lim ppm	594	222	278	743	635	642	1095	366	388	489	1481	753	0	819222_3_cct1
Weight%	0.018518	-0.001504	0.007724	98.66832	-0.036901	0.053424	-0.008909	0.016066	0.003941	0.001402	-0.063195	0.060528	98.82992	819223_1_cu1
Atomic%	0.037172	-0.001762	0.008901	99.92643	-0.036324	0.04589	-0.002767	0.009585	0.002256	0.000741	-0.020648	0.030528	100.0615	819223_1_cu1
Det Lim ppm	427	217	267	791	668	779	883	364	396	509	1546	705	0	819223_1_cu1
Weight%	0.01812	0.002849	-0.011665	84.63823	-0.01607	0.047413	0.029961	0.014411	-0.003929	-0.004543	-0.021143	0.050977	84.80197	819223_1_cup?1
Atomic%	0.042393	0.00389	-0.015667	99.90299	-0.018436	0.047467	0.010846	0.010021	-0.002621	-0.002799	-0.008051	0.029966	100.0476	819223_1_cup?1
Det Lim ppm	410	197	249	740	612	784	871	340	378	479	1438	682	0	819223_1_cup?1
Weight%	29.93473	-0.001367	0.499244	70.01995	-0.000762	-0.00102	-0.21242	-0.010027	-0.01834	0.004629	-0.135158	0.03083	100.4894	819226_1_cov1
Atomic%	45.70759	-0.001218	0.437613	53.93988	-0.000571	-0.000667	-0.050186	-0.00455	-0.007987	0.001861	-0.033591	0.011828	100.0988	819226_1_cov1
Det Lim ppm	530	222	298	703	611	632	1119	372	396	495	1490	738	0	819226_1_cov1
Weight%	21.74112	0.00601	1.359823	74.04329	0.00524	-0.016909	-0.149559	0.017789	0.005294	0.005289	-0.103114	0.035393	97.21925	819226_1_dju1
Atomic%	36.3237	0.005859	1.304231	62.41217	0.004293	-0.012089	-0.038663	0.008834	0.002523	0.002327	-0.028041	0.014857	100.0788	819226_1_dju1
Det Lim ppm	583	212	300	733	612	691	1076	355	392	501	1466	741	0	819226_1_dju1
Weight%	31.27137	0.006633	0.964931	62.95578	-0.05218	0.032974	-0.267199	0.002096	-0.012636	0.003141	-0.00878	0.015492	95.25241	819226_2_cov1
Atomic%	49.21611	0.006092	0.871807	49.98864	-0.04027	0.022207	-0.065068	0.000981	-0.005672	0.001302	-0.002249	0.006126	100.1133	819226_2_cov1
Det Lim ppm	559	214	291	687	609	619	1168	371	397	496	1403	753	0	819226_2_cov1
Weight%	23.23564	-0.010357	0.776278	75.72243	-0.062204	0.004877	-0.166622	0.011053	-0.017187	0.002271	-0.038164	0.024197	99.77675	819230_1_cov1
Atomic%	37.58408	-0.009777	0.720826	61.7944	-0.049338	0.003376	-0.041702	0.005314	-0.007929	0.000967	-0.010048	0.009834	100.1188	819230_1_cov1
Det Lim ppm	588	227	285	733	642	673	1103	363	401	507	1466	744	0	819230_1_cov1
Weight%	23.41446	-0.007046	1.205297	75.54656	-0.018045	0.024943	-0.138896	0.016113	-0.005573	-0.030352	-0.016399	0.075367	100.2827	819230_1_cov2
Atomic%	37.63865	-0.006609	1.112264	61.26887	-0.014224	0.017158	-0.034547	0.007698	-0.002555	-0.012848	-0.004291	0.03044	100.0751	819230_1_cov2
Det Lim ppm	498	223	290	738	649	668	1060	359	391	511	1475	697	0	819230_1_cov2

Appendix 3
EPMA Results: Copper Sulfides & Gold

	S	Mn	Fe	Cu	Zn	As	Pb	Ag	Cd	Sb	Au	Te	Total	Sample No.
Weight%	25.67124	0.004959	3.281397	67.64072	-0.030715	0.004195	-0.193506	0.004332	-0.014095	0.018404	-0.056745	0.022325	96.64758	819230_1_cov3_rimng py
Atomic%	41.64771	0.004695	3.056094	55.36405	-0.024435	0.002912	-0.048575	0.002089	-0.006522	0.007862	-0.014985	0.0091	100.0945	819230_1_cov3_rimng py
Det Lim ppm	582	219	297	705	613	641	1123	363	389	483	1448	733	0	819230_1_cov3_rimng py
Weight%	55.0228	-0.00334	46.95883	0.045754	0.005828	0.06024	-0.417186	0.002746	-0.027555	-0.044196	-0.028006	-0.137003	102.0962	819230_1_py1
Atomic%	67.17639	-0.00238	32.91205	0.028183	0.003489	0.031471	-0.078809	0.000996	-0.009595	-0.014208	-0.005565	-0.042026	100.1526	819230_1_py1
Det Lim ppm	623	231	385	480	557	418	1264	353	403	498	1393	835	0	819230_1_py1
Weight%	23.65453	0.016104	0.557847	76.39594	-0.002608	0.019354	-0.127499	-0.00075	0.010054	-0.000753	-0.079468	0.047912	100.7017	819230_2_cov1
Atomic%	37.83757	0.015032	0.512257	61.65302	-0.002045	0.013247	-0.031557	-0.000356	0.004587	-0.000317	-0.020691	0.019256	100.055	819230_2_cov1
Det Lim ppm	560	214	276	718	616	638	1084	365	389	498	1474	735	0	819230_2_cov1
Weight%	0.006781	0.008197	62.60818	0.197673	0.001599	0.10566	0.040542	0.01387	-0.031893	-0.016539	0.004038	-0.169305	62.98655	819230_2_hem1
Atomic%	0.018807	0.013268	99.68836	0.276613	0.002175	0.125405	0.017399	0.011434	-0.025229	-0.012079	0.001823	-0.117987	100.1553	819230_2_hem1
Det Lim ppm	315	199	381	432	521	582	714	297	350	431	1268	757	0	819230_2_hem1
Weight%	54.68115	-0.003739	46.52774	-0.022719	-0.005004	0.031479	-0.434152	0.025582	-0.0323	-0.00902	0.02567	-0.071956	101.2916	819230_2_py1
Atomic%	67.25554	-0.002684	32.85232	-0.014098	-0.003018	0.016568	-0.082624	0.009352	-0.011331	-0.002921	0.005139	-0.022237	100.1389	819230_2_py1
Det Lim ppm	625	236	368	476	554	447	1260	349	407	490	1368	807	0	819230_2_py1
Weight%	21.00141	-0.002311	0.333789	78.41243	-0.011542	0.026462	-0.171782	0.082317	-0.002002	0.001876	-0.09675	0.015287	99.87357	819253_1_dju1
Atomic%	34.57386	-0.00222	0.315453	65.12679	-0.009318	0.018641	-0.043757	0.040277	-0.00094	0.000813	-0.025925	0.006323	100.0821	819253_1_dju1
Det Lim ppm	551	224	282	739	644	643	1102	357	391	508	1498	752	0	819253_1_dju1
Weight%	21.55237	-0.000166	0.364922	78.1035	-0.024303	0.038027	-0.185632	0.021998	-0.01107	0.023755	-0.041314	0.055431	100.16	819253_1_dju2
Atomic%	35.24006	-0.000158	0.342536	64.42987	-0.019486	0.026607	-0.046964	0.010691	-0.005162	0.010228	-0.010995	0.022772	100.0828	819253_1_dju2
Det Lim ppm	558	224	292	738	642	650	1115	359	396	492	1485	731	0	819253_1_dju2
Weight%	21.5607	-0.002804	0.887985	76.25652	-0.053433	0.017429	-0.133113	0.036194	-0.015968	0.020941	0.004053	0.024959	98.80877	819253_2_cct1
Atomic%	35.62527	-0.002703	0.842296	63.56933	-0.043294	0.012323	-0.034032	0.017775	-0.007525	0.009111	0.00109	0.010362	100.0875	819253_2_cct1
Det Lim ppm	544	219	285	745	645	674	1072	367	401	509	1459	728	0	819253_2_cct1
Weight%	0.117444	-0.024135	0.170347	2.400188	-0.104647	0.04396	-1.698392	3.036868	0.005799	-0.0153	97.13047	0.114612	103.0197	819253_2_electrum1
Atomic%	0.657741	-0.078879	0.547675	6.781811	-0.28739	0.10535	-1.471759	5.055008	0.009262	-0.022564	88.54247	0.161276	101.8606	819253_2_electrum1
Det Lim ppm	549	346	450	610	745	508	2618	608	603	773	2047	1059	0	819253_2_electrum1
Weight%	0.020825	0.030249	61.8285	0.463166	0.026508	0.108303	0	0.003802	-0.034145	-0.01244	-0.005774	-0.156704	62.48134	819253_3_mag?1
Atomic%	0.058214	0.049345	99.21925	0.653214	0.036337	0.129551	0	0.003159	-0.027222	-0.009157	-0.002627	-0.110062	100.1491	819253_3_mag?1
Det Lim ppm	283	200	375	436	521	567	-1	293	344	419	1272	759	0	819253_3_mag?1
Weight%	21.21469	0.000166	0.383064	77.2806	-0.059991	0.012174	-0.186198	0.009773	-0.007062	-0.013608	-0.02504	0.084731	98.98521	819233_1_cct1
Atomic%	35.13208	0.000161	0.364168	64.56734	-0.048716	0.008627	-0.047711	0.00481	-0.003335	-0.005934	-0.00675	0.035255	100.1124	819233_1_cct1
Det Lim ppm	556	219	293	740	645	673	1090	361	390	501	1477	701	0	819233_1_cct1
Weight%	0.019481	0.00239	0.02464	83.97358	-0.024535	0.013582	-0.024307	-0.007288	0.014034	0.009742	-0.019736	0.085153	84.14261	819233_1_cup1
Atomic%	0.045931	0.003288	0.03335	99.88771	-0.028366	0.013703	-0.008867	-0.005107	0.009437	0.006049	-0.007574	0.050444	100.0499	819233_1_cup1
Det Lim ppm	377	198	261	733	616	769	861	359	367	469	1427	667	0	819233_1_cup1
Weight%	0.011609	-0.007592	0.001158	84.05904	-0.019851	0.005803	-0.05508	-0.009993	-0.007571	0.014224	-0.039787	0.03102	84.12285	819237_1_cup1
Atomic%	0.027379	-0.010449	0.001568	100.0189	-0.022958	0.005857	-0.0201	-0.007004	-0.005093	0.008834	-0.015273	0.018381	100.0809	819237_1_cup1
Det Lim ppm	379	202	258	733	617	774	910	350	384	460	1428	679	0	819237_1_cup1
Weight%	-0.013813	-0.005209	0.010882	84.89528	-0.020915	0.042556	-0.00661	0.004314	-0.022706	0.020464	-0.026671	0.021649	84.99515	819237_2_cup1
Atomic%	-0.032252	-0.007097	0.014586	100.0056	-0.023946	0.042519	-0.002388	0.002994	-0.01512	0.012582	-0.010136	0.0127	100.0909	819237_2_cup1
Det Lim ppm	434	202	245	732	624	730	862	344	380	467	1429	701	0	819237_2_cup1
Weight%	34.65117	0.017525	28.80344	35.34018	0.029825	0.073834	-0.370141	0.008321	0.000523	-0.001565	0.002329	-0.057484	98.92714	819250_1_cpy
Atomic%	50.21666	0.014821	23.96282	25.8389	0.021195	0.045787	-0.082999	0.003584	0.000216	-0.000597	0.000549	-0.020931	100.1045	819250_1_cpy
Det Lim ppm	598	220	351	631	592	547	1269	363	395	497	1431	796	0	819250_1_cpy
Weight%	21.32833	-0.008869	0.654737	77.9337	0.010548	-0.012232	-0.275393	0.025182	-0.018759	-0.00456	0.010524	0.000474	99.9635	819250_1_cct
Atomic%	34.97713	-0.008487	0.616393	64.48042	0.008483	-0.008584	-0.06988	0.012274	-0.008774	-0.001969	0.002809	0.000195	100.0977	819250_1_cct
Det Lim ppm	518	227	293	745	631	674	1181	376	403	516	1487	750	0	819250_1_cct

Appendix 3

EPMA Results: Copper Sulfides & Gold

	S	Mn	Fe	Cu	Zn	As	Pb	Ag	Cd	Sb	Au	Te	Total	Sample No.
Weight%	20.82252	-0.006804	0.086808	78.44256	-0.011608	-0.002221	-0.274423	0.017009	-0.022157	0.01774	0.045017	0.09029	99.52194	819250_1_electrum
Atomic%	34.45825	-0.006571	0.082468	65.49181	-0.00942	-0.001573	-0.070267	0.008366	-0.010457	0.00773	0.012126	0.037542	100.0983	819250_1_electrum
Det Lim ppm	503	223	290	749	633	656	1178	375	392	493	1516	695	0	819250_1_electrum
Weight%	35.15416	0.007203	29.45791	34.77678	0.000795	0.041616	-0.447459	-0.001561	-0.046601	-0.014877	-0.063785	-0.066572	99.43845	819250_2_cpy1
Atomic%	50.56781	0.006046	24.32557	25.23841	0.000561	0.025616	-0.099592	-0.000667	-0.019118	-0.005635	-0.014934	-0.024061	100.164	819250_2_cpy1
Det Lim ppm	566	224	359	627	598	548	1325	371	421	509	1456	800	0	819250_2_cpy1
Weight%	35.21635	-0.001107	29.74619	34.56491	-0.000398	0.039761	-0.417677	0.008832	-0.025353	-0.00899	0.012558	-0.085797	99.58862	819250_2_cpy2
Atomic%	50.55729	-0.000927	24.51514	25.03515	-0.00028	0.024426	-0.09278	0.003768	-0.010381	-0.003398	0.002934	-0.030947	100.1387	819250_2_cpy2
Det Lim ppm	596	233	351	615	588	547	1267	367	399	501	1439	817	0	819250_2_cpy2
Weight%	25.53753	0.00511	10.88541	61.71396	-0.02473	0.042984	-0.278982	0.023085	-0.019238	0.001497	-0.067342	-0.012668	98.20958	819250_2_dig1
Atomic%	40.61576	0.004743	9.938572	49.51929	-0.019287	0.029254	-0.068654	0.010912	-0.008726	0.000627	-0.017433	-0.005062	100.1192	819250_2_dig1
Det Lim ppm	548	219	324	683	627	619	1199	352	398	487	1459	787	0	819250_2_dig1
Weight%	25.72677	-0.001912	10.71514	62.74969	-0.03213	0.046044	-0.308562	-0.009128	0.001531	-0.002676	-0.061438	-0.011997	99.23918	819250_2_dig2
Atomic%	40.53035	-0.001758	9.690729	49.87489	-0.024821	0.03104	-0.075216	-0.004274	0.000688	-0.00111	-0.015755	-0.004749	100.1277	819250_2_dig2
Det Lim ppm	555	221	320	688	640	633	1218	367	404	494	1471	775	0	819250_2_dig2
Weight%	19.28306	-0.003302	0.131904	77.80707	-0.027996	0.017367	-0.280477	0.044804	0.014536	-0.003383	-0.021786	0.04617	97.34491	819250_2cct1
Atomic%	32.9137	-0.003289	0.129248	67.00314	-0.023433	0.012685	-0.074075	0.02273	0.007076	-0.001521	-0.006053	0.0198	100.1084	819250_2cct1
Det Lim ppm	512	221	286	749	647	656	1204	361	383	486	1490	711	0	819250_2cct1
Weight%	21.70443	0.009326	3.011687	73.94269	-0.037966	0.023167	-0.243557	0.024031	-0.015024	-0.023287	-0.017929	0.028052	98.74339	819250_2_cct2
Atomic%	35.75773	0.008967	2.848362	61.45995	-0.030672	0.016332	-0.062086	0.011767	-0.007059	-0.010102	-0.004808	0.011612	100.1147	819250_2_cct2
Det Lim ppm	557	213	302	719	643	665	1164	362	397	519	1484	720	0	819250_2_cct2
Weight%	0.000358	-0.001047	0.000698	84.40314	-0.032773	-0.004538	-0.023252	0.003195	-0.00438	0	-0.040865	0.04359	84.45098	819250_3_cup1
Atomic%	0.000841	-0.001435	0.000941	100.041	-0.037756	-0.004562	-0.008452	0.002231	-0.002935	0	-0.015627	0.02573	100.0707	819250_3_cup1
Det Lim ppm	378	201	264	728	627	753	884	340	380	448	1437	706	0	819250_3_cup1
Weight%	0.001068	-0.002583	0.010875	62.96772	-0.058966	0.030935	0.021378	0.001391	0.000703	0.014523	0.067843	-0.000952	63.11644	819250_3_cup2
Atomic%	0.003362	-0.004744	0.019647	99.97269	-0.090993	0.041658	0.01041	0.001301	0.000631	0.012035	0.034751	-0.000753	100.0965	819250_3_cup2
Det Lim ppm	389	182	226	637	563	664	727	314	336	434	1287	654	0	819250_3_cup2
Weight%	25.97795	0.004859	11.20511	62.5306	-0.033963	0.015958	-0.348747	0.002275	-0.025954	0.020967	0.013259	-0.016385	99.77097	819250_4_bor1
Atomic%	40.65785	0.004438	10.06745	49.37504	-0.026065	0.010687	-0.084455	0.001058	-0.011585	0.008641	0.003378	-0.006443	100.1285	819250_4_bor1
Det Lim ppm	563	220	313	716	620	641	1253	362	402	499	1456	780	0	819250_4_bor1
Weight%	25.99119	-0.018959	11.82172	61.37353	-0.030566	0.064629	-0.322216	0.03035	0.013747	0.01564	-0.061296	0.005079	99.31588	819250_4_bor2
Atomic%	40.80139	-0.017368	10.65352	48.60771	-0.023529	0.043414	-0.078265	0.01416	0.006155	0.006465	-0.015662	0.002003	100.1348	819250_4_bor2
Det Lim ppm	584	234	319	685	637	593	1222	349	381	491	1474	760	0	819250_4_bor2
Weight%	20.95881	0.002277	0.189857	78.25987	0.003295	-0.022254	-0.25133	0.025742	-0.014558	0.008137	-0.132257	0.025141	99.47314	819250_4_cct1
Atomic%	34.64487	0.002196	0.180162	65.26595	0.002671	-0.015741	-0.064282	0.012647	-0.006863	0.003542	-0.035585	0.010442	100.1225	819250_4_cct1
Det Lim ppm	528	216	293	736	619	682	1161	360	397	489	1486	735	0	819250_4_cct1
Weight%	21.05064	-0.00553	0.050893	78.5261	-0.043046	0.070989	-0.302223	0.019198	-0.019324	0.011053	-0.088538	0.078777	99.80766	819250_4_cct2
Atomic%	34.69963	-0.005319	0.048159	65.30535	-0.034795	0.050073	-0.077083	0.009406	-0.009085	0.004798	-0.023755	0.032626	100.15	819250_4_cct2
Det Lim ppm	546	225	293	743	649	652	1219	364	403	499	1505	715	0	819250_4_cct2
Weight%	34.06369	-0.004929	27.95316	36.6334	-0.02283	0.019799	-0.460381	0.018798	-0.00907	-0.020931	-0.031841	-0.081389	98.68885	819250_4_cpy1
Atomic%	49.73681	-0.004199	23.43046	26.98602	-0.016346	0.01237	-0.104011	0.008158	-0.003777	-0.008048	-0.007567	-0.029858	100.1738	819250_4_cpy1
Det Lim ppm	589	226	354	625	595	551	1318	354	400	496	1410	812	0	819250_4_cpy1
Weight%	35.1447	0.005026	29.5106	35.00637	-0.025659	0.079951	-0.460141	0.01416	-0.023749	-0.029201	-0.047876	-0.060816	99.7608	819250_4_cpy2
Atomic%	50.4466	0.00421	24.31721	25.35096	-0.018061	0.049108	-0.102197	0.006041	-0.009722	-0.011037	-0.0111186	-0.021933	100.1741	819250_4_cpy2
Det Lim ppm	594	228	363	613	601	535	1327	364	401	518	1477	811	0	819250_4_cpy2
Weight%	19.49774	-0.004974	0.11321	79.42359	-0.037505	0.040596	-0.263067	0.010501	-0.013846	0.015479	-0.023261	0.050597	99.15173	819250_4_cct3
Atomic%	32.7139	-0.00487	0.109043	67.23151	-0.030857	0.029146	-0.068295	0.005236	-0.006626	0.006839	-0.006352	0.02133	100.117	819250_4_cct3
Det Lim ppm	525	222	295	758	640	636	1183	357	390	485	1482	711	0	819250_4_cct3

Appendix 3

EPMA Results: Copper Sulfides & Gold

	S	Mn	Fe	Cu	Zn	As	Pb	Ag	Cd	Sb	Au	Te	Total	Sample No.
Weight%	20.53815	0.001825	0.29317	79.114	-0.020588	0.020617	-0.246798	0.023254	0.013339	0.012076	-0.126008	0.040886	100.0573	819250_4_cct4
Atomic%	33.89915	0.001758	0.277786	65.88039	-0.016663	0.014562	-0.063029	0.011408	0.006279	0.005248	-0.033853	0.016956	100.1135	819250_4_cct4
Det Lim ppm	551	220	294	754	635	645	1149	356	386	491	1514	741	0	819250_4_cct4
Weight%	35.02521	0.003664	28.75761	35.70815	-0.028827	0.026363	-0.348305	0.006718	-0.010139	-0.001166	-0.039782	-0.062571	99.52771	819250_5_cpy1
Atomic%	50.41675	0.003078	23.7635	25.93204	-0.020348	0.016239	-0.077576	0.002874	-0.004163	-0.000442	-0.009321	-0.02263	100.1345	819250_5_cpy1
Det Lim ppm	595	223	336	632	614	573	1260	364	395	505	1429	812	0	819250_5_cpy1
Weight%	25.64109	-0.000519	11.03665	62.42859	-0.04835	0.059166	-0.312204	0.003532	0.013457	-0.022065	-0.104481	-0.011559	99.18248	819250_5_bor1
Atomic%	40.43998	-0.000478	9.992526	49.67448	-0.037393	0.03993	-0.076188	0.001656	0.006053	-0.009164	-0.026822	-0.004581	100.1546	819250_5_bor1
Det Lim ppm	540	226	310	704	633	624	1200	364	384	505	1487	772	0	819250_5_bor1
Weight%	25.72783	0.009135	11.04424	62.69253	-0.020477	0.035507	-0.366027	0.03379	0.008503	0.018534	-0.062966	-0.001509	99.57008	819250_5_bor2
Atomic%	40.41573	0.008375	9.959714	49.68649	-0.015773	0.023868	-0.088968	0.015776	0.00381	0.007667	-0.0161	-0.000595	100.1214	819250_5_bor2
Det Lim ppm	607	224	325	689	632	634	1231	362	401	490	1485	776	0	819250_5_bor2
Weight%	20.94405	0.007483	0.476784	77.80516	0.011358	0.039046	-0.279708	0.021069	0.002466	0.00001	-0.050756	0.023934	99.33138	819250_5_cct1
Atomic%	34.64127	0.007223	0.452709	64.92573	0.009212	0.027635	-0.071583	0.010357	0.001163	0.000004	-0.013664	0.009946	100.0852	819250_5_cct1
Det Lim ppm	520	211	276	747	617	653	1170	359	388	2840620	1467	717	0	819250_5_cct1
Weight%	20.81227	-0.002492	0.118842	78.11318	-0.009745	-0.006669	-0.289261	0.020033	-0.011597	-0.007557	-0.00091	0.048908	99.11324	819250_5_cct2
Atomic%	34.54386	-0.002413	0.113236	65.41103	-0.007931	-0.004737	-0.074287	0.009883	-0.00549	-0.003303	-0.000246	0.020396	100.0984	819250_5_cct2
Det Lim ppm	545	217	266	755	629	669	1212	365	396	506	1482	732	0	819250_5_cct2
Weight%	25.87064	-0.004033	10.98876	62.7048	-0.033934	0.01302	-0.322171	0.028115	-0.01132	0.019658	-0.09797	0.00091	99.6259	819245_1_bor1
Atomic%	40.58403	-0.003692	9.896016	49.6277	-0.026104	0.00874	-0.0782	0.013109	-0.005065	0.008121	-0.025016	0.000359	100.1381	819245_1_bor1
Det Lim ppm	567	224	325	708	624	640	1224	365	403	486	1483	770	0	819245_1_bor1
Weight%	22.10233	0.006029	0.57721	76.74808	0.018667	-0.014985	-0.280662	0.084563	0.00444	0.008873	-0.034652	0.031301	99.58149	819245_1_dig1
Atomic%	36.14554	0.005753	0.541894	63.32272	0.01497	-0.010486	-0.071019	0.041102	0.002071	0.003821	-0.009224	0.012861	100.0908	819245_1_dig1
Det Lim ppm	530	215	283	730	606	655	1182	356	390	494	1481	726	0	819245_1_dig1
Weight%	25.76033	-0.007677	10.90955	62.56807	-0.043358	0.018143	-0.388868	0.029753	0.00256	0.014191	-0.043222	0.009556	99.31214	819245_1_bor2
Atomic%	40.55447	-0.007053	9.859571	49.69532	-0.033472	0.012223	-0.094725	0.013922	0.001149	0.005883	-0.011076	0.00378	100.1463	819245_1_bor2
Det Lim ppm	568	227	314	701	637	644	1246	362	399	499	1475	787	0	819245_1_bor2
Weight%	20.88882	-0.000994	0.257416	76.51517	-0.008962	0.026443	-0.229337	0.065157	-0.006281	0.010546	-0.088394	0.06117	97.82472	819245_1_cct2
Atomic%	35.02959	-0.000973	0.247811	64.7357	-0.007369	0.018975	-0.059507	0.032475	-0.003004	0.004657	-0.024128	0.025774	100.095	819245_1_cct2
Det Lim ppm	519	216	285	739	628	658	1189	362	401	498	1506	716	0	819245_1_cct2
Weight%	25.69213	0.002072	10.22427	62.63992	-0.042916	0.068825	-0.33278	0.053426	-0.014459	-0.009882	-0.048272	-0.011348	98.68064	819245_1_bor3
Atomic%	40.70298	0.001915	9.298698	50.06713	-0.03334	0.046658	-0.081575	0.025157	-0.006533	-0.004122	-0.012448	-0.004517	100.1425	819245_1_bor3
Det Lim ppm	559	220	314	708	634	612	1233	353	403	503	1456	759	0	819245_1_bor3
Weight%	20.60873	0.008405	0.051624	76.92543	-0.03158	0.010451	-0.275523	0.044242	-0.010006	0.003	-0.132688	0.034978	97.68686	819245_1_cct3
Atomic%	34.69598	0.008258	0.049894	65.33909	-0.026071	0.007529	-0.071773	0.022138	-0.004804	0.00133	-0.03636	0.014796	100.139	819245_1_cct3
Det Lim ppm	553	212	289	746	633	669	1181	374	399	501	1503	725	0	819245_1_cct3
Weight%	25.40012	0.001403	10.77793	62.7143	0.016584	0.029285	-0.372107	0.042426	-0.025473	-0.006555	-0.032375	-0.028794	98.98204	819245_2_bor1
Atomic%	40.201	0.001296	9.79265	50.07753	0.012871	0.019833	-0.091126	0.019958	-0.011499	-0.002732	-0.00834	-0.01145	100.1251	819245_2_bor1
Det Lim ppm	573	226	322	695	610	625	1256	354	412	516	1489	806	0	819245_2_bor1
Weight%	26.07934	0.002791	11.15909	62.44225	-0.006137	0.05114	-0.318884	0.028972	0.002814	-0.01763	-0.048244	-0.027921	99.7664	819245_2_bor2
Atomic%	40.78107	0.002547	10.01739	49.26242	-0.004706	0.03422	-0.077156	0.013465	0.001255	-0.00726	-0.012279	-0.01097	100.1124	819245_2_bor2
Det Lim ppm	555	227	311	701	619	606	1232	358	396	516	1476	778	0	819245_2_bor2
Weight%	23.19478	-0.006579	1.523961	75.17054	-0.017355	0.014128	-0.273809	0.090996	-0.005341	0.04459	-0.14577	0.077465	100.1165	819245_2_dig1
Atomic%	37.42377	-0.006195	1.411546	61.18997	-0.013731	0.009755	-0.068356	0.043636	-0.002458	0.018945	-0.038282	0.031403	100.129	819245_2_dig1
Det Lim ppm	535	228	292	726	640	653	1232	365	402	487	1510	700	0	819245_2_dig1
Weight%	23.93305	-0.008582	0.685665	74.68541	-0.03047	0.019385	-0.34265	0.104689	-0.008141	0.008764	-0.108471	0.064364	99.50133	819245_2_dig2
Atomic%	38.61936	-0.008082	0.63516	60.80204	-0.02411	0.013385	-0.085552	0.050209	-0.003747	0.003724	-0.02849	0.026095	100.15	819245_2_dig2
Det Lim ppm	567	223	296	739	623	656	1243	364	398	491	1499	722	0	819245_2_dig2

Appendix 3

EPMA Results: Copper Sulfides & Gold

	S	Mn	Fe	Cu	Zn	As	Pb	Ag	Cd	Sb	Au	Te	Total	Sample No.
Weight%	34.83204	0.002027	28.90565	35.16665	-0.020647	0.034977	-0.463543	-0.002338	-0.014116	-0.015243	-0.004185	-0.025047	98.94135	819245_2_cpy1
Atomic%	50.41793	0.001712	24.01887	25.68103	-0.014655	0.021664	-0.103817	-0.001006	-0.005827	-0.00581	-0.000986	-0.009109	100.1412	819245_2_cpy1
Det Lim ppm	595	228	352	616	596	539	1301	354	400	510	1448	789	0	819245_2_cpy1
Weight%	22.22149	-0.002819	0.203685	75.18085	0.000742	0.009748	-0.269404	0.112346	-0.011556	-0.014306	-0.079035	0.049334	97.7782	819245_3_dig1
Atomic%	36.8788	-0.00273	0.194056	62.94862	0.000604	0.006923	-0.06918	0.055415	-0.00547	-0.006252	-0.02135	0.020572	100.105	819245_3_dig1
Det Lim ppm	579	218	293	746	630	660	1188	353	397	498	1487	725	0	819245_3_dig1
Weight%	22.49245	-0.004852	1.645839	75.19552	-0.020609	0.023349	-0.302654	0.049141	0.001261	-0.015503	-0.087634	0.058699	99.46626	819245_3_dig2
Atomic%	36.67074	-0.004617	1.540402	61.85148	-0.016476	0.016289	-0.076349	0.023812	0.000586	-0.006656	-0.023256	0.024045	100.1273	819245_3_dig2
Det Lim ppm	530	220	286	743	634	648	1211	355	395	506	1495	714	0	819245_3_dig2
Weight%	22.46618	0.002702	1.472347	75.59743	-0.025349	0.028553	-0.30477	0.07697	-0.008154	-0.010693	-0.068793	0.043809	99.688	819245_4_dig1
Atomic%	36.57599	0.002567	1.37607	62.09393	-0.020237	0.019892	-0.076774	0.037244	-0.003786	-0.004584	-0.01823	0.01792	100.1236	819245_4_dig1
Det Lim ppm	538	216	286	747	619	663	1233	360	398	507	1502	752	0	819245_4_dig1
Weight%	22.76938	0.009329	0.574187	76.5382	-0.021312	0.057035	-0.268265	0.059142	-0.008826	-0.021536	-0.046255	-0.018672	100.0073	819245_4_dig2
Atomic%	36.91005	0.008825	0.534331	62.59605	-0.016941	0.039563	-0.067287	0.028494	-0.004081	-0.009193	-0.012205	-0.007605	100.1173	819245_4_dig2
Det Lim ppm	558	218	293	740	638	633	1190	361	391	511	1476	752	0	819245_4_dig2
Weight%	26.21102	-0.005747	11.05267	61.86964	-0.011097	0.048822	-0.369418	0.017	-0.013282	-0.009565	0.018793	-0.012835	99.21795	819245_4_bor1
Atomic%	41.13224	-0.005263	9.95702	48.98368	-0.00854	0.032784	-0.0897	0.007929	-0.005944	-0.003952	0.0048	-0.00506	100.1185	819245_4_bor1
Det Lim ppm	552	231	320	704	603	611	1260	364	400	491	1453	777	0	819245_4_bor1
Weight%	35.04278	0.002197	29.90513	34.28411	0.018534	0.02482	-0.38898	0.007475	-0.00389	-0.001939	-0.11306	-0.092048	99.28504	819245_4_cpy1
Atomic%	50.47418	0.001847	24.72749	24.91374	0.01309	0.015298	-0.086691	0.0032	-0.001598	-0.000735	-0.026506	-0.033312	100.1488	819245_4_cpy1
Det Lim ppm	577	230	346	617	591	556	1257	367	393	501	1447	822	0	819245_4_cpy1
Weight%	26.06811	0.013086	16.97658	51.328	-0.028535	0.014281	-0.352149	3.396727	0.022765	0.038659	0.030145	1.658331	99.54667	819245_4_AuAgTell1
Atomic%	41.3106	0.012101	15.44421	41.03756	-0.022174	0.009684	-0.086348	1.599866	0.010289	0.016132	0.007776	0.660292	100.1085	819245_4_AuAgTell1
Det Lim ppm	554	230	335	680	628	654	1239	358	445	482	1465	771	0	819245_4_AuAgTell1
Weight%	0.115384	-0.035243	0.018477	0.824108	-0.099489	0.009448	-1.707437	3.748494	0.028067	-0.053196	89.77831	0.037016	94.5593	819245_5_Electrum1
Atomic%	0.723739	-0.129001	0.066532	2.607927	-0.306007	0.025359	-1.657122	6.988173	0.05021	-0.087863	91.65972	0.058336	102.18	819245_5_Electrum1
Det Lim ppm	518	347	453	593	725	499	2640	596	587	778	1998	1090	0	819245_5_Electrum1
Weight%	0.064626	-0.016746	0.021301	0.791455	-0.104491	0.047365	-1.778274	3.918052	-0.002325	-0.017644	91.3309	0.014989	96.1887	819245_5_Electrum2
Atomic%	0.399199	-0.060365	0.075533	2.466494	-0.316501	0.125196	-1.699618	7.193164	-0.004096	-0.0287	91.82642	0.023264	102.1093	819245_5_Electrum2
Det Lim ppm	528	343	449	591	731	496	2672	609	609	768	2024	1056	0	819245_5_Electrum2
Weight%	22.7252	-0.002535	1.03585	74.47356	-0.000001	0.010398	-0.33149	0.037311	-0.006642	0.026401	-0.032587	0.03257	98.34129	819245_5_cct1
Atomic%	37.33786	-0.002431	0.977017	61.73325	-0.000001	0.00731	-0.084273	0.01822	-0.003112	0.011422	-0.008715	0.013445	100.0985	819245_5_cct1
Det Lim ppm	561	225	293	730	634	663	1213	370	396	498	1490	734	0	819245_5_cct1
Weight%	28.62506	0.006168	6.68082	56.27197	-0.025056	0.023437	-0.2043	0.046731	-0.011744	0.019888	0.012013	0.064365	91.75045	819254_1_cov1
Atomic%	47.03886	0.005915	6.302368	46.6528	-0.020191	0.01648	-0.051946	0.022824	-0.005504	0.008606	0.003213	0.026575	100.0776	819254_1_cov1
Det Lim ppm	575	215	302	663	609	573	1115	350	389	490	1405	712	0	819254_1_cov1
Weight%	24.06237	0.006219	0.421422	74.86431	-0.060232	0.005399	-0.159452	0.059684	0.014755	-0.040761	-0.009582	0.029592	99.46376	819254_1_cct1
Atomic%	38.78313	0.00585	0.389929	60.87719	-0.047605	0.003724	-0.039766	0.028591	0.006783	-0.0173	-0.002514	0.011984	100.1072	819254_1_cct1
Det Lim ppm	555	215	284	739	643	666	1080	351	393	526	1461	739	0	819254_1_cct1
Weight%	31.18205	-0.012699	5.403444	59.92776	-0.019293	0.000993	-0.257463	0.010187	-0.019426	-0.005878	-0.027308	0.013998	96.53842	819254_2_cov1
Atomic%	48.37631	-0.011497	4.812408	46.90633	-0.014677	0.000659	-0.061804	0.004697	-0.008595	-0.002402	-0.006896	0.005456	100.1059	819254_2_cov1
Det Lim ppm	631	223	293	697	617	607	1161	356	398	489	1437	729	0	819254_2_cov1
Weight%	0.310871	-0.011294	43.4252	0.897684	0.067084	0.09651	0.033669	0.006865	-0.013302	-0.003655	-0.009876	-0.111232	44.83788	819254_2_goe-rim1
Atomic%	1.208049	-0.025612	96.87445	1.759959	0.127833	0.160485	0.020245	0.007929	-0.014742	-0.003741	-0.006247	-0.108604	100.1589	819254_2_goe-rim1
Det Lim ppm	316	188	322	403	482	560	663	271	320	372	1182	661	0	819254_2_goe-rim1
Weight%	18.805	0.005232	8.778892	66.40396	-0.01241	0.01854	-0.14709	-0.011605	-0.018902	-0.031006	-0.07026	0.02477	94.03639	819254_2_cpy-rim-cct1
Atomic%	32.81478	0.005328	8.794265	58.46089	-0.010619	0.013844	-0.039715	-0.006019	-0.009407	-0.014248	-0.019956	0.01086	100.1	819254_2_cpy-rim-cct1
Det Lim ppm	488	210	296	709	607	680	1059	361	392	503	1425	713	0	819254_2_cpy-rim-cct1

Appendix 3

EPMA Results: Copper Sulfides & Gold

	S	Mn	Fe	Cu	Zn	As	Pb	Ag	Cd	Sb	Au	Te	Total	Sample No.
Weight%	34.03637	-0.000183	25.5098	39.25184	0.797787	0.071614	-0.259814	0.003371	-0.016956	-0.007022	-0.052477	-0.023426	99.67078	819257_1_cpy1
Atomic%	49.43886	-0.000155	21.2714	28.76475	0.568239	0.044513	-0.058393	0.001455	-0.007024	-0.002686	-0.012407	-0.008549	100.0892	819257_1_cpy1
Det Lim ppm	639	228	344	638	599	543	1178	365	402	504	1465	781	0	819257_1_cpy1
Weight%	22.62272	0.013204	1.290741	76.17229	-0.032979	0.04573	-0.224148	0.00978	-0.004795	-0.010964	-0.056339	0.102729	100.2572	819257_1_dig1
Atomic%	36.61489	0.012471	1.199267	62.19925	-0.026174	0.031671	-0.056133	0.004705	-0.002213	-0.004673	-0.014842	0.041775	100.104	819257_1_dig1
Det Lim ppm	565	212	308	741	635	647	1139	373	399	505	1490	716	0	819257_1_dig1
Weight%	21.34728	0.005475	0.328988	78.03719	0.000742	0.007728	-0.196099	0.040973	0.002766	0.015077	-0.014073	0.074794	99.86102	819257_2_cctmyk1
Atomic%	35.04314	0.005244	0.310031	64.63047	0.000598	0.005428	-0.049809	0.019991	0.001295	0.006517	-0.00376	0.030849	100.0536	819257_2_cctmyk1
Det Lim ppm	557	220	292	741	637	678	1125	362	398	492	1479	693	0	819257_2_cctmyk1
Weight%	21.75154	0.001828	0.601231	77.95036	-0.035161	0.012105	-0.150152	0.022517	-0.000252	-0.020375	-0.114443	-0.000657	100.3396	819257_2_cctmyk2
Atomic%	35.44203	0.001738	0.562385	64.07993	-0.028094	0.00844	-0.037856	0.010905	-0.000117	-0.008742	-0.030352	-0.000269	100.1054	819257_2_cctmyk2
Det Lim ppm	529	220	283	750	624	671	1099	377	388	518	1489	756	0	819257_2_cctmyk2
Weight%	0.102909	-0.039678	0.040622	0.821248	-0.16228	0.007243	-1.784525	2.253957	0.010093	0.001785	98.1979	0.106766	101.5425	819257_3_electrum1
Atomic%	0.610792	-0.137431	0.13841	2.459175	-0.472306	0.018395	-1.63884	3.976094	0.017085	0.00279	94.86662	0.159215	102.2486	819257_3_electrum1
Det Lim ppm	532	345	451	597	745	508	2668	597	588	773	2031	1038	0	819257_3_electrum1
Weight%	26.55508	0.01252	11.11521	62.02362	-0.035929	0.070757	-0.124668	0.031424	-0.007394	0.000764	-0.081507	0.021017	99.83039	819257_3_bor1
Atomic%	41.345	0.011376	9.934746	48.72007	-0.027431	0.047141	-0.030033	0.014541	-0.003283	0.000313	-0.020656	0.008222	100.0814	819257_3_bor1
Det Lim ppm	623	217	313	703	623	611	1070	362	395	499	1473	759	0	819257_3_bor1
Weight%	31.53543	-0.004155	22.62532	44.11982	0.038757	0.061286	-0.108899	0.02107	-0.023779	0.010832	-0.054534	-0.031576	98.41251	819257_4_cpy-smeared1
Atomic%	47.21257	-0.00363	19.44542	33.32483	0.028453	0.039262	-0.025226	0.009375	-0.010154	0.004271	-0.013289	-0.011878	100.0642	819257_4_cpy-smeared1
Det Lim ppm	603	223	344	644	607	588	1161	370	405	487	1456	800	0	819257_4_cpy-smeared1
Weight%	23.10946	0.000335	1.938145	75.28245	-0.012014	0.044434	-0.192592	0.027116	-0.002021	-0.020441	0.0191	0.035795	100.4568	819257_4_dig1
Atomic%	37.15285	0.000315	1.788761	61.06205	-0.009471	0.030569	-0.047909	0.012957	-0.000927	-0.008654	0.004998	0.014459	100.067	819257_4_dig1
Det Lim ppm	568	219	289	729	635	644	1127	363	389	518	1468	736	0	819257_4_dig1

Abbreviations: Det Lim = detection limit; ppm = parts per million; cpy = chalcopyrite; bor = bornite; py = pyrite; cct = chalcocite; cov = covellite; dig = digenite; dju = djurleite; cup = cuprite; cu = native copper; mag = magnetite; hem = hematite; goe = goethite; Au = gold; Ag = silver; Tel = telluride

APPENDIX 4

EPMA RESULTS: COPPER OXIDES
(Weight % & Atomic %)

Appendix 4

EPMA Results: Copper Oxides

	Na	Mg	Al	Si	P	S	K	Ca	Mn	Fe	Cu	Zn	Sr	Ba	Pb	C	O	Total	Sample No.
Weight%	-0.037	-0.011	0.000	1.549	0.034	0.032	0.003	0.006	-0.002	0.041	54.774	-0.020	0.004	0.079	0.010	7.559	35.786	99.877	819222_2_mal1
Atomic%	-0.043	-0.012	0.000	1.457	0.029	0.026	0.002	0.004	-0.001	0.020	22.777	-0.008	0.001	0.015	0.001	16.630	59.102	100.064	819222_2_mal1
Det Lim ppm	371.000	294.000	0.000	249.000	297.000	208.000	223.000	330.000	576.000	643.000	719.000	710.000	491.000	498.000	710.000	0.000	0.000	0.000	819222_2_mal1
Weight%	-0.026	0.003	0.000	0.047	0.049	-0.007	-0.002	0.018	-0.014	0.092	57.681	0.012	-0.017	0.088	-0.006	7.430	34.455	99.875	819223_1_mal1
Atomic%	-0.031	0.003	0.000	0.045	0.043	-0.006	-0.002	0.012	-0.007	0.045	24.638	0.005	-0.005	0.017	-0.001	16.790	58.452	100.051	819223_1_mal1
Det Lim ppm	360.000	261.000	0.000	240.000	282.000	225.000	225.000	310.000	562.000	479.000	723.000	700.000	502.000	504.000	736.000	0.000	0.000	0.000	819223_1_mal1
Weight%	-0.024	-0.017	0.000	0.162	10.126	0.028	0.002	0.009	-0.002	0.010	54.823	-0.080	-0.021	0.038	-0.022	2.040	32.505	99.741	819223_2_chys1
Atomic%	-0.031	-0.021	0.000	0.170	9.629	0.025	0.001	0.007	-0.001	0.005	25.411	-0.036	-0.007	0.008	-0.003	5.002	59.841	100.100	819223_2_chys1
Det Lim ppm	361.000	295.000	0.000	232.000	371.000	228.000	224.000	321.000	571.000	474.000	713.000	781.000	495.000	510.000	786.000	0.000	0.000	0.000	819223_2_chys1
Weight%	-0.002	-0.012	0.000	0.074	0.044	0.005	0.006	0.009	0.024	0.082	56.896	0.031	-0.027	0.042	0.004	7.697	35.017	99.933	819223_2_mal1
Atomic%	-0.003	-0.013	0.000	0.070	0.038	0.004	0.004	0.006	0.012	0.039	23.997	0.013	-0.008	0.008	0.001	17.175	58.655	100.024	819223_2_mal1
Det Lim ppm	360.000	303.000	0.000	242.000	308.000	226.000	229.000	312.000	535.000	473.000	736.000	698.000	506.000	508.000	742.000	0.000	0.000	0.000	819223_2_mal1
Weight%	-0.020	-0.003	0.012	-0.001	0.138	0.011	0.003	0.003	-0.007	0.081	55.652	-0.011	0.015	0.061	0.048	8.095	35.807	99.927	819237_1_azur1
Atomic%	-0.022	-0.004	0.012	-0.001	0.117	0.009	0.002	0.002	-0.003	0.038	23.083	-0.005	0.005	0.012	0.006	17.763	58.986	100.035	819237_1_azur1
Det Lim ppm	347.000	270.000	234.000	241.000	310.000	205.000	222.000	333.000	558.000	451.000	717.000	694.000	484.000	499.000	678.000	0.000	0.000	0.000	819237_1_azur1
Weight%	-0.032	0.032	0.028	0.016	0.106	0.009	0.005	-0.008	0.033	0.152	57.065	0.046	-0.019	0.079	0.009	7.556	34.771	99.907	819237_1_mal1
Atomic%	-0.037	0.035	0.027	0.015	0.092	0.008	0.004	-0.005	0.016	0.073	24.206	0.019	-0.006	0.016	0.001	16.958	58.578	100.048	819237_1_mal1
Det Lim ppm	371.000	277.000	239.000	232.000	302.000	209.000	218.000	336.000	511.000	464.000	697.000	722.000	495.000	498.000	734.000	0.000	0.000	0.000	819237_1_mal1
Weight%	-0.050	0.006	0.012	0.003	0.186	0.004	0.014	-0.004	-0.004	0.025	55.638	0.022	-0.004	0.074	0.034	8.078	35.801	99.897	819237_2_azur1
Atomic%	-0.057	0.007	0.012	0.003	0.159	0.003	0.010	-0.003	-0.002	0.012	23.089	0.009	-0.001	0.014	0.004	17.736	59.006	100.063	819237_2_azur1
Det Lim ppm	377.000	275.000	229.000	240.000	284.000	222.000	215.000	320.000	538.000	451.000	711.000	700.000	488.000	496.000	678.000	0.000	0.000	0.000	819237_2_azur1
Weight%	0.041	2.941	6.344	8.367	0.018	0.088	0.026	0.045	0.032	2.985	35.504	0.008	0.048	0.046	-0.015	4.467	39.023	99.982	819294_1_chl1
Atomic%	0.044	2.962	5.755	7.292	0.014	0.067	0.016	0.027	0.014	1.308	13.676	0.003	0.014	0.008	-0.002	9.103	59.699	100.002	819294_1_chl1
Det Lim ppm	299.000	233.000	238.000	244.000	311.000	217.000	213.000	315.000	564.000	476.000	637.000	669.000	458.000	500.000	658.000	0.000	0.000	0.000	819294_1_chl1
Weight%	0.170	3.697	7.777	11.763	0.018	0.046	0.161	0.064	0.033	5.906	28.787	0.047	0.088	0.002	-0.008	2.590	38.841	99.990	819294_1_chl2
Atomic%	0.182	3.729	7.067	10.269	0.014	0.035	0.101	0.039	0.015	2.593	11.107	0.018	0.025	0.000	-0.001	5.286	59.520	100.001	819294_1_chl2
Det Lim ppm	287.000	249.000	246.000	249.000	245.000	207.000	246.000	298.000	577.000	460.000	607.000	651.000	437.000	502.000	687.000	0.000	0.000	0.000	819294_1_chl2
Weight%	0.029	6.966	8.128	12.351	0.012	0.025	0.042	0.043	0.176	16.774	8.229	0.166	0.101	-0.005	0.037	3.807	43.110	99.994	819294_2_chl1
Atomic%	0.028	6.397	6.723	9.815	0.008	0.018	0.024	0.024	0.071	6.704	2.890	0.057	0.026	-0.001	0.004	7.075	60.137	100.001	819294_2_chl1
Det Lim ppm	214.000	250.000	229.000	230.000	220.000	196.000	209.000	275.000	545.000	528.000	504.000	599.000	424.000	483.000	620.000	0.000	0.000	0.000	819294_2_chl1
Weight%	0.016	10.924	10.279	15.057	0.010	0.001	0.016	0.042	0.124	10.277	2.022	0.023	0.112	-0.021	-0.006	3.827	47.238	99.966	819294_2_chl2-light
Atomic%	0.014	9.249	7.839	11.032	0.007	0.000	0.008	0.022	0.046	3.787	0.655	0.007	0.026	-0.003	-0.001	6.557	60.754	100.004	819294_2_chl2-light
Det Lim ppm	179.000	228.000	215.000	229.000	285.000	197.000	189.000	266.000	507.000	688.000	466.000	559.000	393.000	445.000	656.000	0.000	0.000	0.000	819294_2_chl2-light
Weight%	0.008	2.492	14.548	18.098	0.018	0.066	0.029	0.033	0.032	3.646	14.641	0.051	0.136	0.013	-0.010	1.653	44.526	99.989	819294_3_chl1-dark
Atomic%	0.007	2.273	11.956	14.288	0.013	0.046	0.016	0.018	0.013	1.448	5.109	0.017	0.034	0.002	-0.001	3.052	61.708	100.001	819294_3_chl1-dark
Det Lim ppm	223.000	213.000	248.000	245.000	318.000	203.000	206.000	294.000	540.000	549.000	545.000	600.000	415.000	476.000	677.000	0.000	0.000	0.000	819294_3_chl1-dark
Weight%	-0.012	2.836	7.078	8.808	0.018	0.057	0.007	0.020	0.026	2.989	44.306	0.007	0.068	0.046	0.006	0.916	32.792	99.980	819294_3_cup-chl2-dark
Atomic%	-0.015	3.265	7.341	8.776	0.016	0.050	0.005	0.014	0.013	1.498	19.512	0.003	0.022	0.009	0.001	2.134	57.355	100.015	819294_3_cup-chl2-dark
Det Lim ppm	301.000	279.000	253.000	241.000	321.000	212.000	210.000	318.000	593.000	507.000	686.000	716.000	486.000	507.000	748.000	0.000	0.000	0.000	819294_3_cup-chl2-dark
Weight%	0.141	2.840	12.108	14.436	0.014	0.126	0.014	0.035	0.035	3.271	26.609	0.029	0.095	0.043	-0.011	0.861	39.331	99.988	819294_4_chl1
Atomic%	0.149	2.849	10.943	12.533	0.011	0.096	0.009	0.022	0.015	1.428	10.211	0.011	0.026	0.008	-0.001	1.749	59.941	100.001	819294_4_chl1
Det Lim ppm	238.000	228.000	239.000	242.000	268.000	198.000	201.000	303.000	519.000	460.000	597.000	639.000	441.000	474.000	705.000	0.000	0.000	0.000	819294_4_chl1
Weight%	0.015	0.612	14.107	5.182	0.028	0.292	0.051	0.117	0.035	2.185	43.427	0.000	0.035	0.068	-0.013	0.779	33.051	99.985	819294_4_cup-chl2-red
Atomic%	0.018	0.699	14.516	5.123	0.025	0.253	0.036	0.081	0.017	1.086	18.973	0.000	0.011	0.014	-0.002	1.800	57.349	100.002	819294_4_cup-chl2-red
Det Lim ppm	316.000	251.000	263.000	246.000	289.000	184.000	226.000	351.000	563.000	462.000	678.000	727.000	478.000	509.000	678.000	0.000	0.000	0.000	819294_4_cup-chl2-red

Appendix 4

EPMA Results: Copper Oxides

	Na	Mg	Al	Si	P	S	K	Ca	Mn	Fe	Cu	Zn	Sr	Ba	Pb	C	O	Total	Sample No.
Weight%	-0.048	-0.025	0.004	0.130	10.573	0.012	0.007	0.022	-0.003	-0.015	65.291	0.055	0.011	0.087	0.022	0.000	30.262	106.477	819235_1_chrys1
Atomic%	-0.064	-0.032	0.004	0.142	10.457	0.011	0.006	0.017	-0.002	-0.008	31.475	0.026	0.004	0.019	0.003	0.000	57.941	100.106	819235_1_chrys1
Det Lim ppm	388.000	321.000	242.000	261.000	338.000	213.000	215.000	338.000	564.000	485.000	759.000	763.000	515.000	534.000	738.000	0.000	0.000	0.000	819235_1_chrys1
Weight%	-0.029	-0.011	0.010	0.123	10.140	0.019	0.002	0.017	-0.010	0.027	55.304	0.057	0.004	0.054	-0.007	1.892	32.253	99.903	819235_1_chrys2
Atomic%	-0.037	-0.013	0.011	0.130	9.694	0.017	0.002	0.013	-0.005	0.014	25.773	0.026	0.001	0.012	-0.001	4.665	59.697	100.056	819235_1_chrys2
Det Lim ppm	355.000	297.000	232.000	249.000	355.000	217.000	220.000	329.000	566.000	454.000	718.000	714.000	497.000	510.000	732.000	0.000	0.000	0.000	819235_1_chrys2
Weight%	-0.020	-0.017	0.012	0.138	10.335	0.002	0.002	0.012	0.003	-0.044	55.420	0.071	-0.009	0.055	-0.009	1.724	32.060	99.833	819235_2_chrys1
Atomic%	-0.026	-0.021	0.013	0.146	9.937	0.002	0.002	0.009	0.002	-0.023	25.973	0.032	-0.003	0.012	-0.001	4.274	59.674	100.075	819235_2_chrys1
Det Lim ppm	346.000	310.000	232.000	236.000	322.000	227.000	225.000	338.000	564.000	547.000	697.000	702.000	501.000	515.000	740.000	0.000	0.000	0.000	819235_2_chrys1
Weight%	-0.042	-0.032	-0.005	0.137	10.105	0.013	-0.001	0.008	0.000	0.044	55.467	0.031	0.000	0.078	-0.010	1.845	32.096	99.825	819235_2_CuPhos1
Atomic%	-0.055	-0.039	-0.006	0.145	9.702	0.012	-0.001	0.006	0.000	0.024	25.958	0.014	0.000	0.017	-0.001	4.567	59.657	100.103	819235_2_CuPhos1
Det Lim ppm	371.000	323.000	238.000	235.000	341.000	229.000	231.000	325.000	583.000	444.000	705.000	699.000	500.000	503.000	758.000	0.000	0.000	0.000	819235_2_CuPhos1
Weight%	-0.038	-0.021	0.003	0.123	10.209	0.008	0.010	0.009	0.001	0.006	55.507	0.005	-0.004	0.045	-0.024	1.808	32.118	99.853	819235_2_CuPhos2
Atomic%	-0.049	-0.026	0.003	0.131	9.798	0.007	0.008	0.007	0.001	0.003	25.965	0.002	-0.001	0.010	-0.004	4.476	59.670	100.080	819235_2_CuPhos2
Det Lim ppm	382.000	325.000	249.000	246.000	355.000	243.000	222.000	323.000	555.000	490.000	715.000	726.000	495.000	516.000	757.000	0.000	0.000	0.000	819235_2_CuPhos2
Weight%	-0.006	0.007	0.007	2.003	1.223	0.020	0.019	0.087	0.021	52.330	3.701	0.105	0.002	0.002	0.037	5.602	34.825	99.990	819235_2_Goe1
Atomic%	-0.007	0.008	0.006	1.900	1.051	0.017	0.013	0.058	0.010	24.955	1.551	0.043	0.001	0.000	0.005	12.422	57.967	100.007	819235_2_Goe1
Det Lim ppm	297.000	266.000	231.000	232.000	298.000	198.000	212.000	325.000	581.000	620.000	553.000	652.000	460.000	463.000	710.000	0.000	0.000	0.000	819235_2_Goe1
Weight%	-0.036	-0.021	0.003	0.244	10.051	0.003	-0.015	0.030	-0.004	0.093	55.281	0.005	-0.031	0.084	0.030	1.856	32.143	99.821	819235_2_CuPhos3
Atomic%	-0.047	-0.025	0.003	0.258	9.638	0.002	-0.011	0.022	-0.002	0.049	25.839	0.002	-0.011	0.018	0.004	4.589	59.670	100.096	819235_2_CuPhos3
Det Lim ppm	373.000	310.000	242.000	243.000	325.000	224.000	236.000	307.000	572.000	478.000	709.000	729.000	505.000	513.000	732.000	0.000	0.000	0.000	819235_2_CuPhos3
Weight%	-0.041	0.000	0.014	0.047	0.128	-0.001	-0.005	-0.013	0.009	0.041	58.195	-0.030	-0.005	0.092	0.005	7.214	34.101	99.846	819224_1_mal1
Atomic%	-0.049	0.000	0.014	0.046	0.113	-0.001	-0.003	-0.009	0.004	0.020	25.070	-0.012	-0.002	0.018	0.001	16.443	58.345	100.076	819224_1_mal1
Det Lim ppm	387.000	286.000	243.000	238.000	312.000	224.000	218.000	350.000	534.000	432.000	714.000	723.000	495.000	496.000	739.000	0.000	0.000	0.000	819224_1_mal1
Weight%	-0.031	-0.087	0.008	0.145	9.582	0.031	0.005	-0.008	0.023	0.016	55.622	0.000	-0.015	0.080	-0.021	2.083	32.093	99.687	819224_1_CuPhos1
Atomic%	-0.039	-0.106	0.008	0.153	9.190	0.029	0.004	-0.006	0.012	0.009	26.002	0.000	-0.005	0.017	-0.003	5.152	59.584	100.160	819224_1_CuPhos1
Det Lim ppm	365.000	410.000	231.000	240.000	350.000	222.000	222.000	341.000	522.000	460.000	715.000	718.000	500.000	501.000	761.000	0.000	0.000	0.000	819224_1_CuPhos1
Weight%	-0.059	-0.104	0.003	0.133	9.528	0.034	-0.011	0.019	-0.004	-0.001	55.512	0.029	0.018	0.051	0.062	2.135	32.111	99.636	819224_1_CuPhos2
Atomic%	-0.076	-0.127	0.004	0.141	9.138	0.032	-0.009	0.014	-0.002	-0.001	25.950	0.013	0.006	0.011	0.009	5.280	59.617	100.214	819224_1_CuPhos2
Det Lim ppm	390.000	427.000	242.000	244.000	346.000	228.000	230.000	325.000	566.000	481.000	715.000	705.000	487.000	519.000	694.000	0.000	0.000	0.000	819224_1_CuPhos2
Weight%	0.012	0.000	0.352	2.946	0.228	0.061	0.029	0.070	-0.010	52.304	3.735	-0.018	0.024	0.025	0.014	5.496	34.663	99.959	819224_1_Goe1
Atomic%	0.014	0.000	0.348	2.797	0.196	0.051	0.020	0.047	-0.005	24.977	1.567	-0.007	0.007	0.005	0.002	12.203	57.777	100.012	819224_1_Goe1
Det Lim ppm	281.000	264.000	223.000	229.000	256.000	232.000	206.000	291.000	580.000	634.000	542.000	679.000	458.000	459.000	699.000	0.000	0.000	0.000	819224_1_Goe1
Weight%	-0.025	0.021	0.057	0.068	0.224	0.001	0.005	0.017	0.019	0.008	57.666	0.004	0.003	0.067	-0.011	7.319	34.466	99.945	819224_2_mal1
Atomic%	-0.030	0.023	0.057	0.066	0.197	0.001	0.004	0.012	0.009	0.004	24.632	0.002	0.001	0.013	-0.001	16.540	58.472	100.031	819224_2_mal1
Det Lim ppm	376.000	265.000	221.000	241.000	281.000	219.000	215.000	312.000	524.000	441.000	709.000	706.000	495.000	510.000	704.000	0.000	0.000	0.000	819224_2_mal1
Weight%	-0.025	-0.098	0.000	0.151	9.538	0.070	0.007	0.023	-0.009	0.141	55.480	-0.030	-0.010	0.035	0.057	2.079	32.077	99.658	819224_2_CuPhos1
Atomic%	-0.032	-0.119	0.000	0.160	9.152	0.065	0.006	0.017	-0.005	0.075	25.950	-0.014	-0.004	0.008	0.008	5.144	59.588	100.174	819224_2_CuPhos1
Det Lim ppm	359.000	416.000	237.000	235.000	358.000	229.000	222.000	296.000	561.000	474.000	698.000	724.000	499.000	514.000	730.000	0.000	0.000	0.000	819224_2_CuPhos1
Weight%	-0.025	-0.035	0.021	1.101	6.913	0.033	0.001	0.039	-0.018	16.113	39.942	-0.033	-0.010	0.033	-0.021	2.913	32.654	99.761	819224_2_CuPhos2-repl goe
Atomic%	-0.032	-0.041	0.022	1.132	6.446	0.030	0.000	0.028	-0.009	8.333	18.154	-0.015	-0.003	0.007	-0.003	7.004	58.946	100.103	819224_2_CuPhos2-repl goe
Det Lim ppm	348.000	336.000	224.000	243.000	326.000	202.000	228.000	308.000	601.000	531.000	675.000	723.000	497.000	504.000	767.000	0.000	0.000	0.000	819224_2_CuPhos2-repl goe
Weight%	0.530	1.616	15.558	22.404	0.016	0.007	4.291	0.105	-0.019	2.302	0.895	0.013	0.194	-0.008	0.001	2.605	49.422	99.959	819206_1_Clay-faintgreen1
Atomic%	0.467	1.346	11.672	16.148	0.010	0.005	2.222	0.053	-0.007	0.835	0.285	0.004	0.045	-0.001	0.000	4.390	62.527	100.008	819206_1_Clay-faintgreen1
Det Lim ppm	180.000	180.000	215.000	240.000	262.000	176.000	200.000	272.000	554.000	445.000	441.000	540.000	361.000	438.000	599.000	0.000	0.000	0.000	819206_1_Clay-faintgreen1

Appendix 4

EPMA Results: Copper Oxides

	Na	Mg	Al	Si	P	S	K	Ca	Mn	Fe	Cu	Zn	Sr	Ba	Pb	C	O	Total	Sample No.
Weight%	1.035	0.680	12.718	21.977	0.011	0.007	1.663	0.220	-0.019	1.988	6.466	0.041	0.191	-0.014	-0.014	3.572	49.367	99.937	819206_1_Clay-faintgreen2
Atomic%	0.919	0.571	9.624	15.976	0.007	0.004	0.869	0.112	-0.007	0.727	2.078	0.013	0.044	-0.002	-0.001	6.073	62.993	100.010	819206_1_Clay-faintgreen2
Det Lim ppm	214.000	176.000	228.000	249.000	255.000	199.000	209.000	292.000	538.000	446.000	481.000	547.000	364.000	457.000	629.000	0.000	0.000	0.000	819206_1_Clay-faintgreen2
Weight%	0.118	3.838	13.318	21.088	0.006	0.007	7.194	0.053	0.007	3.219	1.772	0.034	0.172	0.013	0.025	2.121	47.017	100.000	819206_1_Clay-faintgreen3
Atomic%	0.107	3.292	10.290	15.653	0.004	0.005	3.836	0.028	0.003	1.202	0.581	0.011	0.041	0.002	0.002	3.682	61.262	100.000	819206_1_Clay-faintgreen3
Det Lim ppm	179.000	192.000	225.000	256.000	245.000	180.000	191.000	285.000	556.000	480.000	463.000	567.000	381.000	447.000	625.000	0.000	0.000	0.000	819206_1_Clay-faintgreen3
Weight%	2.158	0.216	5.146	20.469	0.017	0.027	0.564	0.379	0.000	0.532	15.827	0.003	0.176	0.019	-0.009	5.775	48.680	99.989	819206_1_Clay-faintgreen4
Atomic%	1.943	0.184	3.947	15.084	0.012	0.018	0.298	0.196	0.000	0.197	5.155	0.001	0.042	0.003	-0.001	9.952	62.971	100.001	819206_1_Clay-faintgreen4
Det Lim ppm	249.000	208.000	207.000	241.000	254.000	189.000	206.000	312.000	497.000	442.000	528.000	567.000	372.000	444.000	636.000	0.000	0.000	0.000	819206_1_Clay-faintgreen4
Weight%	-0.050	-0.013	0.032	0.014	0.093	0.013	0.000	0.009	-0.017	0.006	57.935	0.006	-0.028	0.073	-0.005	7.337	34.298	99.815	819248_1_mal1
Atomic%	-0.059	-0.014	0.032	0.014	0.082	0.011	0.000	0.006	-0.008	0.003	24.849	0.002	-0.009	0.015	-0.001	16.650	58.427	100.091	819248_1_mal1
Det Lim ppm	383.000	288.000	234.000	241.000	295.000	207.000	219.000	317.000	561.000	444.000	710.000	703.000	505.000	501.000	736.000	0.000	0.000	0.000	819248_1_mal1
Weight%	-0.010	-0.002	0.014	0.007	0.050	0.011	0.007	0.002	-0.001	0.010	55.951	-0.004	0.009	0.042	-0.025	8.091	35.750	99.944	819248_1_azur1
Atomic%	-0.011	-0.002	0.014	0.006	0.042	0.009	0.005	0.001	-0.001	0.005	23.223	-0.001	0.003	0.008	-0.003	17.768	58.933	100.018	819248_1_azur1
Det Lim ppm	364.000	276.000	221.000	228.000	283.000	219.000	211.000	320.000	552.000	428.000	704.000	704.000	485.000	509.000	733.000	0.000	0.000	0.000	819248_1_azur1
Weight%	0.001	0.082	10.377	15.303	-0.003	0.013	0.039	0.054	0.023	0.116	7.596	-0.023	0.118	0.001	-0.003	10.233	55.997	99.952	819248_1_chrys1-faint blue
Atomic%	0.001	0.062	7.109	10.071	-0.002	0.008	0.019	0.025	0.008	0.038	2.209	-0.007	0.025	0.000	0.000	15.747	64.687	100.008	819248_1_chrys1-faint blue
Det Lim ppm	198.000	175.000	206.000	208.000	275.000	183.000	187.000	242.000	439.000	445.000	472.000	549.000	360.000	419.000	569.000	0.000	0.000	0.000	819248_1_chrys1-faint blue
Weight%	-0.006	0.034	10.102	15.037	0.004	0.020	0.051	0.047	-0.005	0.155	8.143	-0.031	0.129	0.009	-0.007	10.339	55.858	99.929	819248_1_chrys2-faint blue
Atomic%	-0.005	0.026	6.936	9.919	0.002	0.011	0.024	0.022	-0.002	0.051	2.374	-0.009	0.027	0.001	-0.001	15.946	64.675	100.016	819248_1_chrys2-faint blue
Det Lim ppm	200.000	189.000	201.000	208.000	222.000	163.000	168.000	271.000	489.000	375.000	461.000	554.000	352.000	411.000	611.000	0.000	0.000	0.000	819248_1_chrys2-faint blue
Weight%	0.073	0.102	1.243	17.967	0.025	0.146	0.054	0.242	0.027	0.292	29.915	0.048	0.143	0.025	-0.016	5.455	44.225	99.982	819289_1_chrys1-faint green
Atomic%	0.072	0.096	1.046	14.529	0.019	0.104	0.031	0.137	0.011	0.119	10.691	0.017	0.037	0.004	-0.002	10.314	62.775	100.002	819289_1_chrys1-faint green
Det Lim ppm	263.000	223.000	196.000	230.000	243.000	193.000	196.000	299.000	523.000	466.000	595.000	623.000	394.000	472.000	648.000	0.000	0.000	0.000	819289_1_chrys1-faint green
Weight%	-0.006	0.182	0.584	13.264	0.006	0.007	0.008	0.095	-0.004	0.178	20.373	0.030	0.093	0.012	0.003	12.046	53.104	99.982	819289_1_chrys2-interior
Atomic%	-0.005	0.145	0.420	9.168	0.004	0.004	0.004	0.046	-0.002	0.062	6.224	0.009	0.021	0.002	0.000	19.469	64.431	100.007	819289_1_chrys2-interior
Det Lim ppm	237.000	183.000	175.000	207.000	261.000	181.000	189.000	259.000	470.000	381.000	543.000	562.000	371.000	440.000	631.000	0.000	0.000	0.000	819289_1_chrys2-interior
Weight%	-0.026	-0.041	0.216	0.505	9.056	0.006	0.006	-0.004	-0.056	0.110	51.342	-0.024	-0.021	0.063	-0.007	3.551	34.836	99.692	819289_2_mal1
Atomic%	-0.031	-0.047	0.222	0.500	8.128	0.005	0.004	-0.003	-0.028	0.055	22.459	-0.010	-0.007	0.013	-0.001	8.218	60.523	100.128	819289_2_mal1
Det Lim ppm	339.000	343.000	228.000	220.000	316.000	220.000	214.000	323.000	597.000	478.000	695.000	730.000	490.000	504.000	733.000	0.000	0.000	0.000	819289_2_mal1

Appendix 4

EPMA Results: Copper Oxides

	Na	Mg	Al	Si	P	S	K	Ca	Mn	Fe	Cu	Zn	Sr	Ba	Pb	C	O	Total	Sample No.
Weight%	-0.029	-0.030	0.017	0.353	9.645	0.023	-0.004	0.007	-0.017	0.041	55.777	0.005	-0.025	0.102	-0.001	1.886	31.961	99.814	819289_2_malrim1-green
Atomic%	-0.038	-0.036	0.019	0.374	9.278	0.021	-0.003	0.005	-0.009	0.022	26.154	0.002	-0.008	0.022	0.000	4.678	59.521	100.095	819289_2_malrim1-green
Det Lim ppm	360.000	336.000	253.000	244.000	416.000	237.000	226.000	330.000	573.000	457.000	729.000	736.000	507.000	508.000	790.000	0.000	0.000	0.000	819289_2_malrim1-green
Weight%	-0.003	0.100	1.022	17.968	0.025	0.039	0.032	0.192	-0.007	0.370	26.881	-0.004	0.129	0.006	-0.007	6.739	46.468	99.970	819289_2_malrim2-clear
Atomic%	-0.003	0.089	0.826	13.952	0.018	0.026	0.018	0.104	-0.003	0.145	9.225	-0.001	0.032	0.001	-0.001	12.235	63.336	100.008	819289_2_malrim2-clear
Det Lim ppm	266.000	207.000	199.000	240.000	248.000	198.000	199.000	287.000	542.000	459.000	598.000	631.000	401.000	467.000	672.000	0.000	0.000	0.000	819289_2_malrim2-clear
Weight%	1.265	2.777	16.517	13.630	0.007	-0.006	0.011	0.742	-0.015	9.978	0.018	0.021	0.201	-0.048	-0.019	5.190	49.510	99.869	819252_1_radxtals1
Atomic%	1.102	2.288	12.260	9.720	0.005	-0.004	0.006	0.371	-0.006	3.578	0.006	0.006	0.046	-0.007	-0.002	8.655	61.975	100.018	819252_1_radxtals1
Det Lim ppm	214.000	215.000	219.000	230.000	241.000	195.000	198.000	273.000	552.000	485.000	443.000	535.000	374.000	451.000	634.000	0.000	0.000	0.000	819252_1_radxtals1
Weight%	0.958	4.408	21.653	9.680	0.001	-0.005	0.005	0.950	441.857	4.352	0.050	0.019	0.116	-0.027	-0.024	0.000	163.864	647.914	819252_1_radxtals2
Atomic%	0.211	0.918	4.062	1.744	0.000	-0.001	0.001	0.120	40.706	0.394	0.004	0.001	0.007	-0.001	-0.001	0.000	51.834	100.002	819252_1_radxtals2
Det Lim ppm	267.000	296.000	259.000	200.000	192.000	169.000	153.000	239.000	23.000	376.000	385.000	463.000	348.000	335.000	528.000	0.000	0.000	0.000	819252_1_radxtals2
Weight%	0.206	0.455	1.789	3.866	0.082	0.072	0.007	0.011	-0.029	49.379	2.481	0.135	0.018	-0.022	0.034	5.460	35.932	99.927	819252_1_goe1
Atomic%	0.232	0.485	1.717	3.564	0.069	0.058	0.005	0.007	-0.014	22.893	1.011	0.054	0.005	-0.004	0.004	11.769	58.146	100.018	819252_1_goe1
Det Lim ppm	285.000	249.000	210.000	225.000	282.000	213.000	220.000	303.000	646.000	671.000	543.000	658.000	452.000	465.000	692.000	0.000	0.000	0.000	819252_1_goe1
Weight%	-0.031	-0.005	0.005	0.013	0.025	0.018	0.009	0.000	0.030	0.132	57.797	0.008	-0.019	0.058	0.013	7.404	34.398	99.910	819252_1_mal1
Atomic%	-0.036	-0.006	0.005	0.012	0.022	0.016	0.006	0.000	0.015	0.064	24.716	0.003	-0.006	0.012	0.002	16.752	58.423	100.048	819252_1_mal1
Det Lim ppm	375.000	282.000	238.000	246.000	305.000	213.000	216.000	209.000	539.000	466.000	707.000	715.000	498.000	509.000	713.000	0.000	0.000	0.000	819252_1_mal1
Weight%	-0.057	0.006	0.021	0.023	0.125	0.015	0.011	0.009	-0.001	0.108	57.669	0.003	-0.023	0.073	-0.022	7.371	34.412	99.846	819252_2_mal1
Atomic%	-0.067	0.007	0.021	0.022	0.109	0.013	0.007	0.006	0.000	0.053	24.670	0.001	-0.007	0.014	-0.003	16.684	58.468	100.077	819252_2_mal1
Det Lim ppm	396.000	262.000	232.000	245.000	308.000	226.000	213.000	313.000	538.000	469.000	729.000	710.000	508.000	496.000	747.000	0.000	0.000	0.000	819252_2_mal1
Weight%	1.552	3.727	15.667	15.069	0.002	-0.001	0.017	0.540	0.018	8.212	0.068	0.000	0.153	-0.006	-0.003	4.978	49.983	99.985	819252_2_radxtals1
Atomic%	1.340	3.042	11.519	10.645	0.001	-0.001	0.009	0.267	0.007	2.917	0.021	0.000	0.035	-0.001	0.000	8.223	61.977	100.002	819252_2_radxtals1
Det Lim ppm	211.000	207.000	217.000	223.000	280.000	185.000	191.000	255.000	515.000	485.000	429.000	1173329	377.000	428.000	628.000	0.000	0.000	0.000	819252_2_radxtals1
Weight%	1.690	4.192	16.627	16.350	0.002	0.001	0.037	0.400	0.025	6.027	0.095	0.049	0.137	-0.023	-0.006	4.259	50.074	99.965	819252_2_radxtals2-clear
Atomic%	1.455	3.414	12.199	11.524	0.001	0.001	0.019	0.197	0.009	2.136	0.029	0.015	0.031	-0.003	-0.001	7.019	61.954	100.004	819252_2_radxtals2-clear
Det Lim ppm	212.000	208.000	223.000	234.000	245.000	179.000	164.000	311.000	479.000	483.000	439.000	529.000	390.000	438.000	621.000	0.000	0.000	0.000	819252_2_radxtals2-clear
Weight%	1.574	3.780	15.414	15.496	0.019	0.001	0.017	0.578	0.032	9.112	0.119	-0.031	0.176	-0.017	-0.009	4.441	49.165	99.923	819252_2_radxtals3-greencore
Atomic%	1.377	3.128	11.490	11.097	0.012	0.001	0.009	0.290	0.012	3.282	0.038	-0.010	0.040	-0.002	-0.001	7.436	61.802	100.013	819252_2_radxtals3-greencore
Det Lim ppm	215.000	202.000	234.000	219.000	248.000	183.000	180.000	281.000	486.000	492.000	441.000	571.000	384.000	443.000	658.000	0.000	0.000	0.000	819252_2_radxtals3-greencore
Weight%	-0.024	-0.005	0.000	0.010	0.026	0.008	-0.001	0.001	0.001	0.128	57.744	-0.002	0.005	0.049	0.020	7.456	34.494	99.943	819250_3_mal1
Atomic%	-0.029	-0.006	0.000	0.010	0.023	0.006	0.000	0.001	0.001	0.062	24.637	-0.001	0.002	0.010	0.003	16.831	58.451	100.036	819250_3_mal1
Det Lim ppm	375.000	285.000	0.000	238.000	346.000	221.000	231.000	328.000	547.000	454.000	735.000	713.000	494.000	505.000	716.000	0.000	0.000	0.000	819250_3_mal1
Weight%	-0.037	-0.004	0.000	0.013	0.023	0.007	-0.007	-0.011	0.016	0.035	57.584	-0.032	-0.011	0.037	-0.011	7.523	34.585	99.824	819250_3_mal2
Atomic%	-0.043	-0.004	0.000	0.013	0.020	0.006	-0.005	-0.007	0.008	0.017	24.532	-0.013	-0.003	0.007	-0.001	16.957	58.518	100.078	819250_3_mal2
Det Lim ppm	359.000	291.000	0.000	240.000	292.000	219.000	233.000	320.000	532.000	472.000	729.000	722.000	497.000	500.000	754.000	0.000	0.000	0.000	819250_3_mal2
Weight%	-0.031	-0.009	0.000	0.045	0.013	0.524	0.010	0.015	-0.014	0.190	58.395	-0.035	-0.003	0.043	-0.043	6.816	33.749	99.799	819250_5_goe1
Atomic%	-0.037	-0.011	0.000	0.044	0.012	0.452	0.007	0.010	-0.007	0.094	25.415	-0.015	-0.001	0.009	-0.006	15.695	58.338	100.076	819250_5_goe1
Det Lim ppm	367.000	293.000	0.000	237.000	289.000	231.000	227.000	320.000	552.000	487.000	719.000	718.000	497.000	507.000	787.000	0.000	0.000	0.000	819250_5_goe1

Appendix 4

EPMA Results: Copper Oxides

	Na	Mg	Al	Si	P	S	K	Ca	Mn	Fe	Cu	Zn	Sr	Ba	Pb	C	O	Total	Sample No.
Weight%	0.002	0.001	0.000	0.065	0.023	0.611	0.027	-0.009	-0.001	0.351	58.894	-0.010	-0.043	0.037	0.030	6.528	33.340	99.908	819250_5_goe2
Atomic%	0.003	0.001	0.000	0.065	0.020	0.532	0.019	-0.007	-0.001	0.176	25.868	-0.004	-0.014	0.007	0.004	15.171	58.159	100.025	819250_5_goe2
Det Lim ppm	403.000	290.000	0.000	246.000	343.000	242.000	220.000	334.000	563.000	468.000	712.000	729.000	508.000	510.000	739.000	0.000	0.000	0.000	819250_5_goe2
Weight%	-0.026	-0.006	0.019	0.016	0.045	0.002	0.002	-0.001	-0.005	-0.106	57.332	-0.034	-0.022	0.044	-0.036	7.563	34.625	99.646	800921_1_mal1
Atomic%	-0.030	-0.006	0.019	0.015	0.039	0.001	0.001	0.000	-0.002	-0.052	24.419	-0.014	-0.007	0.009	-0.005	17.042	58.571	100.116	800921_1_mal1
Det Lim ppm	341.000	292.000	246.000	235.000	342.000	213.000	224.000	323.000	542.000	588.000	726.000	719.000	508.000	515.000	745.000	0.000	0.000	0.000	800921_1_mal1
Weight%	-0.022	-0.012	0.032	-0.001	0.040	0.010	-0.001	0.006	0.017	-0.001	57.504	-0.022	-0.046	0.094	0.017	7.519	34.594	99.833	800921_1_mal2
Atomic%	-0.026	-0.013	0.032	-0.001	0.035	0.009	0.000	0.004	0.008	0.000	24.492	-0.009	-0.014	0.019	0.002	16.943	58.520	100.064	800921_1_mal2
Det Lim ppm	342.000	310.000	230.000	255.000	332.000	203.000	227.000	303.000	549.000	454.000	725.000	714.000	513.000	497.000	717.000	0.000	0.000	0.000	800921_1_mal2
Weight%	-0.045	-0.008	0.017	0.032	0.057	-0.001	0.005	0.007	0.058	-0.106	57.332	-0.012	0.001	0.096	-0.031	7.517	34.561	99.682	800921_1_mal3
Atomic%	-0.053	-0.009	0.017	0.031	0.050	-0.001	0.003	0.005	0.029	-0.052	24.455	-0.005	0.000	0.019	-0.004	16.963	58.551	100.123	800921_1_mal3
Det Lim ppm	388.000	280.000	228.000	232.000	335.000	220.000	218.000	327.000	525.000	570.000	717.000	694.000	499.000	504.000	759.000	0.000	0.000	0.000	800921_1_mal3
Weight%	-0.003	0.014	0.141	0.204	0.015	0.012	0.018	0.032	8.587	0.058	4.198	0.003	0.016	0.340	0.070	22.445	63.841	99.994	800921_1_neot1
Atomic%	-0.002	0.010	0.086	0.119	0.008	0.006	0.008	0.013	2.562	0.017	1.083	0.001	0.003	0.041	0.006	30.633	65.408	100.002	800921_1_neot1
Det Lim ppm	201.000	164.000	155.000	160.000	221.000	162.000	168.000	231.000	587.000	440.000	410.000	489.000	326.000	378.000	468.000	0.000	0.000	0.000	800921_1_neot1
Weight%	-0.001	0.012	0.065	0.068	0.004	0.012	0.022	0.020	8.095	0.007	4.067	-0.001	-0.002	0.296	0.078	22.828	64.420	99.994	800921_1_neot2
Atomic%	-0.001	0.008	0.039	0.039	0.002	0.006	0.009	0.008	2.397	0.002	1.041	0.000	0.000	0.035	0.006	30.915	65.493	100.001	800921_1_neot2
Det Lim ppm	189.000	166.000	147.000	167.000	211.000	149.000	160.000	211.000	570.000	452.000	406.000	492.000	323.000	360.000	505.000	0.000	0.000	0.000	800921_1_neot2
Weight%	-0.023	-0.004	0.033	0.018	0.045	0.030	0.016	0.001	0.040	0.043	57.427	-0.034	0.001	0.071	0.006	7.516	34.653	99.900	800921_2_mal1
Atomic%	-0.027	-0.005	0.033	0.018	0.039	0.025	0.011	0.000	0.020	0.021	24.423	-0.014	0.000	0.014	0.001	16.910	58.531	100.046	800921_2_mal1
Det Lim ppm	362.000	284.000	242.000	249.000	285.000	223.000	209.000	319.000	562.000	459.000	713.000	709.000	489.000	501.000	722.000	0.000	0.000	0.000	800921_2_mal1
Weight%	0.011	0.004	0.064	0.104	0.020	0.016	0.017	0.020	8.345	0.055	4.368	0.012	-0.013	0.353	0.121	22.551	63.921	99.982	800921_2_neot1
Atomic%	0.008	0.003	0.039	0.061	0.011	0.008	0.007	0.008	2.488	0.016	1.126	0.003	-0.002	0.042	0.010	30.748	65.426	100.002	800921_2_neot1
Det Lim ppm	188.000	182.000	149.000	159.000	211.000	159.000	162.000	234.000	560.000	441.000	415.000	484.000	332.000	364.000	522.000	0.000	0.000	0.000	800921_2_neot1
Weight%	0.013	0.007	0.056	0.102	0.007	0.023	0.018	0.008	8.740	0.070	4.452	-0.010	0.002	0.358	0.109	22.394	63.624	99.985	800921_2_neot2
Atomic%	0.009	0.005	0.034	0.060	0.004	0.012	0.008	0.003	2.615	0.021	1.152	-0.003	0.000	0.043	0.009	30.653	65.375	100.003	800921_2_neot2
Det Lim ppm	184.000	166.000	155.000	160.000	222.000	172.000	168.000	258.000	510.000	470.000	416.000	477.000	332.000	373.000	521.000	0.000	0.000	0.000	800921_2_neot2
Weight%	-0.036	-0.003	0.091	0.064	0.046	0.018	0.010	0.003	0.050	0.052	57.133	0.005	-0.022	0.042	-0.012	7.568	34.807	99.888	800921_2_green-core1
Atomic%	-0.042	-0.004	0.091	0.061	0.040	0.015	0.007	0.002	0.025	0.025	24.216	0.002	-0.007	0.008	-0.002	16.970	58.592	100.054	800921_2_green-core1
Det Lim ppm	362.000	290.000	226.000	232.000	331.000	209.000	223.000	319.000	537.000	452.000	721.000	698.000	498.000	505.000	756.000	0.000	0.000	0.000	800921_2_green-core1
Weight%	-0.035	-0.001	0.078	0.039	0.048	0.013	-0.002	0.005	0.033	0.046	57.132	-0.012	-0.006	0.086	-0.039	7.584	34.800	99.864	800921_2_green-needle1
Atomic%	-0.040	-0.001	0.078	0.037	0.041	0.011	-0.001	0.004	0.016	0.022	24.222	-0.005	-0.002	0.017	-0.005	17.011	58.596	100.055	800921_2_green-needle1
Det Lim ppm	380.000	287.000	236.000	249.000	354.000	211.000	220.000	329.000	549.000	456.000	725.000	715.000	491.000	491.000	755.000	0.000	0.000	0.000	800921_2_green-needle1
Weight%	0.003	0.078	0.642	7.123	0.015	0.020	0.004	0.112	0.058	0.112	10.069	0.031	0.044	0.006	-0.009	19.170	62.505	99.990	800921_2_green-needle2
Atomic%	0.002	0.054	0.400	4.263	0.008	0.010	0.002	0.047	0.018	0.034	2.663	0.008	0.008	0.001	-0.001	26.825	65.659	100.001	800921_2_green-needle2
Det Lim ppm	189.000	186.000	150.000	175.000	212.000	143.000	180.000	232.000	410.000	397.000	443.000	499.000	334.000	391.000	555.000	0.000	0.000	0.000	800921_2_green-needle2
Weight%	-0.022	0.009	0.136	0.181	0.035	0.016	0.004	0.024	0.047	0.050	53.848	-0.017	-0.003	0.025	-0.020	8.610	36.926	99.910	800921_2_green-core2
Atomic%	-0.025	0.009	0.130	0.166	0.029	0.013	0.003	0.015	0.022	0.023	21.802	-0.007	-0.001	0.005	-0.002	18.442	59.377	100.035	800921_2_green-core2
Det Lim ppm	352.000	265.000	217.000	233.000	236.000	208.000	220.000	294.000	527.000	460.000	698.000	711.000	473.000	516.000	686.000	0.000	0.000	0.000	800921_2_green-core2

Abbreviations: cup = cuprite; mal = malachite; chrys = chrysocolla; azur = azurite; chl = chlorite; CuPhos = copper phosphate; neot = neotocite; geo = goethite; malrim = malachite rim; repl = replaced by; radxtals = radiating crystals

APPENDIX 5

EPMA RESULTS: COPPER OXIDES
(Weight % of Oxide Cations)

Appendix 5
EPMA Results: Copper Oxides

Wt%	Na2O	K2O	MgO	CaO	MnO	FeO	CuO	ZnO	SrO	BaO	PbO	Al2O3	CO2	SiO2	P2O5	SO3	Total	Samp No
Wt% Oxide	-0.0503	0.0035	-0.0189	0.0077	-0.0022	0.0534	68.5652	-0.0254	0.0052	0.0886	0.0107	0.0000	27.6975	3.3135	0.0778	0.0801	99.9033	819222_2_mal1
Wt% Oxide	-0.0356	-0.0027	0.0046	0.0254	-0.0175	0.1183	72.2046	0.0151	-0.0199	0.0987	-0.0064	0.0000	27.2237	0.1002	0.1112	-0.0163	99.9016	819223_1_mal1
Wt% Oxide	-0.0325	0.0024	-0.0289	0.0124	-0.0029	0.0000	68.6260	-0.0993	-0.0251	0.0424	-0.0242	0.0000	7.4734	0.3462	23.2029	0.0688	99.7871	819223_2_chrys1
Wt% Oxide	-0.0030	0.0074	-0.0192	0.0131	0.0316	0.1053	71.2218	0.0388	-0.0321	0.0474	0.0043	0.0000	28.2042	0.1579	0.1011	0.0130	99.9458	819223_2_mal1
Wt% Oxide	-0.0264	0.0035	-0.0054	0.0046	-0.0084	0.1042	69.6649	-0.0141	0.0183	0.0684	0.0520	0.0227	29.6603	-0.0031	0.3163	0.0274	99.9425	819237_1_azur1
Wt% Oxide	-0.0426	0.0062	0.0527	-0.0107	0.0420	0.1955	71.4331	0.0575	-0.0226	0.0887	0.0095	0.0520	27.6879	0.0335	0.2423	0.0233	99.9241	819237_1_mal1
Wt% Oxide	-0.0675	0.0172	0.0100	-0.0054	-0.0047	0.0322	69.6463	0.0268	-0.0045	0.0830	0.0361	0.0233	29.5995	0.0075	0.4270	0.0091	99.9180	819237_2_azur1
Wt% Oxide	0.0554	0.0317	4.8766	0.0626	0.0409	3.8396	44.4429	0.0104	0.0573	0.0509	-0.0165	11.9875	16.3672	17.9001	0.0410	0.2193	99.9836	819294_1_chl1
Wt% Oxide	0.2295	0.1945	6.1308	0.0900	0.0422	7.5979	36.0354	0.0586	0.1037	0.0021	-0.0089	14.6942	9.4891	25.1662	0.0419	0.1152	99.9911	819294_1_chl2
Wt% Oxide	0.0390	0.0503	11.5516	0.0596	0.2272	21.5799	10.3005	0.2064	0.1189	-0.0055	0.0402	15.3571	13.9513	26.4226	0.0270	0.0630	99.9945	819294_2_chl1
Wt% Oxide	0.0212	0.0194	18.1146	0.0587	0.1603	13.2219	2.5307	0.0286	0.1320	-0.0240	-0.0069	19.4214	14.0236	32.2119	0.0233	0.0014	99.9692	819294_2_chl2-light
Wt% Oxide	0.0104	0.0349	4.1317	0.0466	0.0414	4.6910	18.3273	0.0635	0.1603	0.0144	-0.0104	27.4878	6.0566	38.7176	0.0411	0.1649	99.9896	819294_3_chl1-dark
Wt% Oxide	-0.0162	0.0084	4.7028	0.0282	0.0339	3.8455	55.4621	0.0081	0.0800	0.0512	0.0066	13.3732	3.3553	18.8431	0.0418	0.1434	99.9838	819294_3_cup-chl2-dark
Wt% Oxide	0.1896	0.0169	4.7092	0.0495	0.0449	4.2087	33.3086	0.0366	0.1118	0.0479	-0.0114	22.8788	3.1565	30.8829	0.0321	0.3146	99.9886	819294_4_chl1
Wt% Oxide	0.0198	0.0610	1.0147	0.1643	0.0446	2.8104	54.3618	0.0005	0.0414	0.0765	-0.0144	26.6558	2.8537	11.0864	0.0648	0.7299	99.9856	819294_4_cup-chl2-red
Wt% Oxide	-0.0648	0.0090	-0.0416	0.0313	-0.0041	-0.0189	81.7300	0.0689	0.0125	0.0972	0.0241	0.0066	0.0000	0.2783	24.2281	0.0297	106.5157	819235_1_chrys1
Wt% Oxide	-0.0389	0.0027	-0.0175	0.0239	-0.0127	0.0343	69.2291	0.0711	0.0051	0.0600	-0.0077	0.0194	6.9332	0.2635	23.2338	0.0471	99.9233	819235_1_chrys2
Wt% Oxide	-0.0269	0.0028	-0.0290	0.0170	0.0043	-0.0562	69.3738	0.0880	-0.0112	0.0614	-0.0099	0.0227	6.3163	0.2948	23.6818	0.0040	99.8669	819235_2_chrys1
Wt% Oxide	-0.0573	-0.0016	-0.0527	0.0116	-0.0005	0.0569	69.4331	0.0382	0.0003	0.0876	-0.0110	-0.0104	6.7594	0.2928	23.1543	0.0323	99.8666	819235_2_CuPhos1
Wt% Oxide	-0.0509	0.0126	-0.0351	0.0131	0.0016	0.0075	69.4828	0.0065	-0.0046	0.0497	-0.0263	0.0058	6.6265	0.2638	23.3940	0.0189	99.8830	819235_2_CuPhos2
Wt% Oxide	-0.0076	0.0228	0.0117	0.1214	0.0266	67.3219	4.6328	0.1311	0.0025	0.0019	0.0399	0.0124	20.5284	4.2862	2.8021	0.0507	99.9924	819235_2_Goe1
Wt% Oxide	-0.0487	-0.0180	-0.0342	0.0424	-0.0050	0.1190	69.1998	0.0060	-0.0370	0.0934	0.0318	0.0058	6.7990	0.5227	23.0305	0.0067	99.8571	819235_2_CuPhos3
Wt% Oxide	-0.0550	-0.0054	0.0000	-0.0184	0.0110	0.0533	72.8477	-0.0371	-0.0060	0.1026	0.0053	0.0256	26.4351	0.1010	0.2942	-0.0020	99.8759	819224_1_mal1
Wt% Oxide	-0.0411	0.0063	-0.1444	-0.0108	0.0297	0.0209	69.6270	-0.0005	-0.0173	0.0889	-0.0230	0.0143	7.6326	0.3094	21.9564	0.0774	99.7628	819224_1_CuPhos1
Wt% Oxide	-0.0795	-0.0138	-0.1720	0.0263	-0.0047	-0.0017	69.4896	0.0364	0.0213	0.0570	0.0670	0.0065	7.8223	0.2844	21.8320	0.0856	99.7283	819224_1_CuPhos2
Wt% Oxide	0.0166	0.0354	0.0000	0.0983	-0.0125	67.2885	4.6752	-0.0218	0.0279	0.0274	0.0154	0.6654	20.1386	6.3020	0.5221	0.1530	99.9657	819224_1_Goe1
Wt% Oxide	-0.0341	0.0066	0.0348	0.0238	0.0241	0.0099	72.1849	0.0050	0.0035	0.0750	-0.0117	0.1075	26.8181	0.1451	0.5139	0.0020	99.9542	819224_2_mal1
Wt% Oxide	-0.0333	0.0090	-0.1620	0.0317	-0.0115	0.1811	69.4495	-0.0373	-0.0124	0.0389	0.0614	-0.0007	7.6172	0.3240	21.8545	0.1757	99.7428	819224_2_CuPhos1
Wt% Oxide	-0.0339	0.0008	-0.0572	0.0547	-0.0229	20.7287	49.9985	-0.0415	-0.0122	0.0364	-0.0227	0.0394	10.6730	2.3547	15.8399	0.0835	99.8096	819224_2_CuPhos2-repl goe
Wt% Oxide	0.7145	5.1694	2.6802	0.1466	-0.0249	2.9620	1.1200	0.0164	0.2299	-0.0091	0.0012	29.3967	9.5439	47.9302	0.0367	0.0185	99.9660	819206_1_Clay-faintgreen1
Wt% Oxide	1.3955	2.0039	1.1274	0.3077	-0.0242	2.5575	8.0945	0.0508	0.2255	-0.0153	-0.0150	24.0310	13.0903	47.0181	0.0257	0.0176	99.9456	819206_1_Clay-faintgreen2
Wt% Oxide	0.1593	8.6660	6.3648	0.0741	0.0089	4.1408	2.2183	0.0422	0.2036	0.0142	0.0264	25.1634	7.7733	45.1143	0.0128	0.0176	100.0000	819206_1_Clay-faintgreen3
Wt% Oxide	2.9087	0.6791	0.3574	0.5305	0.0003	0.6840	19.8119	0.0038	0.2086	0.0213	-0.0102	9.7230	21.1616	43.7913	0.0398	0.0685	99.9898	819206_1_Clay-faintgreen4
Wt% Oxide	-0.0668	-0.0004	-0.0211	0.0123	-0.0214	0.0074	72.5218	0.0070	-0.0337	0.0820	-0.0053	0.0606	26.8854	0.0307	0.2124	0.0320	99.8514	819248_1_mal1
Wt% Oxide	-0.0132	0.0089	-0.0027	0.0023	-0.0014	0.0131	70.0385	-0.0045	0.0106	0.0467	-0.0264	0.0266	29.6482	0.0142	0.1142	0.0285	99.9518	819248_1_azur1
Wt% Oxide	0.0014	0.0475	0.1359	0.0758	0.0292	0.1495	9.5081	-0.0286	0.1397	0.0006	-0.0034	19.6073	37.4949	32.7392	-0.0062	0.0326	99.9617	819248_1_chrys1-faint blue
Wt% Oxide	-0.0077	0.0619	0.0569	0.0659	-0.0060	0.1997	10.1935	-0.0381	0.1525	0.0100	-0.0079	19.0884	37.8837	32.1704	0.0082	0.0495	99.9405	819248_1_chrys2-faint blue
Wt% Oxide	0.0978	0.0646	0.1696	0.3385	0.0355	0.3756	37.4466	0.0602	0.1697	0.0276	-0.0167	2.3481	19.9868	38.4390	0.0582	0.3656	99.9833	819289_1_chrys1-faint green
Wt% Oxide	-0.0085	0.0092	0.3013	0.1325	-0.0058	0.2285	25.5023	0.0370	0.1099	0.0139	0.0033	1.1033	44.1379	28.3763	0.0142	0.0163	99.9857	819289_1_chrys2-interior
Wt% Oxide	-0.0351	0.0067	-0.0682	-0.0054	-0.0726	0.1417	64.2696	-0.0305	-0.0243	0.0709	-0.0076	0.4080	13.0109	1.0812	20.7521	0.0153	99.7564	819289_2_mal1
Wt% Oxide	-0.0397	-0.0047	-0.0493	0.0093	-0.0218	0.0527	69.8206	0.0060	-0.0291	0.1138	-0.0011	0.0318	6.9090	0.7542	22.1003	0.0565	99.8543	819289_2_malrim1-green
Wt% Oxide	-0.0041	0.0381	0.1653	0.2684	-0.0084	0.4763	33.6489	-0.0054	0.1520	0.0065	-0.0079	1.9318	24.6913	38.4410	0.0584	0.0963	99.9743	819289_2_malrim2-clear
Wt% Oxide	1.7056	0.0131	4.6053	1.0388	-0.0199	12.8370	0.0224	0.0260	0.2380	-0.0533	-0.0205	31.2087	19.0188	29.1599	0.0168	-0.0160	99.8903	819252_1_radxtals1
Wt% Oxide	1.2917	0.0058	7.3099	1.3295	570.5413	5.5991	0.0631	0.0234	0.1372	-0.0303	-0.0257	40.9135	0.0000	20.7102	0.0018	-0.0127	647.9266	819252_1_radxtals2
Wt% Oxide	0.2781	0.0085	0.7543	0.0153	-0.0377	63.5254	3.1060	0.1686	0.0209	-0.0244	0.0365	3.3810	20.0052	8.2712	0.1878	0.1789	99.9379	1819252_1_goe1
Wt% Oxide	-0.0416	0.0105	-0.0083	0.0000	0.0382	0.1701	72.3490	0.0100	-0.0226	0.0650	0.0138	0.0088	27.1313	0.0276	0.0576	0.0457	99.9276	819252_1_mal1
Wt% Oxide	-0.0764	0.0128	0.0101	0.0123	-0.0008	0.1389	72.1888	0.0040	-0.0274	0.0813	-0.0234	0.0397	27.0103	0.0494	0.2859	0.0385	99.8720	819252_2_mal1

Appendix 5
EPMA Results: Copper Oxides

Wt%	Na2O	K2O	MgO	CaO	MnO	FeO	CuO	ZnO	SrO	BaO	PbO	Al2O3	CO2	SiO2	P2O5	SO3	Total	Samp No
Wt% Oxide	2.0924	0.0208	6.1800	0.7549	0.0235	10.5643	0.0847	0.0000	0.1804	-0.0064	-0.0034	29.6019	18.2413	32.2391	0.0042	-0.0028	99.9874	819252_2_radxtals1
Wt% Oxide	2.2783	0.0448	6.9513	0.5591	0.0320	7.7542	0.1183	0.0607	0.1625	-0.0253	-0.0069	31.4170	15.6043	34.9781	0.0043	0.0028	99.9678	819252_2_radxtals2-clear
Wt% Oxide	2.1213	0.0208	6.2682	0.8085	0.0412	11.7224	0.1495	-0.0385	0.2083	-0.0188	-0.0092	29.1245	16.2717	33.1514	0.0424	0.0035	99.9336	819252_2_radxtals3-greencore
Wt% Oxide	-0.0327	-0.0008	-0.0083	0.0015	0.0018	0.1651	72.2837	-0.0030	0.0064	0.0542	0.0214	0.0000	27.3207	0.0214	0.0298	0.0000	99.8320	819250_3_mal1
Wt% Oxide	0.0033	0.0320	0.0019	-0.0131	-0.0018	0.4519	73.7221	-0.0121	-0.0504	0.0409	0.0321	0.0000	23.9217	0.1393	0.0519	1.5255	99.9226	819250_5_goe2
Wt% Oxide	-0.0349	0.0020	-0.0092	-0.0008	-0.0059	-0.1368	71.7670	-0.0423	-0.0264	0.0486	-0.0384	0.0363	27.7111	0.0332	0.1034	0.0039	99.7055	800921_1_mal1
Wt% Oxide	-0.0296	-0.0008	-0.0192	0.0085	0.0222	-0.0008	71.9826	-0.0271	-0.0549	0.1049	0.0181	0.0612	27.5503	-0.0031	0.0913	0.0254	99.8644	800921_1_mal2
Wt% Oxide	-0.0607	0.0054	-0.0128	0.0100	0.0751	-0.1366	71.7670	-0.0151	0.0014	0.1069	-0.0330	0.0316	27.5428	0.0688	0.1309	-0.0020	99.7399	800921_1_mal3
Wt% Oxide	-0.0044	0.0219	0.0237	0.0448	11.0877	0.0742	5.2555	0.0035	0.0191	0.3794	0.0758	0.2670	82.2421	0.4358	0.0347	0.0304	99.9956	800921_1_neot1
Wt% Oxide	-0.0011	0.0267	0.0199	0.0276	10.4529	0.0088	5.0914	-0.0012	-0.0029	0.3308	0.0835	0.1219	83.6454	0.1457	0.0092	0.0312	99.9949	800921_1_neot2
Wt% Oxide	-0.0311	0.0187	-0.0073	0.0008	0.0520	0.0559	71.8864	-0.0422	0.0015	0.0796	0.0064	0.0619	27.5392	0.0394	0.1032	0.0744	99.9193	800921_2_mal1
Wt% Oxide	0.0144	0.0208	0.0073	0.0284	10.7750	0.0702	5.4673	0.0152	-0.0154	0.3936	0.1304	0.1211	82.6327	0.2235	0.0459	0.0388	99.9846	2800921_2_neot1
Wt% Oxide	0.0178	0.0220	0.0120	0.0117	11.2849	0.0899	5.5732	-0.0129	0.0023	0.3999	0.1179	0.1064	82.0570	0.2178	0.0165	0.0579	99.9871	800921_2_neot2
Wt% Oxide	-0.0487	0.0117	-0.0055	0.0038	0.0647	0.0673	71.5181	0.0065	-0.0257	0.0467	-0.0127	0.1727	27.7304	0.1365	0.1049	0.0442	99.9075	800921_2_green-core1
Wt% Oxide	-0.0465	-0.0023	-0.0018	0.0077	0.0428	0.0592	71.5170	-0.0151	-0.0075	0.0964	-0.0425	0.1475	27.7885	0.0831	0.1090	0.0332	99.8843	800921_2_green-needle1
Wt% Oxide	0.0037	0.0046	0.1288	0.1561	0.0749	0.1435	12.6045	0.0382	0.0522	0.0065	-0.0097	1.2128	70.2415	15.2386	0.0345	0.0499	99.9903	800921_2_green-needle2
Wt% Oxide	-0.0299	0.0051	0.0144	0.0333	0.0604	0.0642	67.4066	-0.0209	-0.0040	0.0277	-0.0213	0.2567	31.5480	0.3880	0.0792	0.0405	99.9240	800921_2_green-core2

Abbreviations: cup = cuprite; mal = malachite; chrys = chrysocolla; azur = azurite; chl = chlorite; CuPhos = copper phosphate; neot = neotocite; geo = goethite; malrim = malachite rim; repl = replaced by; radxtals = radiating crystals

APPENDIX 6

CARBON & OXYGEN ISOTOPE RESULTS

Appendix 6

Carbon & Oxygen Isotope Results

SampNo	HoleID	Depth	Date	Wt (mg)	Yield (mm Hg)	Transducer (mBar)	Reference Ion Gauge	Sample Ion Gauge	Delta 45	Delta 46	Delta 13C wrt PDB	Precision Delta 13C	Delta 18O wrt PDB	Precision Delta 18O	Delta 18O wrt SMOW	Description
819216	TSD18	65.70	11/6/03	31.7		16.3	0.000000152	0.000000152	-12.159	8.55	**-19.483**	0.017	**-4.031**	0.006	**26.705**	Fracture-filling malachite
819219	TSD18	111.00	11/6/03	39.5		20.8	0.000000151	0.00000015	-11.2	9.239	**-18.489**	0.005	**-3.353**	0.012	**27.404**	Fracture-filling malachite in hydrothermal breccia
819246	TSD38	85.25	11/6/03	42.5		25.7	0.00000015	0.00000015	-12.511	8.78	**-19.865**	0.007	**-3.804**	0.010	**26.939**	Fracture-filling malachite
819249	TSD38	97.15	11/6/03	20.8		23.6	0.00000015	0.00000015	6.283	11.595	**-0.014**	0.015	**-1.065**	0.009	**29.762**	Azurite in fracture
819251	TSD38	110.60	11/6/03	21.4		27.3	0.000000149	0.000000148	11.978	10.642	**6.062**	0.007	**-2.019**	0.017	**28.779**	Coarse crystal of azurite
819276	TSD62	71.00	11/6/03	13.6		27.8	0.000000153	0.000000153	-3.185	7.365	**-9.920**	0.013	**-5.222**	0.010	**25.477**	Shells in sandstone
819277	TSD13	55.00	11/6/03	16.8		20.8	0.000000151	0.000000154	-3.846	6.836	**-10.603**	0.010	**-5.742**	0.013	**24.941**	Buff-coloured shells in mudstone
819278	TSD45	11.40	11/6/03	17.6		19	0.000000152	0.00000015	-1.857	8.605	**-8.552**	0.021	**-4.000**	0.014	**26.737**	Shells in sandstone-mudstone
819279	TSD30	176.30	11/6/03	19.0		26	0.000000155	0.000000157	-4.685	8.683	**-11.556**	0.012	**-3.917**	0.013	**26.822**	Shells in mudstone
819281	JSD11	180.85	11/6/03	16.5		23.9	0.000000155	0.000000152	1.63	9.075	**-4.867**	0.012	**-3.543**	0.011	**27.208**	Cream massive limestone (Timamana)
819282	JSD16	166.80	11/6/03	16.6		26.4	0.000000154	0.000000155	7.197	6.318	**1.134**	0.018	**-6.279**	0.018	**24.387**	Cream massive limestone (Ttimamana)
819283	JSD04	459.40	11/6/03	15.9		18.5	0.000000153	0.000000154	5.646	5.771	**-0.494**	0.008	**-6.815**	0.008	**23.835**	Dark limestone (Bacuag)
819284	JSD02	387.00	11/6/03	16.0		18	0.000000152	0.000000152	7.044	6.563	**0.963**	0.024	**-6.036**	0.019	**24.638**	Gray massive limestone (Bacuag)
819285	JSD19	297.95	11/6/03	16.1		16.4	0.000000152	0.000000151	4.662	3.636	**-1.466**	0.020	**-8.921**	0.016	**21.664**	Brown to gray limestone (Bacuag)
819286	JSD20	192.40	11/6/03	15.8		28.7	0.000000153	0.000000152	7.602	3.571	**1.656**	0.015	**-8.992**	0.029	**21.591**	Gray fossiliferous limestone (Bacuag)
819287	BSD11	101.10	11/6/03	16.0		35.5	0.000000148	0.000000148	7.036	6.891	**0.943**	0.012	**-5.712**	0.013	**24.972**	Brown to gray limestone (Bacuag)
819274	TSD18	53.2	11/12/03	4.7	24.2						**-27.20**		**0.00**		**0.00**	Wood (Tugunan)
819275	TSD11	279.6	11/12/03	6.3	29.4						**-26.90**		**0.00**		**0.00**	Wood (Tugunan)

Abbreviations: PDB = standard derived from the belemnite *Belemnita americana*, from the Pee Dee Formation in South Carolina, USA; SMOW = standard mean ocean water; C = carbon; O = oxygen